

**MATERIALS FOR ADAPTIVE STRUCTURAL
ACOUSTIC CONTROL**

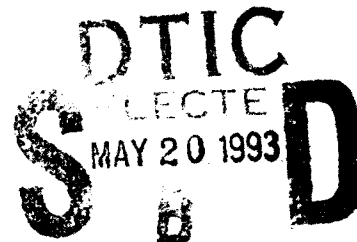
AD-A264 619


Period February 1, 1992 to January 31, 1993

Annual Report



VOLUME I



**OFFICE OF NAVAL RESEARCH
Contract No. N00014-92-J-1510**

APPROVED FOR PUBLIC RELEASE - DISTRIBUTION UNLIMITED

Reproduction in whole or in part is permitted for any purpose
of the United States Government

L. Eric Cross

PENNSTATE



**THE MATERIALS RESEARCH LABORATORY
UNIVERSITY PARK, PA**

93 5 15 070

93-11222



REPORT DOCUMENTATION PAGE

Form Approved
OMB No. 0704-0188

Public reporting burden for this collection of information is estimated to average 1 hour per response, including the time for reviewing instructions, searching existing data sources, gathering and maintaining the data needed, and completing and reviewing the collection of information. Send comments regarding this burden estimate or any other aspect of this collection of information, including suggestions for reducing this burden, to Washington Headquarters Services, Directorate for Information Operations and Reports, 1215 Jefferson Davis Highway, Suite 1204, Arlington, VA 22202-4302, and to the Office of Management and Budget, Paperwork Reduction Project (0704-0188), Washington, DC 20503.

1. AGENCY USE ONLY (Leave blank)		2. REPORT DATE 04/06/93		3. REPORT TYPE AND DATES COVERED ANNUAL REPORT 02/01/92 TO 01/31/93	
4. TITLE AND SUBTITLE MATERIALS FOR ADAPTIVE STRUCTURAL ACOUSTIC CONTROL				5. FUNDING NUMBERS	
6. AUTHOR(S) L. ERIC CROSS					
7. PERFORMING ORGANIZATION NAME(S) AND ADDRESS(ES) MATERIALS RESEARCH LABORATORY THE PENNSYLVANIA STATE UNIVERSITY UNIVERSITY PARK, PA 16802				8. PERFORMING ORGANIZATION REPORT NUMBER N00014-92-J-1510	
9. SPONSORING/MONITORING AGENCY NAME(S) AND ADDRESS(ES) OFFICE OF NAVAL RESEARCH DOUGLAS E. HEATON CODE 1513:NRJ DEPT. NAVY/ONR, RES. REP. 800 NORTH QUINCY STREET THE OHIO STATE UNIV. RES. CTR. ARLINGTON, VA 22217 1960 KENNY ROAD COLUMBUS, OH 43210-1063				10. SPONSORING/MONITORING AGENCY REPORT NUMBER	
11. SUPPLEMENTARY NOTES					
12a. DISTRIBUTION/AVAILABILITY STATEMENT				12b. DISTRIBUTION CODE	
13. ABSTRACT (Maximum 200 words) SEE FOLLOWING PAGE					
14. SUBJECT TERMS				15. NUMBER OF PAGES	
				16. PRICE CODE	
17. SECURITY CLASSIFICATION OF REPORT	18. SECURITY CLASSIFICATION OF THIS PAGE	19. SECURITY CLASSIFICATION OF ABSTRACT	20. LIMITATION OF ABSTRACT		

ABSTRACT

This report documents work carried out in the Materials Research Laboratory of the Pennsylvania State University over the first year of a new ONR sponsored University Research Initiative (URI) entitled "Materials for Adaptive Structural Acoustic Control." For this report the activities have been grouped under the following topic headings:

1. General Summary Papers.
2. Materials Studies.
3. Composite Sensors.
4. Actuator Studies.
5. Integration Issues.
6. Processing Studies.
7. Thin Film Ferroelectrics.

In material studies important advances have been made in the understanding of the evaluation of relaxor behavior in the PLZT's and of the order disorder behavior in lead scandium tantalate:lead titanate solid solutions and of the Morphotropic Phase Boundary in this system. For both composite sensors and actuators we have continued to explore and exploit the remarkable versatility of the flextensional moonie type structure. Finite element (FEA) calculations have given a clear picture of the lower order resonant modes and permitted the evaluation of various end cap metals, cap geometries and load conditions. In actuator studies multilayer structures have been combined with flextensional moonie endcaps to yield high displacement (50 μ meter) compact structures. Electrically controlled shape memory has been demonstrated in lead zirconate stannate titanate compositions, and used for controlling a simple latching relay. Detailed study of fatigue in polarization switching compositions has highlighted the important roles of electrodes, grain size, pore structures and microcracking and demonstrated approaches to controlling these problems. For practical multilayer actuators a useful lifetime prediction can be made from acoustic emission analysis.

New modelling of 2:2 and 1:3 type piezoceramic:polymer composites has given more exact solutions for the stress distribution and good agreement with ultradilatometer measurements of local deformations. Composites with 1:3 connectivity using thin wall ceramic tubes appear to offer excellent hydrostatic sensitivity, unusual versatility for property control and the possibility to use field biased electrostrictors in high sensitivity configurations. Processing approaches have continued to use reactive calcining and have supplied the group with the wide range of ceramics used in these studies. For lead magnesium niobate:lead

**MATERIALS FOR ADAPTIVE STRUCTURAL
ACOUSTIC CONTROL**

Period February 1, 1992 to January 31, 1993

Annual Report

VOLUME I

**OFFICE OF NAVAL RESEARCH
Contract No. N00014-92-J-1510**

APPROVED FOR PUBLIC RELEASE – DISTRIBUTION UNLIMITED

Reproduction in whole or in part is permitted for any purpose
of the United States Government

L. Eric Cross

PENNSSTATE



**THE MATERIALS RESEARCH LABORATORY
UNIVERSITY PARK, PA**

TABLE OF CONTENTS

ABSTRACT	6
INTRODUCTION	7
1.0 GENERAL SUMMARY PAPERS	10
2.0 MATERIALS STUDIES	10
3.0 SENSOR STUDIES	12
4.0 ACTUATOR STUDIES	13
5.0 INTEGRATION ISSUES	14
6.0 PROCESSING STUDIES	14
7.0 THIN FILM FERROELECTRICS	15
8.0 HONORS AND AWARDS	15
9.0 APPRENTICE PROGRAM	17
10.0 PAPERS PUBLISHED IN REFEREED JOURNALS	18
11.0 INVITED PAPERS PRESENTED AT NATIONAL AND INTERNATIONAL MEETINGS	21
12.0 INVITED PRESENTATIONS AT UNIVERSITY, INDUSTRY AND GOVERNMENT LABORATORIES	23
13.0 CONTRIBUTED PAPERS AT NATIONAL AND INTERNATIONAL MEETINGS	24

APPENDICES

General Summary of Papers

1. R. E. Newnham, "Memories of Arthur Von Hippel," *Ferroelectrics* 137, 17 (1992).
2. C. Rosen, B. V. Hiresmath and R. E. Newnham, "Piezoelectricity," American Inst. of Physics, New York (1991).
3. R. E. Newnham, "Ferroelectric Sensors and Actuators Smart Electroceramics," *Ferroelectric Ceramics*, Editor N. Setter, Proc. of Summer School on Ferroelectrics, Ascona (1991).
4. R. E. Newnham, "Smart Electroceramics in the 1990's and Beyond," *J. European Ceramic Soc.* (1992).
5. V. Sundar and R. E. Newnham, "Electrostriction and Polarization," *Ferroelectrics* 135, 431 (1992).

Materials Studies

6. J. R. Giniewicz, A. S. Bhalla and L. E. Cross, "Identification of the Morphotropic Phase Boundary in Lead Scandium Tantalate-Lead Titanate Solid Solution System."
7. J. R. Giniewicz, A. S. Bhalla and L. E. Cross, "Variable Structure Ordering in Lead Scandium Tantalate-Lead Titanate Materials."
8. J. R. Giniewicz, A. S. Bhalla and L. E. Cross, "Lead Scandium Tantalate-Lead Titanate Materials for Field Stabilized Pyroelectric Device Applications," *Ferroelectrics Letters* **14**, 21 (1992).
9. A. S. Bhalla, R. Guo, L. E. Cross, G. Burns, F. H. Dacol and R. R. Neurgaonkar, "Glassy Polarization in the Ferroelectric Tungsten Bronze (BaSr) Nb₂O₆," *J. Appl. Phys.* **71** (11), 5591 (1992).
10. J. S. Yoon, V. S. Srikanth and A. S. Bhalla, "The Electrical Properties of Antiferroelectric Lead Zirconate-Ferroelectric Lead Zinc Niobate Ceramics with Lanthanum," *Proc. ISAF 1992, Greenville, South Carolina*, pp. 556.
11. E. F. Alberta, D. J. Taylor, A. S. Bhalla and T. Takenaka, "The DC Field Dependence of the Piezoelectric, Elastic and Dielectric Constants for a Lead Zirconate Based Ceramic," *Proc. ISAF 1992, Greenville, South Carolina*, pp. 560.
12. W. Cao and L. Eric Cross, "The Ratio of Rhombohedral and Tetragonal Phases at the Morphotropic Phase Boundary in Lead Zirconate Titanate," *Japan Journal of Applied Physics* **31** (Pt. 1, No. 5A), 1399 (1992).
13. C. A. Randall, M. G. Matsko, W. Cao and A. S. Bhalla, "A Transmission Electron Microscope Investigation of the R3m - R3c Phase Transition in Pb(ZrTi)O₃ Ceramics," *Solid State Comm.* **85** (3), 193 (1993).
14. Shaoping Li, Chi Yeun Huang, A. S. Bhalla and L. E. Cross, "90° Domain Reversal in Pb(Zr_xTi_{1-x})O₃ Ceramics," *Proc. ISAF 1992, Greenville, South Carolina*.
15. Shaoping Li, Jyh Sheen, Q. M. Zhang, Sei-Joo Jang, A. S. Bhalla and L. E. Cross, "Quasi Lumped Parameter Method for Microwave Measurements of Dielectric Dispersion in Ferroelectric Ceramics," *Proc. ISAF 1992, Greenville, South Carolina*.
16. H. Wang, Q. M. Zhang, L. E. Cross and A. O. Sykes, "Piezoelectric Dielectric and Elastic Properties of Poly (Vinylidene Fluoride/Trifluoroethylene)."
17. H. Wang, Q. M. Zhang, L. E. Cross and A. O. Sykes, "Clamping Effect on Piezoelectric Properties of Poly (Vinylidene Fluoride/Trifluoroethylene) Copolymers."

Composite Sensors

18. Ki-Young Oh, Yutaka Saito, Atsushi Furuta and Kenji Uchino, "Piezoelectricity in the Field Induced Ferroelectric Phase of Lead Zirconate Based Antiferroelectrics," *J. Amer. Ceram. Soc.* **75** (4), 795 (1992).

Composite Sensors (continued)

19. R. E. Newnham, Q. C. Xu, K. Onitsuka and S. Yoshikawa, "A New Type of Flexensional Transducer," Proc. 3rd Int. Mtg. on Transducers for Sonics and Ultrasonics (May 1992).
20. C. A. Randall, D. V. Miller, J. H. Adair and A. S. Bhalla, "Processing of Electroceramic-Polymer Composites Using the Electrorheological Effect," J. Mat. Res. 8 (4), 1 (1993).
21. C. A. Randall, S. Miyazaki, K. L. More, A. S. Bhalla and R. E. Newnham, "Structural-Property Relations in Dielectrophoretically Assembled BaTiO₃ Nanocomposites," Materials Letters 15, 26 (1992).
22. C. A. Randall, S. F. Wang, D. Laubscher, J. P. Dougherty and W. Huebner, "Structure Property Relations in Core-Shell BaTiO₃:LiF Ceramics," J. Mat. Res. (in press).
23. C. A. Randall, G. A. Rossetti and W. Cao, "Spatial Variations of Polarization in Ferroelectrics and Related Materials."
24. Jayu Chen, Qi Chang Xu, M. Blaszkiewicz, R. Meyer, Jr. and R. E. Newnham, "Lead Zirconate Titanate Films on Nickel-Titanium Shape Memory Alloys: SMARTIES," J. Amer. Ceram. Soc. 75 (10), 2891 (1992).

Actuator Studies

25. D. Damjanovic and R. E. Newnham, "Electrostrictive and Piezoelectric Materials for Actuator Applications," J. Intell. Mat. Syst. and Struct. 3, 190 (1992).
26. Y. Sugawara, K. Onitsuka, S. Yoshikawa, Q. C. Xu, R. E. Newnham and K. Uchino, "Metal-Ceramic Composite Actuators," J. Amer. Ceram. Soc. 75 (4), 996 (1992).
27. Q. C. Xu, A. Dogan, J. Tressler, S. Yoshikawa and R. E. Newnham, "Ceramic-Metal Composite Actuators," Ferroelectrics Special Issue.
28. K. Uchino, "Piezoelectric Ceramics in Smart Actuators and Systems," Proc. 1st European Conference on Smart Structures and Materials.
29. A. Furuta, Ki-Young Oh and K. Uchino, "Shape Memory Ceramics and Their Application to Latching Relays," Sensors and Materials 3 (4), 205 (1992).
30. K. Uchino and A. Furuta, "Destruction Mechanisms in Multilayer Ceramic Actuators," Proc. ISAF 1992, Greenville, South Carolina, pp. 195.
31. Q. Jiang, Wenwu Cao and L. E. Cross, "Electric Fatigue Initiated by Surface Contamination in High Polarization Ceramics," Proc. ISAF 1992, Greenville, South Carolina, pp. 107.
32. Q. Jiang, Wenwu Cao and L. E. Cross, "Electric Fatigue in PLZT Ceramics."

Integration Issues

33. Wenwu Cao, Q. M. Zhang and L. E. Cross, "Theoretical Study on the Static Performance of Piezoelectric Ceramic-Polymer Composite with 1-3 Connectivity," *J. Appl. Phys.* 72 (12), 5814 (1992).
34. Q. M. Zhang, Wenwu Cao, H. Wang and L. E. Cross, "Characterization of the Performance of 1-3 Type Piezocomposites for Low Frequency Applications," *J. Appl. Phys.* 73 (3), 1403 (1993).
35. Q. M. Zhang, Wenwu Cao, H. Wang and L. E. Cross, "Strain Profile and Piezoelectric Performance of Piezocomposites with 2-2 and 1-3 Connectivities," *Proc. ISAF 1992, Greenville, South Carolina*, pp. 252.
36. Q. M. Zhang, H. Wang and L. E. Cross, "Piezoelectric Tubes and 1-3 Type Tubular Composites as Tunable Actuators and Sensors."
37. Q. M. Zhang, H. Wang and L. E. Cross, "Piezoelectric Tubes and Tubular Composites for Actuator and Sensor Applications."

Processing Studies

38. Thomas R. Shrout and Scott L. Swartz, "Processing of Ferroelectric and Related Materials: A Review."
39. G. A. Rossetti, D. J. Watson, R. E. Newnham and J. H. Adair, "Kinetics of the Hydrothermal Crystallization of the Perovskite Lead Titanate," *J. Crystal Growth* 116, 251 (1992).
40. A. V. Prasadaraao, U. Selvaraj, S. Komarneni and A. S. Bhalla, "Sol-Gel Synthesis of $\text{Ln}_2(\text{Ln} = \text{La}, \text{Nd}) \text{Ti}_2\text{O}_7$," *J. Mat. Res.* 7 (10), 2859 (1992).
41. A. V. Prasadaraao, U. Selvaraj, S. Komarneni and A. S. Bhalla, "Sol Gel Synthesis of Strontium Pyroniobate and Calcium Pyroniobate," *J. Amer. Ceram. Soc.* 75 (10), 2697 (1992).
42. A. V. Prasadaraao, U. Selvaraj, S. Komarneni and A. S. Bhalla, "Fabrication of $\text{La}_2\text{Ti}_2\text{O}_7$ Thin Films by A Sol-Gel Technique," *Ferroelectrics Letters* 14, 65 (1992).
43. S. F. Wang, U. Kumar, W. Huebner, P. Marsh, H. Kankel and C. G. Oakley, "Grain Size Effects on the Induced Piezoelectric Properties of 0.9 PMN-0.1PT Ceramic," *Proc. ISAF 1992, Greenville, South Carolina*, pp. 148.
44. C. A. Randall, A. D. Hilton, D. J. Barber and T. R. Shrout, "Extrinsic Contributions to the Grain Size Dependence of Relaxor Ferroelectric $\text{Pb}(\text{Mg}_{1/3}\text{Nb}_{2/3})\text{O}_3\text{:PbTiO}_3$ Ceramics," *J. Mat. Res.* 8 (4) (1993).
45. B. V. Hiremath, R. E. Newnham and L. E. Cross, "Barrier Layer Capacitor Using Barium Bismuth Plumbate and Barium Plumbate," *J. Amer. Ceram. Soc.* 75 (11), 2953 (1992).
46. U. Kumar, S. F. Wang, S. Varanasi and J. P. Dougherty, "Grain Size Effects on the Dielectric Properties of Strontium Barium Titanate," *Proc. ISAF 1992, Greenville, South Carolina*, pp. 55.

Processing Studies (continued)

47. U. Kumar, S. F. Wang and J. P. Dougherty, "Preparation of Dense Ultra-Fine Grain Barium Titanate-Based Ceramics," Proc. ISAF 1992, Greenville, South Carolina, pp. 70.

Thin Film Ferroelectrics

48. J. Chen, K. R. Udayakumar, K. G. Brooks and L. E. Cross, "Dielectric Behavior of Ferroelectric Thin Films at High Frequencies," Proc. ISAF 1992, Greenville, South Carolina, pp. 182.
49. K. Uchino, N-Y. Lee, T. Toba, N. Usuki, H. Aburatani and Y. Ito, "Changes in the Crystal Structure of RF-Magnetron Sputtered BaTiO₃ Thin Films," J. Chem. Soc. Japan 100 (9), 1091 (1992).
50. R. E. Newnham, K. R. Udayakumar and S. Trolier-McKinstry, "Size Effects in Ferroelectric Thin Films," *Chemical Processing of Advanced Materials*, Edited by Larry L. Hench and Jon K. West, John Wiley and Sons, Inc. (1992).
51. S. Trolier-McKinstry, H. Hu, S. B. Krupanidhi, P. Chindaudom, K. Vedam and R. E. Newnham, "Spectroscopic Ellipsometry Studies on Ion Beam Sputter Deposited Pb(Zr, Ti)O₃ Films on Sapphire and Pt-Coated Silicon Substrates."

ABSTRACT

This report documents work carried out in the Materials Research Laboratory of the Pennsylvania State University over the first year of a new ONR sponsored University Research Initiative (URI) entitled "Materials for Adaptive Structural Acoustic Control." For this report the activities have been grouped under the following topic headings:

1. General Summary Papers.
2. Materials Studies.
3. Composite Sensors.
4. Actuator Studies.
5. Integration Issues.
6. Processing Studies.
7. Thin Film Ferroelectrics.

In material studies important advances have been made in the understanding of the evaluation of relaxor behavior in the PLZT's and of the order disorder behavior in lead scandium tantalate:lead titanate solid solutions and of the Morphotropic Phase Boundary in this system. For both composite sensors and actuators we have continued to explore and exploit the remarkable versatility of the flextensional moonie type structure. Finite element (FEA) calculations have given a clear picture of the lower order resonant modes and permitted the evaluation of various end cap metals, cap geometries and load conditions. In actuator studies multilayer structures have been combined with flextensional moonie endcaps to yield high displacement (50 μ meter) compact structures. Electrically controlled shape memory has been demonstrated in lead zirconate stannate titanate compositions, and used for controlling a simple latching relay. Detailed study of fatigue in polarization switching compositions has highlighted the important roles of electrodes, grain size, pore structures and microcracking and demonstrated approaches to controlling these problems. For practical multilayer actuators a useful lifetime prediction can be made from acoustic emission analysis.

New modelling of 2:2 and 1:3 type piezoceramic:polymer composites has given more exact solutions for the stress distribution and good agreement with ultradilatometer measurements of local deformations. Composites with 1:3 connectivity using thin wall ceramic tubes appear to offer excellent hydrostatic sensitivity, unusual versatility for property control and the possibility to use field biased electrostrictors in high sensitivity configurations. Processing approaches have continued to use reactive calcining and have supplied the group with the wide range of ceramics used in these studies. For lead magnesium niobate:lead

ABSTRACT *(continued)*

titanate solid solutions grain size effects in samples of commercial purity have been traced to a thin (~20 nm) glassy layer at the grain boundary. In parallel with the ONR URI the laboratory has extensive DARPA and Industry sponsored research on ferroelectric thin films, a very short selection of most relevant papers has been included for the convenience of users.

INTRODUCTION

This report documents work carried out in the Materials Research Laboratory at the Pennsylvania State University over the first year of a new ONR sponsored University Research Initiative (URI) entitled "Materials for Adaptive Structural Acoustic Control." The proposed program is being carried out largely in five sections, each reporting to a senior faculty member. The sections are:

Materials Studies	Dr. A. S. Bhalla
Composite Sensors	Dr. R. E. Newnham
Actuator Studies	Dr. K. Uchino
Integration Issues	Dr. J. Dougherty
Processing Studies	Dr. T. R. Shrout

There is of course very strong overlap between these different topic areas, as for example the same piezoelectric composite may be both sensor and actuator and may itself be a highly integrated subsystem. In the circumstance we deliberately maintain very fuzzy boundaries between sections. Faculty, post doctorals and students often work in more than one section and between section bounds a necessary.

Following precedent established now over more than sixteen earlier annual reports, this document will present a brief narrative description of the work which has been accomplished, making reference for backup to the published studies from the groups which are included as technical appendices and form the bulk of the report.

For this report the activities have been grouped under the following topic headings.

1. GENERAL SUMMARY PAPERS.
2. MATERIALS STUDIES.
3. COMPOSITE SENSORS.
4. ACTUATOR STUDIES.
5. INTEGRATION ISSUES.
6. PROCESSING STUDIES.
7. THIN FILM FERROELECTRICS.

In materials, the phenomenology of the lead lanthanum zirconate titanate (PLZT) family at the x:65:35 composites was completed and presented as an invited paper at ECAPD2 Meeting in London. New work on the strongly ferroelectric lead lanthanum titanate, shows clearly how even at low lanthanum concentrations the lattice softens rapidly reducing the "first orderness" of the Curie transition and giving rise to sub domain modulation of the polarization in the ferroelectric phase. Detailed studies of the lead scandium tantalate:lead titanate (PST:PT) system have identified the composition of the pseudo morphotropic phase boundary (PMPB) and have explored the limits for order:disorder in the Sc:Ta cation system with increasing PT

content and its influence on crystal properties. For lead zirconate:lead zinc niobate antiferroelectric:ferroelectric switching compositions have been identified for switchable transducer applications (see Section 3).

Work on the composite sensors has continued to explore and exploit the remarkable versatility of the flextensional moonie type structure. In the metal-ceramic moonies the finite element (FEA) calculations have given a clear picture of strain patterns in the lower order vibrational modes allowing direct comparison with frequency behavior. The FEA calculations were also used to evaluate various end cap metals, cap geometries and load conditions. Clearly as well as being an excellent pressure sensor, the moonies makes a superb actuator in which a wide range of force:displacement characteristics are possible (Section 4). New switchable transducers with high remanent d_{ij} characteristics have been explored in the PZ:PZN composition family.

In more basic studies, it has always been our ambition to upgrade the "simple" Landau Devonshire function for PZT to include Ginsburg terms for the gradient of the polarization. Using the new experimental technique of electron holography the group is working with the Oak Ridge National laboratory to explore electric fields in polydomain perovskites and thus to explore the spacial variation of the polarization.

Actuator Studies have focused upon three topics: A detailed examination of the very versatile flextensional moonie, has demonstrated amplification of multilayer actuator displacements permitting the realization of compact high displacement (50 μ meter) scanners. The shape memory phenomena has been explored for room temperature in compositions in the modified PZSnT system, and electrically controlled shape change applied to a simple latching relay concept. Examination of the damage mechanisms in both materials and systems which lead to the fatigue effects on repeated switching have been explored, highlighting the complexity of the phenomena involved and requiring control of electrodes, grain size, pore structures and microcracking. For practical multilayer actuators a useful lifetime prediction can be made based on acoustic emission engendered by microcracking.

In integration issues, as a step to understanding the more complex systems more exact treatments for the 2:2 and 1:3 type PZT piezoceramic:Polymer composite systems are being examined. For the low frequency quasi-static case, the new calculated and the measured surface profiles are in excellent accord. For 1:3 composite structures using ceramic tubes rather than rods, it is shown that the properties can be tuned over a wide range by choosing suitable ratios of tube diameter to wall thickness. The thin walled tubes also give the possibility to use electrostriction materials in agile configurations and to make use of the very large field induced d_{31} values characteristic of these families.

In processing studies, the group has continued to explore the reactive calcination method for generating inexpensive high quality PZT powders. The group does also back-up all processing for the many new ceramics which are used in the program. The lead magnesium niobate:lead titanate (PMN:PT) solid solutions, the reduction of dielectric response with grain size in samples with commercial purity has been shown to be extrinsic and to come from a very thin coating (~20 nm) of a low K glassy phase at the grain boundary. In related studies sponsored by the Dielectric Center in the Laboratory grain size effects in BaTiO_3 and in $(\text{BaSr})\text{TiO}_3$ solid solutions have been explored.

In parallel with the ONR URI program the Laboratory has extensive DARPA and Industry sponsored research on ferroelectric thin films. Since the film structures involve materials like PZT, PMN:PT, PLT and PLZT families of compositions and do explore piezoelectric effects and applications, a small group of the most relevant papers from these programs are appended for reference.

1.0 GENERAL SUMMARY PAPERS

There is probably no better way to begin this report of work on the new URI on Materials for Adaptive Structures Acoustic Control than with a tribute to Arthur Von Hippel (Appendix 1). Von Hippel's Laboratory for Insulation Research was a model for many future Interdisciplinary Materials Research Laboratories, and many of the topics on which he initiated study are still the subject of concern today. The book "Piezoelectricity" in the American Institute of Physics series Key Papers in Physics, edited by C. Z. Rosen, B. V. Hiremath and R. E. Newnham collects 33 papers key on piezoelectrics, their properties, their electro-thermo-mechanical couplings and their device applications (Appendix 2). The subject of smart materials is covered in two papers. The first is the final form of the account by R. E. Newnham of Ferroelectric Sensors and Actuators, given at the Summer School on Ferroelectrics in Ascona (Appendix 3). The second was presented at the European Meeting on Ceramics and covers more general aspects of smart materials and structures (Appendix 4). Electrostriction is the basic underpinning phenomenon for all the most useful ferroelectric piezoelectrics. The article by Sundar and Newnham (Appendix 5) points up some of the qualitative features on the electrostrictive behavior in different insulators and firmly underscores the need for more complete study of electrostriction in simple solids.

2.0 MATERIALS STUDIES

In papers by Giniewicz, Bhalla and Cross (Appendices 6, 7, 8) the system $\text{PbSc}_{1/2}\text{Ta}_{1/2}\text{O}_3\text{:PbTiO}_3$ has been examined in detail. It is shown that there is a Pseudo Morphotropic Phase Boundary (PMPB) at composition in the range 0.4 to 0.45 PbTiO_3

separating a pseudo Rhombohedral Relaxor Ferroelectric phase from a purely ferroelectric tetragonal phase (Appendix 6). Studies of compositions close to pure PST reveal that the range of PbTiO_3 solid solution over which the scandium/tantalum ordering can be thermally controlled is strictly limited to concentrations below 0.075 PT. Again however the ordered phases show sharp first order transitions to a rhombohedral ferroelectric phase, whilst the disordered materials show strong relaxor ferroelectric character (Appendix 7). For compositions in the variable order region studies of the field induced pyroelectric response (Appendix 8) suggest properties superior to those of pure PST.

Excellent optical quality single crystals are available for a range of tungsten bronze structure relaxor ferroelectrics through the group of R. R. Neurgaonkar at Rockwell. Appendix 9 explores the optical refractive index, birefringence and lattice strain for BSN 25 and several $(\text{Ba}_{2-x}\text{Sr}_x)_2(\text{K}_{1-y}\text{Na}_y)_2(\text{NbO}_3)_{10}$ (BSKNN) compositions to show that in all crystals RMS polarization persists to well above the dielectric maximum of ϵ , behavior consistent with previously proposed fluctuation models for the relaxor behavior.

The electrical properties of compositions in the lead zirconate:lead zinc niobate (PZ:PZN) system near the ferroelectric:antiferroelectric phase boundary $[0.929 \text{ PbZrO}_3:0.071 \text{ Pb}(\text{Zn}_{1/3}\text{Nb}_{2/3})\text{O}_3]$ have been explored as a function of La_2O_3 doping in the range 1 to 5 mole% (Appendix 10). A field forced ferroelectric phase with remanence could be induced in compositions containing upto 3 mole% La_2O_3 . In a second study elastic, piezoelectric and dielectric properties have been explored more fully in the pure PZ:PZN system revealing the AF to FE transition of between 93.2 and 93.0% PZN. Large hysteresis is again observed in field forced transitions. (Appendix 11).

In the next three papers important aspects of the lead zirconate:lead titanate solid solution system are explored. A critical question which has not been addressed earlier is the proportioning of rhombohedral and tetragonal ferroelectric phases at the MPB composition in $\text{PbZrO}_3:\text{PbTiO}_3$. In work which was sponsored by AFOSR, but is included here because of its high relevance (Appendix 12), it is shown that the correct ratio of rhombohedral/tetragonal is in fact 3:2 not 1:1 as has been assumed previously. This moves the effective MPB composition towards the rhombohedral side, in good agreement with experimental results*. A second neglected area in PZTs is the nature of the domain structures in rhombohedral 1 and in the crumpled rhombohedral 2 phases $\text{R3m} \rightarrow \text{R3c}$. New TEM work (Appendix 13) shows clear evidence of the antiphase domain boundaries in the R3c phase and a most interesting interaction between antiphase and normal domain walls. It has always been a contention that if wall motion is to contribute strongly to piezoelectricity in PZTs, non 180° motion must be preferred over 180° motion. Appendix 14 adduces evidence from x-ray studies of the poling process to confirm this expectation. High frequency coaxial line measurements of high K

dielectrics are fraught with many difficulties. Appendix 15 suggests some necessary corrections to the simple interpretation for K values $\sim 1,000$. Two papers which report new data upon elastic, dielectric and piezoelectric properties in PVDF:TrFE copolymers (Appendix 16) and upon electrode clamping effects (Appendix 17) are included for interest. These studies have used an ultradilatometer at Penn State, together with an elastic stressing jig designed by Dr. Sykes of Acoustic Associates and the work has been carried out under Navy/SBIR sponsorship.

3.0 SENSOR STUDIES

Earlier ONR sponsored studies have highlighted the high strain capability of systems using Antiferroelectric ferroelectric switching in the niobium modified lead zirconate titanate stannate system. Appendix 18 explores the piezoelectric response in the field induced ferroelectric phase in the $\text{Pb}_{0.99}\text{Nb}_{0.02}[(\text{Zr}_{0.6}\text{Sn}_{0.4})_{1-y}\text{Ti}_y]\text{O}_3$ family. High piezoelectric anisotropy with $K_t/K_p = 4.5$ and K_t values larger than 0.62 suggest that this system will be of major interest in agile transducers. A discussion of the moonie type flextensional transducer is given in Appendix 19, highlighting the exceptional effective $d_{33} > 4,000$ pC/N the very high hydrostatic $d_h > 600$ pC/N and the excellent pressure tolerance over 1,000 psi. The paper applies finite element analysis (FEA) to explore stress concentrations, effects of geometry, the possibility of generating very large volume velocity and the actuation capability for the metal end cap moonie. Preliminary studies of the possible use of electrophoretic, dielectrophoretic and electrorheological effects to assemble unusual types of ceramic polymer composites are discussed in Appendix 20. Fibril formation under field leads to 1:3 type composite connectivities, and patterned distributions have been demonstrated using suitable electrode configurations. A clear demonstration of the capability for fibril formulation has been given for dielectrophoretically assembled BaTiO_3 nanocomposites (Appendix 21).

Formulation of a very difficult type of microstructure has been demonstrated in $\text{BaTiO}_3\text{:LiF}$ ceramics fired at low temperature where a most interesting core:shell structure can be achieved (Appendix 22). The high permittivity and highly twinned cores suggest that these materials may be of interest both in electrostrictive actuators and high K dielectrics. New and most interesting evidence of the break up of the conventional ferroelectric domain structure in higher La_2O_3 doped PbTiO_3 has been adduced from direct observation in Transmission Electron Microscopy (Appendix 23). The change from conventional to a modulated then finally to a tweed type microstructure corresponds to the change from strongly first order ferroelectric to relaxor ferroelectric behavior. The paper also underscores the potential advantage of moving to the use of electron holography to explore more quantitatively these exciting changes.

The first successful attempt to combine ferroelectrics with shape memory alloys is discussed in Appendix 24 where firmly adhering sol-gel derived PZT films are shown to survive exercising of the alloy up to strain levels of 0.4%.

4.0 ACTUATOR STUDIES

A very useful introduction to the phenomena of piezoelectricity and electrostriction in ferroelectric ceramics and their application to electrically controlled actuation is given in Appendix 25. The various contributions to the effects in the PZT family of materials are clearly distinguished and specific uses which maximize the capability of both poled ceramics and relaxor ferroelectrics are discussed. Two papers which underscore the superior capability of the moonie type flextensional structure for moderate actuation force are presented in Appendices 26 and 27. The transforming capability of the moon shaped cavities in the end caps is underscored in the manner in which both d_{33} and d_{31} of the piezoceramic are constructively enhanced. It is clear that both piezoelectric and electrostrictive systems can be used and multilayer configurations also utilized. Both single and stacked moonie structures are discussed. Passive and active smart actuators are discussed in Appendix 28 which summarizes work on soft piezoelectrics, electrostrictors, monolithic bimorphs and shape memory materials. In actuator systems walking devices are described and drive waveforms for step actuation discussed.

The close analogy between the phase switching modified PSnZT ceramics and the shape memory alloys is emphasized in Appendix 29. A cardinal advantage of the ceramic is however that both forward and backward switching can be effected by the electric field, without temperature change. The phenomenon is very clearly presented and a practical latching relay developed from the appropriate composition is presented. The destructive breakdown of multilayer actuators is addressed in Appendix 30. By using a design of actuator which exaggerated the elastic stress, cracking mechanism were explored and shown to be different in soft PNNT as compared to phase switching PNBZSnT. Crack initiation is shown to give rise to acoustic emission and the AE count shown to be a reliable number for estimating soft PNNT lifetime under cyclic field.

Materials issues in fatigue of soft piezoelectrics are addressed in Appendices 31 and 32. It is shown that a frequent cause of early fatigue is a poor electrode:ceramic interface. Paper 32 is the first of a sequence which will address electrode, pore structure, grain size and composition effects in PZT and PLZT materials.

5.0 INTEGRATION ISSUES

A challenging problem in the initial integration of stiff ceramic piezoelectric rods into a soft polymer matrix is the nature of the stress transfer which occurs when the 1:3 type composite structure is subjected to uniaxial or hydrostatic stress. In Appendix 33 the inhomogeneous deformation profiles have been calculated exactly for single rod and single tube composites. It is found from these solutions that only polymer in the close vicinity of the rod or tube participates strongly in stress transfer so that the results can be used to predict given 1:3 structures and optimize the design. In Appendix 34, the strain profiles in the 1:3 composite are analyzed and compared to direct measurement obtained using the MRL laser ultradilatometer good agreement is observed between calculated and measured profiles for low frequency excitation. A more detailed analysis for the 2:2 type composite, together with data for the 1:3 type system is given in Appendix 35. New and we believe very important analysis for a composite using piezoelectric tubes are given in Appendices 36 and 37. It is shown that by chasing the ratio of outer and inner diameter for end capped thin walled tubes it is possible to tune the response over a very wide range.

The thin wall section lends itself to the possible use of polarization biased electrostrictor elements giving exceedingly light low impedance ultra-sensitive hydrostatic response.

6.0 PROCESSING STUDIES

The review of processing for ferroelectric and related materials by Shrout and Swartz provides an excellent summary of the basic steps and a very balanced account of modern developments in the field (appendix 38). The authors have combined inputs from a wide range of both commercial and research studies to cover the major aspects in the preparation of dielectrics, piezoelectrics, and electro-optic ceramics. The more specialized synthesis of lead titanate by hydrothermal methods is described in Appendix 39. Sol-gel synthesis of a range of pyroniobates and tantalates and pyrotitanates are covered in Appendices 40, 41 and 42. Dense ceramics have been prepared in compositions $\text{La}_2\text{Ti}_2\text{O}_7$, $\text{Nd}_2\text{Ti}_2\text{O}_7$, $\text{Sr}_2\text{Nb}_2\text{O}_7$ and $\text{Ca}_2\text{Nb}_2\text{O}_7$. Spin-on sol-gel thin films with thickness up to $0.3 \mu\text{m}$ have also been prepared for $\text{La}_2\text{Ti}_2\text{O}_7$. These samples are now under study for their dielectrics, piezoelectric and ferroelectric properties. Grain size effects in lead magnesium niobate:lead titanate (PMN:PT) ceramics are considered in Appendices 43 and 44. In a practical study (Appendix 43) it is shown that grain size of order 3.5μ meters is required to reach the highest induced d_{31} values. For Appendix 44 a more fundamental study suggests that in reagent grade oxide preparations of PMN:PT a thin (20 nm) glassy layer coats the grains giving rise to a series mixing model which reduces the observed weak field permittivity very strongly as the grain size is reduced. Clear

evidence of the second phase is presented in TEM studies of thin sections and the dielectric data fit closely to the series model.

In Appendix 45 an interesting type of barrier layer capacitor structure is described using barium bismuth plumbate and barium plumbate. Leading to low temperature coefficients of capacitance and high dispersion frequencies. Studies of grain size effects in BaTiO_3 and in $(\text{BaSr})\text{TiO}_3$ are presented in Appendices 46 and 47.

7.0 THIN FILM FERROELECTRICS

Several reports have suggested that ferroelectric thin films of PZT may be dispersive at quite low frequencies. Appendix 48 shows that these dispersions may be traced to improper processing which leads to interfacial layers at the electrodes. Properly processed films do not relax up to GHz frequencies. The unusual response of thin film BaTiO_3 is discussed in Appendix 49, which shows that for small grains (6-8 nm) the structure is cubic nonferroelectric, but that on annealing to the range 0.1 to 0.2 μ meter the ferroelectric phase appears. Size effects in ferroelectric films are discussed in a more general manner in Appendix 50. Evidence for critical size effects are reviewed both for powders and for thin films and it is shown that PbTiO_3 retains ferroelectricity down to much smaller particle sizes than BaTiO_3 .

A technique which we believe is of major importance for the characterization of both bulk and thin film ferroelectric surfaces is discussed in Appendix 51. Spectroscopic ellipsometry permits a nondestructive but highly refined analysis of local density variations. Recent work at Penn State now permits the method to be applied to highly transparent crystals with uniaxial anisotropy. In applications to $\text{Pb}(\text{ZrTi})\text{O}_3$ films the method has shown that several descriptions of apparent thickness effects in these films are due to low density regions near the substrate film interface.

8.0 HONORS AND AWARDS

Over the year 1992 the Ferroelectric Group in MRL has continued to receive outstanding recognition from both domestic and international societies. For the 1992 94th Annual Meeting of the American Ceramic Society, Dr. L. Eric Cross was invited to give the Orton Lecture and for the same meeting Dr. R. E. Newnham gave the Sosman Lecture. Each individually is an outstanding honor for the program and to be invited for both in the same year speaks volumes for the standing of the group. In July 1992 also, Dr. Newnham was named for the First International Award from the Academy of Ceramics in Assisi Italy, perhaps the most prestigious international award in ceramics today. At the 1992 International Society for Hybrid Microelectronic (ISHM) meeting, W. Hackenberger, T. Shrout and J. Dougherty were given the award for the best paper at the meeting and in December, at the MRS meeting in

Boston, Dr. Cross was honored by the Society's Medal and Award for Outstanding Innovation.

List of Honors/Awards

<u>Name of Person Receiving Award</u>	<u>Recipient's Institution</u>	<u>Name, Sponsor and Purpose of Award</u>
L. Eric Cross	Penn State University	American Ceramic Society Orton Lecture and Award
R. E. Newnham	Penn State University	American Ceramic Society Sosman Lecture and Award
R. E. Newnham	Penn State University	International Research Award Academy of Ceramics Assisi, Italy
L. Eric Cross	Penn State University	Materials Research Society Medal and Award 1992 Boston, Massachusetts
W. Hackenburger T. R. Shrout J. Dougherty	Penn State University	Best paper of the Session International Society for Hybrid Microelectronics (ISHM 1992 Meeting)

9.0 APPRENTICE PROGRAM

1992 ONR APPRENTICE PARTICIPANTS

1. Name: David L. Cade
 Home Address: 105 E. Cliveder Street
 Philadelphia, PA 19119
 College: Villa Nova, Pennsylvania
 Major: Mechanical Engineering [Freshman, Fall 1992]
-

David Cade performed library research on scientific literature relevant to the area of ferroelectrics. He also assisted in the fabrication and preparation of fine scale single crystals of $\text{Pb}(\text{Zr}_{1/3}\text{Nb}_{2/3})\text{O}_3$ to be use in domain studies.

10.0 PAPERS PUBLISHED IN REFEREED JOURNALS

1. Newnham, R. E., "Memories of Arthur Von Hippel," *Ferroelectrics* **137**, 17 (1992).
2. Rosen, C., B. V. Hiremath, R. E. Newnham, "Piezoelectrics," American Inst. of Physics, New York (1991).
3. Newnham, R. E., "Ferroelectric Sensors and Actuators Smart Electroceramics," *Ferroelectric Ceramics*, Editor N. Setter, Proc. of Summer School on Ferroelectrics, Ascona (1991).
4. Newnham, R. E., "Smart Electroceramics in the 1990s and Beyond," *J. European Ceramic Soc.* (1992).
5. Sundar, V., and R. E. Newnham, "Electrostriction and Polarization," *Ferroelectrics* **135**, 431 (1992).
6. Giniewicz, J. R., A. S. Bhalla and L. E. Cross, "Identification of the Morphotropic Phase Boundary in Lead Scandium Tantalate:Lead Titanate Solid Solutions System," *J. Amer. Ceram. Soc.* (in press).
7. Giniewicz, J. R., A. S. Bhalla and L. E. Cross, "Variable Structural Ordering in Lead Scandium Tantalate:Lead Titanate Materials," *J. Mat. Sci.* (in press).
8. Giniewicz, J. R., A. S. Bhalla and L. E. Cross, "Lead Scandium Tantalate:Lead Titanate Materials for Field Stabilizer Pyroelectric Device Applications," *Ferroelectrics Letters* **14**, 21 (1992).
9. Bhalla, A. S., R. Guo, L. E. Cross, G. Burns, F. H. Dacol and R. R. Neurgaonkar, "Glassy Polarization in the Ferroelectric Tungsten Bronze (BaSr)Nb₂O₆," *J. Appl. Phys.* **71**, 11 (1992).
10. Yoon, J. S., V. S. Srikanth, A. S. Bhalla, "The Electrical Properties of Antiferroelectric Lead Zirconate-Ferroelectric Lead Zinc Niobate Ceramics with Lanthanum," *Proc. ISAF 1992*, Greenville, South Carolina, pp. 556.
11. Alberta, E. F., D. J. Taylor, A. S. Bhalla and T. Takenaka, "The DC Field Dependence of the Piezoelectric, Elastic and Dielectric Constants for a Lead Zirconate Based Ceramic," *Proc. ISAF 1992*, Greenville, S. Carolina.
12. Cao, W., and L. Eric Cross, "The Ratio of Rhombohedral and Tetragonal Phases at the Morphotropic Phase Boundary in Lead Zirconate Titanate," *Japan J. of Applied Physics* **31**, 1399 (1992).
13. Randall, C. A., M. G. Matsko, W. Cao and A. S. Bhalla, "A Transmission Electron Microscope Investigation of the R3m - R3c Phase Transition in Pb(ZrTi)O₃ Ceramics," *Solid State comm.* **84** (3), 193 (1993).
14. Li, Shaoping, Chi Yuen Huang, A. S. Bhalla and L. E. Cross, "90° Domain Reversal in Pb(Zr_xTi_{1-x})O₃ Ceramics," *Proc. ISAF 1992*, Greenville, South Carolina.
15. Li, Shaoping, Jyh Sheen, Q. M. Zhang, Sei-Joo Jang, A. S. Bhalla and L. E. Cross, "Quasi Lumped Parameter Method for Microwave Measurements of Dielectric Dispersion in Ferroelectric Ceramic," *Proc. ISAF 1992*, Greenville, South Carolina.

10.0 PAPERS PUBLISHED IN REFEREED JOURNALS *(continued)*

16. Oh, Ki-Young, Yutaka Saito, Atsushi Furuta and Kenji Uchino, "Piezoelectricity in the Field Induced Ferroelectric Phase of Lead Zirconate Based Antiferroelectrics," *J. Amer. Ceram. Soc.* 75, 795 (1992).
17. Newnham, R. E., Q. C. Xu, K. Onitsuka and S. Yoshikawa, "A New Type of Flexensional Transducer," *Proc. 3rd Int'l. Mtg. on Transducers for Sonics and Ultrasonics* (May 1992).
18. Randall, C. A., D. V. Miller, J. H. Adair and A. S. Bhalla, "Processing of electroceramic-polymer composites Using the Electro Rheological Effect," *J. Mat. Res.* 8, 1 (1993).
19. Newnham, R. E., "Structural-Property Relations in Dielectrophoretically Assembled BaTiO₃ Nanocomposites," *Materials Letters* 15, 26 (1992).
20. Huebner, W., "Structure Property Relations in Core-Shell BaTiO₃:LiF Ceramic," *J. Mat. Res.* 8 (4), 21 (1993).
21. Randall, C. A., G. A. Rossetti and W. Cao., "Spacial Variation of Polarization in Ferroelectrics and Related Materials," *Special Issue of Ferroelectrics, Williamsburg Meeting on Critical Experiments.*
22. Newnham, R. E., "Lead Zirconate Titanate Films on Nickel - Titanium Shape Memory Alloys: SMARTIES," *J. Amer. Ceram. Soc.* 75, 2891 (1992).
23. Sugawara, Y., K. Onitsuka, S. Yoshikawa, Q. C. Xu, R. E. Newnham and K. Uchino, "Metal-Ceramic Composite Actuators," *J. Amer. Ceram. Soc.* 75 (4), 996 (1992).
24. Damjanovic, D., and R. E. Newnham, "Electrostrictive and Piezoelectric Materials for Actuator Applications," *J. Intell. Mt. Syst. and Struct.* 3, 190 (1992).
25. Xu, Q. C, A. Dogan, J. Tressler, S. Yoshikawa and R. E. Newnham, "Ceramic-Metal Composite Actuators," *Ferroelectrics Special Issue on Actuators.*
26. Uchino, K., and A. Furuta, "Destruction Mechanisms in Multilayer Ceramic Actuators," *Proc. ISAF 1992, Greenville, South Carolina*, pp. 195.
27. Uchino, K., "Piezoelectric Ceramics in Smart Actuators and Systems," *Proc. 1st European Conference on Smart Structures and Materials.*
28. Furuta, A., Ki-Young Oh and K. Uchino, "Shape Memory Ceramics and Their Applications to Latching Relays," *Sensors and Materials*, 3 (4), 205 (1992).
29. Jiang, Q., Wenwu Cao and L. E. Cross, "Electric Fatigue Initiated by Surface Contaminate in High Polarization Ceramics," *Proc. ISAF 1992, Greenville, South Carolina*, pp. 107.
30. Jiang, Q., Wenwu Cao and L. E. Cross, "Electric Fatigue in PLZT Ceramics," *J. Mat. Sci.* (in press).

10.0 PAPERS PUBLISHED IN REFEREED JOURNALS (continued)

31. Cao, Wenwu, Q. M. Zhang and L. E. Cross., "Theoretical Study on the Static Performance of Piezoelectric Ceramic-Polymer Composites with 1:3 connectivity," J. Appl. Phys. 72, 5814 (1992).
32. Zhang, Q. M., Wenwu Cao, H. Wang and L. E. Cross, "Characterization of the Performance of 1-3 Type Piezocomposites for Low Frequency Applications," J. Appl. Phys. 73, 1403 (1993).
33. Zhang, Q. M., Wenwu Cao, H. Wang and L. E. Cross, "Strain Profile and Piezoelectric Performance of Piezocomposites with 2:2 and 1:3 Connectivities," Proc. ISAF 1992, Greenville, South Carolina, pp. 252.
34. Zhang, Q. M., H. Wang and L. E. Cross, "Piezoelectric Tubes and 1-3 type Tubular Composites as Tuneable Actuators and Sensors," J. Mat. Sci. (in press).
35. Shrout, Thomas R., and Scott L. Swartz, "Processing of Ferroelectric and Related Materials: A Review," Proc. ISAF 1992, Greenville, South Carolina.
36. Rossetti, G. A., D. J. Watson, R. E. Newnham and J. H. Adair, "Kinetics of the Hydrothermal Crystallization of the Perovskite Lead Titanate," J. Crystal Growth 116, 251 (1992).
37. Prasadarao, A. V., U. Selvaraj, S. Komarneni and A. S. Bhalla, "Sol-Gel Synthesis of $\text{Ln}_2(\text{Ln} = \text{La}, \text{Nd})\text{Ti}_2\text{O}_7$," J. Mat. Res. 7, 2859 (1992).
38. Prasadarao, A. V., U. Selvaraj, S. Komarneni and A. S. Bhalla, "Sol-Gel Synthesis of Strontium Pyroniobate and Calcium Pyroniobate," J. Amer. Ceram. Soc. 75 (10), 2697 (1992).
39. Prasadarao, A. V., U. Selvaraj, S. Komarneni and A. S. Bhalla, "Fabrication of $\text{La}_2\text{Ti}_2\text{O}_7$ Thin Films by a Sol-Gel Technique," Ferroelectrics Letters 14, 65 (1992).
40. Wang, S. F., U. Kumar, W. Huebner, P. Marsh, H. K. Kunkel and C. G. Oakley, "Grain Size Effects on the Induced Piezoelectric Properties of 0.9 PMN:0.1PT Ceramics," Proc. ISAF 1992, Greenville, South Carolina.
41. Randall, C. A., A. D. Hilton, D. J. Barber and T. R. Shrout, "Extrinsic Contributions to the Grain Size Dependence of Relaxor Ferroelectric $\text{Pb}(\text{Mg}_{1/3}\text{Nb}_{2/3})\text{O}_3\text{:PbTiO}_3$ Ceramics," J. Mat. Res. 8 (4) (1993).
42. Hiremath, B. V., R. E. Newnham and L. E. Cross, "Barrier Layer Capacitor using Barium Bismuth Plumbate:Barium Plumbate," J. Amer. Ceram. Soc. 75, 2953 (1992).
43. Kumar, U., S. F. Wang, S. Varanasi and J. P. Dougherty, "Grain Size Effects on the Properties of Strontium Barium Titanate," Proc. ISAF 1992, Greenville, South Carolina, pp. 55.
44. Kumar, U., S. F. Wang and J. P. Dougherty, "Preparation of Dense Ultra-Fine Grain Barium Titanate-Based Ceramics," Proc. ISAF 1992, Greenville, South Carolina, pp. 70.

10.0 PAPERS PUBLISHED IN REFEREED JOURNALS *(continued)*

45. Chen, J., K. R. Udayakumar, K. G. Brooks and L. E. Cross, "Dielectric Behavior of Ferroelectric Thin Films at High Frequency," Proc. ISAF 1992, Greenville, South Carolina, pp. 182.
46. Uchino, K., N-Y Lee, T. Toba, N. Usuki, H. Aburatani and Y. Ito, "Changes in the Crystal Structure of RF-Magnetron Sputtered BaTiO₃ Thin Films," J. Chem. Soc. Japan 100 (9), 1091 (1992).
47. Newnham, R. E., K. R. Udayakumar and S. Trolier-McKinstry, "Size Effects in Ferroelectric Thin Films," Chemical Processing of Advanced Materials, Edited by Lary L. Hench and Jon K. West, John Wiley (1992).

11.0 INVITED PAPERS PRESENTED AT NATIONAL AND INTERNATIONAL MEETINGS

1. Newnham, R. E. "Multifunctional Ceramics in the 21st Century," International Forum on Fine Ceramics, Nagoya, Japan (March 10, 1992).
2. Bhalla, A. S. "Single Crystals Fibers for Electrical and Optical Applications," ISIF Meeting, Monterey, California (March 9-11, 1992).
3. Cross, L. E. "Ceramic Sensors and Actuators for Smart Materials and Adaptive Structures," INDO-US Workshop, Perspective in New Materials, Delhi (March 23-24, 1992).
4. Cross, L. E. "Ceramic Sensors and Actuators for Smart Materials and Adaptive Structures," Orton Lecture, Amer. Ceram. Soc. Mtg., Minneapolis, Minnesota (April 1992).
5. Newnham, R. E. "Structure-Property Relationships in Composite Electroceramics," Sosman Lecture, Amer. Ceram. Soc. Mtg., Minneapolis, Minnesota (April 1992).
6. Newnham, R. E. "Smart Electroceramics," Amer. Ceram. Soc. Mtg., Minneapolis, Minnesota (April 1992).
7. Ravindranathan, P., S. Komaraneni, A. S. Bhalla and R. Roy. "Low Temperature Chemical Routes in Smart Materials," Amer. Ceram. Soc. Mtg., Minneapolis, Minnesota (April 1992).
8. Cross, L. E. "Plenary Lecture: Ceramic Sensors and Actuators for Smart Materials and Adaptive Structures," ECAPD-2, Imperial College, London (April 12-15, 1992).
9. Newnham, R. E. "Electromechanical Properties of Smart Materials," Symposium on Intelligent Systems, Virginia Polytechnic Institute and State University, Blacksburg, Virginia (April 27-29, 1992).
10. Newnham, R. E., and Q. C. Xu. "A New Type of Flexensional Transducer," Third International Workshop on Transducers for Sonics and Ultrasonics, Orlando, Florida (May 6-8, 1992).

11.0 INVITED PAPERS PRESENTED AT NATIONAL AND INTERNATIONAL MEETINGS *(continued)*

11. Cross, L. E. "Materials for Adaptive Structural Acoustic Control: Topic on the Penn State URI Program," ONR Workshop on "Adaptive Structures with Active Materials," Washington, DC (May 18-19, 1992).
12. Newnham, R. E. "Structure-Property Relationships in Actuator Materials," Army Symposium on "Materials by Design," Jekyll Island, Georgia (May 20-22, 1992).
13. Newnham R. E. "Piezoelectric Sensors and Actuators: Smart Materials," IEEE Frequency Control Symposium Keynote Address, Hershey, Pennsylvania (May 27-28, 1992).
14. Newnham, R. E. "Smart Materials for Sensors and Actuators," Physical Metallurgy Gordon Conference, Plymouth, New Hampshire (June 15-19, 1992).
15. Newnham, R. E. "Intelligent Electroceramics," International Research Award, Academy of Ceramics, Assisi, Italy (June 26-28, 1992).
16. Cross, L. E. "Ferroelectric Thin Films and Their Applications," Seminar on Ferroelectricity, Tsukuba Science City, Tokyo, Japan (July 22-23, 1992).
17. Newnham, R. E. "Tunable Transducers: Nonlinear Phenomena in Nanocrystalline Electroceramics," American Crystallographic Association Meeting, Pittsburgh, Pennsylvania (August 14, 1992).
18. Newnham, R. E. "Structure-Property Relations in Integrated Ceramics," International Symposium on the Reactivity of Solids, Madrid, Spain (September 28-30, 1992).
19. Cross, L. E. "Recent Developments in Piezoelectric and Electrostrictive Sensors and Actuators for Smart Structures," AGARD Conference, Lindau Germany (October 5, 1992).
20. Newnham, R. E. (keynote lecture). "Structure Property Relationships in Composite Electroceramics," American Society for Composite Materials (October 13-15, 1992).
21. Cross, L. E. "Piezoelectric Sensors and Actuators for Smart Materials," Stein Conference, Drexel University, Philadelphia, Pennsylvania (October 20-21, 1992).
22. Newnham, R. E., Q. C. Xu and S. Yoshikawa. "Composite Actuators," Third Int'l. Ceramic Science and Tech. Congress, San Francisco, California (November 1-4, 1992).
23. Newnham, R. E., S. Trolier-McKinstry, J. P. Dougherty and T. R. Shrout. "Structure Property Relations in High Permittivity Ceramics," Third Int'l. Ceramic Science and Tech. Congress, San Francisco, California (November 1-4, 1992).
24. Cross, L. E. "Relaxor Ferroelectrics," Third Int'l. Ceramic Science and Tech. Congress, San Francisco, California (November 1-4, 1992).
25. Cross, L. E. "Relaxor Ferroelectrics: Useful Self Assembling Self Limiting Nanocomposites," Materials Research Society Medal/Award Lecture, Boston, Massachusetts (December 1-4, 1992).

12.0 INVITED PRESENTATIONS AT UNIVERSITY, INDUSTRY AND GOVERNMENT LABORATORIES

1. January 6-10, 1992, "Oxide Engineering," R. E. Newnham and S. McKinstry, short course at Corning Glass Works, Corning, New York.
2. January 21, 1992, "Ferroelectric Thin Films," R. E. Newnham, seminar at Army Electronics Laboratory, Fort Monmouth, New Jersey.
3. February 21, 1992, "Low Permittivity Dielectrics for Electronic Packages," R. E. Newnham, International Society for Hybrid Microelectronics, Ojai, California.
4. February 25, 1992, "Advanced Piezoelectric Materials," R. E. Newnham, Workshop on Materials and Systems for Space Applications, Pentagon, Washington, D. C.
5. February 26, 1992, "Biomimetic Sensors and Actuators," R. E. Newnham, Naval Research Laboratory seminar, Washington, D. C.
6. March 10, 1992, "Multifunction Ceramics in the 21st Century," R. E. Newnham, International Forum on Fine Ceramics, Nagoya, Japan.
7. March 11, 1992, "Smart Ceramics," R. E. Newnham, TDK Research Laboratory Narita, Japan.
8. March 13, 1992, "Smart Ceramics," R. E. Newnham, Nippon Steel Research and Development Center, Yokohama, Japan.
9. March 23, 1992, "Microwaves and Matter," R. E. Newnham, Centre for Dielectric Studies spring meeting, Penn State University, University Park, Pennsylvania.
10. April 3, 1992, "Electroceramics in the 1990s and Beyond," R. E. Newnham, Ceramics Association of New Jersey, New Brunswick, New Jersey.
11. April 17, 1992, "Particle Alignment in 0-3 Composite Electroceramics," R. E. Newnham, NEDO Symposium, Minneapolis, Minnesota.
12. June 4, 1992, "Japan Fine Ceramics Center: A Model Research Park," R. E. Newnham, Materials Research Institute, Penn State University, University Park, Pennsylvania.
13. June 11, 1992, "Smart Electroceramics," R. E. Newnham, National Research Council, Materials Advisory Board, Washington, D. C.
14. July 2, 1992, "Smart Ceramics," R. E. Newnham, Philips Research Laboratory seminar, Aachen, Germany.
15. July 3, 1992, "Actuators, Sensors, and Transducers," R. E. Newnham, Electrical Engineering Department seminar, Aachen University, Aachen, Germany.
16. July 7, 1992, "Smart Materials," R. E. Newnham, seminar at Max-Planck Institute, Stuttgart, Germany.

12.0 INVITED PRESENTATIONS AT UNIVERSITY, INDUSTRY AND GOVERNMENT LABORATORIES (continued)

17. July 8, 1992, "Ferroelectric Sensors and Actuators," R. E. Newnham, Materials Science Department seminar, Lausanne University, Lausanne, Switzerland.
18. July 13-17, 1992, Short course on Crystal Physics and Crystal Chemistry (five lectures), R. E. Newnham, Department of Chemistry, University of Geneva, Geneva, Switzerland.
19. August 17-21, 1992, Short course on "Oxide Engineering," R. E. Newnham and S. McKinstry, Corning Glass Works, Corning, New York.
20. August 27, 1992, "Metal-Ceramic Composite Actuators," R. E. Newnham, U.S.-Japan Electroceramics meeting, Penn State University, University Park, PA.
21. September 25, 1992, "Electroceramics in the 1990s" (invited), R. E. Newnham, Pennsylvania Ceramics Association meeting, Penn State University, University Park, Pennsylvania.
22. December 14, 1992, "Structure-Property Relations in Composite Electroceramics," R. E. Newnham, National Institute for Research on Inorganic Materials, Tsukuba, Japan.
23. December 15, 1992, "Structure-Property Relations in Composite Sensors and Actuators," R. E. Newnham, Sumitomo Chemical Company Research Laboratories, Tsukuba, Japan.
24. December 15, 1992, "Structure-Property Relations in Composite Electroceramics," R. E. Newnham, Chemistry Department Seminar, University of Tokyo, Tokyo, Japan.
25. December 16, 1992, "Dielectrophoretic Alignment of Particles in Composite Electroceramics," R. E. Newnham, C. Bowen, C. Randall and A. Bhalla, Chemistry Department Seminar, University of Tokyo, Tokyo, Japan.
26. December 17, 1992, "Composite Flextensional Transducers," R. E. Newnham, Omron Corporation Research Laboratories, Tsukuba, Japan.

13.0 CONTRIBUTED PAPERS AT NATIONAL AND INTERNATIONAL MEETINGS

Annual Meeting of the American Ceramic Society, Minneapolis, Minnesota (April 1992)

1. Tressler, J. F., Q. C. Xu and R. E. Newnham, Pennsylvania State University, University Park, PA. "Modified Metal-PZT Composite Flextensional Transducer."
2. Onitsuka, K., Q. C. Xu and R. E. Newnham, Pennsylvania State University, University Park, PA. "Effect of Geometry and Bonding in Flextensional Transducers."
3. Dogan, A., Q. C. Xu and R. E. Newnham, Pennsylvania State University, University Park, PA. "Electrode Bonding in Multilayer Ceramic-Metal Composite."

13.0 CONTRIBUTED PAPERS AT NATIONAL AND INTERNATIONAL MEETINGS *(continued)*

4. Brooks, K. G., J. Chen, K. R. Udayakumar and L. E. Cross, Pennsylvania State University, University Park, PA. "Kinetics of Antiferroelectric to Ferroelectric Phase Switching in Modified Tetragonal Lead Zirconate Titanate Stannate Thin Films."
5. Li, S., C. Y. Huang, Q. M. Zhang and L. E. Cross, Pennsylvania State University, University Park, PA. "90° Domain Reversal in $\text{Pb}(\text{Zr}_x\text{Ti}_{1-x})\text{O}_3$."
6. Uchino, K., M. L. Mulvihill and R. P. Brodeur, Pennsylvania State University, University Park, PA. "Dynamic Observation of the Domain Movement in Relaxor Ferroelectrics."
7. Srivastava, A., A. S. Bhalla and L. E. Cross, Pennsylvania State University, University Park, PA. "Cofired Lead Magnesium Niobate Based Actuators."
8. Kitano, K. and R. E. Newnham, Pennsylvania State University, University Park, PA. "Dielectric and Piezoelectric Properties of Modified $\text{Pb}(\text{Ni}_{1/3}\text{Nb}_{2/3})\text{O}_3$ - PbTiO_3 - PbZrO_3 System Ceramics."
9. Taylor, D. J., E. F. Alberta and A. S. Bhalla. "Complex Piezoelectric, Elastic and dielectric Coefficients of Lead Zirconate-Lead Zinc Niobate Ceramics Under DC Bias."
10. Fielding, J. T., Jr., D. McHenry, C. Randall, S. J. Jang and T. R. Shrout, Pennsylvania State University, University Park, PA. "Classifications of Electrostrictive-Based Materials for Transducers."
11. Srikanth, V., A. S. Bhalla and L. E. Cross, Pennsylvania State University, University Park, PA. "Processing of Lead Indium Niobate (PIN)-Lead Scandium Tantalate (PST) Ceramics."
12. Alberta, E. F., D. J. Taylor and A. S. Bhalla. "The DC Field Dependence of the Piezoelectric, Elastic and Dielectric Coefficients of a Lead Zirconate-Based Ceramic."
13. Yoon, J. S., V. Srikanth and A. S. Bhalla, Pennsylvania State University, University Park, PA. "Processing of Lead Zirconate (PZ)-Lead Zinc Niobate (PZN) Ceramics at High Pressures."
14. Srivastava, A., A. S. Bhalla and L. E. Cross, Pennsylvania State University, University Park, PA. "The Liquid Phase Sintering of Lead Zirconate Titanate for Low-Temperature Cofired Devices."
15. Sunder, V., Q. M. Zhang, L. E. Cross and R. E. Newnham, Pennsylvania State University, University Park, PA. "Electrostriction Coefficients in Low-K Oxide Materials."
16. Dougherty, J. P., W. S. Hackenberger and T. R. Shrout, Pennsylvania State University, University Park, PA. "Real Time Sintering Observations of Multilayer Ceramic Electronic Substrates Using Hot State SEM."

13.0 CONTRIBUTED PAPERS AT NATIONAL AND INTERNATIONAL MEETINGS *(continued)*

17. Srivastava, A., A. S. Bhalla and L. E. Cross, Pennsylvania State University, University Park, PA. "Oxide and Metal-Oxide Electrodes on Dielectric Polycrystalline Ceramics."
18. Wang, H., Q. M. Zhang and L. E. Cross, Pennsylvania State University, University Park, PA. "Piezoelectric Properties of PVDF Copolymer."
19. Fox, G. R. and S. B. Krupanidhi, Pennsylvania State University, University Park, PA; K. L. More and L. F. Allard, Oak Ridge National Lab, Oak Ridge, TN. "Microstructure/Property Relations of Lead Lanthanum Titanate Thin Films."
20. Udayakumar, K. R., J. Chen, K. G. Brooks and L. E. Cross, Pennsylvania State University, University Park, PA; P. J. Schuele, Ramtron International Corporation, Colorado Springs, CO. "Phase Relations and Electrophysical Properties of Thin Films in the Lead Zirconate-lead Zinc Niobate System."
21. Selvaraj, U. A. V. Prasadarao, S. Komarneni and R. Roy, Pennsylvania State University, University Park, PA. "Fabrication of PT and PZT Thin Films by a Modified Sol-Gel Technique."
22. Chen, J., K. G. Brooks, K. R. Udayakumar and L. E. Cross, Pennsylvania State University, University Park, PA. "Microwave Assisted Low Temperature Solid Phase Crystallization of Ferroelectric Thin Films."
23. Selvaraj, U., U. Kumar, S. Komarneni and R. Roy, Pennsylvania State University, University Park, PA. "Preparation of $Ba_{1-x}Sr_xTiO_3$ ($x = 0$ to 1) Dielectric Thin Films by a Sol-Gel Process."
24. Chen, J., K. R. Udayakumar, K. G. Brooks and L. E. Cross, Pennsylvania State University, University Park, PA. "Dielectric Properties of Ferroelectric Thin Films at Microwave Frequencies."
25. Randall, C. A., T. R. Shrout, A. S. Bhalla and L. E. Cross, Pennsylvania State University, University Park, PA; L. F. Allard, Oak Ridge National Lab, Oak Ridge, TN. "A High Resolution Electron Microscopy Study of Ordering in Complete Lead Perovskites."

ISAF 92, Greenville, South Carolina (August 1992).

26. Alberta, E. F., D. J. Taylor and A. S. Bhalla, Pennsylvania State University, University Park, PA. "The DC Field Dependence of Pyroelectric, Piezoelectric, Elastic and Dielectric Constants for a Lead Zirconate-Based Ceramic."
27. Wang, J. F., J. R. Giniewicz and A. S. Bhalla, Pennsylvania State University, University Park, PA. "Soft Piezoelectric Ceramics with High Coupling Factors and Low QM."
28. Ravindranathan, P., S. Komarneni, A. S. Bhalla and R. Roy, Pennsylvania State University, University Park, PA. "Processing Studies and Dielectric Properties of $Pb(Mg_{1/3}Nb_{2/3})O_3$ (PMN) - $PbTiO_3$ (PT) System."

13.0 CONTRIBUTED PAPERS AT NATIONAL AND INTERNATIONAL MEETINGS *(continued)*

29. Li, Shaoping, A. S. Bhalla, Wenwu Cao and L. E. Cross, Pennsylvania State University, University Park, PA. "Extrinsic Contributions to the Response in $\text{Pb}(\text{Zr}_x\text{Ti}_{1-x})\text{O}_3$ Ceramics."
30. Li, Shaoping, Q. Ming Zhang, Sheen Jyh and L. E. Cross, Pennsylvania State University, University Park, PA. "Quasi Lumped Parameter Method of Microwave Measurements for Ferroelectric Ceramics."
31. Yoon, J. S., V. Srikanth and A. S. Bhalla, Pennsylvania State University, University Park, PA. "The Electrical Properties of Lead Zirconate (PZ) - Lead Zinc Niobate (PZN) Ceramics Prepared by High Pressures."
32. Kumar, S., P. Ravindranathan, A. S. Bhalla and L. E. Cross, Pennsylvania State University, University Park, PA. "Smart Thin Layers for Acoustic Control."
33. Kumar, S., A. S. Bhalla and L. E. Cross, Pennsylvania State University, University Park, PA. "Smart Structures Using Electrostrictive Materials for Vibration Control."
34. Giniewicz, J. R., A. S. Bhalla and L. E. Cross, Pennsylvania State University, University Park, PA. "An Investigation of the Lead Scandium Tantalate-Lead Titanate Solid Solution System."
35. Taylor, D. J. and A. S. Bhalla. "The DC Field Dependence of the Complex Piezoelectric, Elastic and Dielectric Coefficients in Normal and Relaxor Ferroelectrics."
36. Srivastava, A., A. S. Bhalla and L. E. Cross, Pennsylvania State University, University Park, PA. "Conductive Perovskites as Potential Electrodes for Ferroelectric Devices."
37. Zhang, Qiming, Wenwu Cao, H. Wang and L. E. Cross, Pennsylvania State University, University Park, PA. "The Static and Dynamic Performance of 1-3 Composite."
38. Jiang, Qiyue, Wenwu Cao and L. E. Cross, Pennsylvania State University, University Park, PA. "The Influence of Surface Conditions on Electric Fatigue of Ferroelectrics."

Other Contributed Presentations

39. Cao, Wenwu and L. E. Cross, Pennsylvania State University, University Park, PA. "Ratio of Rhombohedral and Tetragonal Phases on the Morphotropic Phase Boundary in Lead Zirconate Titanate," Second Williamsburg Workshop on First-Principles Calculations for Ferroelectricity, Williamsburg, VA (February 1992).
40. Cao, Wenwu and L. E. Cross, Pennsylvania State University, University Park, PA. "Elastic Compatibility and charge Neutrality in the Domain Structures of Ferroelectrics," American Physical Society Meeting, Indianapolis, Indiana (March 1992).

13.0 CONTRIBUTED PAPERS AT NATIONAL AND INTERNATIONAL MEETINGS *(continued)*

41. Cao, Wenwu, V. Srikanth, E. C. Subbarao and L. E. Cross, Pennsylvania State University, University Park, PA. "In Situ Study of the Poling Process in Lead Zirconate Titanate Ceramic Using Acoustic Emission," American Physical Society Meeting, Indianapolis, Indiana (March 1992).
42. Cao, Wenwu, Pennsylvania State University, University Park, PA. "Partitioning of Ferroelectric Phases Near the Morphotropic Phase Boundary in Lead Zirconate Titanate," ONR Transducer Materials Review, State College, PA (April 21-23, 1992).

Books (and sections thereof)

1. Newnham, R. E. Composite Electroceramics, Concise Encyclopedia of Composites, Vol. 6, S. Lee, Editor, VCH Publisher, New York, 158-173 (1992).
2. Amin, A. and R. E. Newnham, Thermistors Chapter in Electronic Ceramic Materials, edited by J. Nowotny. Trans. Tech. Publications, Zurich, 559 pp. (1992).
3. Moffat, D. M., J. Runt, W. Huebner, S. Yoshikawa and R. Newnham. PTC Effects in Conductor-Filled Amorphous Polymer Composites. Chapter 3 (pp. 51-64) in Composite Applications: The Role of Matrix, Fiber, and Interface, Edited by T. L. Vigo and b. J. Kinzig, VCH Publishers, New York, 1992, 407 pp. (1992).
4. Newnham, R. E. and T. R. ShROUT. Electronic Ceramics, Kirk-Othmer Encyclopedia (Concise Edition), John Wiley and Sons, New York (1992).
5. Newnham, R. E., K. R. Udayakumar and S. Trolier-McKinstry. Size Effects in Ferroelectric Thin Films, Chemical Processing of Advanced Materials, edited by L. L. Hench and J. K. West, John Wiley & Sons, Inc. 36, 379-393 (1992).

GENERAL SUMMARY PAPERS

APPENDIX 1

MEMORIES OF ARTHUR VON HIPPEL

R. E. NEWNHAM

*251 Materials Research Laboratory, Pennsylvania State University,
University Park, PA 16802*

In 1958, I moved from Cambridge, England, to Cambridge, Massachusetts where I joined the staff of the Laboratory for Insulation Research at M.I.T. Professor von Hippel (the "Prof") directed the lab for more than 20 years. In many ways, the Laboratory for Insulation Research served as a model for contemporary materials research laboratories with a team of chemists, crystal growers, crystallographers, physicists, ceramists, and electrical engineers all working on dielectric materials of all types. At the time, I was there the staff included Alexander Smakula, Janis Kalnajs, Bill Westphal, David Epstein, Perry Miles, George Economos, Arthur Linz, Gene Farrell, Carl Nelson, and Ron Fuchs. Aina Sils was the laboratory secretary, Stan Kingsbury the business manager, and the beautiful illustrations in the lab reports and books were drawn by draftsman John Marra. The main part of the laboratory was housed on the second floor of Building 4 overlooking the courtyard and the Charles River.

For several years, I assisted Professor von Hippel in teaching his graduate course on "Molecular Engineering." The lectures loosely followed the topics in his book "Dielectrics and Waves" beginning with equivalent circuit representations of materials, followed by atomistic and electronic models of permittivity, conductivity, and electric breakdown. Perhaps the most interesting part of the course was the Wednesday afternoon "Round Table Discussion." After coffee and doughnuts, the students gathered around a big table and Professor von Hippel would introduce the topic-of-the-day and a specialist in the field. Topics ranged from high voltage breakdown to molecular biology, reflecting the broad, humanistic interests of Professor von Hippel. Several chapters in his book "Molecular Engineering" grew out of these discussions.

I left the Laboratory for Insulation Research in 1966 when Professor von Hippel retired, but he had a lasting influence over my thoughts and career. My interest in structure-property relationships and in ferroelectricity began with the round table discussions and the research work at M.I.T. The Prof was also a great inspiration in how to deal with people from many countries working in many different disciplines. He knew how to put it all together.

APPENDIX 2

Introduction

his collection of 33 papers presents the material properties of piezoelectrics, and their applications to device technology, along with a thermodynamic description of electro-thermo-mechanical coupling phenomena. The papers fit into four categories: I. General; II. Materials; III. Measurements and Standards; IV. Devices and Applications.

The Cross-Härdtl article appearing in the Kirkthimer *Encyclopedia of Chemical Technology* introduces the collection. The Materials category consists of 13 papers which cover single crystals, ceramics, polymers and composites, and polar glass ceramics. The single crystal subset

contains articles on quartz, lithium niobate, triglycine sulfate, and potassium dihydrogen phosphate. The ceramic subset contains articles on barium titanate, lead titanate, lead zirconium titanate, and lead molybdate. Measurements and Standards contains three articles. The Devices and Applications category contains 16 papers including review articles by Cross, Tanaka, and Onoe. This section treats ferroelectric devices developed for signal processing, underwater acoustic detection, electrostrictive actuators, ink jet printing, watches, and pyroelectric detectors.

The thermodynamic description for these transducing phenomena is given by the equations of state as functions of stress (T), strain (S), electric (E), and displacement (D) fields along with the additional thermodynamic variables temperature (θ) and entropy (σ). Neglecting magnetic and optical coupling these six variables define the following linear physical phenomena: *piezoelectric* and *piezocaloric* effects arising from the mechanical energy of the stress and/or strain; *converse piezoelectric* and *electrocaloric* effects caused by the electric field; *thermal expansion* and *pyroelectric* effects arising from changes in heat content or temperature.

Figure 1 combines these cross-coupled interactions by displaying the primary effects along the main diagonal of a 6×6 matrix of thermodynamic variables taken dependently and independently. The piezoelectric, thermal expansion, and pyroelectric phenomena are placed in appropriate off-diagonal positions. Appendix 1 illustrates this scheme for specific thermodynamic energy functions.

Figure 1. Ferroelectric interactions

Independent variable \ Dependent variable	S	T	D	E	θ	σ
T	Mechanical [M]		Converse Piezoelectric (Electrostriction) [ES]		Thermal Expansion (Pyroelectric) [PE]	
S						
E	Piezoelectric [PZ]		Electrical [E]		Pyroelectric [PE]	
D						
θ	Piezocaloric [PZC]		Electrocaloric [EC]		Thermal [T]	
σ						

Carol Zwick Rosen
Basavaraj V. Hiremath
Robert Newnham

APPENDIX 3

FERROELECTRIC SENSORS AND ACTUATORS: SMART CERAMICS

Robert E. Newnham

"Smart" materials have the ability to perform both sensing and actuating functions. Passively smart materials respond to external change in a useful manner without assistance, while actively smart materials have a feedback loop which allows them to both recognize the change and initiate an appropriate response through an actuator circuit.

One of the techniques used to impart intelligence into materials is "Biomimetics," the imitation of biological functions in engineering materials. Composite ferroelectrics fashioned after the lateral line and swim bladders of fish are used to illustrate the idea. "Very Smart" materials, in addition to sensing and actuating, have the ability to "learn" by altering their property coefficients in response to the environment. Field-induced changes in the nonlinear properties of relaxor ferroelectrics and soft rubber are utilized to construct tunable transducers. Integration of multifunctional ferroic ceramics into compact, robust packages is a major goal in the development of smart materials.

1 Introduction

It has been said that life itself is motion, from the single cell to the most complex organism: the human body. This motion, in the form of mobility, change, and adaptation, is what elevates living beings above the lifeless forms (Rogers, 1990). This concept of creating a higher form of materials and structures by providing the necessary life functions of sensing, actuating, control, and intelligence to those materials is the motivation for studying smart materials.

Smart materials are part of smart systems - functional materials for a variety of engineering applications. Smart medical systems for the treatment of diabetes with blood sugar sensors and insulin delivery pumps. Smart airplane wings that achieve greater fuel efficiency by altering their shape in response to air pressure and flying speed. Smart toilets that analyze urine as an early warning system for health problems. Smart structures in outer space incorporating vibration cancellation systems that compensate for the absence of gravity and prevent metal fatigue. Smart

toys like "Altered Beast" where one is awakened from the dead and must learn to survive in the hostile environment of a different age. Smart houses with electrochromic windows that control the flow of heat and light in response to weather changes and human activity. Smart tennis rackets with rapid internal adjustments for overhead smashes and delicate drop shots. Smart muscle implants made from rubbery gels that respond to electric fields, and smart dental braces made from shape memory alloys. Smart hulls and propulsion systems for navy ships and submarines that detect flow noise, remove turbulence, and prevent detection. Smart water purification systems that sense and remove noxious pollutants. A number of smart systems have already been developed for automobiles, but there are many more to come. In a recent newspaper cartoon, Blondie and Dagwood encountered a smart automobile that drives itself back to the finance company when the owner misses a payment!

In this chapter the idea of "smartness" in a material is discussed, along with a number of examples involving ferroelectric components. Some of these smart ceramics are in production, while others have great potential but are thus far limited to laboratory investigations.

To begin our discussion, we first define "smart" to set the limits for classifying smart materials.

2 How Smart is Smart?

The short answer is "not very." Webster's dictionary gives several definitions for the word SMART, including "alert, clever, capable," "stylish," and "to feel mental distress or irritation." All three definitions are appropriate for the currently fashionable subject, "smart materials." They are "stylish," they are - in some cases - "clever," and it does cause some of us "mental distress" to think that a ceramic might somehow possess intelligence, even in rudimentary form.

There are many words in the English language denoting various degrees of intelligence. Beginning at the bottom, an intelligence scale might look like this: stupid - dumb - foolish - trivial - sensible - smart = clever - intelligent - wise. Many modern day materials have been cleverly designed to carry out useful functions and, in some cases, that we are justified in calling them "smart." They are decidedly better than "sensible" materials, but calling them "intelligent" seems rather presumptuous and self-serving. Perhaps in the future, when we are able to integrate information - processing and feedback circuitry into our sensor and actuator materials, perhaps then we will be justified in calling our materials "intelligent." As pointed out later, such a time is not far off.

To clarify the concept of smart materials, we describe a few examples of passive and active smartness.

3 Passive Smartness

A passively smart material has the ability to respond to environmental conditions in a useful manner. A passively smart material differs from an actively smart material in that there are no external fields or forces or feedback systems used to enhance its behavior. The "S" words in Table I summarize some of the meanings of passive smartness.

Table I: Some Attributes of Passive Smartness

Selectivity
Self Diagnosis
Self Tuning
Sensitivity
Shapeability
Self Recovery
Simplicity
Self Repair
Stability and Multistability
Stand-by Phenomena
Survivability
Switchability

Many passively smart materials incorporate self-repair mechanisms or stand-by phenomena which enable the material to withstand sudden changes in the surroundings. The crack-arresting mechanisms in partially stabilized zirconia are a good example. Here the tetragonal-monoclinic phase change accompanied by ferroelastic twin wall motion are the stand-by phenomena capable of generating compressive stresses at the crack tip. In a similar way, toughness can be improved by fiber pull-out or by multiple crack-branching as in the structural composites used in aircraft, or in machinable glass-ceramics.

Ceramic varistors and PTC thermistors are also passively smart materials. When struck by high-voltage lightning, a zinc oxide varistor loses most of its electrical resistance and the current is by-passed to ground. The resistance change is reversible and acts as a stand-by protection phenomenon. Varistors also have a self-repair mechanism in which its highly nonlinear I-V relationship can be restored by repeated application of voltage pulses. Barium titanate PTC thermistors show a very large increase in electrical resistance at the ferroelectric phase transformation near 130°C. The jump in resistance enables the thermistor to arrest current surges,

again acting as a protection element. The $R(V)$ behavior of the varistor and the $R(T)$ behavior of the PTC thermistor are both highly nonlinear effects which act as standby protection phenomena, and make the ceramics smart in a passive mode.

4 Active Smartness

A smart ceramic can also be defined with reference to sensing and actuating functions, in analogy to the human body. A smart ceramic senses a change in the environment, and using a feedback system, makes a useful response. It is both a sensor and an actuator. Examples include vibration damping systems for outer space platforms and electrically-controlled automobile suspension systems using piezoelectric ceramic sensors and actuators.

The Piezoelectric Pachinko machine illustrates the principle of an actively smart material. Pachinko Parlors with hundreds of vertical pinball machines are very popular in Japan. The Piezoelectric Pachinko game constructed by engineers at Nippon Denso is made from PZT multilayer stacks which act as both sensors and actuators. When a ball falls on the stack the force of impact generates a piezoelectric voltage. Acting through a feedback system, the voltage pulse triggers a response from the actuator stack. The stack expands rapidly throwing the ball out of the hole, and the ball moves up a spiral ramp during a sequence of such events. Eventually, it falls into a hole and begins the spiral climb all over again.

A video tape head positioner developed by Piezoelectric Products, Inc., operates on a similar principle. A bilaminate bender made from tape-cast PZT ceramic has a segmented electrode pattern dividing the sensing and actuating functions of the positioner. The voltage across the sensing electrode is processed through the feedback system resulting in a voltage across the positioning electrodes. This causes the cantilevered bimorph to bend, following the video tape track path. Articulated sensing and positioning electrodes operating at 450Hz near the tape head help keep the head perpendicular to the track.

These two examples illustrate how a smart ceramic operates. Both sensing and actuating functions are involved in its performance, and while the Japanese scientists have a somewhat different perspective on "smart" or "intelligent" materials (Takagi, 1989), the end results of efforts in this area are very similar.

5 Rubber-Like Ceramics

Every baseball and cricket player knows the importance of "soft hands." In catching a baseball, it is important to withdraw the hands slightly on making contact with the ball. This reduces the

momentum of the ball gradually and creates a soft landing. Soft landings are achieved on ceramics in the same way, making them feel as soft as rubber.

To test the concept, controlled compliance experiments have been carried out using PZT sensors and actuators (Newnham et al., 1989). In the test set-up, one actuator is used as the external driver, and the other as the responder. Sandwiched between the two actuator stacks are two sensors and a layer of rubber. The upper actuator is driven at a frequency of 100 Hz and the vibrations are monitored with the upper sensor. The pressure wave emanating from the driver passes through the upper sensor and the rubber separator and impinges on the lower sensor. The resulting signal is amplified using a low noise amplifier and fed back through a phase shifter to the lower actuator to control the compliance.

A smart sensor-actuator system can mimic a very stiff solid or a very compliant rubber. This can be done while retaining great strength under static loading, making the smart material especially attractive for vibration control.

If the phase of the feedback voltage is adjusted to cause the responder to contract in length rather than expand, the smart material mimics a very soft, compliant substance. This reduces the force on the sensors and partially eliminates the reflected signal. The reduction in output signal of the upper sensor is a measure of the effectiveness of the feedback system. In our experiments, the compliance of the actuator-sensor composite was reduced by a factor of six compared to rubber (Newnham et al., 1989).

6 Modulated Suspension Systems

The automobile industry is a very large market in which smart composites and sensors are already widely used. More than fifty electroceramic components can be found in today's high-tech autos, ranging from the air-fuel oxygen sensors used in most autos to the more exotic piezoelectric raindrop sensor, which automatically senses the amount of rain falling and adjusts the windshield wipers to the optimum speed (Taguchi, 1987).

Controlled compliance with piezoelectric ceramics is utilized in Toyota's piezoTEMS (Toyota Electronic Modulated Suspension), a system which has been developed to improve the drivability and stability of the automobile, and at the same time enhance passenger comfort (Tsuka et al., 1990). The TEMS is basically a road stability sensor and shock adjustor, which detects bumps, dips, rough pavement, and sudden lurches by the vehicle, then rapidly adjusts the shock absorbers to apply a softer or firmer damping force, depending on what is necessary to minimize discomfort while maintaining control of the vehicle. The shock absorbers are continuously readjusted as the road conditions change so that rocking or wobbling on soft shocks is eliminated.

The TEMS road surface sensor consists of a five-layer piezoelectric ceramic sensor mounted on the piston rod of the shock absorber. When a bump in the road is encountered, the resulting stress applied to the sensor produces a voltage which is fed into an electronic control unit that amplifies the signal and supplies a high voltage to the piezoelectric actuator. The 88-layer PZT actuator produces a $50\text{ }\mu\text{m}$ displacement on the oil system which is hydraulically enlarged to two millimeters, enough to change the damping force from firm to soft; the entire process takes only about twenty milliseconds (not even enough time to slam on the brakes!) Also figured into the actuator output are the vehicle speed and the driver's preference for a generally softer (American) or firmer (European) ride.

Alternatively, it is possible to damp stresses and vibrations without the need for a sensor-actuator feedback loop; materials which can perform this function are called passive damping materials. In a piezoelectric passive damper, a piezoelectric ceramic is connected in parallel with a properly matched resistor. The external stress creates a polarization in the piezoelectric, which induces a current in the resistor, leading to energy dissipation. A high piezoelectric coupling coefficient is required to induce the maximum voltage and energy dissipation (Ramachandran et al., 1990).

7 Actuator Materials

There are many approaches to controlling vibration and structural deformation. Actuation strain can be controlled by piezoelectric materials (Burke and Hubbard, 1987), electrostrictive materials (Uchino, 1986), magnetostrictive materials (Butler, 1988), shape-memory metal alloys (Schetky, 1979), and thermally-controllable materials (Edberg, 1987). Utilizing a system with distributed actuators, it is possible to design structures with intrinsic vibration and shape control capabilities. Among the most important actuator materials are shape memory metals and ceramics. The shape memory effect is exhibited by alloys which undergo thermoelastic martensite transformations. This is a first order displacive transformation in which a body centered cubic metal transforms by shear on cooling to a martensitic phase. When deformed in the martensitic low temperature phase, shape memory alloys will recover this deformation and return to the original shape when heated to a temperature where the martensite reverts back to the parent body-centered cubic structure. Unlike most ferroelectric and ferromagnetic transitions, the shape memory transformation has a large hysteresis which can be troublesome in practice.

Alloys exhibiting the shape memory effect fall into two general classes: non-ferrous and ferrous. Non-ferrous alloys currently in commercial use are Ni-Ti, Cu-Zn-Al, and Cu-Ni-Al. Ferrous shape memory alloys under development include Fe-Pt, Fe-Ni-C and Fe-Ni-Co-Ti.

Non-ferrous shape memory alloys of nickel-titanium alloy (Nitinol) have been developed by Goodyear Aerospace Corporation for spacecraft antennae (Schetky, 1979). A wire hemisphere of the material is crumpled into a tight ball, less than five centimeters across. When heated above 77°C, the ball opens up into its original shape--a fully formed antenna. Although it has seldom been used in service, this antenna demonstrates the magnitude of deformation and reformation possible in shape memory alloys.

While shape memory alloys are more like a solution looking for a problem, it has been suggested that transient and steady state vibration control can be accomplished with hybrid structures in which the shape memory alloy is embedded inside the material (Rogers et al., 1989).

Some ceramic materials also possess a sizeable shape-memory effect; of particular interest are materials which are simultaneously ferroelectric and ferroelastic. Their ferroelasticity ensures that recoverable spontaneous strain is available for contributing to the shape memory effect, and the ferroelectricity implies that their spontaneous strain can be manipulated not only by mechanical forces but also by electric fields.

Shape-memory has been demonstrated in PLZT ceramics, an important ferroelectric-ferroelastic because of the tremendous potential for applications due to the formation of microdomains smaller than the wavelength of light. In one experiment, a 6.5/65/35 PLZT helix was heated to 200°C, well above the transition temperature for recovery, $T_F (= T_C)$, then mechanically loaded and cooled to 38°C (well below T_F) - the "brittle" PLZT helix was deformed by 30% after the load was removed. Upon heating to 180°C, above T_F , the helix transformed back to its original shape, dramatically demonstrating the shape memory effect in brittle ceramics (Wadhawan et al., 1981).

Researchers at Sophia University in Tokyo have created a multilayer shape memory actuator with a (Pb, Nb)(Zr, Sn, Ti)O₃ ceramic. Twenty rectangular plates of the ceramic were stacked in an MLCC-type structure; the magnitude of the strains that were induced were small by comparison to most shape memory alloys (3-4 microns) but were three times larger than the strains produced using conventional piezoelectric actuators. In this case, a ferroelectric to antiferroelectric phase change is responsible for the shape change (Furuta and Uchino, 1990).

8 Electrorheological Fluids

One of the criteria which separates "smart" materials from "very smart" or "intelligent" materials is the ability of the material to not only sense a change and actuate a response, but to automatically modify one or more of its property coefficients during the sensing/actuating process. In effect, this type of material not only warns the user of a change in its environmental conditions and responds to it, but can in addition adjust itself to compensate for future change.

Electrorheological (ER) fluids (Ghandi and Thompson, 1989) and their magnetic analog, ferrofluids (Rosenweg, 1985), are an example of materials that have great potential for use in smart materials and systems. ER fluids are typically suspensions of fine particles in a liquid medium; the viscosity of the suspension can be changed dramatically by applying an electrical field. The electric field causes alignment of the particles in fibril-like branches in the direction of the applied field. The alignment disappears when the electric field is removed, thus creating the desired property of complete cyclic reproducibility.

ER fluids represent an advanced class of composite materials with self-tuning properties, that will find considerable use in vibration control applications. In addition, the compatibility of this technology with modern solid state electronics makes it an attractive component for integration into multifunction, self-contained smart material packages.

9 Biomimetics - Fish Ears

The word "biomimetic" is not found in most dictionaries so it needs to be defined. It comes from the Greek words "bios," meaning "life," and "mimetikos," meaning "to imitate." Biomimetic means to imitate life, or to use the biological world as a source of ideas for device concepts.

Fish and the other inhabitants of the underwater world have some interesting ways of talking and listening which have been copied using piezoelectric ceramics. For most fish, the principal sensors are the *lateral line* and the *inner ear* coupled to the *swim bladder*. The pulsating swim bladder also acts as a voice, as do chattering teeth in certain fish species.

The lateral line runs from the head to the tail of the fish and resembles a towed array with sensing organs (stitches) spaced at intervals along the nerve fiber. Each stitch contains several neuromasts made up of gelatinous cupulae resembling pimples in shape, within each cupula are several fibers which vibrate as the fish swims through water and acts as sensors for flow noise. The hair-like fibers are extremely thin in diameter ranging from 0.5 to 10 μm . When stimulated by turbulence, the motion of the hairs produces changes in the synapses which are in turn connected to the nerve fiber. The electric signal originates from impedance changes in cell walls which modulate the flow of K^+ ions. The lateral line is especially sensitive to low frequency fluid motion parallel to the length of the fish. In the 50 Hz range, threshold signals are observed for displacements as small as 30 nm ! (Bond, 1979; Moyle and Cech, 1988).

The 1-3 composite hydrophones described later are patterned after the hair-filled cupulae of the lateral line. Thin PZT fibers embedded in polymer provide excellent electromechanical coupling to a liquid medium and can be used as both sensors and actuators.

10 Dr. Dolittle and Fish Talk

Among the most popular children's books of all time are the Doctor Dolittle books written by Hugh Lofting. Doctor Dolittle could talk to the animals. He started with "Pig" and went on to "Duck" and "Cow", and eventually mastered 498 languages. There is a marvelous scene in the movie where young Tommy Stebbins meets Dr. Dolittle in his laboratory and watches him talk to goldfish by blowing bubbles in the fish bowl through a rubber tube. Between bursts of bubbles, Dr. Doolittle listened intently to through a stethoscope pressed against the side of the bowl.

In recent years, great advances have been made in recording and understanding fish talk, largely because of the development of improved hydrophone arrays and high speed spectrum analyses. Much of the talk is in the form of low frequency grunts below 200Hz. Sound functions in a variety of ways for fish, both in offense and in defense, for warning and intimidation. Many fish speak differently during breeding season, and appear to use coded repetition rates to communicate. Our ability to "farm the oceans" could be greatly enhanced by learning how to talk to fish and control their movements and feeding habits.

Although they do not possess a larynx, many species of fish produce high-pitched sound by grinding their teeth, but the vibration of the swim bladder wall provides the greatest repertoire of noises or calls. The croakers of Chesapeake Bay make tapping noises like a woodpecker, by contracting their drumming muscles attached to the swim bladder, and the twilight choruses of sea robins caused great confusion among the operators of antisubmarine echo-location devices during World War II (Urick, 1975).

11 Inner Ears and Swim Bladders

The nature of sound transmission in water has had a great influence on the evolution of hearing in fish. Sound, especially low frequency sound, travels faster and farther than in air. "Near-field" sound consists of small fluid motions or vibrations and are characterized by a displacement direction. They are detected by the inner ear or by the lateral line. The hydrostatic component or "far-field" sound is detected best through the swim bladder.

The inner ear is made up of inertia-sensing chambers resembling accelerometers. Within each chamber is a dense ear stone (otolith) which vibrates in a near-field sound wave. The inertia of the ear stone causes it to lag behind the motion of the fish, and to push against hair cells which line the chamber (sacculus). On bending, the hair cellular membranes deform, stimulating neural transmissions to the brain. Connections to the swim bladder improve the sensitivity to far-field sound.

The primary function of the gas-filled swim bladder is to provide buoyancy, but it is also used for sound and pressure reception and in some species is equipped with drumming muscles for sound production. The flexible swim bladder responds to hydrostatic pressure waves by changing volume. Fish with swim bladders can perceive relative pressure changes equivalent to less than 0.5% of the ambient hydrostatic pressure.

Direct or indirect linkages from the swim bladder to the inner ear promote the hearing sensation. Fish with no connections perceive low frequency sound (less than 500 Hz), while those with good connections have an upper frequency response of 5000 Hz. As might be expected, the swim bladder is reduced in size with depth, and loses much of its sensitivity as a sensor.

12 Hydrophone Materials

The knowledge which comes from the understanding of "fish talk" can be directly applied to research in materials destined to someday "sleep with the fishes". Hydrophones are underwater listening devices made from piezoelectric materials which respond to hydrostatic pressure waves. Among the applications for hydrophones are sonar systems for submarines, off-shore oil platforms, geophysical prospecting equipment, fish finders, and earthquake monitors.

As the earth's population continues to increase, mankind must continue to search for new and efficient sources of food and nutrition. The world's oceans may provide a solution to this problem, not only through fish farming but through the use of new and varied salt water vegetation that could provide an abundant source of food, especially for third world countries in which poor soil and harsh climates prohibit conventional farming. Smart hydrophone transceivers will receive and transmit fish talk and monitor the growth of underwater vegetation.

The figure of merit for hydrophone materials is the product of the hydrostatic piezoelectric charge coefficient (d_h) and the piezoelectric voltage coefficient (g_h). While good piezoelectric materials such as PZT have high d_{33} and d_{31} piezoelectric coupling coefficients, the d_h value is only about 45 pC/N because d_{33} and d_{31} are opposite in sign, and $d_h = d_{33} + 2d_{31}$. $d_h g_h$ is also inversely related to the dielectric permittivity, ϵ_{33} , so that low dielectric constants are desirable as well.

Rather than abandon PZT in search of the ultimate hydrophone material, avoiding this problem is often a matter of appropriate engineering of existing materials. Too often in the field of materials research we put too much emphasis on the synthesis of new materials and too little emphasis on new and unique designs for old materials.

A composite design with 1-3 connectivity is similar in design to the hair-filled gelatinous cupula with thin PZT rods embedded in a polymer matrix. The 1-3 piezocomposites have excellent sensitivity to pressure waves in water (Klicker et al., 1981; Gururaja et al., 1984). The large d_{33} is

maintained because the parallel connection results in stress transfer from polymer to piezoceramic, while the d_{31} is destroyed because of series connection in the lateral dimension where the mechanical load is absorbed by the polymer and not transferred to the PZT rods. Finally, ϵ_{33} is minimized due to the large volume of low ϵ_{33} polymer present. The d_{hg} values are improved by more than an order of magnitude when very thin rods are used.

Another piezoelectric hydrophone composite maximizes d_h by simply redirecting the applied stresses using specially shaped electrodes (Xu et al., in press). These are flextensional transducers which mimic the motions of the swim bladder. Shallow air spaces are positioned under the metal electrodes while the PZT ceramic plays the role of the muscle lining the swim bladder. When subjected to a hydrostatic stress, the thick metallic electrodes convert a portion of the z-direction stress into large radial and tangential stresses of opposite signs. The result is that d_{31} changes from negative to positive, so that its contribution now adds to d_{33} rather than subtracting from it. The d_{hg} of these composites is approximately 250 times that of pure PZT.

13 Very Smart Composites: the Tunable Transducer

By building in a learning function, the definition of a smart material can be extended to a higher level of intelligence: *A very smart material senses a change in the environment and responds by changing one or more of its property coefficients. Such a material can tune its sensor and actuator functions in time and space to optimize future behavior.* With the help a feedback system, a very smart material becomes smarter with age, something even human beings strive for. The distinction between smart and very smart materials is essentially one between linear and nonlinear properties. The physical properties of nonlinear materials can be adjusted by bias fields or forces to control response.

To illustrate the concept of a very smart material, we describe the tunable transducer recently developed in our laboratory. Electromechanical transducers are used as fish finders, gas igniters, ink jets, micropositioners, biomedical scanners, piezoelectric transformers and filters, accelerometers, and motors.

Five important properties of a transducer are the resonant frequency f_r , the acoustic impedance Z_A , the mechanical damping coefficient Q , the electromechanical coupling factor k , and the electrical impedance Z_E . The resonant frequency and acoustic impedance are controlled by the elastic constants and density, as discussed in the next section. The mechanical Q is governed by the damping coefficient (α) and is important because it controls "ringing" in the transducer. Definitions of the coefficients are given in Table II. Electromechanical coupling coefficients are controlled by the piezoelectric coefficient which, in turn, can be controlled and fine-tuned using relaxor ferroelectrics with large electrostrictive effects. The dielectric "constant" of relaxor

ferroelectrics depends markedly on DC bias fields, allowing the electrical impedance to be tuned over a wide range as well. In the following sections we describe the nature of nonlinearity and how it controls the properties of a tunable transducer.

Table II: Important characteristics of an electromechanical transducer.

Fundamental resonant frequency, f , of the thickness mode	$f = \frac{1}{2t} \sqrt{\frac{c}{\rho}}$	where t = thickness dimension, c = elastic stiffness, ρ = density
Acoustic Impedance Z_A	$ Z_A = \sqrt{\rho \cdot c}$	where c = elastic stiffness, ρ = density
Mechanical Q	$Q = \frac{\pi}{\lambda_a \cdot \alpha}$	where λ_a = acoustic wavelength, α = damping coefficient
Electromechanical coupling coefficient k	$k = d \sqrt{\frac{c}{\epsilon}}$	where d = piezoelectric charge coefficient, ϵ = electric permittivity
Electrical impedance Z_e	$ Z_e = \frac{t}{\omega \cdot \epsilon \cdot A}$	where ω = angular frequency, A = electrode area

14 Elastic Nonlinearity: Tuning the Resonant Frequency

Information is transmitted on electromagnetic waves in two ways: amplitude modulation (AM) and frequency modulation (FM). There are a number of advantages to FM signal processing, especially where lower noise levels are important. Atmospheric static is considerably lower in FM radio than in AM.

Signal-to-noise ratios are also important in the ultrasonic systems used in biomedical and nondestructive testing systems, but FM-modulation is difficult because resonant frequencies are controlled by stiffness (c) and transducer dimensions (t). Neither c , t , nor the density (ρ) can be tuned significantly in ceramics and most other materials, but rubber is an exception. To tune the resonant frequency of a piezoelectric transducer, we designed and built a composite transducer incorporating thin rubber layers exhibiting nonlinear elasticity (Xu et al., 1990).

Rubber is a highly nonlinear elastic medium. In the unstressed compliant state, the molecules are coiled and tangled, but under stress the molecules align and the material stiffens noticeably. Experiments carried out on rubber-metal laminates demonstrate the size of the nonlinearity. Young's modulus ($E \approx 1/s_{1111}$) was measured for a multilayer laminate consisting of alternating steel shim and soft rubber layers each 0.1 mm thick. Under compressive stresses of 200 MPa, the stiffness is quadrupled from about 600 to 2400 MPa (Rivin, 1983). The resonant frequency f is therefore doubled, and can be modulated by applied stress.

Rubber, like most elastomers, is not piezoelectric. To take advantage of the elastic nonlinearity, it is therefore necessary to construct a composite transducer consisting of a piezoelectric ceramic (PZT) transducer, thin rubber layers, and metal head and tail masses, all held together by a stress bolt.

The resonant frequency and mechanical Q of such a sandwich structure has been measured as a function of stress bias. Stresses ranged from 20 to 100 MPa in the experiments. Under these conditions the radial resonant frequency changed from 19 to 37 kHz, approximately doubling in frequency as predicted from the elastic nonlinearity. At the same time the mechanical Q increases from about 11 to 34 as the rubber stiffens under stress.

The changes in resonant frequency and Q can be modeled with an equivalent circuit in which the compliance of the thin, rubber layers are represented as capacitors coupling together the larger masses (represented as inductors) of the PZT transducer and the metal head and tail masses. Under low stress bias, the rubber is very compliant and effectively isolates the PZT transducer from the head and tail masses. At very high stress, the rubber stiffens and tightly couples the metal end pieces to the resonating PZT ceramic. For intermediate stresses the rubber acts as an impedance transformer giving parallel resonance of the PZT - rubber - metal - radiation load.

Continuing the biomimetic theme, it is interesting to compare the change in frequency of the tunable transducer with the transceiver systems used in the biological world. The biosonar system of the flying bat is similar in frequency and tunability to our tunable transducer. The bat emits chirps at 30 kHz and listens for the return signal to locate flying insects. To help it differentiate the return signal from the outgoing chirp, and to help in timing the echo, the bat puts an FM signature on the pulse. This causes the resonant frequency to decrease from 30 to 20 kHz near the end of each chirp. Return signals from the insect target are detected in the ears of the bat where neural cavities tuned to this frequency range measure the time delay and flutter needed to locate and identify its prey. Extension of the bat biosonar principle to automotive, industrial, medical and entertainment systems is underway.

15 Piezoelectric Nonlinearity: Tuning the Electromechanical Coupling Coefficient

The difference between a smart and a very smart material can be illustrated with piezoelectric and electrostrictive ceramics. PZT (lead zirconate titanate) is a piezoelectric ceramic in which the ferroelectric domains have been aligned in a very large poling field. Strain is linearly proportional to electric field in a fully poled piezoelectric material which means that the piezoelectric coefficient is a constant and cannot be electrically tuned with a bias field. Nevertheless it is a smart material because it can be used both as a sensor and an actuator.

PMN (lead magnesium niobate) is not piezoelectric at room temperature because its Curie temperature lies near 0°C. Because of the proximity of the ferroelectric phase transformation, however, and because of its diffuse nature, PMN ceramics exhibit very large electrostrictive effects.

Electromechanical strains comparable to PZT can be obtained with electrostrictive ceramics like PMN, and without the troubling hysteretic behavior shown by PZT under high fields. The nonlinear relation between strain and electric field in electrostrictive transducers can be used to tune the piezoelectric coefficient and the dielectric constant.

The piezoelectric d_{33} coefficient is the slope of the strain-electric field curve when strain is measured in the same direction as the applied field. Its value for $\text{Pb}(\text{Mg}_{0.3}\text{Nb}_{0.6}\text{Ti}_{0.1})\text{O}_3$ ceramics is zero at zero field and increases to a maximum value of 1300 pC/N (about three times larger than PZT) under a bias field of 3.7 kV/cm.

This means that the electromechanical coupling coefficient can be tuned over a very wide range, changing the transducer from inactive to extremely active. The dielectric constant also depends on DC bias. The polarization saturates under high fields causing decreases of 100% or more in the capacitance. In this way the electrical impedance can be controlled as well.

Electrostrictive transducers have already been used in a number of applications including adaptive optic systems, scanning tunneling microscopes, and precision micropositioners (Uchino, 1986).

To summarize, two types of nonlinearity are utilized in the fully tunable transducer: elastic nonlinearity and piezoelectric nonlinearity. By incorporating thin rubber layers in an electrostrictive transducer several important properties can be optimized with bias fields and bias stresses. Electromechanical coupling coefficients and electric impedance are tuned with electric field, and mechanical damping, resonant frequency, and acoustic impedance with stress bias.

16 Smart Electroceramic Packages

Up to this point, our discussion has focused primarily on piezoelectric transducers in which the sensing and actuating functions are electromechanical in nature. But the idea of a smart material is much more general than that. There are many types of sensors and many types of actuators, and many different feedback circuits.

Many of these sensors and actuators can be fabricated in the form of multilayer ceramic packages. Until recently multilayer packages consisted of low permittivity dielectric layers with metal circuitry printed on each layer and interconnected through metallized via holes between layers. Buried capacitors and resistors have now been added to the three-dimensional packages, and other components will follow shortly. Smart sensors, adaptive actuators, and display panels, together with thermistors and varistors to guard against current and voltage overloads, are next in line for development (Newnham, 1988).

Integration and miniaturization of electroceramic sensors and actuators is an ongoing process in the automotive and consumer electronics areas. Multilayer packages containing signal processing layers made up of low-permittivity dielectrics and printed metal interconnections are in widespread production. Further integration with embedded resistors and capacitors are under development, and it seems likely that intelligent systems will make use of the same processing technology. Tape casting and screen printing are used most often. Varistors, chemical sensors, thermistors, and piezoelectric transducers can all be fabricated in this way, opening up the possibility of multicomponent, multifunction ceramics with both sensor and actuator capabilities. Silicon chips can be mounted on these multifunctional packages to provide all or part of the control network. Processing is a major challenge because of the high firing temperatures of most ceramics, typically in the range 800°C to 1500°C. Differences in densification shrinkage and thermal contraction, together with adverse chemical reactions between the electroceramic phases, create formidable problems. Nevertheless, the rewards for such an achievement are substantial. An all-ceramic multifunction package would be small, robust, inexpensive, and sufficiently refractory to withstand elevated temperatures.

Electrodes are both a problem and a challenge. At present, precious metals such as palladium and platinum are used in multilayer ceramic components, greatly adding to the cost of the device. Copper and nickel electrodes require that the ceramic be fired in a reducing atmosphere, which may reduce the electroceramic layers and adversely affect the electrical properties. Copper and silver have high electrical conductivity but the melting points (~1000°C) require lower firing temperatures and make it necessary to alter the ceramic compositions and fabrication procedures. Some headway has been made on this problem, but further work is needed. One interesting approach to the problem is ceramic electrodes. There are a number of ceramic phases with

excellent conductivity which could be used, including the copper-oxide superconductors. In actuator devices, there are some special advantages in having electrodes and piezoceramics with matched elastic properties.

Composites are another approach to making sensor-actuator combinations. These can be formed at lower temperatures using low-firing ceramics and high temperature polymers such as polyimides. Sol-gel and chemical precipitation methods are helpful in preparing ceramic powders with low calcining temperatures, but further work on composite fabrication is required to obtain reliable and reproducible electrical behavior.

To miniaturize the sensors and actuators, and to obtain complex shapes, we recommend the use of photolithography and other processing methods employed in the semiconductor industry. Ultraviolet curable polymers incorporated into the tape-casting process make photolithographic processing comparatively easy and should find wide use in preparing ceramic or composite packages for intelligent systems.

The next logical step is to combine the sensor and actuator functions with the control system. This can be done by depositing electroceramic coatings on integrated circuit silicon chips.

Reliability is a major requirement in all complex systems. Further research on electrical and mechanical breakdown of sensor-actuator materials is needed to elucidate the mechanisms responsible for failure. Fail-safe and self-repair phenomena would be very helpful.

Intelligent systems for hostile environments is another topic area of interest. Sensor and actuator systems that can operate at high temperatures inside engines or furnaces are required to monitor combustion and to provide pollution controls. Radioactive and chemical waste sensors are another problem. Intelligent systems for oceanographic studies and oil exploration must withstand high pressures and salinity conditions.

Electroceramics have a vital role to play in intelligent systems, and many new developments will take place in the coming decade and the next century.

References

- Bond, C.E., 1979: "Biology of Fishes," Saunders College Publishing Co., Philadelphia.
- Burke, S., and J.E.Hubbard, 1987: "Active Vibration Control of a Simply-Supported Beam Using a Spatially-Distributed Actuator," IEEE Control Systems Magazine 7, 25-30.
- Butler, J.L., 1988: "Application Manual for Design of Magnetostrictive Transducers," Edge Technologies, Extrema Division, N.Marshfield, MA.

- Edberg, D.L., 1987: "Control of Flexible Structures by Applied Thermal Gradients," *AIAA Journal*, **25**, 877-883.
- Furuta, A., K. Oh, and K. Uchino, 1990: "Mechanical Clamper Using Shape Memory Ceramics," presented at the 7th International Symposium on Applications for Ferroelectrics, June 6-8, Urbana, Illinois.
- Ghandi, M.V., and B.S. Thompson, 1989: in "Smart Materials, Structures, and Mathematical Issues," ed. by C.A. Rogers, Technomic Publishers, Lancaster, PA, 63-68.
- Gururaja, T.R., W.A. Schulze, L.E. Cross, R.E. Newnham, B.A. Auld, and J. Wang, 1984: "Resonant Modes in Piezoelectric PZT Rod-Polymer Composite Materials," *Proc. of IEEE Ultrasonic Symposium*, 523-527.
- Klicker, K.A., J.V. Biggers, and R.E. Newnham, 1981: Composites of PZT and Epoxy for Hydrostatic Transducer Applications," *J. Amer. Cer. Soc.*, **64**, 5-9.
- Moyle, P.B., and J.J. Cech, Jr., 1988: "Fishes: An Introduction to Ichthyology," Prentice Hall, Englewood Cliffs, N.J..
- Newnham, R. E., 1988: "The Golden Age of Electroceramics," *Adv. Ceram. Mat.*, **3**, 12-16.
- Newnham, R.E., Q.C. Xu, S. Kumar, and L.E. Cross, 1989: "Smart Ceramics," *J. Wave-Matl. Int.*, **4**, 3-10.
- Ramachandran, A.R., Q.C. Xu, L.E. Cross, and R.E. Newnham, 1990: "Passive Damping with Piezoelectric Ceramics," presented at the 7th International Symposium on Applications for Ferroelectrics, June 6-8, Urbana, Illinois.
- Rivin, E.I., 1983: "Properties and Prospective Applications of Ultra Thin Layered Rubber-Metal Laminates for Limited Travel Bearings," *Tribology Int.*, **16**, 17-25.
- Rogers, C.A., 1990: "From the Editor" *Journal of Intelligent Material Systems and Structures*, **1**, 3.
- Rogers, C.A., C. Liang, and D.K. Barker, 1989: in "Smart Materials, Structures, and Mathematical Issues," ed. by C.A. Rogers, Technomic Publishers, Lancaster, PA, 39-62.
- Rosenweig, R.E., 1985: "Ferrohydrodynamics," Cambridge University Press, New York.
- Schetty, L., 1979: "Shape Memory Alloys," *Scientific American*, **241**, 74-82.
- Taguchi, M., 1987: "Applications of High-Technology Ceramics in Japanese Automobiles," *Adv. Ceram. Mat.*, **2**, 754-762.
- Takagi, T., 1989: "The Concept of Intelligent Materials and the Guidelines on R&D Promotion", Japan Science and Technology Agency Report.

- Tsuka, H., Nakomo, and Y. Yokoya, 1990: "A New Electronic Controlled Suspension Using Piezoelectric Ceramics," IEEE Workshop on Electronic Applications in Transportation.
- Uchino, K., 1986: "Piezoelectric/Electrostrictive Actuators," Monkita Publishers, Tokyo.
- Urick, R.J., 1975: "Principles of Underwater Sound," McGraw Hill, New York.
- Wadhawan, V.K., M.C.Kernion, T.Kimura, and R.E.Newnham, 1981: "The Shape Memory Effect in PLZT Ceramics," *Ferroelectrics*, **37**, 575-578.
- Xu, Q.C., J.Belsick, S.Yoshikawa, T.T.Srinivasan, and R.E.Newnham, in press: "Piezoelectric Composites with High Sensitivity and High Capacitance for Use at High Pressures," *IEEE Proceedings*.
- Xu, Q.C., R.E.Newnham, M.Blaskiewicz, T.T.Fang, T.T.Srinivasan, and S.Yoshikawa, 1990: "Nonlinear Multilayer Composite Transducers," Presented at the 7th International Symposium on Applications for Ferroelectrics, June 6-8, Urbana, Illinois.

Robert E. Newnham, Materials Research Laboratory, The Pennsylvania State University, University Park, PA 16802, USA

APPENDIX 4

SMART CERAMICS IN THE 1990s AND BEYOND

*R. E. Newnham
251 Materials Research Laboratory
The Pennsylvania State University
University Park, PA 16802*

Abstract

During the next century, we can expect to see a large number of smart ceramic devices combining ceramic sensors and actuators in multicomponent multifunction packages. Through feedback systems, these devices will be capable of responding to changes in the environment by means of linear and nonlinear actuators.

Electroceramics Market

The multibillion dollar electroceramics market includes Mn-Zn ferrites, PZT transducers, BaTiO₃ multilayer capacitors, ZnO varistors, Al₂O₃ packages, and SiO₂ optical fibers. Rapidly developing technologies can be identified within each market segment: barium hexaferrites for perpendicular recording, silver and copper electrode systems for multilayer capacitors, buried resistors and capacitors in ceramic packages, catalytic coatings for chemical sensors, and PZT piezoelectric motors. As in all rapidly evolving fields of science and engineering, there is a sense of excitement as a number of different technologies come together in a synergistic manner.

Structure-Property Relations

An overview of electroceramics is given in Fig. 1, which illustrates the various atomistic mechanisms utilized in ceramic circuit components. Multilayer capacitors, piezoelectric transducers, and PTC thermistors make use of the properties of ferroelectric perovskites with their high-dielectric permittivity, large piezoelectric coefficients, and anomalous electric conductivity. Similar domain phenomena are observed in ferrimagnetic oxide ceramics such as NiFe₂O₄. Hard and soft ferrites are analogous to hard and soft PZT and have found substantial markets in magnetic tape and electric motors.

Several kinds of mechanisms are operative in thermistors and other ceramics used as sensors. Most are based on changes in electrical resistivity, but the causes are different. The critical temperature thermistor involves a semiconductor-metal phase transition. Ceramic Superconductors have a metal to superconductor transition.

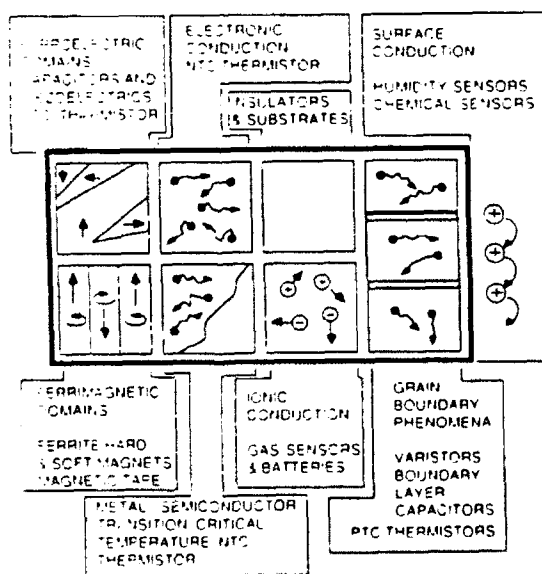


Fig. 1. Ionic and electronic mechanisms involved in electroceramic components.

NTC thermistors make use of the semiconducting properties in doped transition-metal oxides. Ionic conductivity is used in oxygen sensors and batteries. Stabilized zirconia is an excellent anion conductor, and β -alumina is one of the best cation conductors.

Humidity sensors and most chemical sensors make use of surface conduction. Adsorbed water molecules dissociate into hydroxyl and hydronium ions, which alter the electrical resistivity.

Grain-boundary phenomena are involved in boundary layer capacitors, varistors, and PTC thermistors. The formation of thin insulating layers between conducting grains is crucial to the operation of all three electroceramic components. Lastly, the importance of electroceramic insulators and substrates should not be overlooked. Here one strives to eliminate most of the interesting effects just described, but this is not always easy.

Ceramic Circuitry

Miniaturization and integration are technological goals in virtually all electronic materials. Several kinds of circuitry are under study by electroceramists, as shown in Fig. 2.

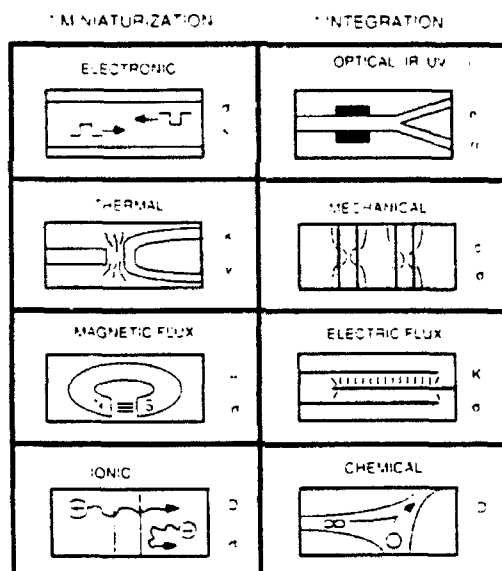


Fig. 2. Circuitry in ceramic materials for use in electronic packages, integrated optics, cooling systems, electromechanical transducers, magnetic recording, multilayer actuators, ionic batteries, and chemical sensors.

Electronic circuitry is the most advanced, especially in thick film and multilayer packaging technology, where control of electrical conductivity and dielectric constant are the key parameters. Integrated optic systems utilizing LiNbO_3 make use of small changes in refractive index to guide and control light waves. Low absorption coefficients are also important in optical circuitry. Thermal circuitry is

important in packaging technology where heat must be removed as efficiently as possible. Thermal conductivity and convective fluid flow are effective means of heat dissipation. Information storage utilizes magnetic circuitry made from high permeability and high conductivity materials to concentrate and manipulate regions of high magnetic flux. Electric flux concentration is used in ceramic actuators to produce large displacements with small voltages. Field concentration is accomplished with multilayer systems made up of internal electrodes with high conductivity, and high permittivity dielectric layers. Multilayer capacitors operate on a similar flux concentration principle. Ionic movement in battery systems constitutes another type of circuitry in ceramics like β -alumina and stabilized zirconia. Ionic conductivities and diffusion coefficients through intervening membranes are crucial property coefficients. Porous ceramics with high surface areas are used in fabricating chemical sensors. The movement of molecules and dissociation products constitutes a type of chemical circuitry controlled by diffusion coefficients and surface electrical resistivity.

Integrated Ceramics

The age of ceramic integration is upon us. Until recently multilayer ceramic packages consisted of dielectric strata with metallic circuitry printed on each layer and interconnected through metallized via holes between layers. Now additional circuit elements are being added. In the past two years buried capacitors and resistors have been added to the three-dimensional packages, and other components will follow shortly. Future developments in the field of integrated ceramics are illustrated by the flowering tree in Fig. 3. Smart sensors, adaptive actuators, and ceramic packages with electroluminescent display panels, enclosed printing units, and voice modules are on the horizon.

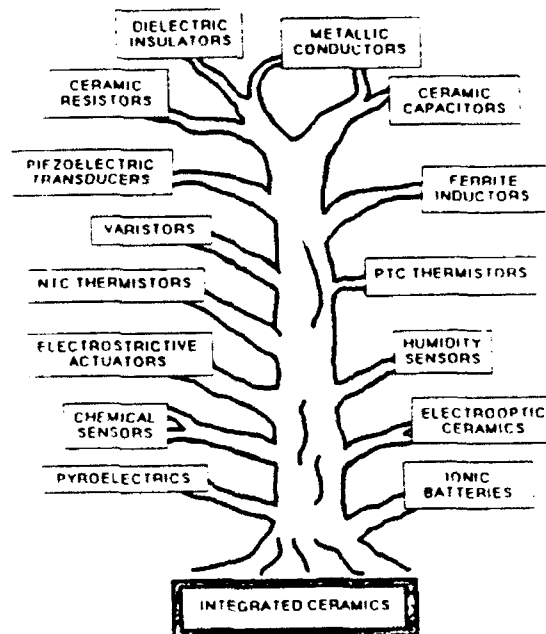


Fig. 3. Integrated ceramic packages of the future will incorporate many different components.

To conduct these functions it will be necessary to incorporate a wide variety of sensors, transducers, and actuators, together with thermistors and varistors to guard against current and voltage overloads. The process of preparing co-fired multicomponent ceramic packages involves a marriage of tape casting and thick film technologies, augmented by photolithography, etching, sol-gel films, and fugitive phases. In these multilayer packages, thick-film conductors, resistors, and dielectrics are screen-printed on green low-firing ceramic tapes to produce patterned circuitry in single layers. Vias are punched through the tapes and metallized to establish interconnects with adjacent layers. Low-permittivity tapes are used for signal transmission layers, and high-K tapes are used for the power plane. After lamination into a single green body, the stack is sintered to produce a monolithic ceramic body with co-fired components buried within it. These substrate packages have the advantages of reduced size and fewer surface-mounted components, as well as low firing temperatures. Moreover, the buried capacitors, resistors, and metal interconnects are hermetically sealed within the ceramic package, thereby protecting the circuit elements against moisture, chemical attack, and mechanical damage.

Smart and Very Smart Materials

Webster's dictionary gives several definitions for the word SMART, including "to feel mental distress or irritation", "alert, clever, capable", and "stylish". All three meanings are appropriate to the currently fashionable subject, "Smart Materials". It causes one mental distress to think a ceramic can in any way be smart, but with the help of a feedback system, it is possible.

The Piezoelectric Pachinko machine illustrates the principle of a smart material. Pachinko Parlors with hundreds of vertical pinball machines are very popular in Japan. The Piezoelectric Pachinko game constructed by engineers at NipponDenso is made from PZT multilayer stacks which act as both sensors and actuators. When a ball falls on the stack, the force of impact generates a piezoelectric voltage. Acting through a feedback system, the voltage pulse triggers a response from the actuator stack. The stack expands rapidly throwing the ball out of the hole, and the ball moves up a spiral ramp during a sequence of such events. Eventually, it falls into a hole and begins the spiral climb all over again.

The video tape head positioner operates on a similar principle. A bilaminate bender made from tape-cast PZT ceramic has a segmented electrode pattern dividing the sensing and actuating functions of the positioner. The voltage across the sensing electrode is processed through the feedback system resulting in a voltage across the positioning electrodes. This causes the cantilevered bimorph to bend, following the video tape track path. Articulated sensing and positioning electrodes near the tape head help keep the head perpendicular to the track. The automatic scan tracking systems operates at 450 Hz.

These two examples illustrate how a smart ceramic operates. A *smart material senses a change in the environment, and using a feedback system, makes a useful response. It is both a sensor and an actuator.*

The definition can be extended to even more clever materials. A *very smart material senses a change in the environment and responds by changing one or more of its property coefficients. Such a material can "tune" its sensor and actuator functions in time and space to optimize behavior.* The distinction between smart and very smart materials is essentially one between linear and nonlinear properties. The physical properties of nonlinear materials can be adjusted by bias fields or forces to control response.

The difference between a smart and a very smart material can be illustrated with piezoelectric and electrostrictive ceramics. PZT is a ferroelectric ceramic in which piezoelectric coefficient is a constant and cannot be electrically tuned with a bias field.

PMN is not piezoelectric at room temperature because its Curie temperature lies near 0°C. Because of the proximity of the ferroelectric phase transformation, however, PMN ceramics exhibit very large electrostrictive effects with a large nonlinear relationship between strain and electric field. Electromechanical strains comparable to PZT can be obtained with electrostrictive ceramics like PMN, and without the troubling hysteretic behavior shown by ferroelectric PZT. The nonlinear relation between strain and electric field can be used to tune the piezoelectric coefficient. The piezoelectric d_{33} coefficient is the slope to a maximum value of 1500 pC/N (about three times larger than PZT) under a bias field of 3.7 kV/cm.

Eventually, of course, we would like to include a feedback system within a smart ceramic, but there seems to be no simple way to do this at present. A promising approach is to deposit ceramic films on silicon chips. Limited success has been achieved with lead titanate and lead zirconate-titanate films on silicon for long-term ferroelectric random access memories (FRAM). By utilizing these ferroelectric films as sensors and actuators, a family of extremely intelligent materials could be obtained in which the feedback electronics could be fully integrated in the material. The time is not far off for such intelligent composites.

Up to this point, our discussion of smart materials has focused primarily on piezoelectric transducers in which the sensing and actuating functions are electromechanical in nature. But the idea of a smart material is much more general than that. There are many types of sensors and many types of actuators, and many different feedback circuits. A few possible combinations are shown in in Fig. 4.

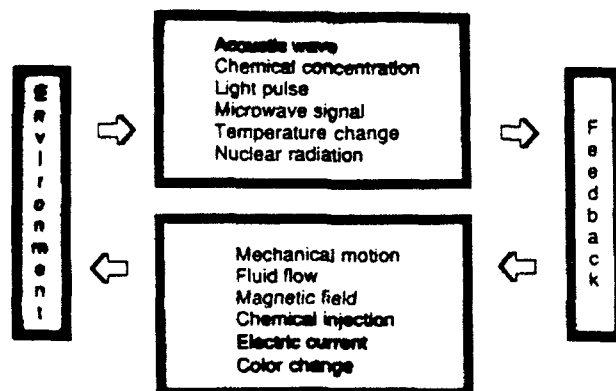


Fig. 4. Schematic of some possibilities for smart electroceramic packages. Smart devices bring together a number of sensor-actuator combinations.

Summary

Rapid progress in the integration and miniaturization of ceramic components has led to the development of multipurpose electronic packages containing complex three-dimensional circuitry. At the same time, wide variety of smart sensors, transducers, and actuators are being constructed utilizing composite materials to concentrate fields and forces. At present, the processing methods make use of tape casting the thick film techniques, but several upset technologies loom on the horizon. During the years ahead, we can expect electroceramic devices to follow in the footsteps of semiconductor technology as the component sizes drop below 100 μm and nanocomposite devices become a reality.

A great deal has been written about the importance of scale in magnetic, optical, and semiconductor materials, and many of the same effects occur in electroceramics: critical domain sizes, resonance phenomena, electron tunneling, and nonlinear effects.

The Golden Age of electroceramics will not last forever. The age of integration, followed by the age of miniaturization will inevitably lead to new ideas and new systems. Integrated ceramic systems will reach limits--grain size for one--as ceramists strive to make optoelectronic systems with extremely small feature size. A marriage of materials will emerge to replace integrated ceramic packages. Patterned thin film systems, involving oxides on silicon, or silicon on oxide substrates are already under study, and others will follow. Sensor, actuator, and information processing systems as complex and compact as the human body will one day emerge in the world of tomorrow.

APPENDIX 5

ELECTROSTRICTION AND POLARIZATION

V. SUNDAR and R. E. NEWNHAM

*Materials Research Laboratory, The Pennsylvania State University,
University Park, PA 16802 USA*

(Received February 12, 1992)

Electrostriction, the mechanical strain x resulting from electric polarization P , is a second order effect: $x = QP^2$. In this paper, the phenomenological and physical origins of the Q coefficients are discussed from a qualitative point of view. As pointed out by von Hippel, the mechanisms of electric polarization are space charge effects, dipole reorientation, ionic displacements and electronic polarizability. Not all of these mechanisms are equally effective in producing electrostriction. We have examined the Q coefficients reported for a number of solids in order to understand the relationships between the polarization mechanisms and electrostrictive strain. Trends were identified in the structure-property relationships but several important questions remain unanswered.

INTRODUCTION

Electrostriction is the basic electromechanical coupling in all insulator materials. Recently, there has been renewed interest in this effect arising from its applications in actuator devices deploying relaxor ferroelectric materials.

An examination of the so-called "very smart" materials leads us to the basic premise that these exploit, in the main, tunable, nonlinear properties. Electrostriction is a second order property that matches this premise, and thus finds application in sensor-actuator vibration control devices.

As a fundamental anharmonic property, electrostriction is of great interest from a theoretical viewpoint, as well.

In this review, we examine electrostriction from different viewpoints—phenomenology, macroscopic nature, empirical correlations of electrostriction with other material properties, the tunable nature of electrostrictive actuators, the relationships to the ionic nature of the compounds, and the structures in which these 'active' ions such as titanium or tungsten ions are housed. We also examine lead magnesium niobate (PMN), that is generally regarded as the prototype electrostrictive material.

PHENOMENOLOGY AND MEASUREMENTS

The phenomenology of electrostriction in ferroelectrics is well discussed in many texts.^{1,2} A brief outline is presented here, following the Devonshire phenomenology.

Using the Elastic Gibbs function,

$$G_1 = U - TS - X_{ij}x_{ij}$$

as a starting point, we may derive, under suitable boundary conditions, the following contributions to the electromechanical strain x_{ij} in an insulating solid.

$$x_{ij} = g_{imj}P_m + Q_{mnij}P_mP_n + W_{mnopij}P_mP_nP_oP_p.$$

In this expression, the electromechanical coupling effects arise from piezoestriction, quadratic electrostriction and higher order electrostriction respectively. This allows us to formulate the coefficients in terms of strain and polarizations P_m , as:

$$g_{imj} = \left(\frac{\delta x_{ij}}{\delta P_m} \right)_{P=0} \quad \left(g = \frac{dx}{dP} \right)$$

$$Q_{ijmn} = \left(\frac{\delta^2 x_{ij}}{\delta P_m \delta P_n} \right)_{P=0} \quad \left(Q = \frac{d^2 x}{dP^2} \right)$$

$$W_{ijmnop} = \left(\frac{\delta^4 x_{ij}}{\delta P_m \delta P_n \delta P_o \delta P_p} \right)_{P=0} \quad \left(W = \frac{d^4 x}{dP^4} \right)$$

Assuming a material with a center of symmetry, so all odd rank tensors vanish, and neglecting higher order electrostriction, we obtain the relation:

$$x_{ij} = Q_{ijmn}P_mP_n, \quad (x = QP^2)$$

defining the polarization-related electrostriction tensor coefficient. The Q coefficients are seen as the preferable mode of casting the electrostriction tensor in that they reflect the quadratic nature (Figure 1) of the phenomenon when strain is plotted as a function of polarization. Strain vs. electric field plots do not exhibit a quadratic nature except in linear dielectrics; in ferroelectrics, the nonlinear nature of the P - E relationship (Figure 2) makes the Q coefficients preferable to the field-related M coefficients, defined by:

$$M_{ijmn} = \left(\frac{\delta^2 x_{ij}}{\delta E_m \delta E_n} \right)_{X,T} \quad \left(M = \frac{d^2 x}{dE^2} \right)$$

Direct electrostriction may be expressed in terms of the elastic stress/strain observed in a material under the action of an applied field or induced polarization; the effects are described by the tensor relationships:

$$x_{ij} = Q_{ijmn}P_mP_n \quad X_{ij} = q_{ijmn}P_mP_n$$

$$= M_{ijmn}E_mE_n \quad = m_{ijmn}E_mE_n$$

The converse effect may be described in terms of the field/polarization developed under the action of stress/strain and a differently oriented polarization/field as:

$$E_m = -2 Q_{ijmn}X_{ij}P_n \quad P_m = 2 M_{ijmn}X_{ij}E_n$$

$$= -2 q_{ijmn}x_{ij}P_n \quad = 2 m_{ijmn}x_{ij}E_n$$

The more familiar forms of these converse effects are:

$$M_{ijmn} = \frac{1}{2} \left(\frac{\partial \eta_{mn}}{\partial X_{ij}} \right)_{P,T} \quad \text{and} \quad Q_{ijmn} = \frac{-1}{2} \left(\frac{\partial \chi_{mn}}{\partial x_{ij}} \right)_{P,T}$$

involving the dielectric susceptibility η and the dielectric stiffness χ .

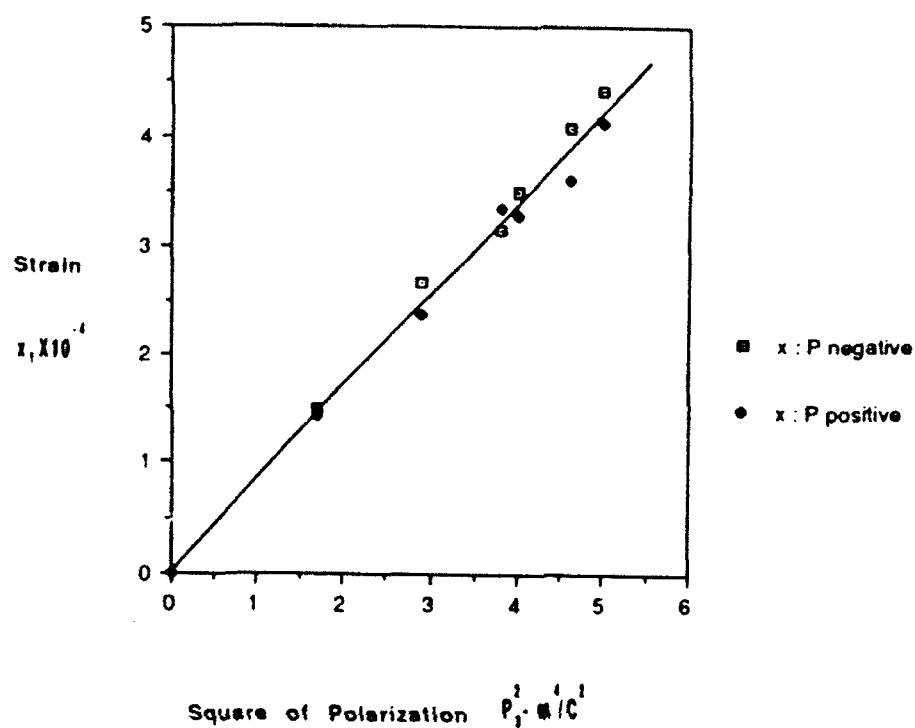


FIGURE 1 Strain (x_1) as a function of the square of the polarization (P_1^2) in PMN. The quadratic $x = QP^2$ nature of the strain—electrostriction relation is illustrated (Reference 36).

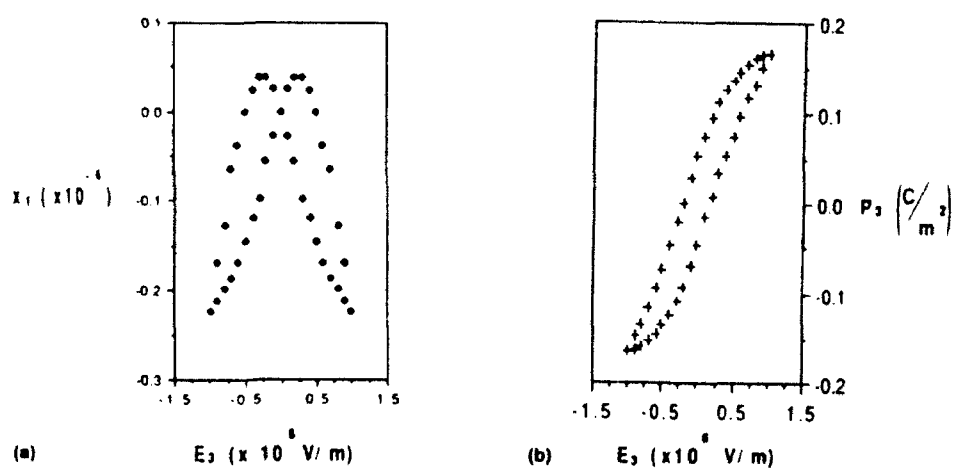


FIGURE 2 Strain (x_1) (2-A) and induced polarization (P_1) (2-B) as a function of applied cyclic (0.01 Hz) electric field (E_1) in PMN, in the ferroelectric phase at -110°C . A "butterfly loop" hysteresis is observed for the strain (Reference 36).

Another converse effect is the polarization dependence of the piezoelectric voltage coefficient g_{jmn} , expressed as:

$$Q_{ijmn} = \left(\frac{\delta g_{jmn}}{\delta P_i} \right)$$

This effect is dealt with in more detail later in the article.

The electrostriction tensor is a fourth rank tensor, that may be cast in matrix form using the collapsed Voigt notation. For crystals of PMN having the point group $m3m$, the matrix notation may be expressed as follows:

$$\begin{bmatrix} x_1 \\ x_2 \\ x_3 \\ x_4 \\ x_5 \\ x_6 \end{bmatrix} = \begin{bmatrix} Q_{11} Q_{12} Q_{12} 0 & 0 & 0 \\ Q_{12} Q_{11} Q_{12} 0 & 0 & 0 \\ Q_{12} Q_{12} Q_{11} 0 & 0 & 0 \\ 0 & 0 & 0 & Q_{44} 0 & 0 \\ 0 & 0 & 0 & 0 & Q_{44} 0 \\ 0 & 0 & 0 & 0 & 0 & Q_{44} \end{bmatrix} \begin{bmatrix} P_1^2 \\ P_2^2 \\ P_3^2 \\ P_2 P_3 \\ P_3 P_1 \\ P_1 P_2 \end{bmatrix}$$

This matrix contains three independent elements, while that for an isotropic material is of identical form, but with one less independent element, as in:

$$Q_{44} = 4 Q_{1212} = 2 (Q_{11} - Q_{12})$$

The above formulations suggest ways to measure electrostriction: direct measurements involve the evaluation of strains produced in the direct effect. This has been achieved using strain gauge methods,³ capacitance dilatometry,⁴ differential transformer methods,⁵ and laser interferometric dilatometry.^{6,7}

Converse method measurements involve the evaluation of changes in permittivity of the material under test, with respect to oriented or hydrostatic applied stress. The sensitivity required in low strain detection for the direct methods is here transferred to dielectric measurements. This method is seen as particularly suitable for low permittivity materials.^{8,9}

Other methods that have been employed to calculate electrostriction coefficients employ ultrasonic pulse delay and transit time methods to derive the electroelastic tensor of the material. This has been performed for quartz.¹⁰ However, the results from these methods for the electrostriction coefficients do show some differences from values established in the literature.¹¹

In ferroelectrics, the variation of the transition temperature T_c with pressure gives us another method³ to evaluate the hydrostatic electrostriction coefficient Q_h :

$$\left(\frac{\delta T_c}{\delta P} \right) = -2 \epsilon_0 C Q_h,$$

where C is the Curie-Weiss constant. The second converse effect²⁴ discussed earlier is another way to evaluate the electrostriction coefficient.

APPLICATIONS

Despite the fact that electrostriction was initially relegated to the role of an esoteric and at best secondary effect, the number of applications of the phenomenon, both

theoretical and practical, has been increasing significantly since the introduction of PMN as a prototype electrostrictive material.¹²

Most applications take advantage of the electrostrictor as an actuator, exploiting the nonhysteretic, tunable nature of the electromechanical response. Mechanical applications range from stacked actuators¹³ through inchworms, microangle adjusting devices, and oil pressure servo valves.¹⁴ These are in the main servo-transducers, deployed as micropositioning devices, featuring a reproducible, non-hysteretic deformation response on the application of an electric signal of suitable magnitude.

The linear change in capacitance with applied stress of an electrostrictor may be characterized and the electrostrictor can now serve as a capacitive stress gauge,³ harnessing the first converse effect. The second converse effect is used in field tunable piezoelectric transducers.²⁴

Electrostrictors have also been integrated into "smart" optical systems such as bistable optical devices, interferometric dilatometers¹⁵ and deformable mirrors.¹⁶ Electrostrictive correction of optical aberrations is a significant tool in active optics.

More theoretical applications of the effect exploit its nature as a fundamental property in all insulators. These include the correlation of electrostrictive stresses with optical Kerr effect phenomena¹⁷ and hydration effects¹⁸ in liquids. Electrostrictive coefficients and phenomena are essential inputs to anharmonic shell models¹⁹ that further our understanding of the behavior of the solid state. It has been proposed that electrostrictive stresses may play a significant role in the generation of pressure waves by microwave pulses in dielectrics²⁰ with thermal or dielectric discontinuities. Electrostrictive self-trapping of light in laser glasses is one of the proposed mechanisms²¹ for initiation of laser damage in these glasses.

A shape memory effect arising from inverse hysteretic behavior and electrostriction in PZT family antiferroelectrics²² is also of interest.

ELECTROSTRICTION AS THE ORIGIN OF PIEZOELECTRICITY

Electrostriction is seen to be the origin of piezoelectricity in ferroelectric materials—in conventional ceramic ferroelectrics² such as BaTiO₃ as well as in organic polymer ferroelectrics²³ such as PVDF copolymers.

The Devonshire phenomenology provides a clear basis for this, as outlined below. In a ferroelectric material that exhibits both spontaneous and induced polarizations, P_i^s and P_i^i , the strains arising from spontaneous polarization, piezoelectricity, and electrostriction may be formulated as:

$$x_{ij} = Q_{ijk} P_k^s P_i^s + 2 Q_{ijk} P_k^s P_i^i + Q_{ijk} P_k^i P_i^i$$

In the paraelectric state, we may express the strain as:

$$x_{ij} = Q_{ijk} P_k P_i, \quad \text{whence:}$$

$$\left(\frac{dx_{ij}}{dP_k} \right) = g_{ijk} = 2 Q_{ijk} P_i$$

Converting to the commonly used d_{ijk} coefficients:

$$d_{ijk} = \eta_{mk} g_{ijm} = 2 \eta_{mk} Q_{ijmn} P_n$$

This origin of piezoelectricity in electrostriction provides us an avenue into non-linearity: the ability to tune the piezoelectric coefficient and the dielectric behavior of a transducer. The piezoelectric coefficient varies with the polarization induced in the material, and may be controlled by an applied electric field.

The electrostrictive element may be tuned from an inactive to a highly active state; the electrical impedance of the element may be tuned by exploiting the dependence of permittivity on the biasing field for these materials, and the saturation of polarization under high fields.²⁴

The coupling factors k_{33} and k_{31} of a transducer and the planar coupling factor k_p may be measured by transmission methods, and are related to the d_{ij} coefficients by the relations:

$$k_{33} = \frac{d_{33}}{\sqrt{\epsilon_0 \epsilon_3 s_{33}}}, \quad k_{31} = \frac{d_{31}}{\sqrt{\epsilon_0 \epsilon_3 s_{11}}} \quad \text{and} \quad k_p = k_{31} \left(\sqrt{\frac{2}{1 - \sigma}} \right)$$

where σ is the Poisson ratio and the s_{ij} coefficients are elastic compliances, with the 3-axis as the poling axis. Here, the slope of the (d_{ij}/ϵ_i) vs. P_i curves (Figure 3) gives us the Q_{ij} coefficients. This method employs the second converse effect mentioned before, quantifying electrostriction from the variation of the piezoelectric coefficients with polarization induced.

PMN AS A PROTOTYPE ELECTROSTRICTIVE MATERIAL

Lead magnesium niobate, $\text{Pb}(\text{Mg}_{1/3}\text{Nb}_{2/3})\text{O}_3$ type compounds were first synthesized more than thirty years ago.²⁵ Since then, the PMN system has been well characterized in both single crystal and ceramic forms, and may be considered the prototype ferroelectric electrostrictor.

A significant feature of the PMN system is that the quadratic strain-polarization relation holds into the ferroelectric phase, well below the average Curie temperature of 0°C for this relaxor ferroelectric. The strain-electric field loops show hysteresis of a form often referred to as the "butterfly loop" (Figures 1 and 2).

The longitudinal and transverse electrostriction coefficients have been established to be, for this material in the m3m point group⁵:

$$Q_{11} = 2.5 (\pm 0.14) \times 10^{-2} \text{ m}^4/\text{C}^2$$

$$Q_{12} = -0.96 (\pm 0.2) \times 10^{-2} \text{ m}^4/\text{C}^2$$

The averaged values for poled ceramic PMN are:

$$Q_{33} = 2.3 (\pm 0.2) \times 10^{-2} \text{ m}^4/\text{C}^2$$

$$Q_{13} = -0.64 (\pm 0.05) \times 10^{-2} \text{ m}^4/\text{C}^2$$

$$Q_h = 0.60 (\pm 0.08) \times 10^{-2} \text{ m}^4/\text{C}^2$$

The maxima in the induced piezoelectric coefficients as a function of biasing electric field (Figure 4) are at $E \sim 1.2 \text{ MV/m}$, with $d_{33} = 240 \text{ pC/N}$ and $-d_{31} = 72 \text{ pC/N}$. The (d_{33}/ϵ_3) and $(-d_{31}/\epsilon_3)$ plotted (Figure 3) as a function of P_3 give

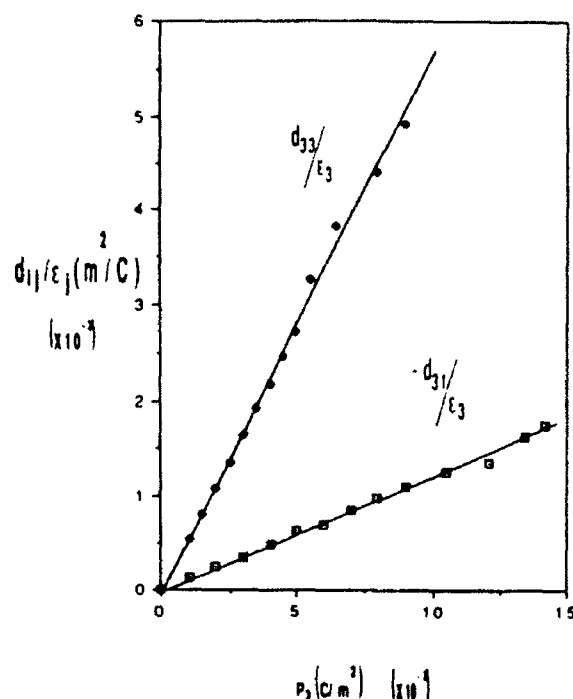


FIGURE 3 Electrostriction coefficients Q_{33} and Q_{31} may be calculated from the slopes of the plots of d_{33}/ϵ_3 and d_{31}/ϵ_3 , shown here for ceramic PMN (Reference 36).

values of Q_{33} and Q_{31} that are in accord with values measured by other methods. The coefficients Q_{11} and Q_{12} appear fairly independent of temperature (Figure 5).

The addition of PbTiO_3 (PT) to PMN gives rise to compositions in the PMN-PT system⁵ that have a higher Curie range and better induced electromechanical coupling coefficients (Figure 6). The composition $\text{Pb}(\text{Mg}_{0.3}\text{Nb}_{0.6}\text{Ti}_{0.1})\text{O}_3$ displays this effect, with a maximum $d_{33} = 1300$ pC/N at a biasing field of 3.7 kV/cm.

One feature common to many nonlinear systems is that the nonlinearity is linked to nanoscale structural features. PMN may be regarded as a self-assembling nanocomposite,²⁴ with ordered and disordered regions. On the nanometer scale, the system is partitioned into Mg-rich and Nb-rich regions. The Mg-rich regions undergo ordering, and the local stoichiometry of these regions (1:1-Mg:Nb) is different from the system stoichiometry (1:2-Mg:Nb). The system relaxes the condition of charge neutrality on a local scale to permit ordering of the B-site cations, so charge neutrality is accomplished now on the order-disorder scale.³⁸ The relaxor behavior of PMN is seen to arise from the scale of the structure (the cluster size) rather than the chemical inhomogeneity. A simple cube model²⁴ estimates these islands to extend over 6 unit cells, or about 24 Å. TEM images give typical dimensions of 30 Å for the ordered regions.³⁸ The highly inhomogeneous nanostructure gives rise to polarization inhomogeneities as well. The size of these regions affects the magnitudes of polarization fluctuations caused by thermal motion near the diffuse ferroelectric phase transition. Dipoles in the Nb-rich regions are tightly coupled to each other, but not to the crystal lattice. The nature of the system (arising from

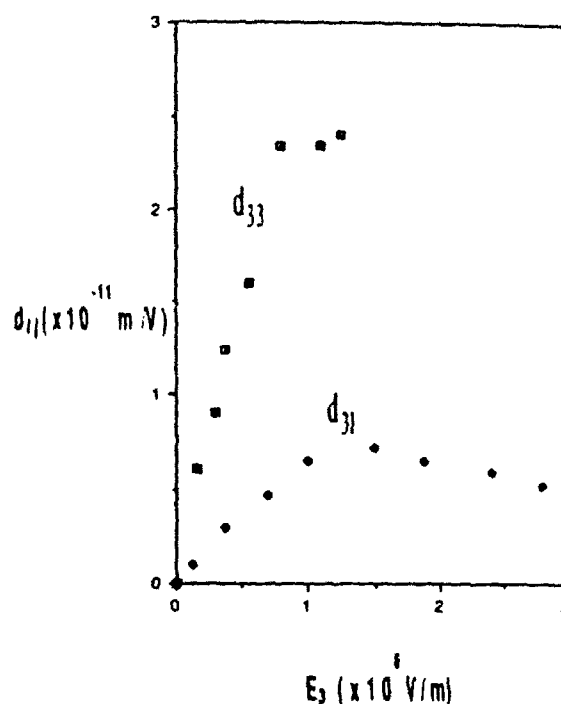


FIGURE 4 Induced piezoelectric coefficients d_{33} and $-d_{31}$ as a function of applied biasing field for PMN, 18°C (Reference 36).

the nanoscale structure and the diffuseness of the phase transition) is such that it is maintained on the verge of instability.²⁴ In response to changes in the state variables such as temperature, stress, electric or magnetic fields, the dipoles are able to reorient themselves, giving rise to large dielectric and electrostrictive effects.

The dielectric, polarization, and electromechanical responses of the relaxor ferroelectrics have been shown to be glassy, and similar to the responses of spin and orientational glasses,^{39,40} and extending the superparaelectric model.⁴¹ For example, magnetic spin glasses display cluster sizes on a nanometer scale, nonlinear magnetic susceptibilities and bias dependence of stiffness. In PMN, the dielectric susceptibility is similarly glassy and nonlinear, and the stiffness varies with bias. This is of particular interest because the changes in linear elastic response may be traced back to local electrostrictive strains. With the onset of local polarization around 330°C, the electrostrictive strains arising from the induced polarization soften the lattice, leading to a softening in the elastic stiffness over a broad temperature range. On the application of a biasing field, the randomness of orientation in the local electrostrictive strains is destroyed, and the elastic response is stiffened.

POLARIZATION MECHANISMS IN ELECTROSTRICTION

The basic mechanisms contributing to the polarization in dielectric materials have been identified and treated extensively.⁴³ Their individual contributions are illus-

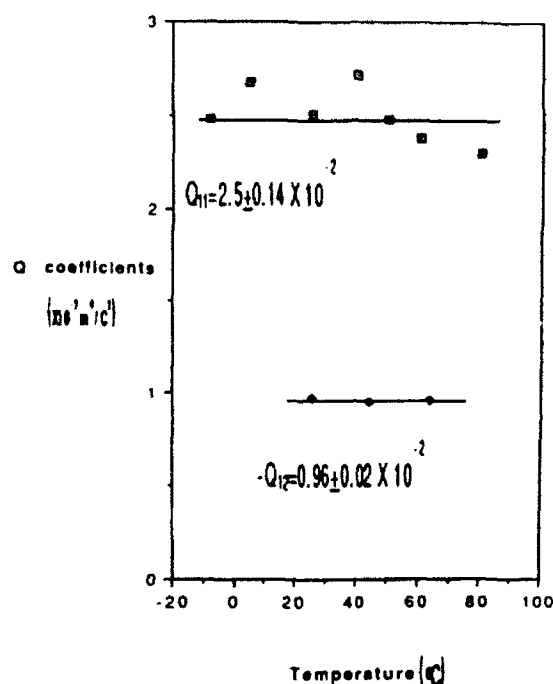


FIGURE 5 Q_{11} and Q_{12} variations with temperature for PMN (Reference 5).

trated by the frequency dispersion of the linear dielectric response (Figure 7), that separates the contributions from these mechanisms. Space charge effects and defects contribute to interfacial polarization, that has a frequency regime of typically 10^5 Hz and below. Orientation or dipolar polarization may be seen in materials that have permanent dipoles, in the range 10^5 – 10^{10} Hz. Ionic or atomic polarization occurs from the relative displacement of the ions in the material, in the range 10^{10} – 10^{13} Hz. Electronic polarization arises from the distortions of the charge distributions around the ions of the material, in the optical frequency ranges of 10^{14} Hz and above.

Electrostriction is a polarization related effect as defined ($x = QP^2$), and an understanding of the mechanisms of polarization that contribute to the electrostriction is thus of fundamental interest. Of the mechanisms outlined above, the effects of the ionic and electronic contributions are of main interest. The separation of the contributions from these effects offers further insight into the mechanisms of the effect and is useful in discerning trends in the electrostrictive behavior, especially in low permittivity linear dielectrics.

Electrostriction measurements on most crystalline materials have been performed over limited frequency ranges (10^5 Hz and below). Little variation of the Q coefficients with the frequency of measurement is seen. Measurements over wider ranges of frequencies may be necessary to directly study the frequency dependence of electrostriction. Glasses, however, display a dispersion in the values of their Q coefficients with frequency. The Q_{11} coefficient of sodium trisilicate glass decreases from $0.85 \text{ m}^4/\text{C}^2$ ($\epsilon = 15.5$), at 10^2 Hz to $0.43 \text{ m}^4/\text{C}^2$ ($\epsilon = 8.82$), at 40 kHz,

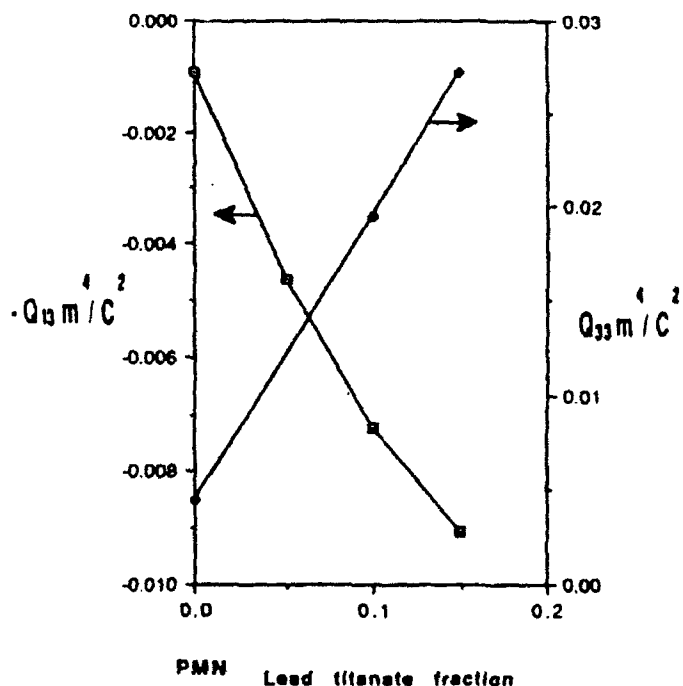


FIGURE 6 Variation of Q_{13} and Q_{33} with addition of PT to the PMN system (Reference 5).

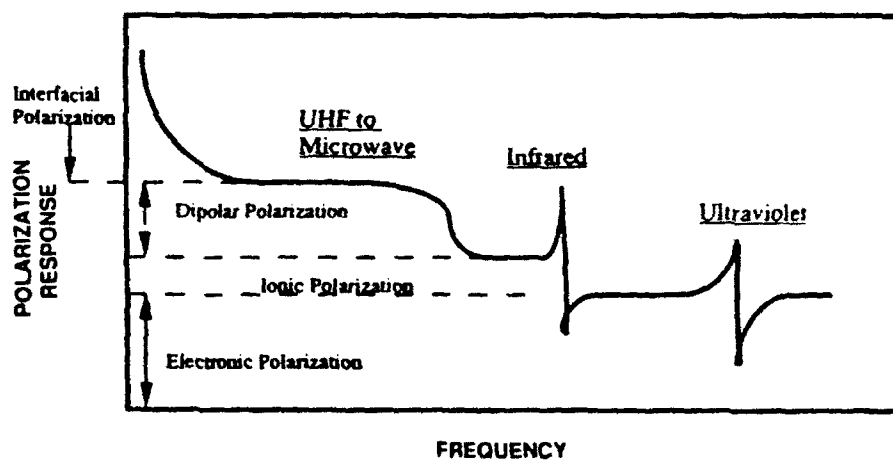


FIGURE 7 Frequency dependence of polarization mechanisms in linear dielectrics (Reference 42).

indicating a decreasing contribution from ionic polarization mechanisms. The high frequency value tends to the value of the Q_h coefficient for fused silica ($Q_h \approx 0.44$, 2.5 kHz), indicating that the response at these frequencies is that of the silicate network alone.²⁸

It is possible to analyze the individual contributions of the ionic and electronic polarizations to electrostriction indirectly by comparing their contributions to the dielectric response of the material. It is known that the high frequency relative

dielectric permittivity ϵ_r is related to the optical refractive index n by the relation $n^2 \sim \epsilon_r$. The pressure dependencies of n and ϵ_r , the relative permittivity, may be analyzed independently. The difference in the pressure dependencies between these is then a measure of the pressure dependence of ϵ_i , the relative ionic permittivity, as expressed by the equation:

$$\left(\frac{\Delta\epsilon_r}{\Delta p}\right) - \left(\frac{\Delta\epsilon_e}{\Delta p}\right) = \left(\frac{\Delta\epsilon_i}{\Delta p}\right)$$

Measurements of this nature performed on KMgF_3 , a fluoride perovskite,⁴² show that the ionic polarization contribution to electrostriction, as reflected by $(\Delta\epsilon_i/\Delta p)$, is about 30 times as large as the electronic polarization contribution $(\Delta\epsilon_e/\Delta p)$, and of opposite sign, typically -3 kbar^{-1} as compared to 0.09 kbar^{-1} . The ionic contribution clearly dominates the effect for linear dielectrics in low frequency (1–100 kHz) regime.

The evaluation of the contribution of the electronic polarization for various fluorides and oxides reveals a significant trend. The values of $(\Delta n^2/\Delta p)$ for fluorides are of similar magnitude and sign positive ($\sim 2 \times 10^{-4} \text{ kbar}^{-1}$), while those for oxides are negative ($\sim -1 \times 10^{-4} \text{ kbar}^{-1}$).⁴³ This indicates that the anion species governs the electronic polarization contribution in ionic solids. In covalent diamond, where only the electronic polarization contributes, the small magnitude of the contribution, combined with the high elastic stiffness of the material, gives rise to an electrostriction coefficient ($Q_h = 0.03 \text{ m}^4 \text{ C}^{-2}$) that is anomalously low for a low permittivity dielectric.

The contribution of the ionic polarization, on the other hand, is governed by both cation species and crystal structure. Viewing electrostriction as the interactive response of ions to an applied electric field, it is expected that ions with higher valences or higher polarizabilities would lead to larger electrostrictive effects. The electrostriction coefficients may be seen to vary inversely with Z^2 , where Z is the ionic valence of the solid reduced to a two atom chain model.²⁹ This reflects the trends of decreasing Q_h coefficients from alkali halides ($Z = 1$) through fluoride perovskites ($Z = 1.5$), oxides such as MgO ($Z = 2$) to ferroelectric oxide perovskites ($Z = 3$) (Tables I-A and I-B).

It must be emphasized here that large Q coefficients in a material do not imply that it exhibits large electrostrictive strains. The figure of merit used to compare electrostrictive strains generated in insulators is $Q\epsilon^2$, where ϵ is the permittivity. Relaxor ferroelectrics display Q coefficients two orders of magnitude smaller than common linear dielectrics (10^{-2} , compared to 10^0). But their permittivities are three orders of magnitude larger (10^4 as against 10^1), and the figures of merit are thus four orders of magnitude larger (10^6 compared to 10^2). Between two materials of comparable permittivities, the material with a larger Q coefficient may be expected to display larger electrostrictive strains.

The contribution of the crystal structure to electrostriction arises from the bonding between the ions in the structure. Electrostrictive strains must act against the bonding of the ionic solid, displacing the ions from their equilibrium positions. We may then expect solids with short, strong bonds to have weaker electrostrictive effects (smaller volume strains and dilations, for hydrostatic electrostriction) as compared to solids with longer, and weaker bonds. Among the alkali halides that

TABLE I-A
Electrostrictive and dielectric data on some ferroelectric and non-ferroelectric oxides, ferroelectrics

COMPOSITION	$Q_h \times 10^{-3} \text{ m}^4/\text{C}^2$	Curie constant $C \times 10^5 \text{ K}$	$Q_h C \times 10^3 \text{ m}^4/\text{C}^2 \text{ K}$	Ref.
$\text{Pb}(\text{Mg}_{1/3}\text{Nb}_{2/3})\text{O}_3$	0.6	4.7	2.8	31
$\text{Pb}(\text{Zn}_{1/3}\text{Nb}_{2/3})\text{O}_3$	0.66	4.7	3.1	31
BaTiO_3	2.0	1.5	3.0	37
PbTiO_3	3.7	1.0	3.7	32
SrTiO_3	4.7	0.77	3.6	33
KTaO_3	5.2	0.5	2.6	37
PbZrO_3	2.0	1.6	3.2	37
$\text{Pb}(\text{Mg}_{1/2}\text{W}_{1/2})\text{O}_3$	6.2	0.42	2.8	31
$\text{Pb}(\text{Sc}_{1/2}\text{Ta}_{1/2})\text{O}_3$	0.87	2.8	2.4	34
$\text{Pb}(\text{Sc}_{1/2}\text{Nb}_{1/2})\text{O}_3$	0.83	3.5	2.9	37

TABLE I-B
Electrostrictive and dielectric data on some ferroelectric and non-ferroelectric oxides, non-ferroelectric, low permittivity materials

MATERIAL AND TYPE	$Q_h \cdot \text{m}^4/\text{C}^2$	Permittivity	Ref.
ALKALI HALIDES			
LiF	0.40	9.04	4
NaCl	1.44	5.91	4
KBr	2.28	4.87	4
ALKALINE EARTH FLUORIDES			
CaF_2	0.39	6.81	8,35
BaF_2	0.44	6.48	8,35
SrF_2	0.29	7.37	8,35
FLUORIDE PEROVSKITES			
KMgF_3	0.24	6.08	29
KZnF_3	0.28	7.9	4
KMnF_3	0.27	11.1	4
OXIDES			
Vitreous silica	0.44	3.8	28
Sodium trisilicate glass	0.76 ($Q_{11} - 1\text{kHz}$)	11.3	28
Sodium aluminosilicate glass	0.52 ($Q_{11} - 1\text{kHz}$)	10.2	28
MgO	0.16	10.0	29
COVALENT MATERIALS			
Diamond	0.03	5.86	4
PVDF (Drawn)	-2.4 (q_{33})	16.0	23

display comparable permittivities, this trend is reflected in Q coefficients that increase with bond length. Using the lattice constant to reflect trends in bond length, Q_h increases from LiF ($a = 4.03 \text{ \AA}$, $Q_h = 0.4$) through NaCl ($a = 5.64 \text{ \AA}$, $Q_h = 1.4$) to KBr ($a = 6.59 \text{ \AA}$, $Q_h = 2.3$).

When an ion responding to applied electric field is contained in a polyhedral 'cage' structure, the total distortion is determined by the strong bonds forming the cage structure rather than the 'rattling' movements of ions within the cage. In an oxide perovskite in its paraelectric state, the B-site cation is surrounded by an oxygen octahedron. In open, disordered perovskite structures, with more 'rattling room', the highly polarizable B-site cation is free to respond to applied fields without distorting the octahedra as much as it would in an ordered perovskite structure.²⁷ Ordered structures thus have larger strains per unit polarization, and larger electrostrictive coefficients (Table I-A). The disordered structures exhibit larger polarizations, and thus larger dielectric permittivities.

A similar model may be used to explain the smaller electrostrictive effects in sodium aluminosilicate glass ($Q_h = 0.85$, 100 Hz) as compared with sodium trisilicate glass ($Q_h = 0.6$, 100 Hz).²⁸ With increasing alumina content, the bridging oxygen fraction in the silicate network is increased, and the coordination shell around the Na^+ ions expands. The ion in an expanded silicate cage may thus respond to applied fields without distorting the cage geometry. The contribution of the Na^+ ion polarizability is thus reduced, and a weaker electrostrictive effect is observed.

The intuitive rigid ion model briefly outlined above may be used to derive a relation between the dielectric permittivity of a solid and the electrostriction coefficients. The model is based on the premise that the properties of solids are controlled by the magnitudes of response to external stimuli from small displacements of ions in the structure of the solid.²⁶ When an insulating solid is subjected to an electric field, we may picture the cations and anions being displaced in opposite directions, by Δr under the action of the field. Assuming to a first approximation that the induced polarization P , the permittivity ϵ , and the electrostrictive strain x are all proportional to Δr , the Q coefficient may be seen to vary inversely with the dielectric permittivity, as illustrated by the relation²⁴:

$$Q = \left(\frac{x}{P^2} \right) \sim \left(\frac{\Delta r}{\Delta r^2} \right) = \frac{1}{\Delta r} \sim \frac{1}{\epsilon}$$

This relation between the electrostrictive coefficients and the permittivity directs the search for actuator materials towards high permittivity materials. The high values of permittivity exhibited by relaxor ferroelectrics, in spite of the small Q values, make these desirable candidates in this field.

EMPIRICAL CORRELATIONS WITH OTHER MATERIAL PROPERTIES

The hydrostatic electrostriction Q_h of a material, its thermal expansion coefficient α , the dielectric permittivity ϵ , the isothermal volume compressibility β , and its pressure dependence $1/\beta (\delta\beta/\delta p)$ are all similar in the sense that all these are defined in the form of compliance coefficients. They all relate the change in strains or

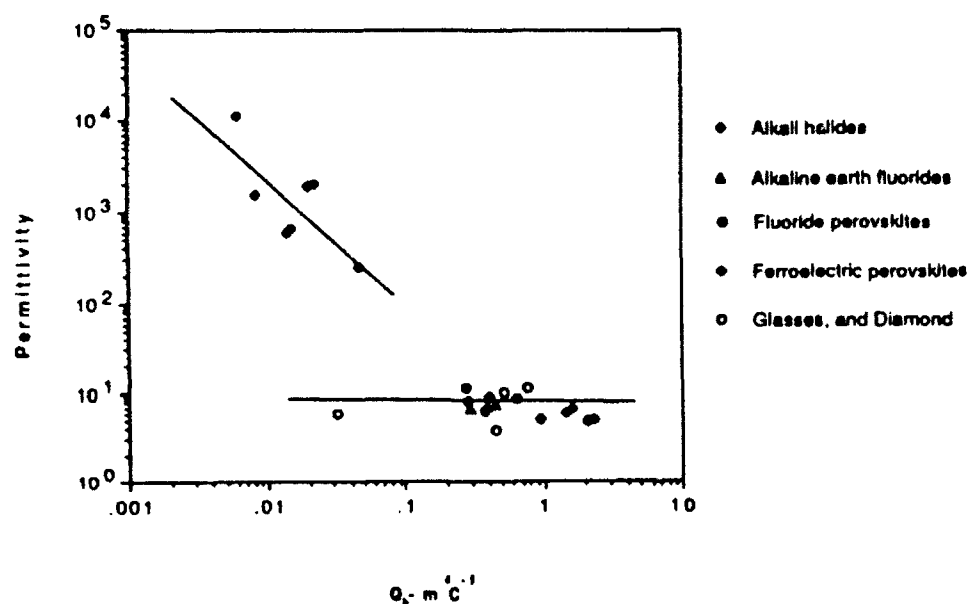


FIGURE 8 Correlation of permittivity with Q_h for both ferroelectric and non-ferroelectric materials.

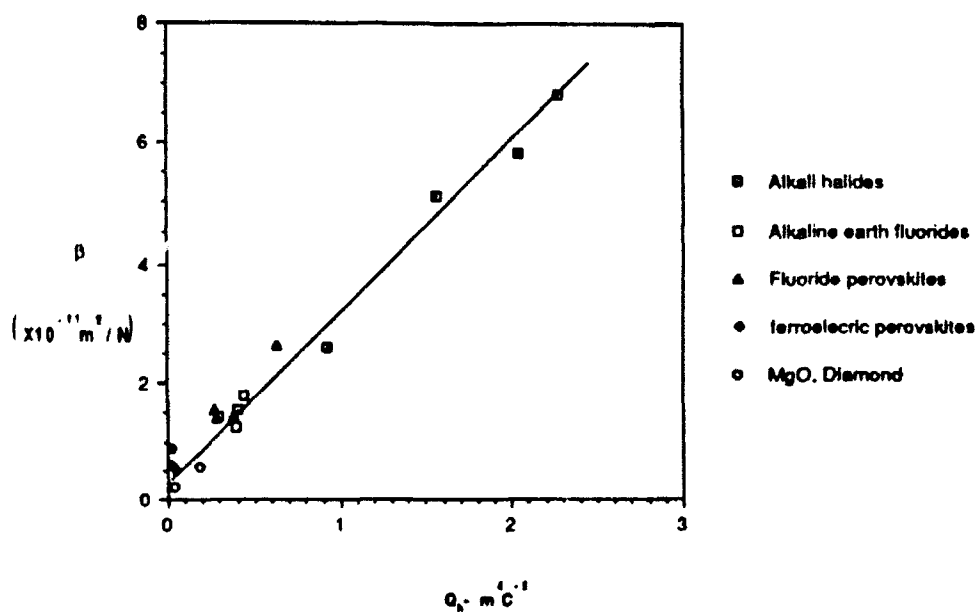


FIGURE 9 Correlation of isothermal volume compressibility β with Q_h for ferroelectrics and non-ferroelectrics is similar, and linear.

polarizations developed in materials in response to changes in state variables such as temperature, stress (pressure) etc. Intuitively, we may expect these properties to exhibit correlations between themselves. All of these coefficients may be formulated using the quasi-harmonic and the harmonic models of the solid state.

Correlations of this nature yield interesting results. The thermal expansion coefficient α is seen to vary³⁰ as $Q_h^{1/2}$. The dielectric permittivity ϵ varies (Figure 8) approximately as Q_h^2 for ferroelectrics, but is independent of Q_h for linear electrics.⁴ Simple, linear relationships are observed for the variations of β (Figure 9) and $1/\beta$ ($\delta\beta/\delta p$). These are both first order anharmonic properties, as is electrostriction.

Another useful correlation observed is the nearly constant value of the product $Q_h C \sim (3.1 \pm 0.4) \times 10^3 \text{ m}^4 \text{ C}^{-2} \text{ K}$ for ferroelectric materials (Table I-A).

SUMMARY

Electrostriction still presents several new possibilities and challenges to investigation. While the basic nature and effects of the phenomenon are well established, there is still a need for analyses that model this effect on a physical basis. Modeling is held back in part by the lack of reliable, accurate measurements of electrostrictive coefficients over wider frequency and temperature ranges, especially in low permittivity dielectrics.

As a fundamental effect, electrostriction may prove to be an important factor in the design of electronic devices. The present focus is on synthesis of materials with large electrostriction effects. The other extreme of the scale may prove to be of interest, too. As microelectronic devices are taken to smaller dimensions, the increased field levels on the materials used could make electrostrictive effects significant enough to prove a limiting factor in such design. It is then tempting to consider designing a material with zero electrostriction coefficients, for applications in areas where field induced damage is a significant risk. Other, more benign options are also offered by the effect—in an increasing array of novel applications, that make it well worth further study.

REFERENCES

1. M. E. Lines and A. M. Glass, *Theory and Applications of Ferroelectric Materials*, Oxford Univ. Press, Oxford (1977).
2. F. Jona and G. Shirane, *Ferroelectric Crystals*, Macmillan, New York (1962).
3. S. Nomura, J. Kuwata, S. J. Jang, L. E. Cross and R. E. Newnham, *Mat. Res. Bull.*, **14**, 769 (1979).
4. K. Rittenmyer, Ph.D. Dissertation, The Pennsylvania State University (1984).
5. S. J. Jang, K. Uchino, S. Nomura and L. E. Cross, *Ferroelectrics*, **27**, 31 (1980).
6. B. J. Luymes, *Rev. Sci. Instrum.*, **54**, 90 (1983).
7. Q. M. Zhang, W. Y. Pan and L. E. Cross, *J. Appl. Phys.*, **63**, 8, 2492 (1988).
8. Z. Y. Meng, Y. M. Sun and L. E. Cross, *Mat. Lett.*, **2**, 6A & B, 544 (1984).
9. Z. Y. Meng and L. E. Cross, *J. Appl. Phys.*, **57**, 2, 488 (1985).
10. E. Kittinger, J. Tichy and W. Friedel, *J. Appl. Phys.*, **60**, 1465 (1986).
11. K. K. Hruska, *J. Appl. Phys.*, **68**, 41 (1990).
12. K. Uchino, *Cera. Bull.*, **65**, 4, 647 (1986).
13. Y. Nakajima, T. Hayashi, I. Hayashi and K. Uchino, *Jpn. J. Appl. Phys.*, **24**, 2, 235 (1985).
14. S. Nomura and K. Uchino, *Ferroelectrics*, **50**, 197 (1983).

15. M. Gomi, Y. Miyazawa, K. Uchino, M. Abe and S. Nomura, *Appl. Optics*, **21**, 2616 (1982)
16. T. Sato, H. Ishikawa, O. Ikeda, S. Nomura and K. Uchino, *Appl. Optics*, **21**, 3669 (1982)
17. P. B. McGrath and R. W. Bradish, *IEEE Trans. on Electrical Insulation*, **23**, 2, 189 (1989)
18. M. Satoh, M. Hayashi, J. Komiyama and T. Iijima, *Polymer Communications*, **29**, 2, 49 (1988)
19. B. N. N. Achar, G. R. Barsch and L. E. Cross, *Phys. Rev. B*, **24**, 1209 (1981)
20. T. C. Guo and W. W. Guo, *IEEE Ann. Rept., Conf. on Electrical Insulation and Dielectric Phenomena*, IEEE New York, 152 (1987).
21. R. M. Waxler, *IEEE J. Quantum Electronics*, **QE-7**, 4, 166 (1971).
22. K. Uchino and S. Nomura, *Ferroelectrics*, **50**, 191 (1983).
23. T. Furukawa and N. Seo, *Jpn. J. Appl. Phys.*, **28**, 2, 675 (1990).
24. R. E. Newnham, *Chemistry of Electronic Ceramic Materials*, Proc. Int. Conf., Jackson, WY, 1990, NIST Special Publication, **804**, 39 (1991)
25. G. A. Smolenskii and A. I. Agranovskaya, *Sov. Phys. Sol. St.*, **1**, 10, 1429 (1959)
26. M. Born and K. Huang, *Dynamical Theory of Crystal Lattices*, Oxford Univ. Press, London (1954)
27. S. Nomura, K. Tonooka, J. Kuwata, L. E. Cross and R. E. Newnham, *Proc. 2nd Meeting on Ferroelectric Materials and Applications*, Kyoto, 1979; 133 (1979)
28. Y. Sun, W. W. Cao and L. E. Cross, *Materials Letters*, **4**, 8-9, 329 (1986).
29. K. Uchino, *J. Phys. Soc. Jpn.*, **53**, 4, 1531 (1984).
30. K. Uchino and L. E. Cross, *Jpn. J. Appl. Phys.*, **19**, L171 (1980)
31. K. Uchino, S. Nomura, L. E. Cross, S. J. Jang and R. E. Newnham, *Jpn. J. Appl. Phys.*, **20**, L398 (1980).
32. G. A. Rossetti Jr., K. R. Udayakumar, M. J. Haun and L. E. Cross, *J. Am. Ceram. Soc.*, **73**, 11, 3334 (1990).
33. Landolt-Bornstein, *Num. Data and Functional Relationships in Sci. and Tech., New Series, Gp. III, vol. 18*, Springer-Verlag (1984).
34. Landolt-Bornstein, *Num. Data and Functional Relationships in Sci. and Tech., New Series, Gp. III, vol. 24*, Springer-Verlag (1990).
35. Z. Y. Meng, Th. Kwaaitaal and W. M. M. van den Eijnden, *J. Appl. Phys.*, **21**, 175 (1988).
36. J. Kuwata, K. Uchino and S. Nomura, *Jpn. J. Appl. Phys.*, **19**, 2099 (1980)
37. K. Uchino, S. Nomura, L. E. Cross, S. J. Jang and R. E. Newnham, *J. Appl. Phys.*, **51**, 2, 1142 (1980)
38. C. Randall and A. S. Bhalla, *J. Mat. Sci.*, **29**, 5 (1990).
39. D. Viehland, S. J. Jang, M. Wuttig and L. E. Cross, *J. Appl. Phys.*, **68**, 2916 (1990).
40. D. Viehland, Ph.D. Dissertation, The Pennsylvania State University (1991)
41. L. E. Cross, *Ferroelectrics*, **76**, 241 (1987).
42. K. Uchino, S. Nomura, K. Vedam, R. E. Newnham and L. E. Cross, *Phys. Rev. B*, **29**, 12, 6921 (1984).
43. A. R. von Hippel, *Dielectrics and Waves*, John Wiley and Sons, New York, NY (1956)

MATERIALS STUDIES

APPENDIX 6

gained from the temperature variation of numerous material properties across the composition range of interest. In particular, exceptionally strong dielectric, pyroelectric, and piezoelectric responses are typically observed at the MPB of binary systems of this type. The dielectric and pyroelectric responses of poled ceramics are also expected to show features which may be indicative of a curved boundary. The compositional range was initially investigated by means of x-ray diffraction. Verification of these determinations and further insight into the nature of the boundary were gained from subsequent investigation of the dielectric, pyroelectric, and piezoelectric properties of the material through the composition range of the morphotropic phase boundary.

Sample preparation

The $(1-x)\text{Pb}(\text{Sc}_{1/2}\text{Ta}_{1/2})\text{O}_3$ - $x\text{PbTiO}_3$ ceramics were produced by a conventional mixed-oxide method involving the use of high purity starting compounds, a precursor-phase formulation, and controlled lead atmosphere sintering. The compositions of interest were initially prepared as powders employing a wolframite ScTaO_4 ² precursor method³ in order to reduce the occurrence of undesirable pyrochlore phases. Starting oxides $\text{Sc}_2\text{O}_3^\dagger$ and $\text{Ta}_2\text{O}_5^\dagger$ were batched and calcined at 1400°C for 6-8 hours to form the ScTaO_4 precursor. Compositions were then formulated from PbO^\dagger , TiO_2^\dagger , and the precursor phase across the entire range so as to adequately represent all phase regions occurring in the system. Each composition was calcined at 900°C for 4 hours and at 1000°C for 1 hour with an intermediate comminution step. Compacted specimens of compositions [$x \leq 0.5$] were fired at 1400°C for one hour and those with compositions [$x > 0.5$] at 1200°C also for one hour within sealed alumina crucibles containing $\text{Pb}(\text{Sc}_{1/2}\text{Ta}_{1/2})\text{O}_3/\text{PbZrO}_3$ source powders. Samples with composition [$x \geq 0.2$] were sufficiently

[†] PbO [Johnson Matthey - Materials Technology UK - Grade A1]; Sc_2O_3 [Boulder Scientific Co. - 99.99%]; Ta_2O_5 [Hermann C. Starck (Berlin) - Stand. Opt. Grade]; TiO_2 [Aesar (Johnson Matthey Inc.) - 99.999%]

Identification of the morphotropic phase boundary in the lead scandium tantalate-lead titanate solid solution system

J.R. Giniewicz, A.S. Bhalla, and L.E. Cross

Materials Research Laboratory, The Pennsylvania State University, University Park, PA 16802

Abstract: A morphotropic phase boundary between rhombohedral and tetragonal phase regions has been identified to lie in the composition range $[x=0.4-0.45]$ by means of x-ray diffraction, and dielectric, pyroelectric, and piezoelectric measurements. Some curvature to this boundary at high temperatures is indicated in the temperature dependences of the dielectric constants and pyroelectric coefficients of poled specimens.

Introduction

Several interesting solid solutions of complex lead perovskite compounds and PbTiO_3 exist from which materials with enhanced properties and variable behaviors have been generated.¹ These have been shown to be useful systems from both a practical and theoretical point of view. Solid solution systems of rhombohedral lead-based complex perovskites with PbTiO_3 generally have so-called "morphotropic phase boundaries" [MPB] that occur between rhombohedral and tetragonal phases at compositions ranging from $[x=0.1]$ to $[x=0.4]$. It should be noted that the "morphotropic phase boundaries" identified for many of these systems show some curvature at high temperatures and, therefore, strictly speaking, are not truly temperature independent as the name suggests; the boundary between rhombohedral and tetragonal phases is, hence, identified as a MPB in the sense that it is a boundary separating phases whose structure-type depends largely on composition, especially at low temperatures. The compositional "location" of the MPB for a given system has been correlated with the relative stabilities of the tetragonal and rhombohedral phases as predicted by consideration of the perovskite tolerance factor, t .¹ Similar consideration of the $(1-x)\text{Pb}(\text{Sc}_{1/2}\text{Ta}_{1/2})\text{O}_3$ - $(x)\text{PbTiO}_3$ system anticipates such a morphotropic phase boundary [MPB] to occur at $[x=0.4]$. The actual position of the MPB is most readily assessed by basic structural analysis, in this study conducted by means of x-ray diffraction. Further verification of the compositional range of the boundary and determination of any possible curvature at high temperature may be

The dielectric constant, K , and dissipation factor, D , were measured as a function of temperature and frequency using an automated system consisting of an oven (Model 2300, Delta Design, Inc.), an LCR meter (Model 4274A, Hewlett Packard, Inc.), and a digital multimeter interfaced with a desk top computer (Model 9816, Hewlett Packard, Inc.). Dielectric runs were made at 1 KHz over a temperature range of $[-150 - 260^{\circ}\text{C}]$. The samples were poled in a stirred oil bath at temperatures near the transition temperature under a poling field of 20 (KV/cm) for 15 minutes and then slowly cooled with the field applied to $\sim 50^{\circ}\text{C}$ before the poling field was removed.

The pyroelectric response was measured by a modified Byer-Roundy method.⁵ The specimens were initially poled in air within a temperature chamber [Model 2300, Delta Design, Inc.] in the vicinity of the transition temperature under a poling field of [20 (KV/cm)] for 15 minutes and cooled with the field applied to $\sim 100^{\circ}\text{C}$. The poling field was then removed. A desk top computer [Model 9816, Hewlett Packard, Inc.] was used to record the pyroelectric current data collected by the picoammeter [Model 4140B, Hewlett Packard, Inc.]. The pyroelectric coefficients were subsequently calculated from the pyroelectric current data.

The longitudinal piezoelectric strain coefficient, d_{33} , was determined for specimens, poled as described for the dielectric measurements, utilizing a Berlincourt d_{33} meter [Model CPDT-3300, Channel Products, Inc.]. The poled specimens were probed at approximately ten different points and the arithmetic mean of these determinations were recorded as the actual value for a particular sample. The rated accuracy for the Berlincourt meter employed is $\pm 2\%$ for the range of responses exhibited by these samples.

Results and discussion

The structure type, lattice parameter, and theoretical density were determined at room temperature by means of x-ray diffraction for samples extending across the entire compositional range of the system. Complete solid solution is apparent with the morphotropic

dense ($\approx 95\%$ theoretical density) after this first-stage sintering step; however, specimens with compositions [$x \leq 0.1$] required a second higher temperature sintering [$1500-1560^\circ\text{C}/20$ minutes] which was conducted in a molybdenum tube furnace with a relatively rapid heating and cooling schedule to avoid excessive lead loss. These samples were 90-95% theoretical density following this second stage sintering step.

The samples prepared for room temperature x-ray diffraction were all fired under the first-stage sintering conditions and ground to a powder for measurement. Solid specimens were prepared for the high-temperature x-ray diffraction studies. X-ray surfaces were ground with $12\ \mu\text{m}\ \text{Al}_2\text{O}_3$ and the samples were subsequently annealed at 500°C for 20 minutes to relieve any surface stresses generated from the grinding.

Specimens for dielectric and pyroelectric measurement were cut as plates from the sintered disks with the dielectric samples typically [0.75 cm] on edge and [0.15 cm] in thickness and pyroelectric samples [0.4 cm] on edge and [0.025-0.03 cm] in thickness. The specimens for piezoelectric d_{33} coefficient measurement were prepared as blocks typically [0.4 cm] on edge and [0.2 cm] in thickness. The electrode surfaces were sputtered with gold to which silver contact points were subsequently applied.

Experimental procedure

The structure type, lattice parameters, and theoretical densities were determined for each composition by means of x-ray diffraction using both Philips APD3600 and Scintag [PADV] automated diffractometers. $\text{CuK}\alpha$ radiation was employed. Scans were made on powder samples incorporating a Si [SRM 640] standard over a range of $42-52^\circ$ (2θ) at a rate of [$0.25^\circ/\text{minute}$] and the 200 and 210 reflections were used to determine the lattice parameters. High-temperature phase transitions were monitored by an x-ray diffraction set-up designed for use at elevated temperatures extending up to 1000°C .⁴

phase boundary [MPB] region occurring at $[x \approx 0.4-0.45]$; the $[x \leq 0.4]$ compositions show a rhombohedral symmetry and compositions $[x > 0.4]$ possess tetragonal symmetry with a c/a ratio which increases steadily across the tetragonal composition range [Figure 1; Table 1]. Samples approaching pure PbTiO_3 , for which the aspect ratio and, hence, the lattice strains are becoming considerable, like pure PbTiO_3 , exhibit very low structural integrity. The $[x=0.9]$ specimen became fragile and fractured easily within 24 hours after sintering. The volume, x-ray density, and aspect ratio, c/a , are given in Table 1. An overall decrease in the unit cell volume and x-ray density is observed.

High-temperature x-ray diffraction revealed the general location of the phase boundary between the high-temperature cubic and lower symmetry phases. The smallest temperature interval practically achieved with this experimental set-up is approximately 15°C and, hence, by these means, transition ranges of $\approx 10-20^\circ\text{C}$ were defined for compositions $[x=0.3-0.5]$ and are recorded in Table 1. No evidence of a high-temperature rhombohedral \longleftrightarrow tetragonal transition was detected and, therefore, any significant curvature of the MPB that may exist is assumed, on the basis of these measurements, to occur over a relatively narrow temperature interval in the vicinity of the $[x=0.4]$ composition. The actual transition temperatures of these compositions were further refined by means of dielectric and pyroelectric property measurements.

The dielectric constant measured at 1 KHz is shown as a function of temperature in Figure 2(a) for poled specimens in the composition range $[x=0.3-0.5]$. The peak value of $K(\text{max})$ is observed for $[x=0.45]$. A "shoulder" appears at the low-temperature side of the $[x=0.4]$ peak [Figure 2(b)] indicative of a possible phase transition preceding the ferroelectric \longleftrightarrow paraelectric transition and, hence, suggestive of some curvature to the MPB at elevated temperatures. It is well-known that the dielectric response, as well as other material properties such as the pyroelectric and piezoelectric responses are particularly enhanced at the MPB of binary systems of this kind and, therefore, the MPB of the $(1-x)\text{Pb}(\text{Sc}_{1/2}\text{Ta}_{1/2})\text{O}_3$ -

(x)PbTiO₃ system may be identified on the basis of these data to be within the composition range $[x=0.4-0.45]$, consistent with that determined by means of x-ray diffraction.

The effect of increasing Ti-content on the pyroelectric response of the material, as manifested in the temperature dependence of the pyroelectric coefficient, for compositions $[x=0.3-0.45]$ is shown in Figures 3(a-d). The change in the shape of $p(T)$ and the magnitudes of the pyroelectric peaks are seen to vary significantly throughout the composition range investigated. A sharp and intense peak is observed for $[x=0.3]$ and $[x=0.35]$, occurring at temperatures slightly lower than the temperatures of the dielectric constant maxima followed by a doublet at $[x=0.4]$ and a somewhat broadened, more intense peak at $[x=0.45]$, which also occur at temperatures lower than but increasingly nearer the temperatures of the dielectric constant maxima for these compositions.

A broad high-temperature "hump" has been reported for compositions $[x=0.3-0.4]$ from this system⁶ which had originally been attributed to a phase transition and, hence, the earlier pyroelectric study identified a broader MPB region with pronounced curvature. It has been determined in this investigation that the currents giving rise to these high-temperature features are apparently non-pyroelectric in nature and more likely some thermally stimulated conduction effect. The marked decrease in the peak pyroelectric response at $[x=0.4]$ may well be due to the occurrence of this non-pyroelectric current which would effectively suppress the full pyroelectric response of the material. A more thorough investigation of the conductivity for these compositions is required to more accurately determine the origin and exact nature of this additional component of the induced current.

It is, therefore, assumed at this time that only the sharp lower temperature peaks in this composition range are representative of the actual pyroelectric response of the material and thereby indicative of the phase transitions occurring at each composition. The position and shape of the MPB as defined by these pyroelectric data only are found to be in reasonable agreement with what was determined by means of x-ray diffraction and dielectric measurement.

The magnitudes of the longitudinal piezoelectric strain coefficient, d_{33} , for specimens in the composition range $[x=0.3-0.5]$ are recorded in Table 2. The maximum longitudinal piezoelectric response is attained for the $[x=0.45]$ composition, occurring, as would be expected for a system of this kind, at the morphotropic phase boundary.

Summary

Room temperature x-ray diffraction determinations have indicated that complete solid solution occurs across the entire compositional range of the $(1-x)\text{Pb}(\text{Sc}_{1/2}\text{Ta}_{1/2})\text{O}_3$ - $(x)\text{PbTiO}_3$ system. High-temperature x-ray diffraction studies revealed the general location of the phase boundary between the high-temperature cubic and lower symmetry phases in the composition range $[x=0.3-0.5]$ which was further refined by dielectric and pyroelectric measurements.

A morphotropic phase boundary [MPB] between rhombohedral and tetragonal phase regions was identified by means of x-ray diffraction, dielectric, pyroelectric, and piezoelectric measurements to lie in the composition range $[x=0.4-0.45]$. Some curvature to this boundary at high temperatures is indicated in the temperature dependences of the dielectric constants and pyroelectric coefficients of poled specimens.

A summary of the material properties measured in this study for compositions $[x=0.3-0.5]$ appear in Table 2. The general location of the MPB as defined by the temperatures of the dielectric constant and pyroelectric coefficient maxima of poled specimens is depicted in Figure 4.

Acknowledgement

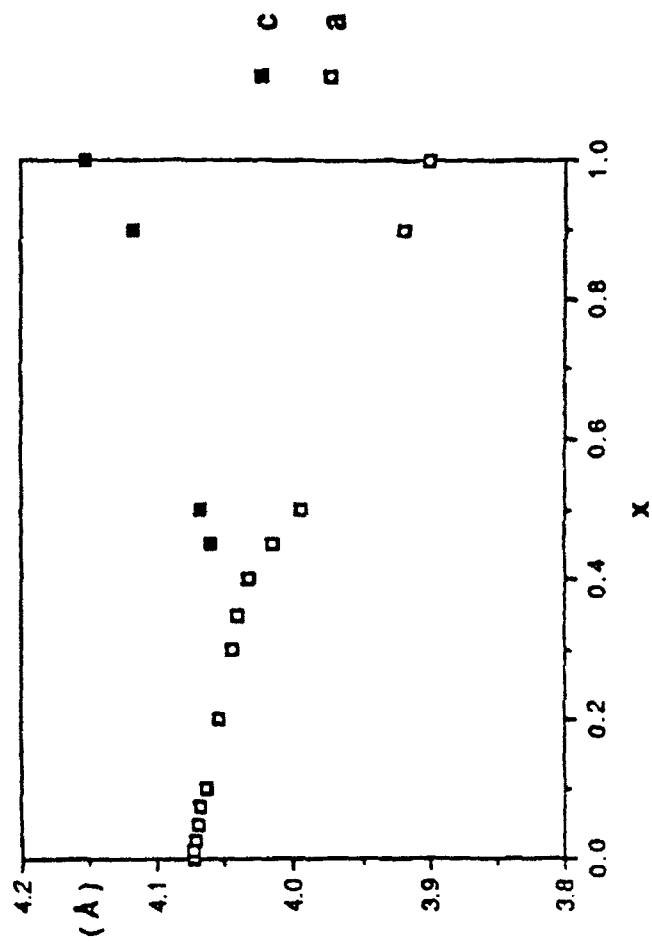
The authors would like to express their appreciation to Dr. Chi-Yuen Huang and Dr. Herbert McKinstry for collecting the high-temperature x-ray diffraction data for this investigation.

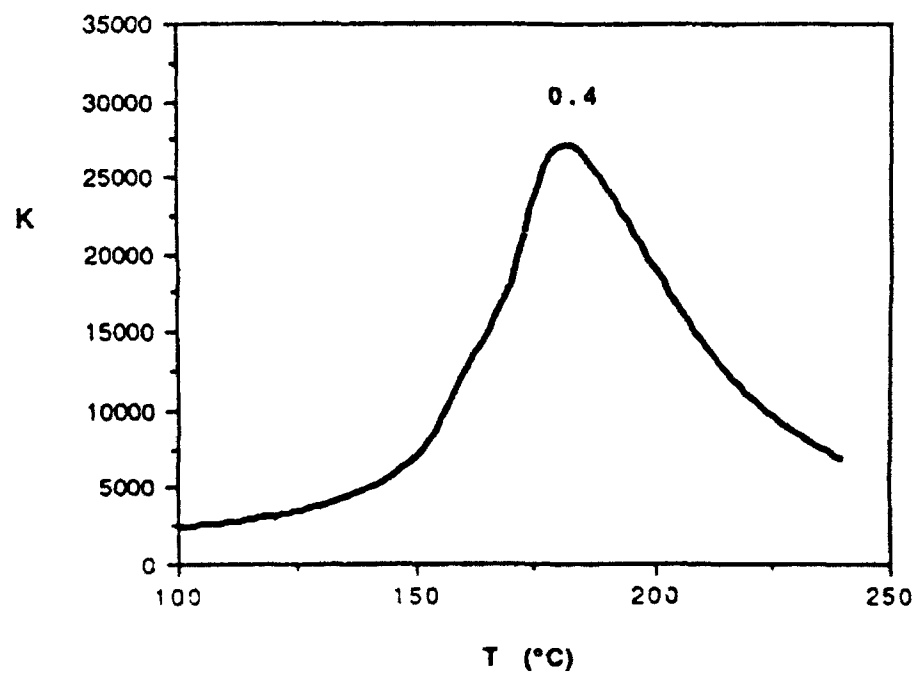
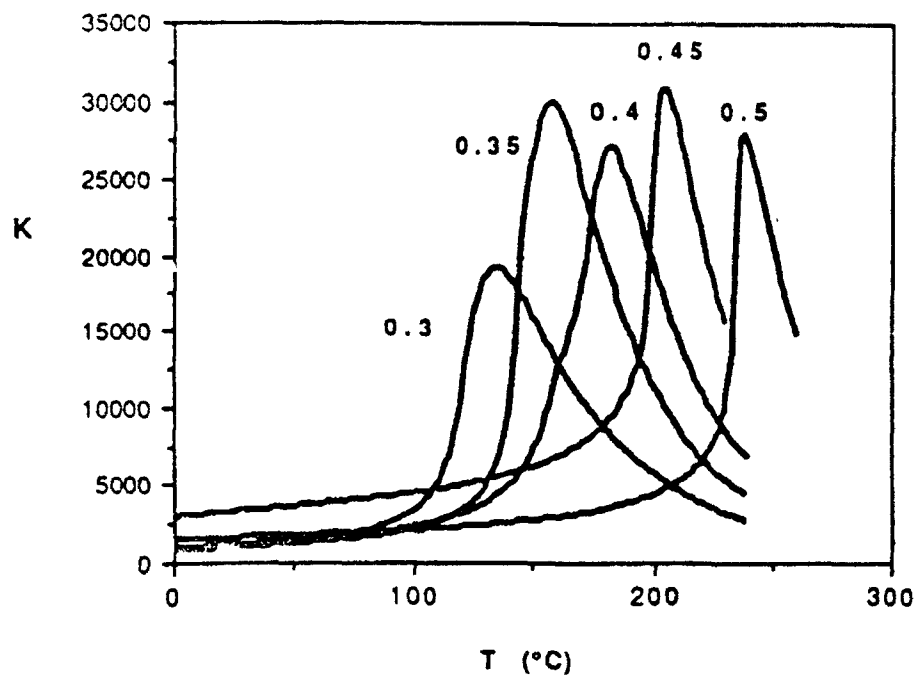
References

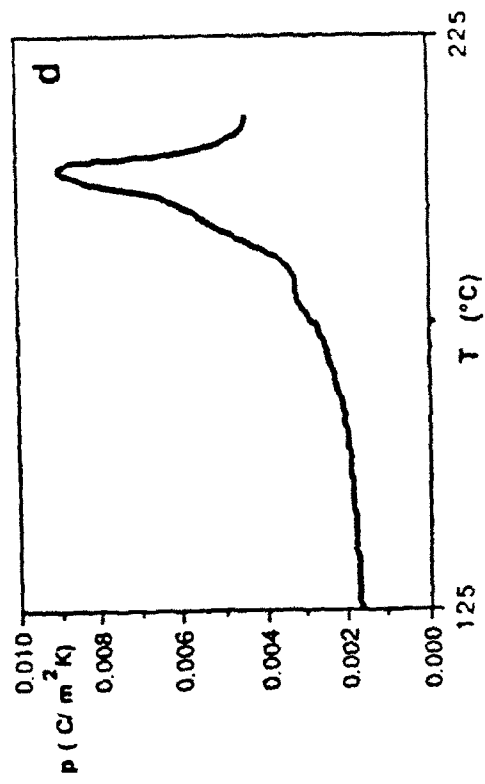
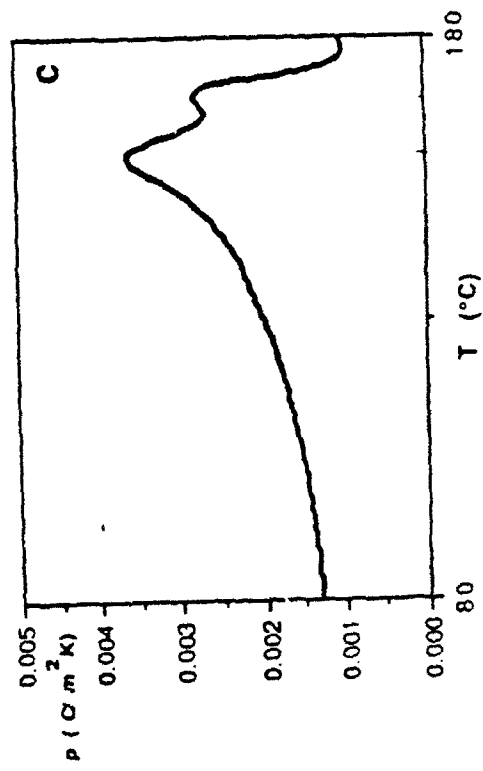
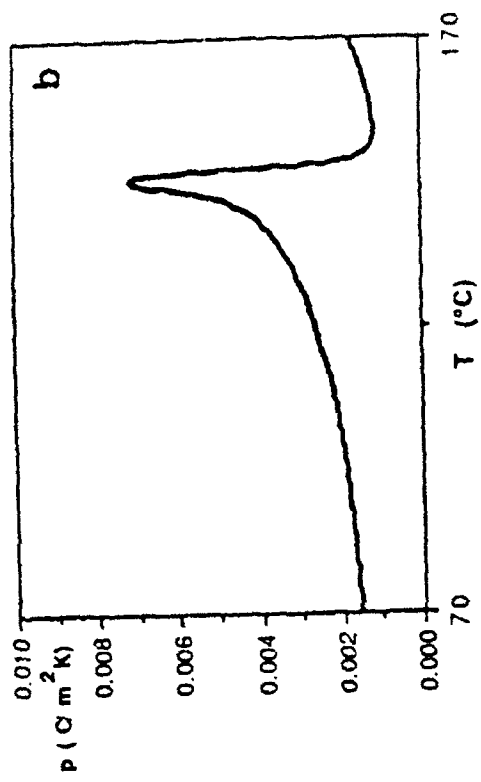
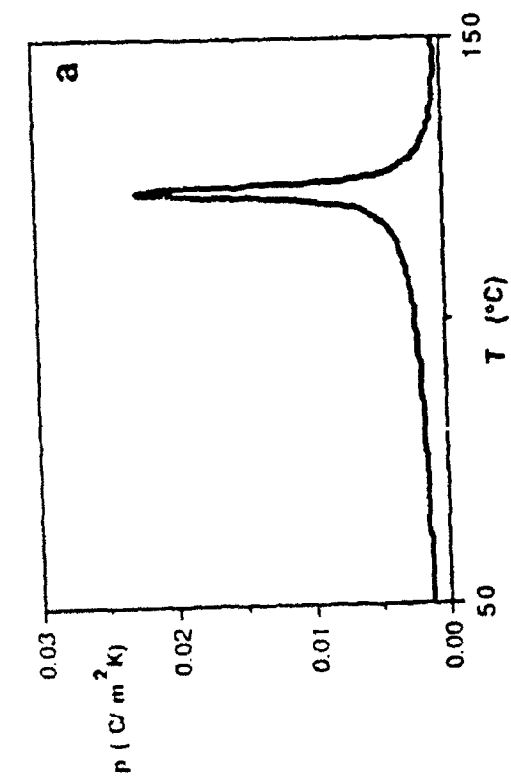
- [1] V.A. Isupov, Bull. Acad. Sciences USSR Phys. Ser. 47 (1983) 565.
- [2] JCPDS #24-1017 [ScTaO₄].
- [3] T.R. Shrout and A.Halliyal, Am. Ceram. Soc. Bull. 66(4) (1987)704.
- [4] H.A.McKinslry and H.L. McKinslry, Computer Interfacing and Programming for a Picker X-Ray Diffractometer/High-Temperature X-Ray Furnace Controller. [Penn State Univ.] (1984).
- [5] R.L. Byer and C.B. Roundy, Ferroelectrics 3 (1972) 333.
- [6] J.R. Giniewicz, A.S. Bhalla, and L.E. Cross, Ferroelectrics Lett. Sect. 12(2) (1990) 35.

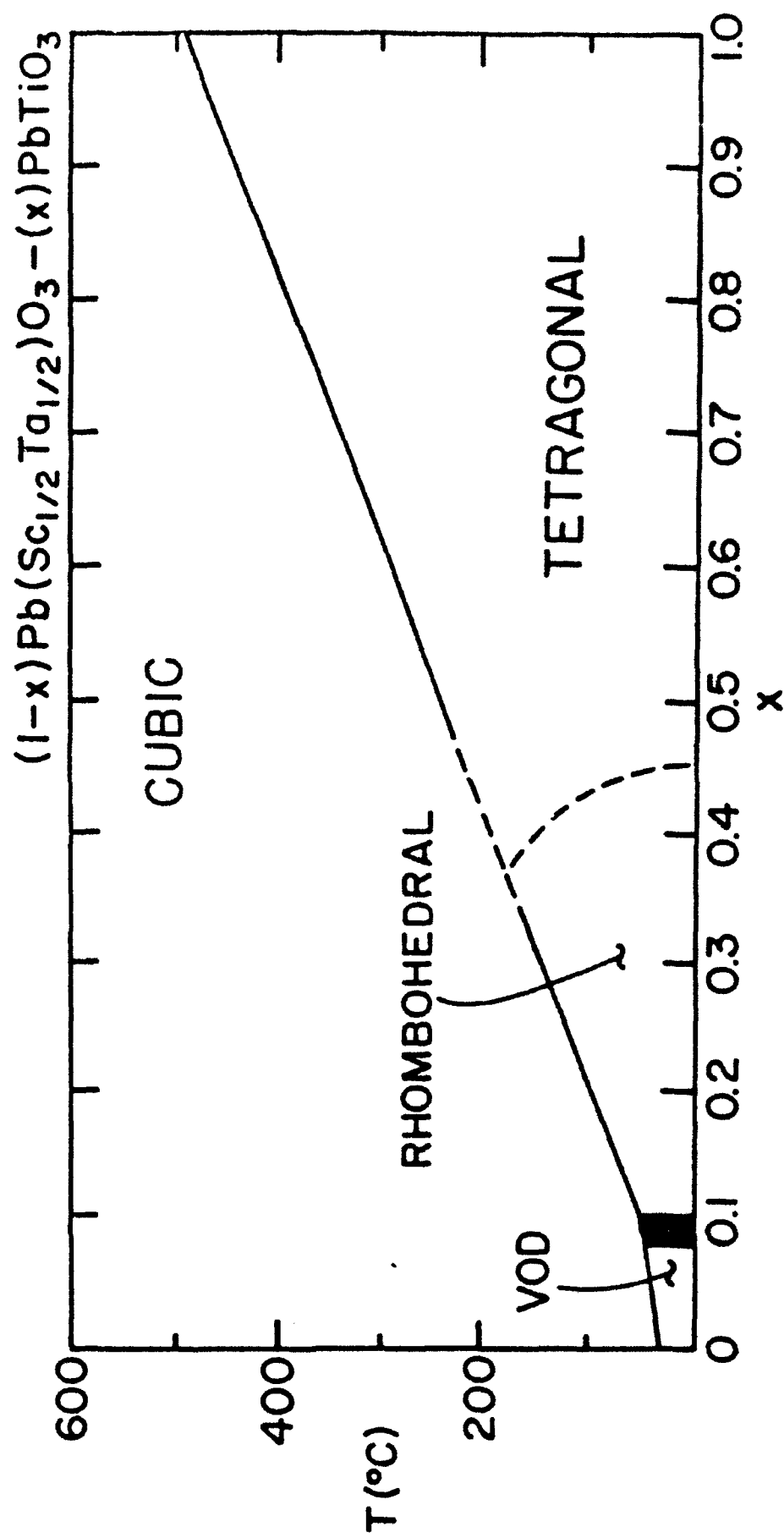
FIGURE /TABLE CAPTIONS:

- Figure 1.** Lattice parameters (25°C) determined for (1-x)Pb(Sc_{1/2}Ta_{1/2})O₃-(x)PbTiO₃ ceramics as a function of composition.
- Figure 2.** The dielectric constant as a function of temperature at 1 KHz for poled (1-x)Pb(Sc_{1/2}Ta_{1/2})O₃-(x)PbTiO₃ ceramics: (a) x=0.3-0.5 (b) x=0.4.
- Figure 3.** The pyroelectric coefficient as a function of temperature for (1-x)Pb(Sc_{1/2}Ta_{1/2})O₃-(x)PbTiO₃ ceramics: (a) x=0.3, (b) x=0.35, (c) x=0.4, and (d) x=0.45.
- Figure 4.** Schematic depiction of the general location of the morphotropic phase boundary as defined by the temperature dependences of the dielectric and pyroelectric responses of poled (1-x)Pb(Sc_{1/2}Ta_{1/2})O₃-(x)PbTiO₃ ceramics.
- Table 1.** Structural data determined by means of x-ray diffraction for various (1-x)Pb(Sc_{1/2}Ta_{1/2})O₃-(x)PbTiO₃ compositions.
- Table 2.** Dielectric, pyroelectric and piezoelectric data for poled (1-x)Pb(Sc_{1/2}Ta_{1/2})O₃-(x)PbTiO₃ ceramics in the vicinity of the morphotropic phase boundary.









α	K(max)	T °C	D(max)	T °C	p(max) (C/m ² K)	T °C	d ₃₃ (pC/N)
0.3	19500	135	0.05	124	0.024	123	150
0.35	30000	160	0.07	154	0.007	145	135
0.4	14500 27500	162 180	0.05 --	175 --	0.0036 0.0028	157 170	180
0.45	31000	204	0.05	202	0.095	202	655
0.5	28200	235	0.03	235	--	--	240

x	$K(\max)$	$T^{\circ}\text{C}$	$D(\max)$	$T^{\circ}\text{C}$	$p(\max)$ ($\text{C}/\text{m}^2\text{K}$)	$T^{\circ}\text{C}$	d_{33} (pC/N)
0.3	19500	135	0.05	124	0.024	123	150
0.35	30000	160	0.07	154	0.007	145	135
0.4	14500 27500	162 180	0.05 --	175 --	0.0036 0.0028	157 170	180
0.45	31000	204	0.05	202	0.095	202	655
0.5	28200	235	0.03	235	--	--	240

x	Volume (Å³)	ρ_{XRD} (g/cc)	c/a	Transition Range (°C)
0.01	67.53	9.04		
0.025	67.47	9.02		
0.05	67.31	9.00		
0.075	67.29	8.96		
0.1	67.01	8.96		
0.2	66.56	8.86		
0.3	66.10	8.76		150-170
0.35	65.87	8.71		150-170
0.4	65.50	8.67		170-190
0.45	65.39	8.61	1.01	200-220
0.5	64.92	8.58	1.02	220-240
0.9	63.30	8.12	1.05	

x	Volume (Å³)	ρ_{XRD} (g/cc)	c/a	Transition Range (°C)
0.01	67.53	9.04		
0.025	67.47	9.02		
0.05	67.31	9.00		
0.075	67.29	8.98		
0.1	67.01	8.98		
0.2	66.56	8.98		
0.3	66.10	8.78		150-170
0.35	65.87	8.71		150-170
0.4	65.50	8.67		170-190
0.45	65.39	8.61	1.01	200-220
0.5	64.92	8.58	1.02	220-240
0.9	63.30	8.12	1.05	

APPENDIX 7

Variable Structural Ordering in Lead Scandium Tantalate-Lead Titanate Materials

J.R. Giniewicz, A.S. Bhalla, and L.E. Cross
Materials Research Laboratory, The Pennsylvania State University,
University Park, Pennsylvania-USA

Abstract: A phase region of variable order-disorder [VOD] has been identified in this study for compositions in the range $[x=0.0-0.075]$ (x : mole fraction PbTiO_3). Materials from this region retain some degree of long-range ordering of B-site cations as evidenced by x-ray and electron diffraction which is enhanced with post-sintering annealing. Annealed ceramics exhibit sharp dielectric responses $[K(T)]$ and near-normal first-order ferroelectric behavior while as-fired specimens with lesser degrees of long-range ordering show the more diffuse and dispersive characteristics of a relaxor ferroelectric.

I. Introduction

The compound $\text{Pb}(\text{Sc}_{1/2}\text{Ta}_{1/2})\text{O}_3$ is a complex perovskite of the type $[\text{A}^{2+}(\text{B}^{3+}_{1/2}\text{B}^{5+}_{1/2})\text{O}_3]$. The difference in the ionic radii of the B ions (0.105 Å) and the charge difference between the two are sufficient to allow for an ordered structure and $\text{Pb}(\text{Sc}_{1/2}\text{Ta}_{1/2})\text{O}_3$ may exist in ordered states ranging from a nearly complete random distribution of B ions to nearly perfect ordering of B' and B'' in alternating planes along $\langle 111 \rangle$. The ordered structure has a double unit cell of the $(\text{NH}_4)_3\text{FeF}_6$ -type pictured in Figure 1 which consists of eight basic perovskite units. The unit cell of the superstructure is face-centered with space group $\text{Fm}\bar{3}\text{m}$ in the cubic (paraelectric) phase. The ordered low-temperature (ferroelectric) phase has been determined to be rhombohedral with a subcell lattice parameter of 4.072 Å and $\alpha=89.82^\circ$.¹ The order/disorder temperature of $\text{Pb}(\text{Sc}_{1/2}\text{Ta}_{1/2})\text{O}_3$ has been reported to be $T_{\text{OD}}=1470^\circ\text{C}$.^{1,2} and specimens with various degrees of long-range order may be produced either by quenching from temperatures above or near T_{OD} , to generate disorder in the compounds, or by annealing at elevated temperatures below T_{OD} so as to induce ordering of the B-site cations. The optimum annealing temperature range for $\text{Pb}(\text{Sc}_{1/2}\text{Ta}_{1/2})\text{O}_3$ ceramics has been determined to be $[1000 - 1100^\circ\text{C}]$ and, with the maintenance of the proper PbO atmosphere, a high degree of long-range ordering is attained in relatively short annealing periods.³

The dielectric response in the radio frequency range of $\text{Pb}(\text{Sc}_{1/2}\text{Ta}_{1/2})\text{O}_3$ materials is observed to vary significantly with the degree of long-range order.^{1,3} The temperature of the

dielectric permittivity maximum ranges from -5°C to 25°C depending upon the degree of order, with the higher transition temperatures occurring for the more highly ordered compounds.^{1,3} In particular, there is observed a marked increase in the magnitude of $K(\text{max})$ and an overall broadening of $K(T)$ in the vicinity of the transition as shown in Figure 2b. A clear trend towards more diffuse and dispersive relaxor-type behavior occurs with decreasing long-range ordering [Figure 3(a,b)]. The pyroelectric response of $\text{Pb}(\text{Sc}_{1/2}\text{Ta}_{1/2})\text{O}_3$ further reflects the effect long-range ordering has on the temperature dependence of the spontaneous polarization. The pyroelectric coefficients for two $\text{Pb}(\text{Sc}_{1/2}\text{Ta}_{1/2})\text{O}_3$ specimens are pictured in Figures 4(a,b). The pyroelectric coefficient peak for the highly ordered sample [Figure 4(b)] is observed to be relatively sharp while the pyroelectric peak for the more disordered sample pictured in Figure 4(a) exhibits double pyroelectric coefficient peaks. The occurrence of double pyroelectric peaks has been observed for some partially ordered $\text{Pb}(\text{Sc}_{1/2}\text{Ta}_{1/2})\text{O}_3$ materials.⁴⁻⁷ A pyroelectric doublet was reported for a partially ordered single crystal specimen;^{4,5} transmission electron microscopy [TEM] of this specimen revealed a bimodal distribution of ordered domains consisting of ordered regions $\sim 1500\text{\AA}$ in diameter and considerably larger ordered areas 100-1000 times the size of the smaller regions.^{4,5}

Highly ordered $\text{Pb}(\text{Sc}_{1/2}\text{Ta}_{1/2})\text{O}_3$ has been shown to be a first-order ferroelectric by means of both dielectric and thermal measurements.^{3,8} A latent heat effect is observed for all partially ordered and highly ordered $\text{Pb}(\text{Sc}_{1/2}\text{Ta}_{1/2})\text{O}_3$ materials which is enhanced as the degree of order is increased.^{1,3} This is manifested in a marked increase in the magnitude and an overall narrowing of the specific heat anomaly at the transition.

A variety of versatile and interesting materials may be derived from the $(1-x)\text{Pb}(\text{Sc}_{1/2}\text{Ta}_{1/2})\text{O}_3$ - $(x)\text{PbTiO}_3$ solid solution system. Previous investigation of this system^{9,10} has shown that complete solid solution occurs across the entire compositional range and a morphotropic phase boundary [MPB] has been identified between rhombohedral and tetragonal phase regions over the composition range $[x=0.4-0.45]$. It is anticipated for this system that some variable structural ordering such as occurs for pure $\text{Pb}(\text{Sc}_{1/2}\text{Ta}_{1/2})\text{O}_3$ will

persist for compositions of low x . Assuming that the introduction of Ti^{4+} into the structure serves largely to disrupt the coherence length of long-range ordering[†] rather than leading to a situation where the Ti ion incorporates itself into some new ordered phase, it is expected that at some concentration of x the variable long-range ordering will disappear. Materials which do possess this particular structural characteristic are, therefore, expected to respond to high-temperature annealing in a manner similar to that of pure $Pb(Sc_{1/2}Ta_{1/2})O_3$ materials. The existence and nature of the positional ordering in these materials will be manifested, as for unmodified $Pb(Sc_{1/2}Ta_{1/2})O_3$, in the x-ray diffraction patterns, the dielectric and pyroelectric responses, and the specific heat characteristics of the specimens. The compositional range between these "orderable" compositions, which may possess varying degrees of long-range order, and those which likely have an invariable, short coherence length long-range order[†] essentially constitute a second structural phase boundary. Examination of this variable order/disorder [VOD] region was carried out by means of x-ray diffraction, dielectric and pyroelectric measurements, and thermal analysis.

II. Sample Preparation

The $(1-x)Pb(Sc_{1/2}Ta_{1/2})O_3-(x)PbTiO_3$ ceramics were produced by a conventional mixed-oxide method involving the use of high-purity starting compounds, a precursor-phase formulation, and controlled lead atmosphere sintering. The compositions of interest were initially prepared as powders employing a wolframite $[ScTaO_4]$ ¹² precursor method¹³ in order to

[†] The coherence length is defined in terms of the size of order domains as determined by TEM.¹¹ Short coherence length long-range order: (20-800Å). Long coherence length long-range order: (>1000Å).

reduce the occurrence of undesirable pyrochlore phases. Starting oxides $\text{Sc}_2\text{O}_3^\dagger$ and $\text{Ta}_2\text{O}_5^\dagger$ were batched and calcined at 1400°C for 6-8 hours to form the ScTaO_4 precursor. Compositions in the range $[x \leq 0.1]$ were then formulated from PbO^\dagger , TiO_2^\dagger , and the precursor phase. Each composition was calcined at 900°C for 4 hours and at 1000°C for 1 hour with an intermediate comminution step. Compacted specimens of compositions were then subjected to firing at 1400°C for 1 hour within sealed alumina crucibles containing $\text{Pb}(\text{Sc}_{1/2}\text{Ta}_{1/2})\text{O}_3$ / PbZrO_3 source powders. The specimens were then subjected to a second higher temperature sintering [1500 - 1560°C / 20 minutes] which was conducted in a molybdenum tube furnace with a relatively rapid heating and cooling schedule to avoid excessive lead-loss. The samples were 90-95% theoretical density following this second-stage sintering step. Specimens of each composition were annealed at 1000°C for 10 hours in a sealed system with a controlled lead atmosphere in order to induce structural ordering.

Specimens for x-ray diffraction, dielectric, and pyroelectric investigation were cut as plates from the sintered disks typically [0.4 cm] on edge and [0.025-0.03 cm] in thickness. The electrode surfaces were ground with $12\ \mu\text{m}$ Al_2O_3 , cleaned, and sputtered with gold. Silver contact points were subsequently applied to the gold sputtered surfaces.

The samples prepared for thermal analysis were all sintered at 1400°C for 1 hour and ground to a powder for measurement. The powder samples, typically 80-100 mg in size, were sealed in aluminum pans.

$^\dagger\text{Sc}_2\text{O}_3$ [Boulder Scientific Co. - 99.99%]; Ta_2O_5 [Hermann C. Starck (Berlin) - Stand. Opt. Grade]; PbO [Johnson Matthey - Materials Technology UK - Grade A1]; TiO_2 [Aesar (Johnson Matthey Inc.) - 99.999%]

III. Experimental Procedure

The degree of long-range order in the $(1-x)\text{Pb}(\text{Sc}_{1/2}\text{Ta}_{1/2})\text{O}_3$ - $(x)\text{PbTiO}_3$ specimens was determined by x-ray diffraction using a Scintag [PADV] automated diffractometer. $\text{CuK}\alpha$ radiation was employed. The degree of structural ordering was evaluated by means of the long-range order parameter, S , which is defined in terms of the relative intensities of the superlattice and normal lattice reflections as:

$$S^2 = \left[\frac{I_{\text{Super}}}{I_{\text{Normal}}} \right]_{\text{OBS}} \left[\frac{I_{\text{Normal}}}{I_{\text{Super}}} \right]_{\text{CALC}} \quad (1)$$

where the superlattice / normal reflection pairs employed are 111/200 and 311/222.^{1,3,8} The long-range order parameter, S , describes the average distribution of B' and B'' ions on the B-site of $\text{Pb}(\text{B}'_{1/2}\text{B}''_{1/2})\text{O}_3$ as expressed by:

$$S = \frac{n - F_{\text{B}'}}{1 - F_{\text{B}'}} \quad (2)$$

where $F_{\text{B}'}$ is the fraction of B' ions in the compound and n is the fraction of the B' sites actually occupied by a B' ion. This expression reduces to:

$$S = 2n - 1 \quad (3)$$

for a 1:1 arrangement of B-site cations. A completely ordered arrangement of ions has $S=1$ while a completely disordered arrangement is denoted by $S=0$. The calculated ratio in Equation (1) has been determined for the completely ordered condition [$S=1$] and has, for $\text{Pb}(\text{Sc}_{1/2}\text{Ta}_{1/2})\text{O}_3$, values 1.33 and 0.59 for the 111/200 and 311/222 pairs respectively.¹ The

311/222 pair [Figure 2a] was used in this investigation to evaluate the degree of long-range order present for the $(1-x)\text{Pb}(\text{Sc}_{1/2}\text{Ta}_{1/2})\text{O}_3$ - $x\text{PbTiO}_3$ materials.

Assuming that the ordering that occurs for these specimens is essentially a 1:1 ordering of Sc^{3+} and Ta^{5+} on the B-site interrupted by the presence of Ti^{4+} , the long-range order parameter as defined above may still be applied to evaluate the degree of long-range ordering present. The results of the present study tend to support this assumption; however, it is acknowledged that a more thorough investigation is required to verify the actual position of the Ti ions in the structure and, in the event that some type of ordering occurs in which the Ti ion itself is incorporated, that the long-range order parameter must be redefined in order to accurately quantify the degree of long-range ordering that exists. In the light of these considerations, however, it should still be feasible to monitor the evolution of the variable structural ordering with composition in terms of the long-range order parameter, S , as defined so as to provide some gauge by which to assess the relative degree of ordering present throughout the compositional range of interest.

The dielectric constant, K , and dissipation factor, D , were measured as a function of temperature and frequency using an automated system consisting of an oven [Model 2300, Delta Design, Inc.], an LCR meter [Model 4274A, Hewlett Packard, Inc.], and a digital multimeter interfaced with a desk top computer [Model 9816, Hewlett Packard, Inc.]. Dielectric runs were made at 1 KHz over a temperature range of $[-150$ - $260^\circ\text{C}]$.

The pyroelectric response was measured by a modified Byer-Roundy¹⁴ method. The specimens were initially poled in air within a temperature chamber [Model 2300, Delta Design, Inc.] in the vicinity of the transition temperature under a poling field of $[20 \text{ (KV/cm)}]$ for 15 minutes and cooled with the field applied to $\sim -100^\circ\text{C}$. The poling field was then removed. A desk top computer [Model 9816, Hewlett Packard, Inc.] was used to record the pyroelectric current data collected by the picoammeter [Model 4140B, Hewlett Packard, Inc.]. The pyroelectric coefficients were subsequently calculated from the pyroelectric current data.

Thermal analysis was conducted by means of differential scanning calorimetry [Model DSC-2, Perkin Elmer]. The specific heat, $C_p(T)$, was determined by referring the thermal curve of the specimen to that of a similarly contained sapphire standard.

IV. Results and Discussion

A series of samples was assembled comprised of as-fired and annealed specimens of compositions $[x=0.025, 0.05, 0.075, \text{ and } 0.1]$. The x-ray diffraction peaks appearing in the 2θ range $[34-42^\circ]$ are pictured in Figure 5(a-d). The as-fired specimens [1], for all compositions, exhibit only the fundamental reflection 222, with, at most, only a very subtle increase in intensity in the vicinity of the 2θ range over which the superlattice reflection, 311, should appear. The 311 reflection does appear for annealed specimens [2], however, decreasing in magnitude with increasing x up to $[x=0.1]$ for which no superlattice reflection is observed. The B parameters evaluated for the annealed specimens are plotted as a function of composition over the range $[x=0-0.1]$ in Figure 6. The degree of long-range ordering present for these specimens is seen to decrease steadily up to $[x=0.1]$ where long-range ordering is no longer detectable by x-ray diffraction.

Dielectric data collected at 1 KHz are given in Table I and the dielectric constant is shown as a function of temperature [1 KHz] in Figure 5(a-d) for as-fired [1] and annealed [2] specimens. A marked sharpening of the dielectric constant peak with annealing is observed for all compositions $[x \leq 0.075]$ similar to what is typically observed for pure $\text{Pb}(\text{Sc}_{1/2}\text{Ta}_{1/2})\text{O}_3$, where a very sharp peak indicates a highly ordered state and the normal ferroelectric behavior generally associated with such a specimen. The development of a more normal ferroelectric response upon annealing is also evident for the $[x \leq 0.075]$ specimens in the marked decrease of the temperature interval between the dielectric constant and the dielectric loss maxima $[\Delta T(\text{max})]$ (Table I). A strong frequency dependence of both the dielectric constant and the dielectric loss for all as-fired specimens, similar to that pictured in Figure 3b for the pure

$\text{Pb}(\text{Sc}_{1/2}\text{Ta}_{1/2})\text{O}_3$ material with a low degree of structural ordering, was observed over the frequency range considered in this study.

Typical of pure $\text{Pb}(\text{Sc}_{1/2}\text{Ta}_{1/2})\text{O}_3$ is a decrease in the dielectric constant maximum upon ordering [Figure 2b]. This tendency is also observed for the modified compositions with the difference between the maxima of as-fired and annealed specimens at a given composition showing a steady decrease on approaching the $[x=0.075]$ composition. Some grain-growth upon annealing for compositions $[x \geq 0.05]$ was apparent in this study which is expected to contribute, at least in part, to the enhanced response of the annealed specimens in this composition range.

The pyroelectric coefficients for as-fired [1] and annealed [2] specimens are shown as a function of temperature in Figure 7(a-d). Distinctive double peaks were observed for all of the as-fired compositions $[x < 0.1]$. A maximum separation of the two peaks occurs at $[x=0.025]$ followed by a steady decrease in the separation up to $[x=0.1]$. The existence of a second peak is barely discernible for the as-fired $[x=0.075]$ composition, appearing more as an asymmetry in the peak response in the form of a "shoulder" on the high-temperature side of the peak. Pyroelectric doublets such as these have been observed for partially ordered $\text{Pb}(\text{Sc}_{1/2}\text{Ta}_{1/2})\text{O}_3$ material which have been associated with the existence of a bimodal size distribution of well-defined ordered regions within the specimen as evidenced by TEM images.⁴ Assuming that this type of response may be associated with the variable nature of the structural ordering that is evident for these compositions, the occurrence of a doublet and the disappearance of such a feature in the response may be correlated with the existence of a variable long-range ordering and the compositional limit to which such ordering can be retained. Such an assumption is further supported by the consistent change in the pyroelectric coefficient doublet to a single peak response with annealing, which has already been shown to enhance the degree of long-range ordering in specimens with compositions in this range. Further, the comparative sharpness and intensity of the peaks associated with the annealed samples with respect to the as-fired ceramics suggests that a nearly optimum and reasonably homogeneous state of ordering is achieved for these specimens.

The specific heat, $C_p(T)$, of as-fired and annealed samples are shown in Figure 8(a-d) and the onset temperatures, T_t , and enthalpies, ΔH , are recorded in Table II. These powdered specimens were all fired only under the first-stage sintering conditions previously described and, hence, the as-fired specimens were already partially ordered with the S parameter values indicated in Table II. The degrees of long-range ordering of the annealed powders were thus somewhat higher than what was achieved for samples which had been densified at higher temperatures and annealed as solids under the same conditions. In all cases, there is observed an enhancement in the maximum specific heat with annealing for a given composition, similar to that occurring for pure $\text{Pb}(\text{Sc}_{1/2}\text{Ta}_{1/2})\text{O}_3$, and a general decrease for both as-fired and annealed specimens with increasing x approaching $[x=0.1]$. The onset temperatures, T_t , [Table II] are generally observed to increase with increasing Ti-content while the enthalpies follow an overall decreasing trend with increasing x .

The general trends observed in the thermal properties of the VOD compositions with differing degrees of long-range order are in accord with those occurring in the dielectric and pyroelectric responses of these materials. In all cases, the more ordered specimens at a given composition show a more pronounced thermal effect which becomes steadily more diffuse with increasing x .

V. Summary

A preliminary depiction of the $(1-x)\text{Pb}(\text{Sc}_{1/2}\text{Ta}_{1/2})\text{O}_3$ - $(x)\text{PbTiO}_3$ solid solution, based on the data that are currently available for ceramic specimens from this system⁹ is shown in Figure 9 in which the VOD phase region [V] as determined for this particular series of samples is identified. The boundary between these compositions of variable order/disorder [VOD] and rhombohedral compositions, which on the basis of x-ray diffraction are evidently unaffected structurally by the post-sintering heat-treatment conditions applied in this study, was determined to be in the composition range $[x=0.075-0.1]$. The proposed high-temperature

Mixed Cubic [XRD] region depicted in Figure 9 over this composition range represents the coexistence of ordered and disordered phases which may be detected by means of x-ray diffraction. Further definition of the VOD phase region and a thorough refinement of the exact structural nature of the materials within it will require a systematic survey of these compositions over a broad range of annealing temperatures and periods. Such an investigation may yield results which indicate that, under different annealing conditions, the compositional range of variable order/disorder [VOD] is extended somewhat beyond the boundary determined in this study.

Also indicated in Figure 9 is a range of compositions [$x=0.1-0.3$] for which, on the basis of electron diffraction, it has been determined that some short coherence length long-range ordering does exist as evidenced by the F-type superlattice spots appearing in the electron diffraction patterns. It is suggested in this initial depiction of the system that this coexistence of ordered and disordered phases, similar to what is shown for the [$x=0-0.1$] compositions, likely extends well into the high-temperature cubic phase region (Mixed Cubic [ED]). Materials with compositions [$x \geq 0.4$] show no evidence of any long or short coherence length long-range ordering by means of x-ray or electron diffraction and, hence, on the basis of these observations, are regarded as completely disordered. The structural characteristics and associated ferroelectric behaviors of these compositions beyond the VOD region are presented in greater detail elsewhere.¹⁵

References

- ¹C.G.F. Stenger and A.J. Burggraaf, "Order-disorder reactions in the ferroelectric perovskites $\text{Pb}(\text{Sc}_{0.5}\text{Nb}_{0.5})\text{O}_3$ and $\text{Pb}(\text{Sc}_{0.5}\text{Ta}_{0.5})\text{O}_3$. I. Kinetics of the ordering process," *phys. stat. sol. (a)*, **61**, 275 (1980).
- ²P. Groves, "Low-temperature studies of ferroelectric lead scandium tantalate," *J. Phys. C*, **18**, L1073 (1985).
- ³N. Setter, "The role of positional disorder in ferroelectric relaxors," Ph.D. Thesis, The Pennsylvania State University (1980).
- ⁴C.A. Randall and A.S. Bhalla, "Anomalously large order domains in the $\text{Pb}(\text{Sc}_{1/2}\text{Ta}_{1/2})\text{O}_3$ single crystals," *Ferroelectr. Lett.*, **9**, 47 (1988).
- ⁵C.A. Randall, "A transmission electron microscopy study of normal and relaxor perovskite ferroelectric materials," Ph.D. Thesis, University of Essex (1987).

⁶C. Zhili, Y. Xi, and L.E. Cross, "Depolarization behavior and reversible pyroelectricity in lead scandium-tantalate ceramics under DC biases," *Ferroelectrics*, **49**, 213 (1983).

⁷C. Zhili, Y. Xi, and L.E. Cross, "Reversible pyroelectric effect in $\text{Pb}(\text{Sc}_{1/2}\text{Ta}_{1/2})\text{O}_3$ ceramics under DC bias," *Ferroelectr. Lett.*, **44**, 271 (1983).

⁸C.G.F. Stenger, F.L. Scholten, and A.J. Burggraaf, "Ordering and diffuse phase transitions in $\text{Pb}(\text{Sc}_{0.5}\text{Ta}_{0.5})\text{O}_3$ ceramics," *Solid State Commun.*, **32** [11] 989 (1979).

⁹J.R. Giniewicz, "An investigation of the lead scandium tantalate-lead titanate solid solution system," Ph.D. Thesis, The Pennsylvania State University (1991).

¹⁰J.R. Giniewicz, A.S. Bhalla, and L.E. Cross, (submitted to *Mat. Lett.*).

¹¹C.A. Randall and A.S. Bhalla, "Nanostructural-property relations in complex lead perovskites," *Jpn. J. Appl. Phys.*, **29** [2] 327 (1990).

¹²JCPDS #24-1017 (ScTaO_4).

¹³T.R. Shrout and A. Halliyal, "Preparation of lead-based ferroelectric relaxors for capacitors," *Am. Ceram. Soc. Bull.*, **66** [4] 704 (1987).

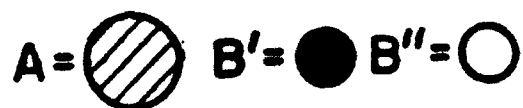
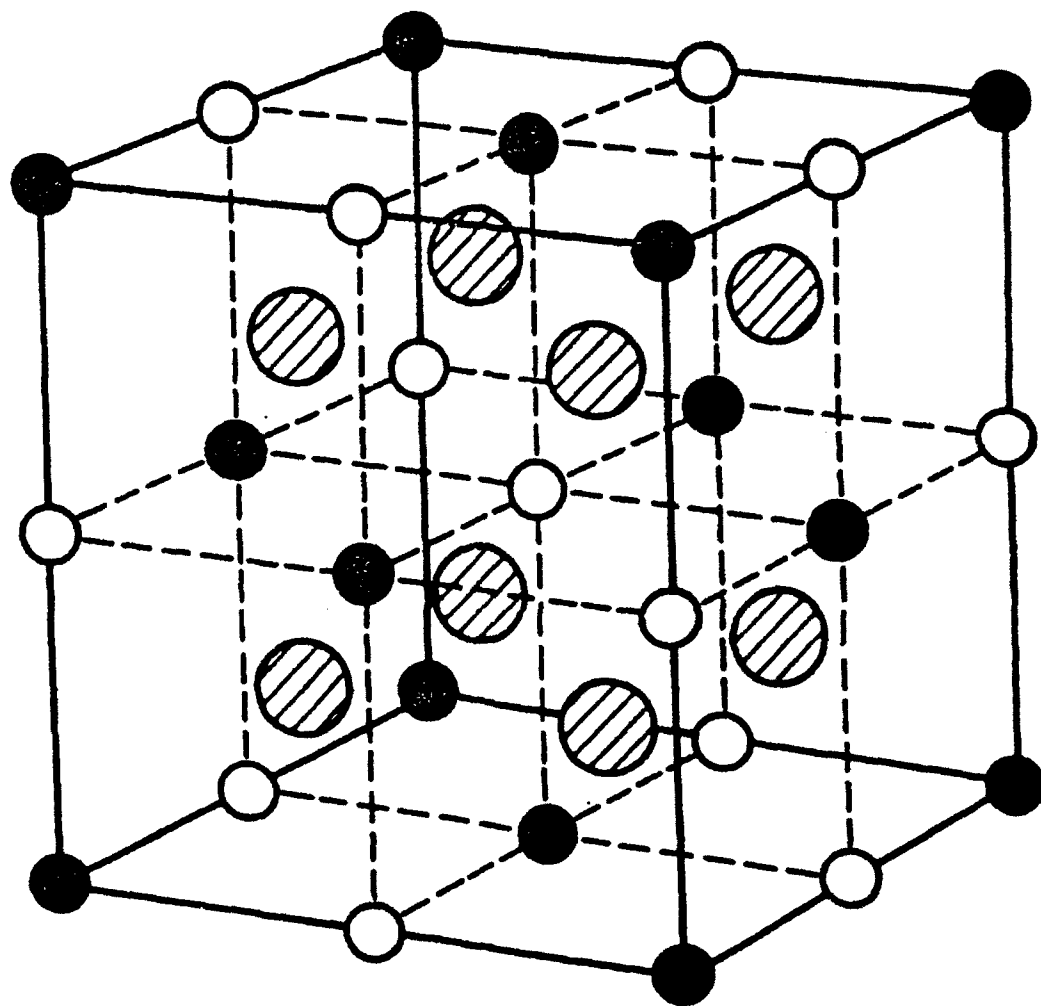
¹⁴R.L. Byer and C.B. Roundy, "Pyroelectric coefficient direct measurement technique and application," *Ferroelectrics*, **3**, 333 (1972).

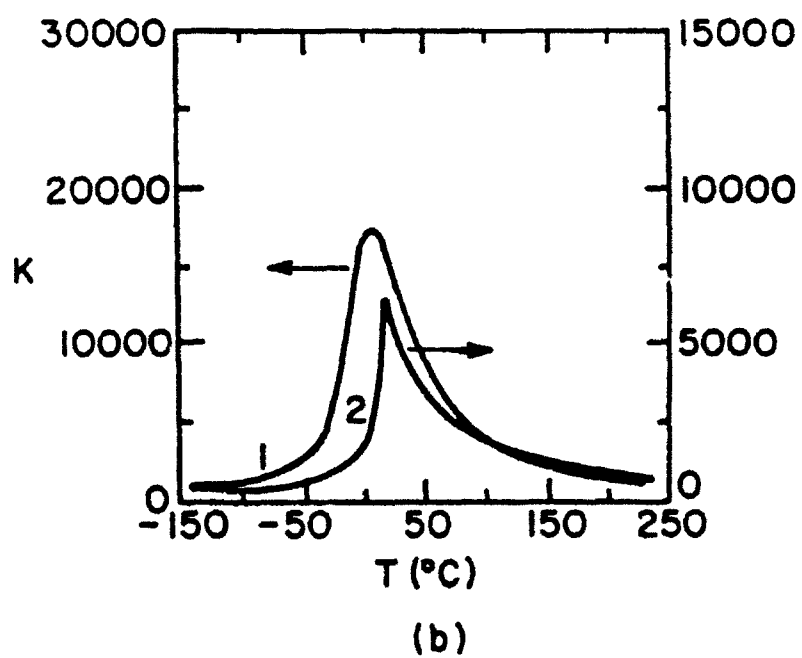
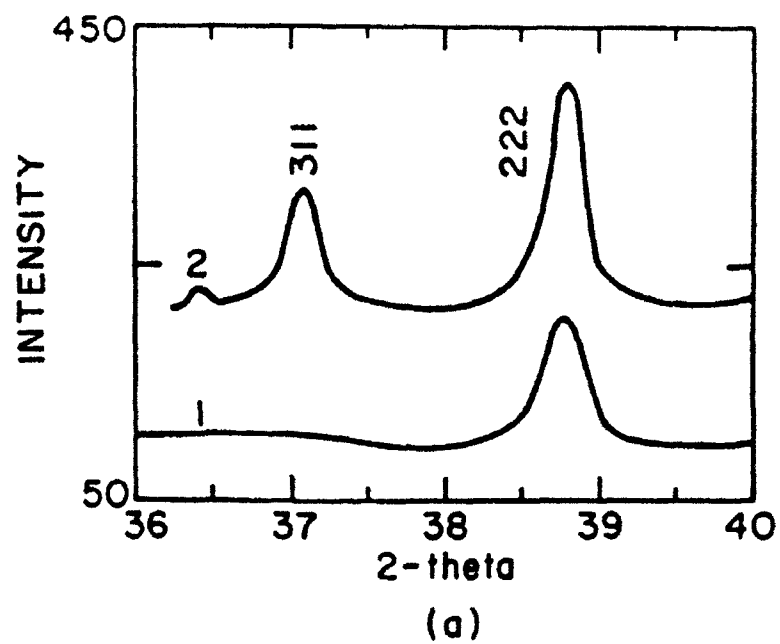
¹⁵G.A. Smolenskii, "Physical Phenomena in Ferroelectrics with Diffused Phase Transitions," *J. Phys. Soc. Japan*, **28**(suppl.), 26 (1970).

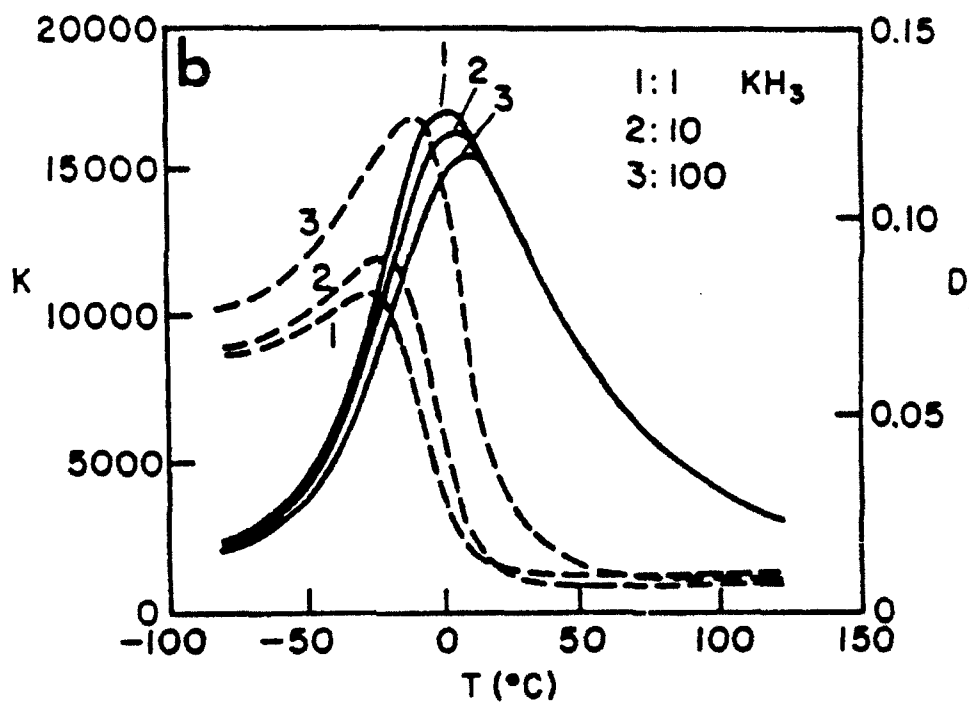
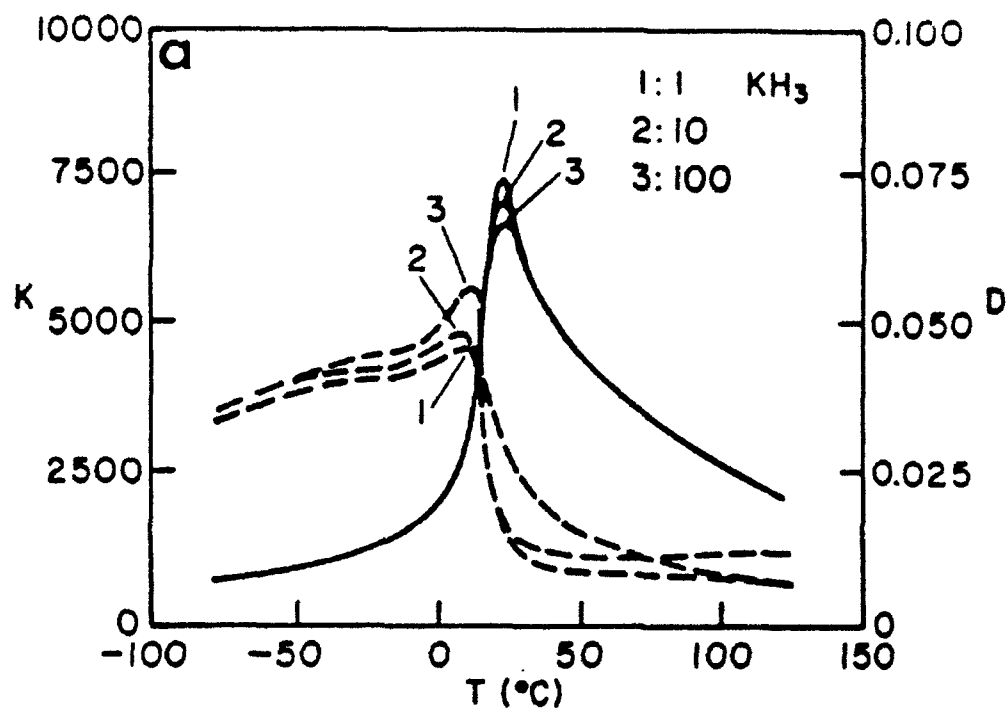
¹⁶C.A. Randall, J.R. Giniewicz, A.S. Bhalla, and L.E. Cross, "An electron diffraction study of lead scandium tantalate-lead titanate ceramics," (to be published).

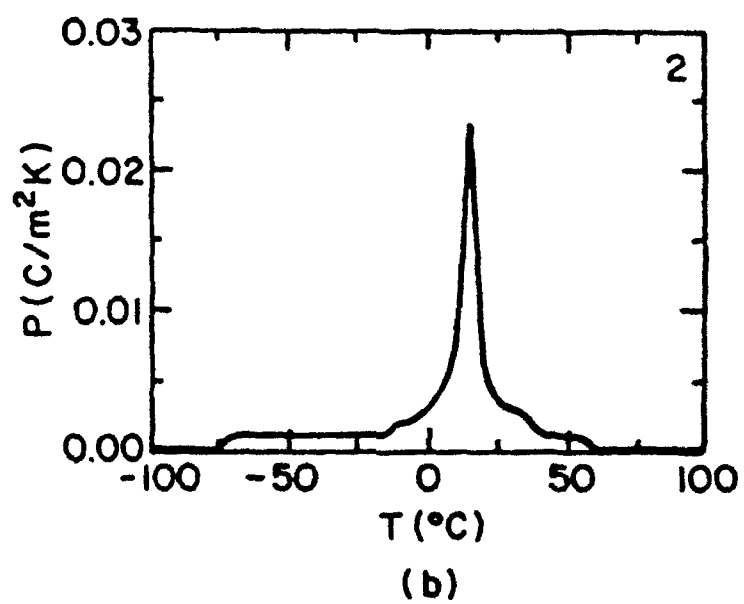
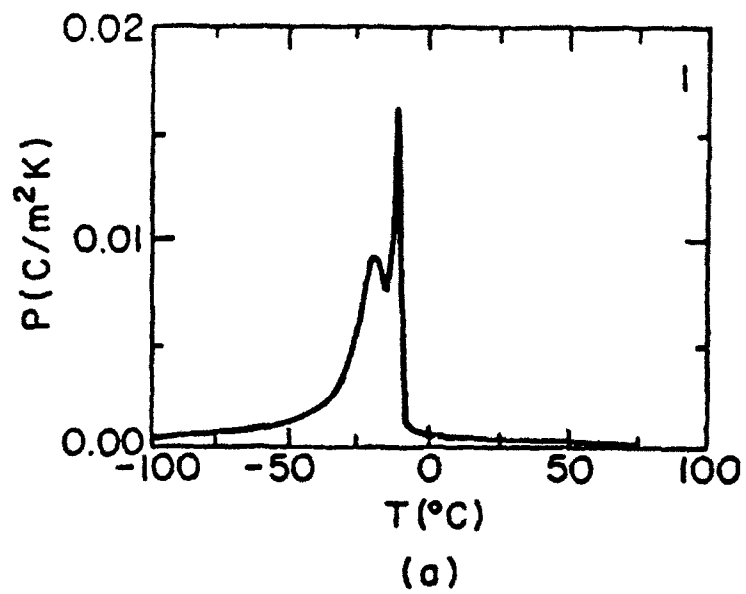
LIST OF FIGURES AND TABLES

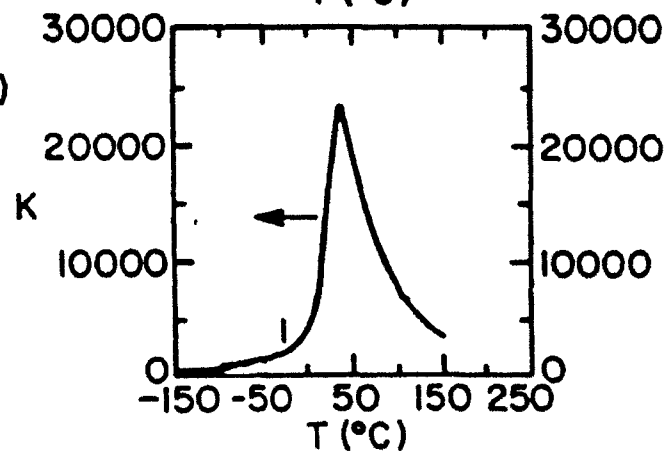
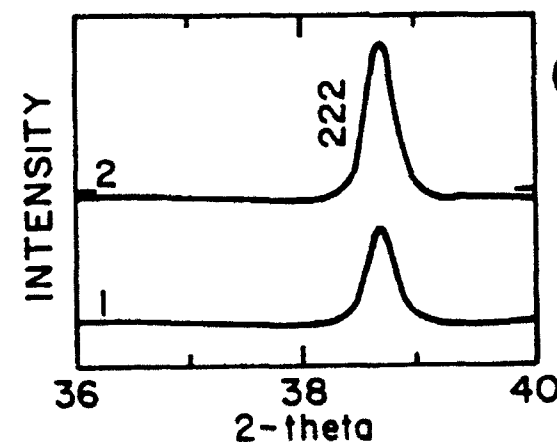
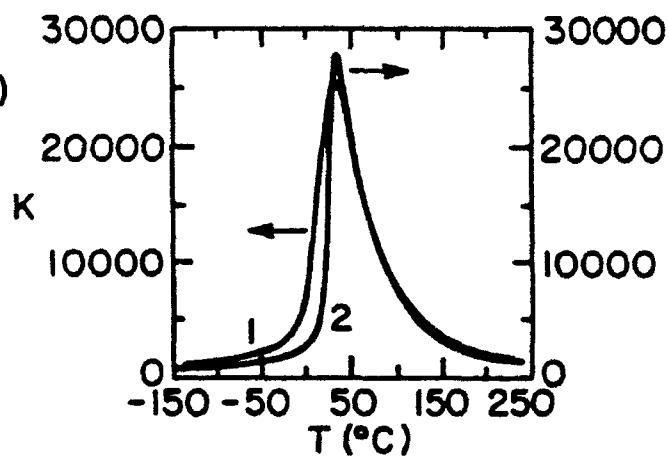
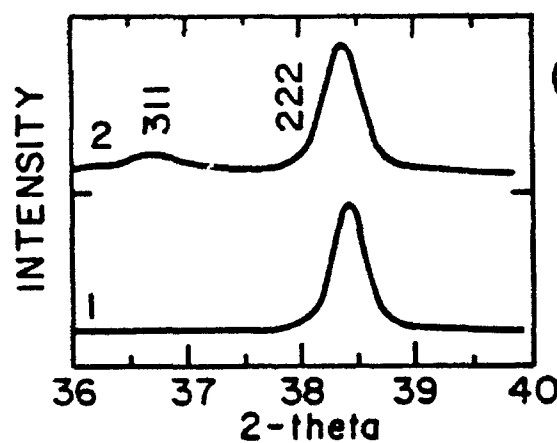
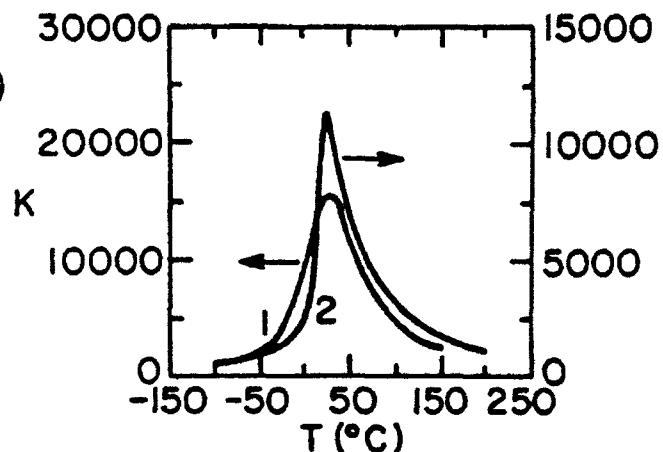
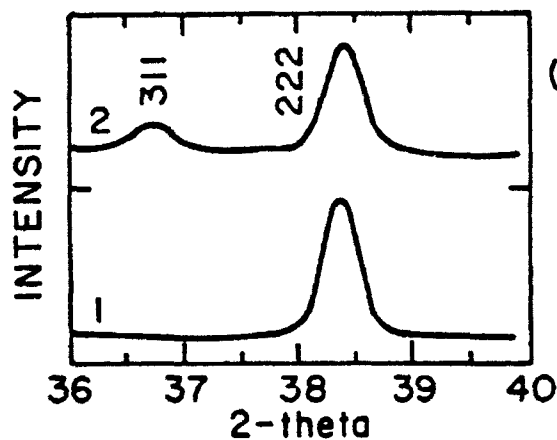
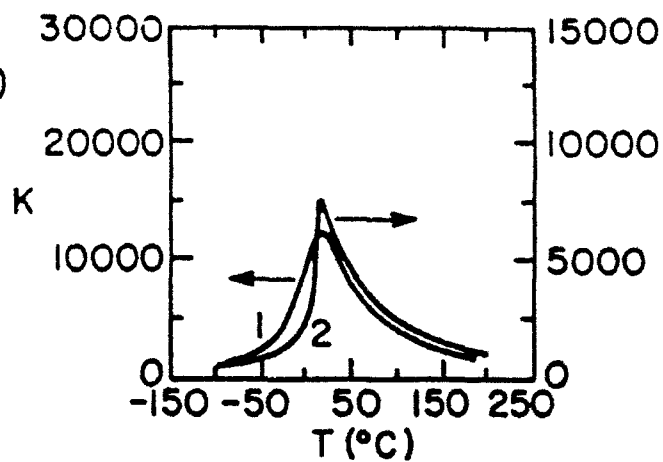
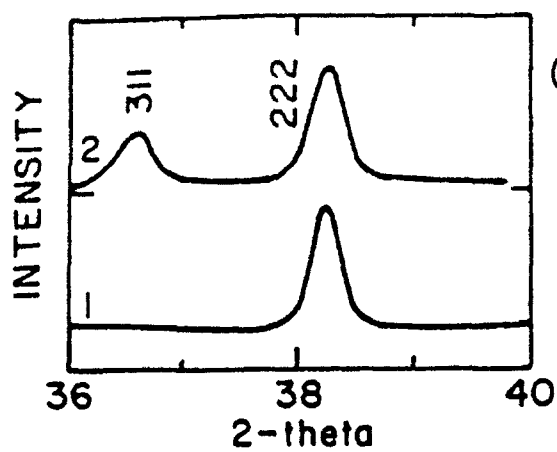
- Figure 1.** The ordered $(\text{NH}_4)_3\text{FeF}_6$ Structure.
- Figure 2.** As-Fired [1] and Annealed [2] $\text{Pb}(\text{Sc}_{1/2}\text{Ta}_{1/2})\text{O}_3$ ceramics.
(a) The 311/222 x-ray diffraction pair and (b) the dielectric constant as a function of temperature at 1 KHz.
- Figure 3.** The dielectric constant and loss of $\text{Pb}(\text{Sc}_{1/2}\text{Ta}_{1/2})\text{O}_3$ as a function of temperature and frequency ⁷. (a) $S=0.87$ and (b) $S=0.4$.
(see Section III for definition of S)
- Figure 4** The pyroelectric coefficient for $\text{Pb}(\text{Sc}_{1/2}\text{Ta}_{1/2})\text{O}_3$.
(a) As-Fired and (b) Annealed ceramics.
- Figure 5.** The 311/222 x-ray diffraction pair and 1 KHz $K(T)$ response of As-Fired [1] and Annealed [2] $(1-x)\text{Pb}(\text{Sc}_{1/2}\text{Ta}_{1/2})\text{O}_3$ - $(x)\text{PbTiO}_3$ ceramics: (a) $x=0.025$, (b) $x=0.05$, (c) $x=0.075$, and (d) $x=0.1$.
- Figure 6** The S parameters evaluated for annealed specimens [$x=0-0.1$].
- Figure 7.** The pyroelectric coefficient for As-Fired [1] and Annealed [2] $(1-x)\text{Pb}(\text{Sc}_{1/2}\text{Ta}_{1/2})\text{O}_3$ - $(x)\text{PbTiO}_3$ ceramics: (a) $x=0.025$, (b) $x=0.05$, (c) $x=0.075$, (d) $x=0.1$.
- Figure 8.** The specific heat, $C_p(T)$, of As-Fired [1] and Annealed [2] $(1-x)\text{Pb}(\text{Sc}_{1/2}\text{Ta}_{1/2})\text{O}_3$ - $(x)\text{PbTiO}_3$ ceramics: (a) $x=0.0$, (b) $x=0.025$, (c) $x=0.050$, (d) $x=0.1$.
- Figure 9.** A preliminary depiction of the $(1-x)\text{Pb}(\text{Sc}_{1/2}\text{Ta}_{1/2})\text{O}_3$ - $(x)\text{PbTiO}_3$ solid solution system. [x : mole fraction PbTiO_3]
- Table I.** Dielectric data for As-Fired [1] and Annealed [2] VOD compositions [$x=0-0.1$].
- Table II:** The enthalpies [ΔH] and onset temperatures [T_i] of selected As-Fired [1] and Annealed [2] VOD compositions.

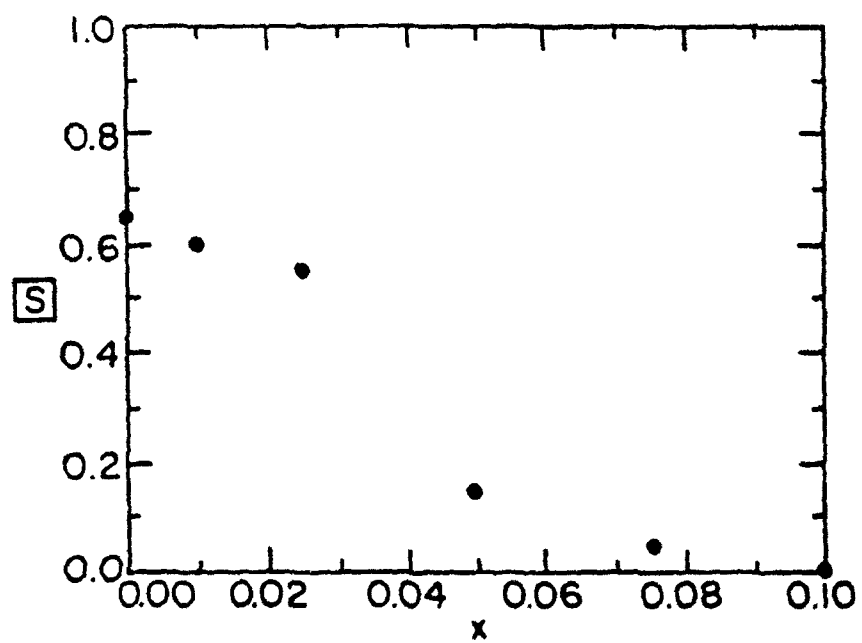


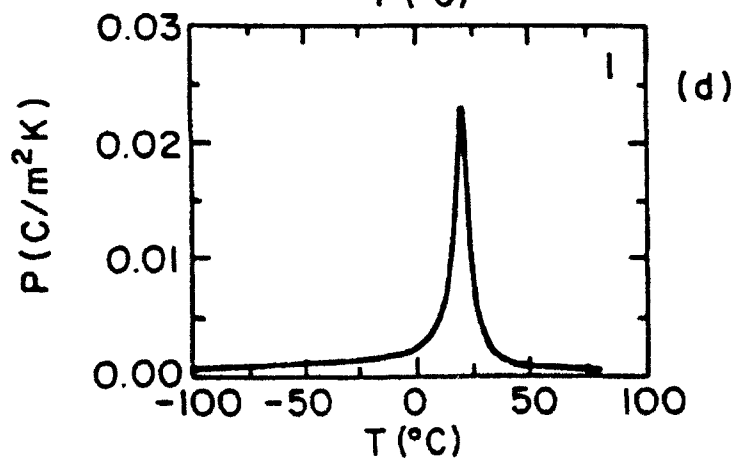
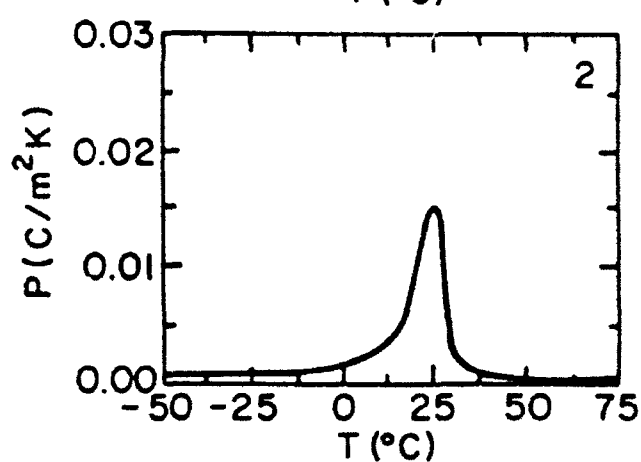
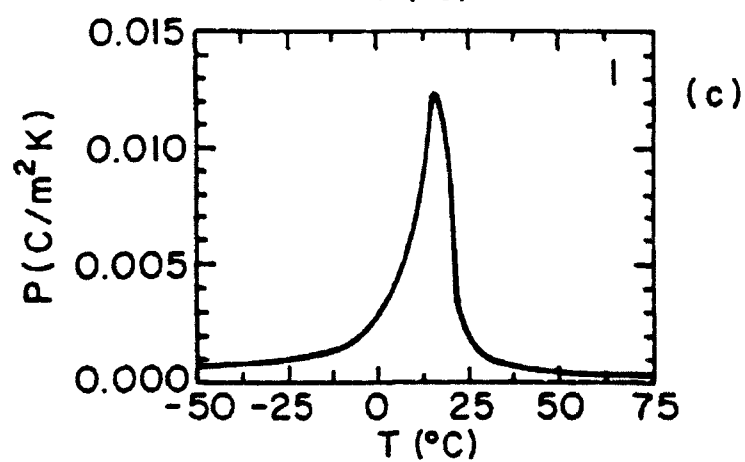
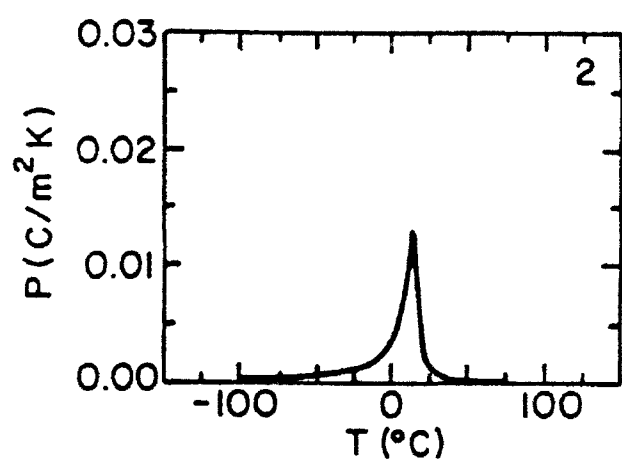
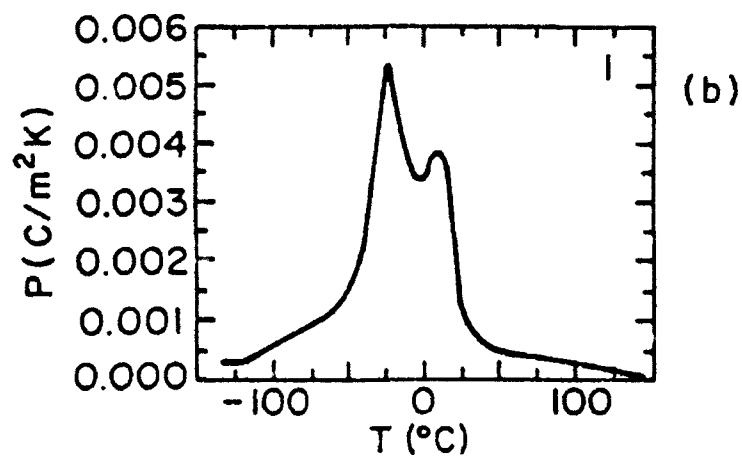
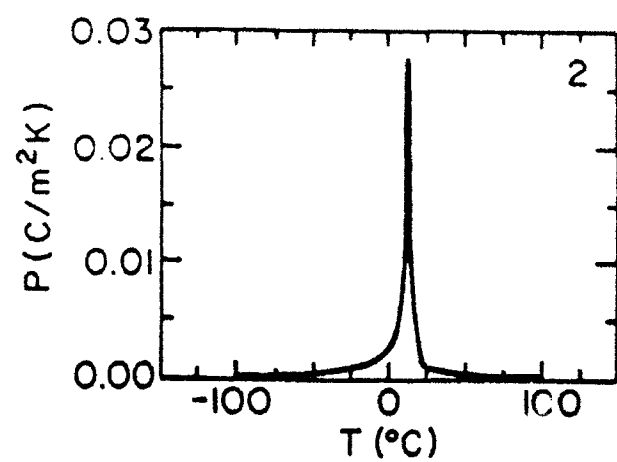
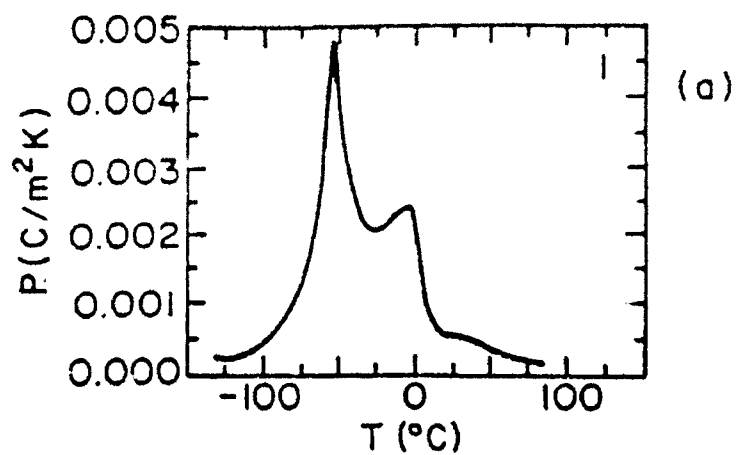




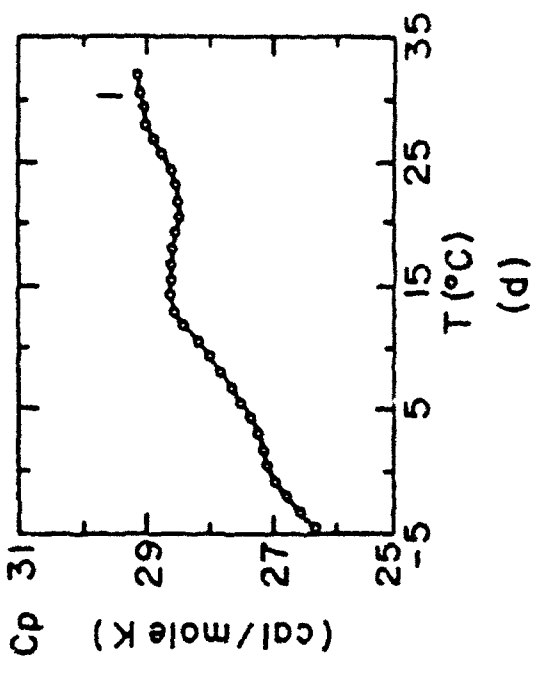
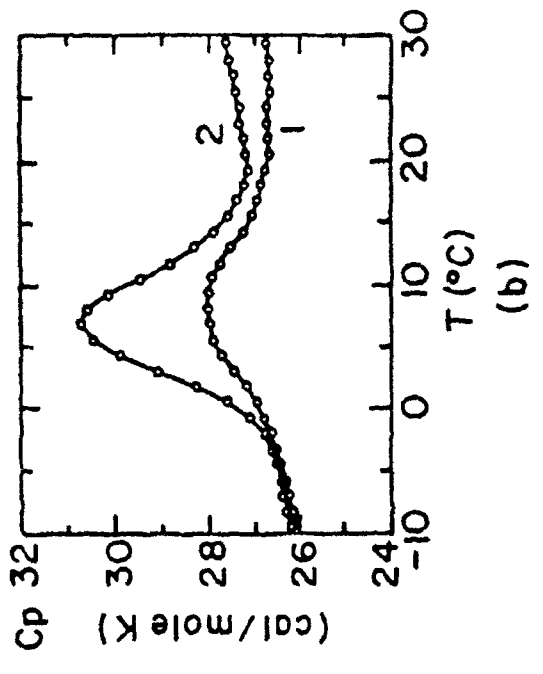
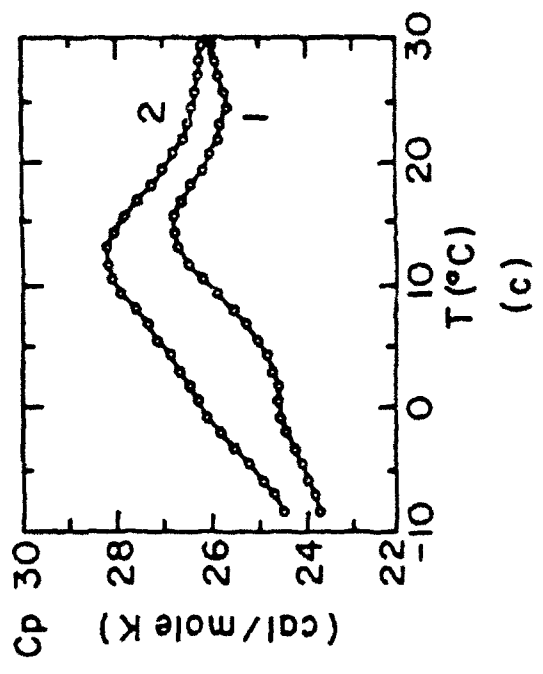
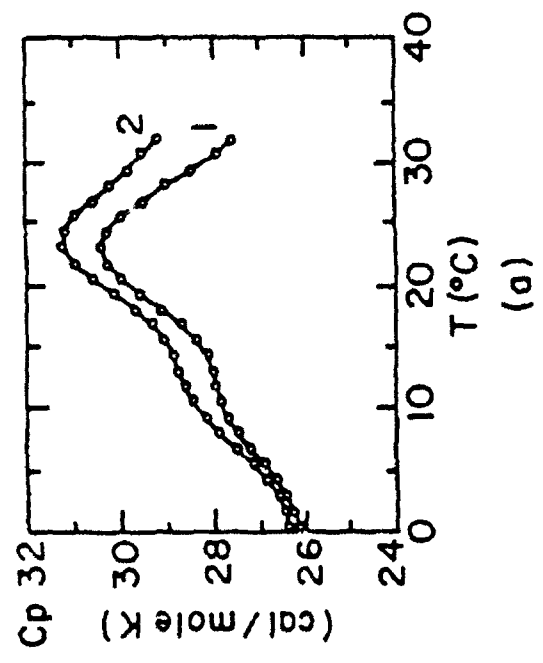


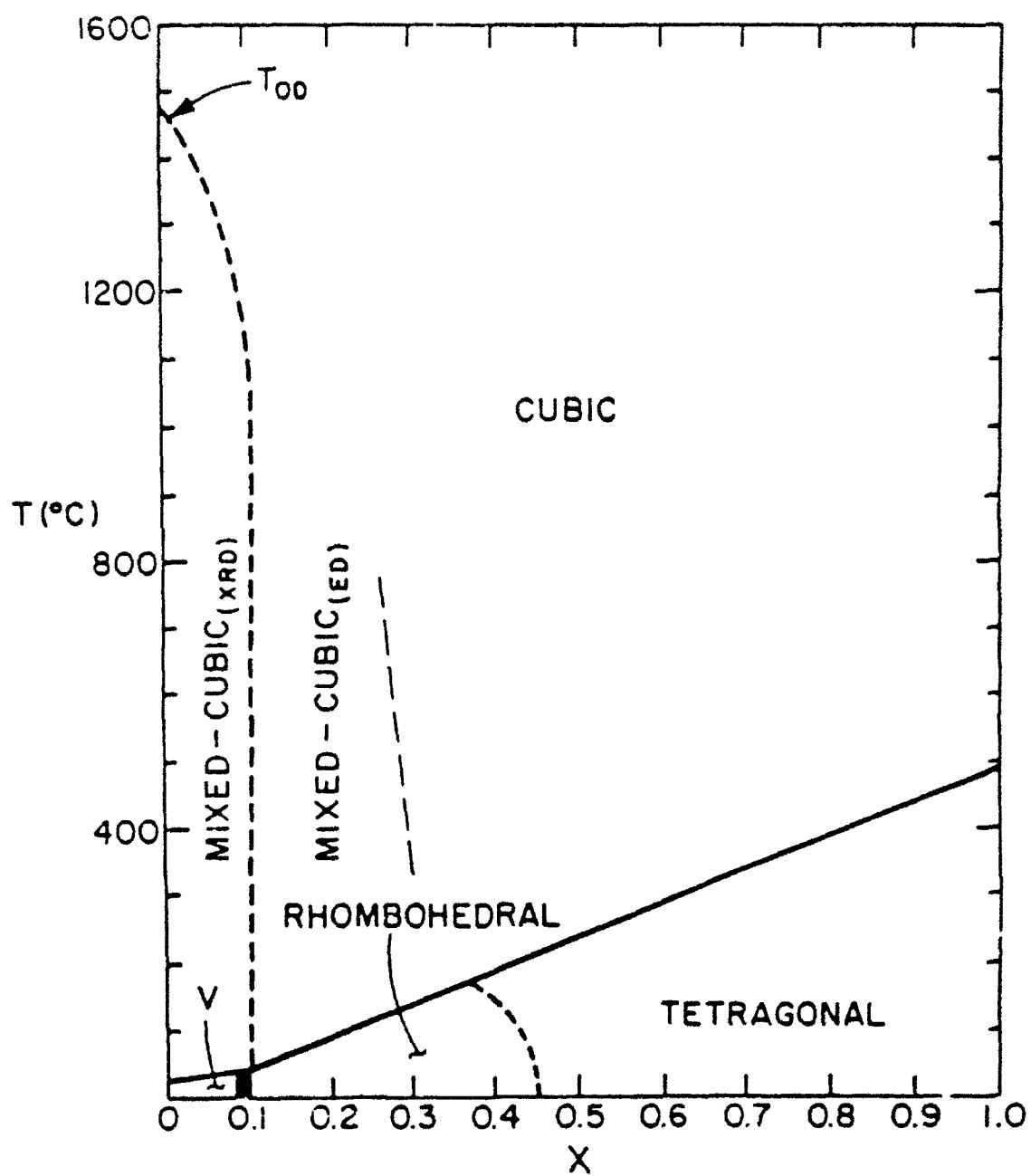






7. 5. 77





x	†	K(max)	T°C	D(max)	T°C	δ °C	ΔT(max)
0.0	1	17700	5	0.08	-12	35	17
0.0	2	6400	20	0.05	9		11
0.025	1	11000	18	0.07	-25	40	42
0.025	2	7400	18	0.05	4		14
0.05	1	14600	25	0.06	-20	35	42
0.05	2	11300	25	0.07	10		14
0.075	1	26300	35	0.07	15	35	16
0.075	2	27600	35	0.06	25		11
0.1	1	22900	38	0.07	25	35	13

† 1: As-Fired 2: Annealed

δ: Defined according to the relationship¹⁵: $\{1/K - (1/K_{max})\} = (T - T_{max})^2 / (2K_{max}\delta^2)$

ΔT(max): difference between the temperatures of the dielectric constant and dielectric loss maxima

x	†	K(max)	T°C	D(max)	T°C	δ °C	ΔT(max)
0.0	1	17700	5	0.08	-12	35	17
0.0	2	6400	20	0.05	9		11
0.025	1	11000	18	0.07	-25	40	42
0.025	2	7400	18	0.05	4		14
0.05	1	14600	25	0.06	-20	35	42
0.05	2	11300	25	0.07	10		14
0.075	1	26300	35	0.07	15	35	16
0.075	2	27600	35	0.06	25		11
0.1	1	22900	38	0.07	25	35	13

† 1: As-Fired 2: Annealed

δ: Defined according to the relationship¹⁵: $((1/K_0 - 1/K_{\max})) = (\Gamma - T_{\max})^2 / (\alpha K_{\max} \delta^2)$

ΔT(max): difference between the temperatures of the dielectric constant and dielectric loss maxima

x	\dagger	S	T_i °C	ΔH (cal/mole)
0.0	1	0.80	16	40
0.0	2	0.96	18	48
0.025	1	0.60	3	22
0.025	2	0.77	3	29
0.05	1	0.50	10	7
0.05	2	0.70	8	18

\dagger 1: As-Fired 2: Annealed

x	†	S	T_t °C	ΔH (cal/mole)
0.0	1	0.80	16	40
0.0	2	0.96	18	48
0.025	1	0.60	3	22
0.025	2	0.77	3	29
0.05	1	0.50	10	7
0.05	2	0.70	8	18

† 1: As-Fired 2: Annealed

APPENDIX 8

LEAD SCANDIUM TANTALATE - LEAD TITANATE MATERIALS FOR FIELD - STABILIZED PYROELECTRIC DEVICE APPLICATIONS

J.R. GINIEWICZ, A.S. BHALLA, and L.E. CROSS
Materials Research Laboratory, The Pennsylvania State University,
University Park, Pennsylvania-USA

(Received for Publication March 9, 1992)

Abstract: A preliminary evaluation of the pyroelectric response of selected compositions from the variable order-disorder [VOD] phase region of this system has been conducted under modest DC biasing conditions in order to assess the performance of these materials for application in small area pyroelectric devices. The figure of merit $[F_D]$ was observed to be significantly enhanced over that of the pure $\text{Pb}(\text{Sc}_{1/2}\text{Ta}_{1/2})\text{O}_3$ material due to the combined effects of Ti doping, ordering, and the application of a biasing field.

INTRODUCTION

The usefulness of pure $\text{Pb}(\text{Sc}_{1/2}\text{Ta}_{1/2})\text{O}_3$ materials operated under moderate DC fields has already been established for small area device applications.^{1,2} The general effect of the biasing field on the pyroelectric coefficient, $[p]$, the dielectric permittivity, $[\epsilon]$, and the dielectric loss, $[\tan\delta]$, is to broaden the peak responses and shift them to higher temperature. The peak responses, as indicated in Table 1, are all depressed under field strengths greater than 10 (KV/cm). The voltage response figure of merit, $F_V = p/c'\epsilon_0$ (c' : the heat capacity), which is commonly used to rate the performance of large area pyroelectric detectors, is observed to be enhanced by a DC bias, but even at the highest field strengths, it is still relatively low. The signal/ noise figure of merit, $F_D = p/c'(\epsilon_0 \tan\delta)^{1/2}$, which is important in the evaluation of small area devices, is significantly enhanced with the applied field, however, showing peak values competitive with many of the leading pyroelectric materials. The optimum operating temperature range of the $\text{Pb}(\text{Sc}_{1/2}\text{Ta}_{1/2})\text{O}_3$ material is reasonably broad and centered at approximately room temperature.¹

A variable order/disorder [VOD] phase region has been identified in the $(1-x)\text{Pb}(\text{Sc}_{1/2}\text{Ta}_{1/2})\text{O}_3-(x)\text{PbTiO}_3$ for the range of compositions $[x=0-0.075]$.³ Ceramic specimens from this VOD region have been found to respond to post-sintering heat-treatment in a manner similar to that observed for unmodified $\text{Pb}(\text{Sc}_{1/2}\text{Ta}_{1/2})\text{O}_3$ materials; the degree of long-range structural ordering is

Communicated by Dr. G. W. Taylor

TABLE 1. The pyroelectric figures of merit F_V and F_D and relevant dielectric properties of $\text{Pb}(\text{Sc}_{1/2}\text{Ta}_{1/2})\text{O}_3$ materials under various DC biasing conditions. ¹

MATERIAL	$E(\text{Bias})$ [KV/cm]	P [C/m ² K]	ϵ [1 KHz]	$\tan(\delta)$ [1 KHz]	F_V [m ² /C]	$T(^{\circ}\text{C})$	F_D [10 ⁻⁵ W ^{1/2}]	$T(^{\circ}\text{C})$
$\text{Pb}(\text{Sc}_{1/2}\text{Ta}_{1/2})\text{O}_3$	0	0.010	10000	0.038	0.019	6	0.9	34
	10	0.058	10500	0.026	0.033	13	5.9	34
	29	0.050	5400	0.008	0.058	25	13.4	44
	54	0.034	2700	0.004	0.074	37	18.2	52

enhanced and the dielectric and pyroelectric responses of the annealed specimens become more sharp at the transition and more first-order in nature. It will be demonstrated that $(1-x)\text{Pb}(\text{Sc}_{1/2}\text{Ta}_{1/2})\text{O}_3$ - $x\text{PbTiO}_3$ materials from the VOD region respond to DC bias in a manner similar to that exhibited by pure $\text{Pb}(\text{Sc}_{1/2}\text{Ta}_{1/2})\text{O}_3$ materials. A preliminary evaluation of the pyroelectric response has been conducted for selected compositions under modest field strengths in order to assess the effect of Ti-content on the performance of the modified $\text{Pb}(\text{Sc}_{1/2}\text{Ta}_{1/2})\text{O}_3$ material for small area pyroelectric device applications.

SAMPLE PREPARATION

The $(1-x)\text{Pb}(\text{Sc}_{1/2}\text{Ta}_{1/2})\text{O}_3$ - $x\text{PbTiO}_3$ ceramics were produced by a conventional mixed-oxide method involving the use of high purity starting compounds, a precursor-phase formulation, and controlled lead atmosphere sintering. The compositions of interest were initially prepared as powders employing a wolframite $[\text{ScTaO}_4]$ ⁴ precursor method⁵ in order to reduce the occurrence of undesirable pyrochlore phases. Starting oxides $\text{Sc}_2\text{O}_3^\dagger$ and $\text{Ta}_2\text{O}_5^\dagger$ were batched and calcined at 1400°C for 6-8 hours to form the ScTaO_4 precursor. Compositions in the range $[x \leq 0.1]$ were then formulated from PbO^\dagger , TiO_2^\dagger , and the precursor phase. Each composition was calcined at 900°C for 4 hours and at 1000°C for 1 hour with an intermediate comminution step. Compacted specimens of all compositions were then subjected to firing at 1400°C for 1 hour within sealed alumina crucibles containing $\text{Pb}(\text{Sc}_{1/2}\text{Ta}_{1/2})\text{O}_3$ / PbZrO_3 source powders. The specimens were then subjected to a second higher temperature sintering [1500-1560°C/20 minutes] which was conducted in a molybdenum tube furnace with a relatively rapid heating and cooling schedule to avoid excessive lead loss. These samples were 90-95% theoretical density following this second-

[†] PbO [Johnson Matthey - Materials Technology UK - Grade A1]; Sc_2O_3 [Boulder Scientific Co. - 99.99%]; Ta_2O_5 [Hermann C. Starck (Berlin) - Stand. Opt. Grade]; TiO_2 [Aesar (Johnson Matthey Inc.) - 99.999%]

stage sintering step. Specimens of each composition were annealed at 1000°C for 10 hours in a sealed system with a controlled lead atmosphere in order to induce structural ordering.

Specimens for x-ray diffraction, dielectric, and pyroelectric investigation were cut as plates from the sintered disks typically [0.4 cm] on edge and [0.025-0.03 cm] in thickness. The electrode surfaces were ground with 12 μm Al_2O_3 , cleaned, and sputtered with gold. Silver contact points were subsequently applied to the gold sputtered surfaces.

EXPERIMENTAL PROCEDURE

The degree of long-range order in the $(1-x)\text{Pb}(\text{Sc}_{1/2}\text{Ta}_{1/2})\text{O}_3$ - $(x)\text{PbTiO}_3$ specimens was determined by x-ray diffraction using a Scintag [PADV] automated diffractometer. $\text{CuK}\alpha$ radiation was employed. The degree of structural ordering was evaluated by means of the long-range order parameter, S , which is defined in terms of the relative intensities of the superlattice and normal lattice reflections as:

$$S^2 = \left[\frac{I_{\text{Super}}}{I_{\text{Normal}}} \right]_{\text{OBS}} \left[\frac{I_{\text{Normal}}}{I_{\text{Super}}} \right]_{\text{CALC}} \quad (1)$$

where the superlattice / normal reflection pairs employed are 111/200 and 311/222.^{6,7} The long-range order parameter, S , describes the average distribution of B ions at the B-site. A completely ordered arrangement of ions has $S=1$ while a completely disordered arrangement is denoted by $S=0$. The calculated ratio in Equation (1) has been determined for the completely ordered condition [$S=1$] and has, for $\text{Pb}(\text{Sc}_{1/2}\text{Ta}_{1/2})\text{O}_3$, values of 1.33 and 0.59 for the 111/200 and 311/222 pairs respectively. The 311/222 pair was used in this investigation to evaluate the degree of long-range order present for the $(1-x)\text{Pb}(\text{Sc}_{1/2}\text{Ta}_{1/2})\text{O}_3$ - $(x)\text{PbTiO}_3$ materials.³

The dielectric constant, K , and dissipation factor, D , were measured as a function of temperature and frequency using an automated system consisting of an oven [Model 2300, Delta Design, Inc.], an LCR meter [Model 4274A, Hewlett

Packard, Inc.), and a digital multimeter interfaced with a desk top computer [Model 9816, Hewlett Packard, Inc.]. Dielectric runs were made at 100 Hz, 1 KHz, 10 KHz, and 100 KHz over a temperature range of [-150 - 260°C] under bias field conditions of $E=0$ and 5 (KV/cm).

The pyroelectric response was measured by a modified Byer-Roundy⁸ method. The specimens were initially poled in air within a temperature chamber [Model 2300, Delta Design, Inc.] in the vicinity of the transition temperature under a poling field of [20 (KV/cm)] for 15 minutes and cooled with the field applied to $\sim -100^\circ\text{C}$. The poling field was then removed. A desk top computer [Model 9816, Hewlett Packard, Inc.] was used to record the pyroelectric current data collected by the picoammeter [Model 4140B, Hewlett Packard, Inc.]. The pyroelectric coefficients were subsequently calculated from the pyroelectric current data. Biasing field conditions of $E=0$, 5, and 10 (KV/cm) were applied.

RESULTS AND DISCUSSION

The effect of a biasing field on the pyroelectric response of as-fired and annealed specimens of $[x=0.025]$ and $[x=0.05]$ is shown in Figure 1(a-d). The pyroelectric doublets which typically occur for the as-fired specimens³ are seen to "coalesce" into one rather broad peak of reduced magnitude with increasing field strength, with the peak response shifting towards room temperature for both compositions [Figure 1(a,b)]. The overall breadth of the response for these as-fired materials at each field strength is generally similar, but somewhat more broad for the composition of lower x . The single pyroelectric peak of the annealed materials [Figure 1(c,d)] is initially enhanced and sharpened at both compositions under a field strength of 5 (KV/cm) above which the peak response is depressed and broadened, effects which are more pronounced with higher concentrations of Ti. The temperature of the peak response is also shifted upward towards room temperature for these compounds. The magnitudes of the peak pyroelectric coefficients are considerably lower for the as-fired specimens as compared with the annealed ones, however, the broader temperature range of the peak response for these materials offers the advantage of a more stable response over a broad operating temperature range.

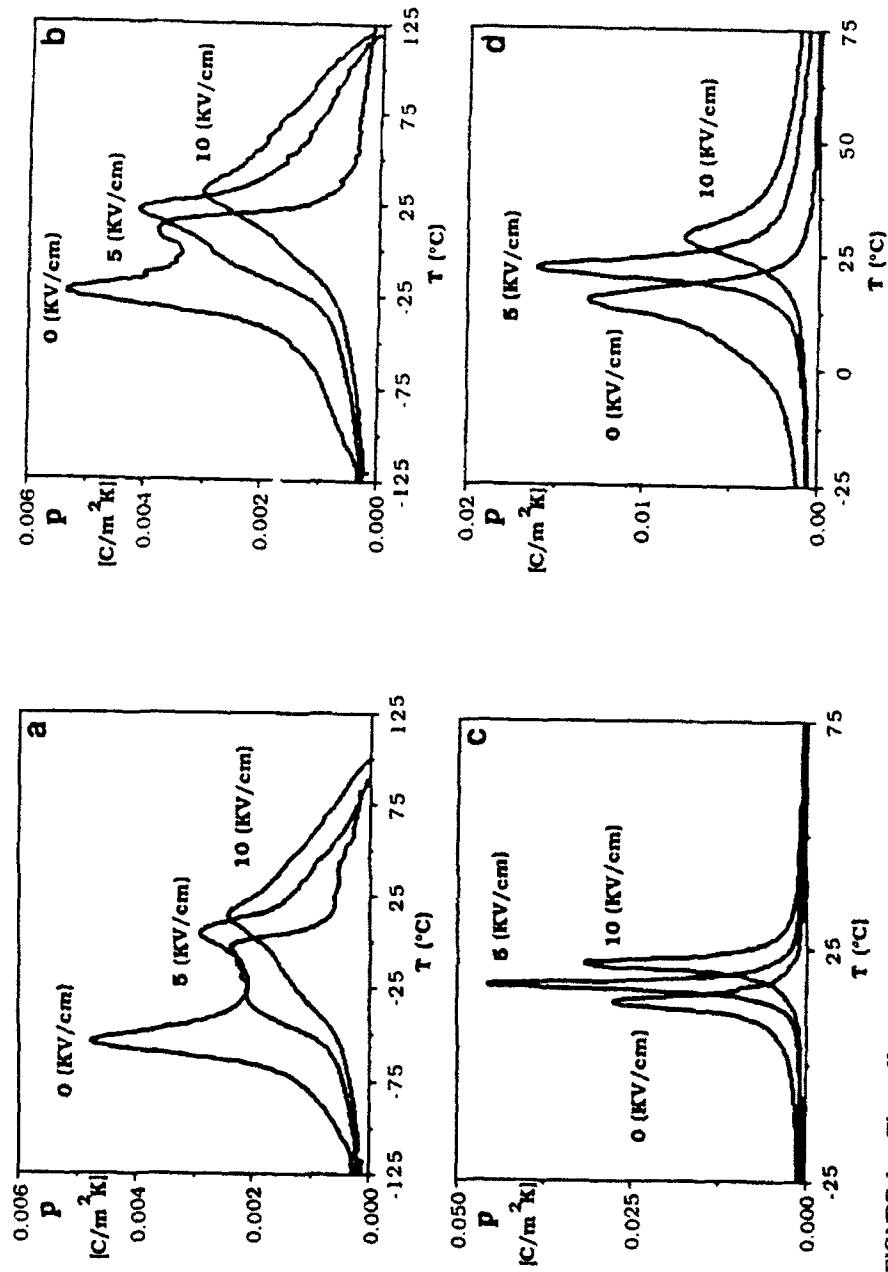


FIGURE 1. The effect of a biasing field on the pyroelectric response: (a) $[x=0.025]$ as-fired, (b) $[x=0.05]$ as-fired, (c) $[x=0.025]$ annealed, and (d) $[x=0.05]$ annealed.

The dielectric response of as-fired and annealed specimens of $[x=0.025]$ and $[x=0.05]$ under DC bias conditions of $E=0$ and 5 (KV/cm) are found to be similar to the unbiased and biased responses of pure $Pb(Sc_{1/2}Ta_{1/2})O_3$ materials: there is observed a decrease in the dielectric constant maxima for the as-fired materials and an increase in the peak dielectric response for the annealed, more highly ordered specimens under a biasing field. The dielectric losses [Table 2] are generally depressed with the application of a DC bias, especially for those specimens which have been annealed.

The figure of merit, F_D , for as-fired and annealed $[x=0.025]$ and $[x=0.05]$ materials appear as a function of temperature in Figure 2(a-d) under biasing conditions of $E=0$ and 5 (KV/cm). Some enhancement of the figure of merit is observed under 5 (KV/cm) for the as-fired specimens, which even under unbiased conditions exhibit stable responses over an extremely broad temperature range. The peak F_D of the annealed $[x=0.025]$ composition [Figure 2(c); Table 2] that occurs at $\sim 20^\circ\text{C}$ shows a more marked enhancement over a narrower temperature interval than its as-fired counterpart [Figure 2(a); Table 2]. Even in an unbiased condition these annealed materials exhibit considerably higher figures of merit over a broader temperature range than unmodified $Pb(Sc_{1/2}Ta_{1/2})O_3$ materials¹ [Table 1] with optimum operating temperatures only slightly lower than room temperature. The F_D of the annealed $[x=0.05]$ material [Figure 2(d)] is still rather high compared with pure $Pb(Sc_{1/2}Ta_{1/2})O_3$, but somewhat lower than the annealed $[x=0.025]$ composition. The effect of the bias field on the annealed $[x=0.05]$ material is less dramatic with respect to the peak F_D attained [Figure 2(c,d); Table 2]; however, similar to the as-fired specimens, this material exhibits an enhanced figure of merit over a broad temperature range above $T(\text{max})$.

It is acknowledged that the Byer-Roundy method used in this study for determining the pyroelectric response of the material does not fully account for the conditions imposed on an element in the actual operation of a pyroelectric array. An investigation by means of an alternative technique such as the Chynoweth method⁹, which more nearly simulates the actual operation conditions of a pyroelectric element, will be useful in further evaluating the full potential of these materials for thermal imaging applications.

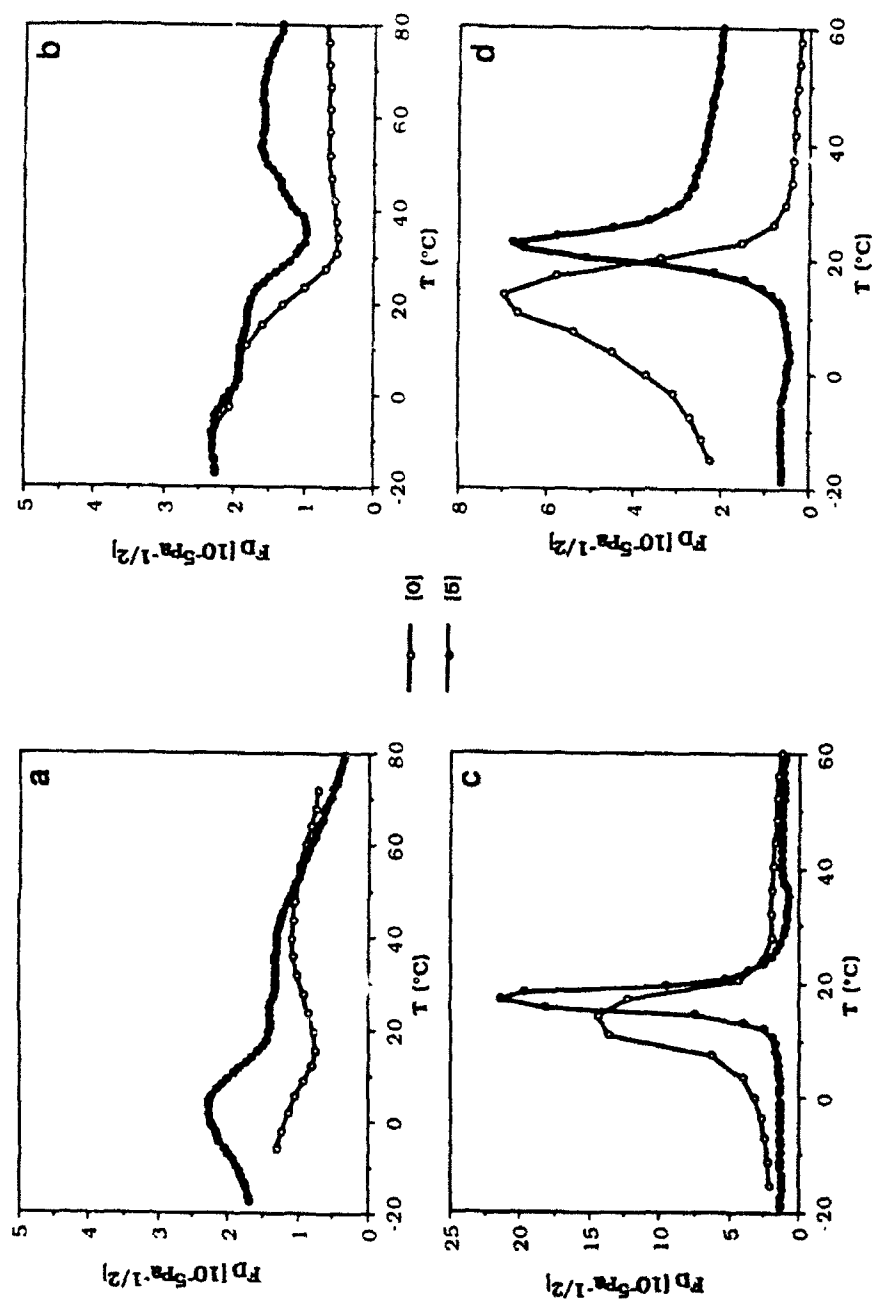


FIGURE 2. The pyroelectric figure of merit $[F_D]$ for as-fired specimens under DC biasing conditions of $E=0$ (KV/cm) [0] and $E=5$ (KV/cm) [5]: (a) $x=0.025$ as-fired, (b) $x=0.05$ as-fired, (c) $x=0.025$ annealed, and (d) $x=0.05$ annealed.

TABLE 2. Pyroelectric figure of merit, F_D , and relevant dielectric properties of selected VOD compositions

X	O/D †	E(Bias) (KV/cm)	T(°C)	P (C/m ² K)	ϵ (1 KIz)	$\tan(\delta)$ (1 KIz)	$F(D)$ (10 ⁻⁵ Pa ^{-1/2})
0.025	O	0	10	0.0280	7200	0.044	130
		5	18	0.0460	9500	0.036	21.5
	D	0	5	0.0014	7800	0.040	0.9
		5	5	0.0028	7500	0.040	2.2
0.05	O	0	10	0.0080	18300	0.070	6.5
		5	25	0.0090	23400	0.025	6.7
	D	0	10	0.0038	9900	0.070	1.8
		5	10	0.0033	8500	0.070	2.0

† O: Annealed D: As-Fired

CONCLUSIONS

The preliminary results obtained in this study obtained under modest field conditions indicate that the materials from the VOD composition range of the $(1-x)\text{Pb}(\text{Sc}_{1/2}\text{Ta}_{1/2})\text{O}_3$ - $(x)\text{PbTiO}_3$ system are highly variable in their pyroelectric performance, both with respect to the maximum response achieved and the breadth of the temperature range over which a stable response is obtained. It is apparent that $(1-x)\text{Pb}(\text{Sc}_{1/2}\text{Ta}_{1/2})\text{O}_3$ - $(x)\text{PbTiO}_3$ materials of low x with a variable state of order/disorder will prove extremely versatile for a variety of point detector applications.

REFERENCES

1. N.M. Shorrocks, R.W. Whatmore, and P.C. Osbond, Ferroelectrics **106**, 387 (1990).
2. R.W. Whatmore, A. Patel, N.M. Shorrocks, and F.W. Ainger, Ferroelectrics **104**, 269 (1990).
3. J.R. Giniewicz, A.S. Bhalla, and L.E. Cross (to be published).
4. JCPDS #24-1017 [ScTaO_4].
5. T.R. Shrout and A. Halliyal, Am. Ceram. Soc. Bull. **66**(4), 704 (1987).
6. N. Setter, Ph.D. Thesis, The Pennsylvania State University, (1980).
7. C.G.F. Stenger and A.J. Burggraaf, phys. stat. solid. (a) **61**, 275 (1980).
8. R.L. Byer and C.B. Roundy, Ferroelectrics **3**, 333 (1972).
9. A.G. Chynoweth, J. Appl. Phys. **27**(1), 78 (1956).

APPENDIX 9

Glassy polarization in the ferroelectric tungsten bronze $(\text{Ba,Sr})\text{Nb}_2\text{O}_6$

A. S. Bhalla, R. Guo, and L. E. Cross

Materials Research Laboratory, The Pennsylvania State University, University Park, Pennsylvania 16802

G. Burns and F. H. Dacol

IBM T. J. Watson Research Center, P.O. Box 218, Yorktown Heights, New York 10598

R. R. Neurgaonkar

Rockwell International Science Center, Thousand Oaks, California 91360

(Received 17 June 1991; accepted for publication 19 February 1992)

We report accurate temperature dependent measurements of optic indices of refraction, the birefringence, and the strain in the ferroelectric tungsten bronze crystals $\text{Ba}_{0.25}\text{Sr}_{0.75}\text{Nb}_2\text{O}_6$ and two compositions of $(\text{Ba}_{1-x}\text{Sr}_x)_2(\text{K}_{1-y}\text{Na}_y)_2(\text{NbO}_3)_{10}$. These results are compared to our previous results in $\text{Ba}_{0.4}\text{Sr}_{0.6}\text{Nb}_2\text{O}_6$. From the experimental data, it appears that far above the ferroelectric T_c up to a temperature T_d , these crystals possess a local, randomly oriented polarization, P_d , with similar T_d values, irrespective of their chemical composition and T_c . Various aspects of our understanding of the polarization behavior and other effects in this ferroelectric system are discussed.

I. INTRODUCTION

In a previous paper¹ we reported measurements, as a function of temperature, of the optic indices of refraction, $n(T)$, and elements of the strain tensor, x_{ij} , of the tetragonal tungsten bronze ferroelectric $\text{Ba}_{0.4}\text{Sr}_{0.6}\text{Nb}_2\text{O}_6$ (BSN40, $T_c \approx 75^\circ\text{C}$). BSN40, as well as other mixed system ferroelectrics, show crystalline ferroelectric behavior but with a glassy polarization phase transition above the ferroelectric transition temperature T_c up to a dipole temperature (T_d). Some aspects of materials with these properties have been reviewed.² Particularly noteworthy in our previous work¹ is that analysis of the $n(T)$ and x_{ij} data yields essentially the same T_d values as well as essentially the same temperature dependent dipole polarization [$P_d \equiv (P_3^2)^{1/2}$] which merges with the ferroelectric reversible polarization (P_r) below T_c .

In this paper we extend our previous measurements to several related crystals. These are $\text{Ba}_{0.25}\text{Sr}_{0.75}\text{Nb}_2\text{O}_6$ (BSN25, $T_c \approx 56^\circ\text{C}$) and $(\text{Ba}_{1-x}\text{Sr}_x)_2(\text{K}_{1-y}\text{Na}_y)_2(\text{NbO}_3)_{10}$ (BSKNN) with several ratios of atoms. In particular, for these materials we report measurements of P_r , n_3 , n_1 , and the optical birefringence, as well as some components of the strains. These results are compared to those obtained from BSN40 and aspects of our understanding of these results are discussed.

II. STRUCTURE

A unit cell of the tetragonal tungsten bronze structure is shown in Fig. 1. Above T_c it has a center of symmetry (space group D_{4h}^2 - $P4/m\bar{b}n$). Below T_c it remains tetragonal (space group C_{4v}^2 - $P4bm$) but develops a reversible polarization along the c axis (3 axis). Figure 1 shows the primitive unit cell viewed along the c axis. The chemical formula can be thought of as $(\text{Ba}_{1-x}\text{Sr}_x)_2(\text{NbO}_3)_{10}$ since there are ten niobium octahedra in this unit cell and the Ba and Sr atoms randomly occupy the two α and four β positions.^{3,4} However, there are six such positions and only five Ba + Sr atoms; thus the structure automatically has

defects. The small, four γ sites tend to be occupied only by smaller ions (such as Li). In fact, none of the tungsten bronze ferroelectrics actually are ordered compounds,⁵ they all have defect structures.^{2,6}

III. THEORETICAL CONSIDERATIONS

A. Thermal expansion

In the tungsten bronze type crystals, the prototype point symmetry is $4/m\bar{m}m$ so that the thermal expansion is anisotropic with components x_3 along the fourfold axis and x_1 in the perpendicular plane. The ferroelectric point symmetry is $4mm$ and the very high dielectric anisotropy at T_c shows that fluctuations are confined to the fourfold axis (i.e., the ferroelectricity is uniaxial). For these cases, the polarization fluctuation induced strains will be given by¹

$$x_3 = \Delta c/c_0 = Q_{33} \bar{P}_3^2, \quad (1)$$

$$x_1 = \Delta a/a_0 = Q_{13} \bar{P}_3^2, \quad (2)$$

where Q , the electrostrictive coefficient, is a fourth rank tensor written in contracted notation.

B. Optical refractive index

In the bronze family, there is a standing birefringence in the uniaxial tetragonal prototype (i.e., $n_3 \neq n_1$) and a birefringence Δn_{31} . Since all polarization occurs along the ferroelectric (c , or 3) axis, then in contracted notation, we have, for the indices of refraction,

$$\Delta n_3 = -g_{33} (n_3^0)^3 \bar{P}_3^2/2, \quad (3)$$

$$\Delta n_1 = -g_{13} (n_1^0)^3 \bar{P}_3^2/2, \quad (4)$$

where n^0 is the index of refraction if there were no polarization of any sort present, whether along the c axis (n_3^0) or perpendicular to it (n_1^0) and g_{ij} are the quadratic electro-optic constants. The change of optical birefringence $\delta(\Delta n_{31})$ will be given by (for $n_3^0 \approx n_1^0 \approx n_0$):

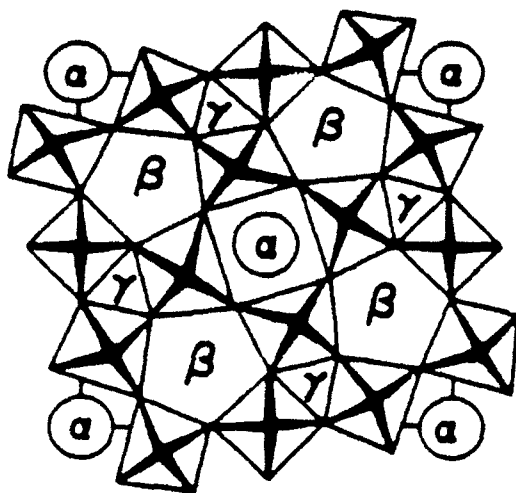


FIG. 1. A unit cell of the tetragonal tungsten bronze structure.

$$\delta(\Delta n_{31}) = -\frac{1}{2}n_0^3(g_{33} - g_{11})\bar{P}_3^2. \quad (5)$$

IV. EXPERIMENTAL TECHNIQUE

The reversible polarization, P_r , was obtained by the integration of the pyroelectric current versus temperature measured by a method developed by Byer and Roundy.⁷ The poled single-crystal sample was heated in an air oven with automatic heating rate control. The pyroelectric current was measured by a picoammeter.

Thermal expansion measurements were carried out from room temperature to about 500 °C by using a high sensitivity linear variable differential transformer (LVDT) dilatometer. Heating/cooling rate of 0.5 °C/min was chosen and regulated by a microprocessor based temperature controller. Single-crystal rods cut with length parallel to either c or a axis were mounted inside a fused silica holder which is set upright in a vertical furnace, and the thermal expansion or contraction was recorded on an X - Y recorder.

The indices of refraction parallel to P_r (n_3) and perpendicular to P_r (n_1) were measured by the minimum deviation technique.⁸ Oriented single-crystal prisms were used in an oven in conjunction with various lasers as light sources.

The birefringence, Δn_{31} , was also directly measured. An a -cut plate was polished into a wedge shape with a known wedge angle (5°–7°). Δn_{31} was measured using a polarizing microscope with a hot stage and the sodium D lines as a light source ($\lambda = 589.3$ nm). The birefringence was determined by

$$\Delta n_{31} = \lambda/d \sin \theta, \quad (6)$$

where θ is the wedge angle, and d is the separation between the interference fringes resulting from the varying thickness of the wedge.

TABLE I. Values of the Q and g coefficients used for calculation of $(P_3^2)^{1/2}$.

Electrostrictive constant (m^4/C^2)	$Q_{31} = -0.71 \times 10^{-1}$
	$Q_{33} = 3 \times 10^{-1}$
Quadratic electro-optic coefficient (m^4/C^2)	$(g_{31} - g_{11}) = 0.068$

V. RESULTS AND DISCUSSION

Room-temperature values of several physical constants derived experimentally and used for the calculations of $(P_3^2)^{1/2}$ are summarized in Table I.

Figure 2(a) shows the indices of refraction both parallel and perpendicular to the tetragonal c axis of single-crystal BSN25. As can be seen, the changes in n_3 are considerably larger than those perpendicular to the tetragonal axis (n_1). Continuous change in values of both n_1 and n_3 rather than a classical soft mode behavior can be seen.

Figure 2(b) shows birefringence, Δn_{31} , as a function of temperature for the same BSN25 single crystal. As is evident from Fig. 2(b), Δn_{31} decreases with temperature, goes through zero for $\lambda = 589.3$ nm at a temperature well above T_c , and the crystal changes from optically positive to negative.

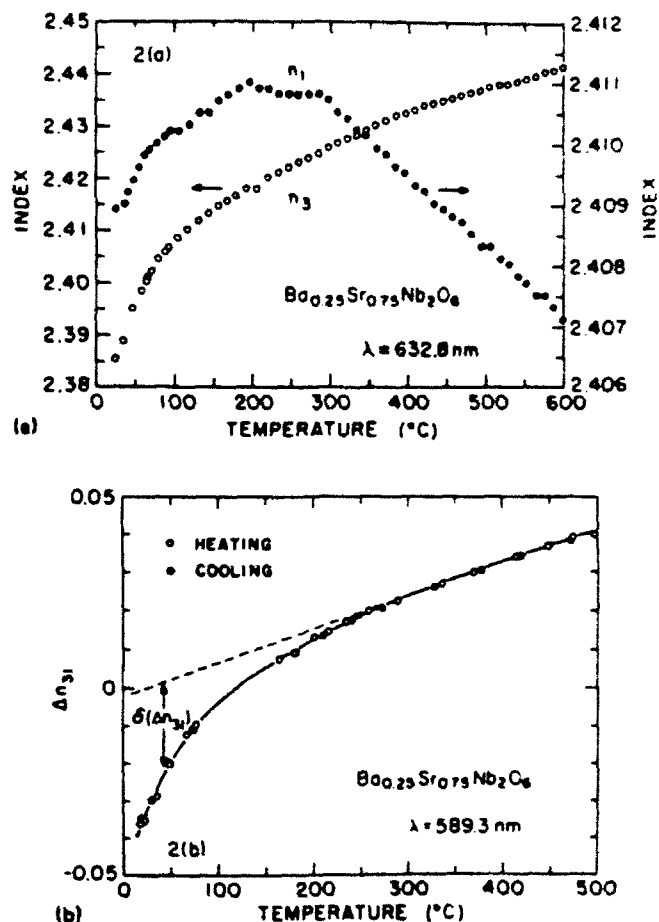


FIG. 2. (a) The measured n_1 and n_3 for BSN25 single crystal at 632.8 nm (b) Optical birefringence Δn_{31} for a BSN25 at 589.3 nm. The results for heating and cooling overlap.

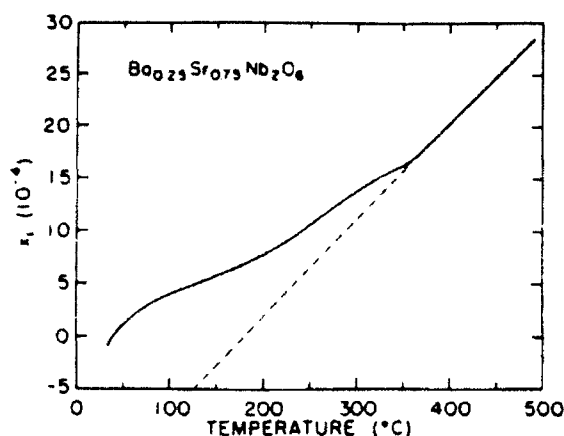


FIG. 3. Thermal strain for BSN25 along the a axis.

Figure 3 shows the thermal strain data, $x_1 = \Delta a/a$, measured by LVDT for a BSN25 single crystal. Using an extrapolation of the high-temperature curve, it is possible to calculate the arrest of the change which is due to the onset of $(P_3^2)^{1/2}$. As can be seen from Fig. 3, the deviation from the linear high-temperature behavior occurs at a temperature ($\sim 360^\circ\text{C}$) approximately.

Temperature dependence of the pyroelectric coefficient p and the integrated reversible polarization P_r of single-crystal BSN25 are plotted in Fig. 4. BSN25 is a typical relaxor-type ferroelectric in which a ferroelectric-paraelectric phase transition is frequency dependent.⁹

The Q and g coefficients for BSN25 have not been measured. However, those for BSN40 have been measured^{10,11} (Table I) and they have been used for deducing the data of BSN25 (and for BSKNN, discussed later). Due to the similarity of these materials, this should cause little error. Then, using these Q and g values (Table I), Fig. 5 summarizes the value of $(P_3^2)^{1/2}$, obtained from independent measurements. That is, P_d or $(P_3^2)^{1/2}$ is obtained from the n_3 , n_1 , Δn_{31} , and $\Delta a/a$ experimental results, using the

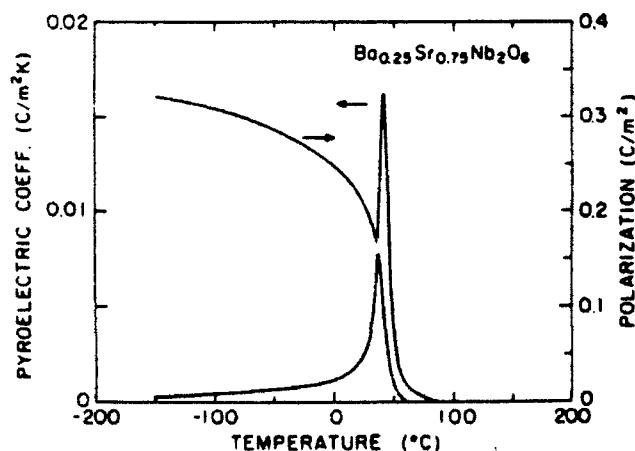


FIG. 4. Temperature dependence of the pyroelectric coefficient p and reversible spontaneous polarization P_r for a BSN25 single crystal.

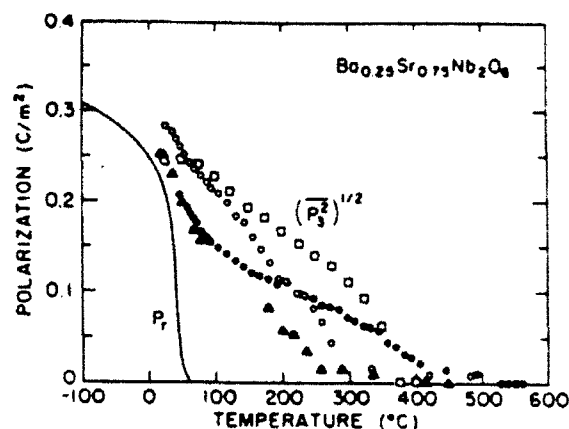


FIG. 5. $(P_3^2)^{1/2}$ vs T for BSN25, as calculated from n_3 vs T (in solid circles), n_1 vs T (in open circles), Δn_{31} vs T (in solid triangles), and $\Delta a/a$ vs T (in open rectangles). P_r vs T , from p vs T , is also shown.

corresponding equations (1) through (5). Also plotted is the reversible polarization data P_r from Fig. 4. It is evident that the polarization calculated from the $(P_3^2)^{1/2}$ is larger than P_r and extends several hundred degrees above T_c . However, note that below T_c , both P_d and P_r appear to merge.

It has been known⁹ that the ferroelectric-paraelectric phase transition becomes more diffuse when the Sr:Ba ratio increases. Figure 6 shows the results¹ of similar measurements performed on BSN40. BSN25 shows more pronounced relaxor behavior for which the $(P_3^2)^{1/2}$ decays slowly with temperature compared to BSN40. Nevertheless, both BSN40 and BSN25 show similar T_d value, even though there are differences in their compositions. It has been reported that T_d of (PLZT) $[\text{Pb}_{1-x}\text{La}_x(\text{Zr,Ti}_{1-y})_{1-x/4}\text{O}_3]$ is approximately equal to T_c of PZT⁸ and T_d of $\text{Pb}(\text{Ti}_{1-x}\text{Sn}_x)\text{O}_3$ is found¹² to be equal to T_c of PbTiO_3 . In BSN crystals, there is no end member from which an estimate of T_d can be made. How-

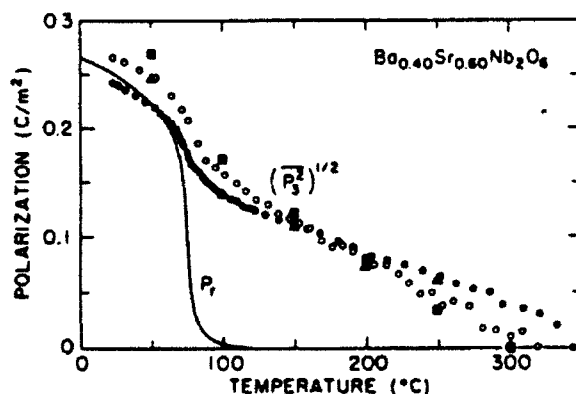


FIG. 6. $(P_3^2)^{1/2}$ vs T for BSN40, as calculated from n_3 vs T (in solid circles), n_1 vs T (in open circles), Δn_{31} vs T (in solid triangles), and $\Delta c/c$ vs T (in solid rectangles). P_r vs T , from p vs T , is also shown as the solid line.

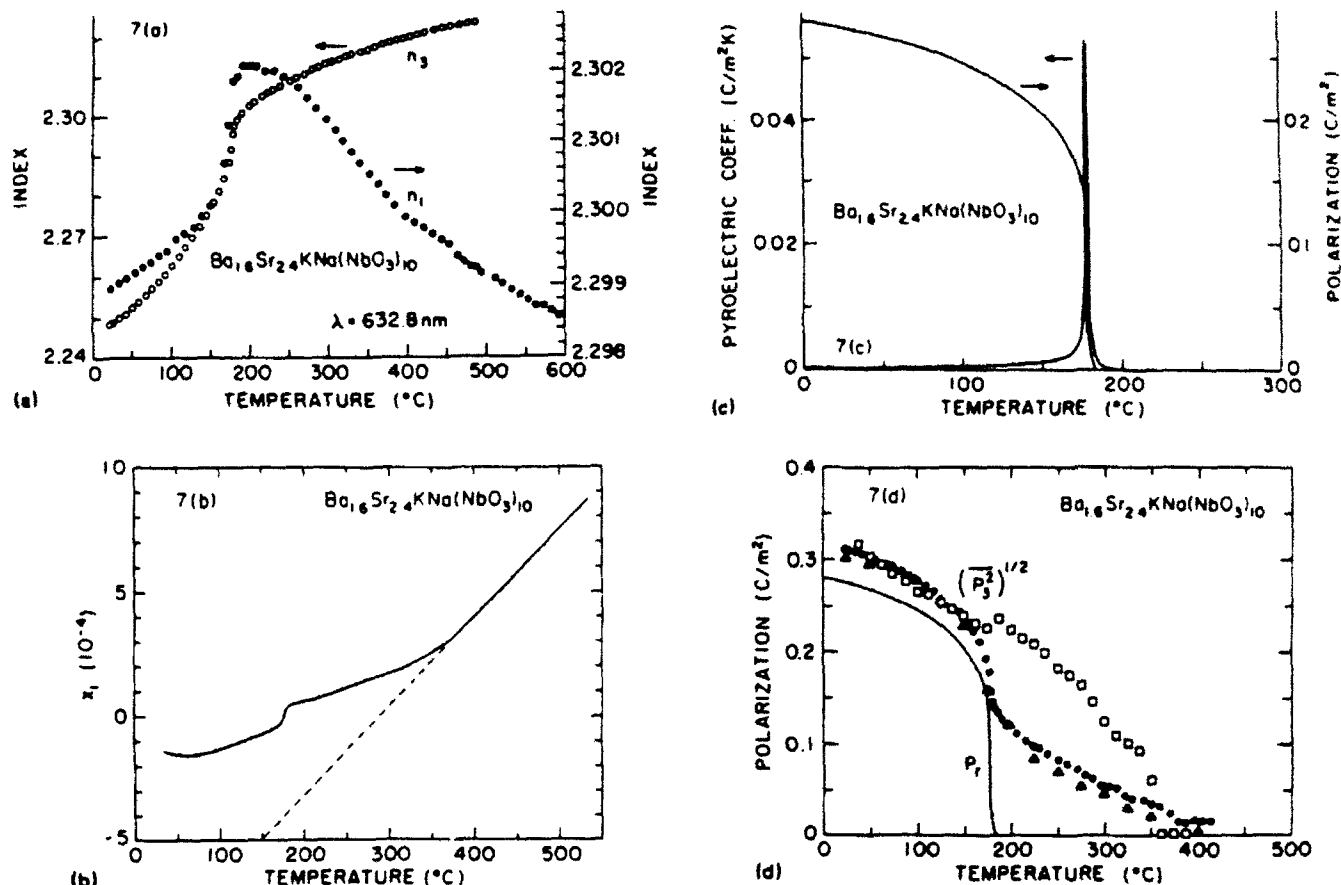


FIG. 7. (a) The indices of refraction both parallel and perpendicular to the tetragonal c axis at $\lambda = 632.8 \text{ nm}$; (b) the thermal strain $\Delta a/a$ measured by LVDT dilatometry method; (c) the temperature dependence of the pyroelectric coefficient p and the integrated reversible spontaneous polarization P_r , and (d) a summary of the values of $(P_3^2)^{1/2}$ obtained from n_3 (in solid circles), Δn_{11} (in solid triangles), and $\Delta a/a$ (in open rectangles) of a single crystal BSKNN(1). P_r is also shown.

ever, a T_d that is approximately compositional insensitive does seem to exist in this system.

We have carried out similar studies on related "stuffed" tungsten bronze crystals with the formula $(\text{Ba}_{2-x}\text{Sr}_x)_2(\text{K}_{1-y}\text{Na}_y)_2(\text{NbO}_3)_{10}$ or BSKNN as well as rare-earth doped BSKNN. These stuffed tungsten bronzes have six atoms for the six $\alpha + \beta$ sites (Fig. 1). However, since the various atoms occupy both the α and β sites, the fundamental randomness in this structure is maintained. We have measured two such stuffed crystals with the formulas, abbreviations, and T_c values listed here:



Figure 7(a) shows the indices of refraction both parallel and perpendicular to the tetragonal c axis of single-crystal BSKNN(1) for $\lambda = 632.8 \text{ nm}$. Figure 7(b) shows the thermal strain $\Delta a/a$ measured by LVDT for BSKNN(1) single crystal. The temperature dependence of the pyroelectric coefficient p and the reversible spontaneous polarization P_r of single crystal BSKNN(1) are plotted in Fig. 7(c). A summary of the $(P_3^2)^{1/2}$, or P_d , results for BSKNN(1) are shown in Fig. 7(d). Similar to the results

for BSN (Figs. 5 and 6), for BSKNN(1) P_d obtained from the index and strain measurements extended to $T_d \sim 350\text{--}400^\circ\text{C}$. This T_d value is several hundred degrees above the ferroelectric T_c ($\approx 175^\circ\text{C}$) indicating glassy polarization behavior over this range. This T_d value is similar to those found for the BSN25 and BSN40 crystals (Figs. 5 and 6). Also note that below T_c , P_d is approximately equal to the reversible polarization P_r , indicating a common origin of both of these properties.

Figure 8 shows plots of $(P_3^2)^{1/2}$ (determined from birefringence data) versus the temperature for several related BSKNN compositions, as indicated. BSKNN(2) shows a sharper drop of the P_d at the T_c , while BSKNN(1) shows a slow decay of it. Although T_c for BSKNN(1) and BSKNN:Nd are 175 and 145°C , respectively, their T_d values are almost the same.

The results reported here for BSN25, and several BSKNN materials, are similar to those found earlier¹ for BSN40. It appears that a local nonreversible polarization P_d starts to become observable below a dipole temperature T_d . The latter is several hundred degrees above the ferroelectric transitions. Related measurements have been re-

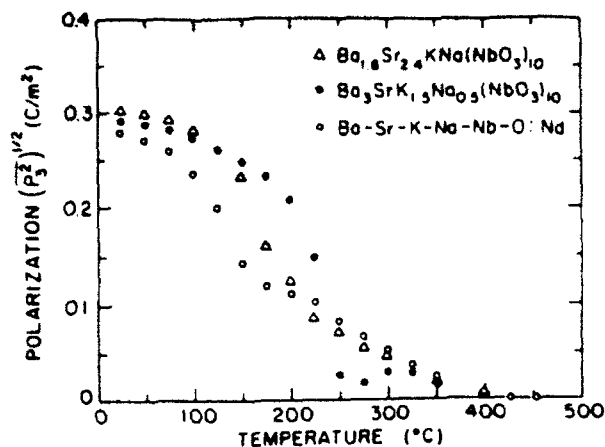


FIG. 8. $(P_3)^{1/2}$ data derived from optical birefringence measurements for BSKNN(1), BSKNN(2), and Nd doped BSKNN.

ported¹³ in the tungsten bronze ferroelectric system $K_2Sr_4(NbO_3)_{10}$.

The optic index of refraction (Δn) and the strain (Δx) measurements yield similar P_d and T_d results. Experimentally, the optic index of refraction results are totally independent of strain measurements, each being interpreted by different coefficients (Table I). Thus, the qualitative and quantitative agreement [Figs. 5, 6, and 7(d)] for P_d and T_d in the ferroelectric systems measured here gives strong support to the interpretation that local, randomly orientated (along the $\pm c$ axis) polarization exists in these crystals far above T_c . Similar agreement was found previously.¹ We note, however, that the agreement of the Δn and Δx measurements results from general symmetry considerations and not from any detailed microscopic model. The fact that we expect $\Delta n \propto P^2$ and $\Delta x \propto P^2$ comes from the expectation that the high-temperature phase can be treated as centrosymmetric and any polarization (local or macroscopic) can be treated as an expansion about $P = 0$. Thus, the first term in an expansion will be a P^2 term.

Discussion of these and similar results in related materials has been reviewed.² Basically the effects have been discussed in terms of two microscopic models. Smolenskii¹⁴ has emphasized compositional fluctuations with a dimension $\sim 1 \mu m$ in order to understand these materials. On the other hand, Burns *et al.*^{2,13,15} have emphasized compositional fluctuations on the scale of the dimension of a unit cell, and using these ideas, some of these types of results can be significantly understood with fluctuations on this ($\sim 4 \text{ \AA}$) scale.^{13,15} Work by Setter and Cross^{16,17} support the small-scale fluctuations idea. They^{16,17} studied $Pb(Sc_{1/2}Ta_{1/2})O_3$ and varied the degree of order on the B site (Sc^{3+} and Ta^{5+}) to obtain sharp or diffuse phase transitions by annealing and quenching the crystals. Since in their work the B site ions would be expected to diffuse a distance of only one or two unit cells, their results support the ideas of Burns *et al.*

It was suggested that dynamic polarization fluctuations in normal nonglassy uniaxial ferroelectrics will exist

above T_c as a general property.¹⁸ One can therefore, expect some perturbations to properties related to P^2 term. However, here we are considering a somewhat complicated situation as, for this type of glassy polarization fluctuation that is the implication of local chemical inhomogeneity, the correlated effective-field theory of ferroelectricity from which the nonglassy type polarization fluctuations are determined does not apply to the system as a whole. In tungsten bronze BSN solid solution family as addressed earlier, the chemical composition is homogeneous locally that allows the local symmetry to be lower than the global symmetry and prevents the establishment of short range correlations in chains along the incipient polar axis beyond the dimension of the local area. Sizes of these polar local regions are such that the orientations of the polarization are thermally reversible,¹⁷ analogous to superparamagnetism.¹⁹ The polarization fluctuation depends on the local polar island dimension distribution and hence is found prominent in broad temperature region well above the average Curie temperature, T_c . For T approaches to T_c , a polarization vector dynamic freezing-in model has been suggested¹⁷ based upon the experimental evidence of the temperature dependence of the electrostrictive coefficients Q_{33} and Q_{13} measured on BSN60,²⁰ as both Q_{33} and Q_{13} are markedly temperature dependent and approach zero near T_c while Q_{11} is essentially independent of temperature to T_c .

To summarize, in these materials it appears that a local, nonreversible polarization can appear, below a temperature T_d that is far above the ferroelectric transition temperature (T_c). In the tungsten bronze crystals discussed here, T_d is in the 350–400°C neighborhood and only weakly depending on the particular composition. The similarity of these T_d values probably is related to the similarity of the orientation sizes of the NbO_6 octahedra that play the fundamental polarization role.

¹ A. S. Bhalla, R. Guo, L. E. Cross, G. Burns, F. H. Dacol, and R. R. Neurgaonkar, *Phys. Rev. B* **36**, 2030 (1987).

² G. Burns and F. H. Dacol, *Ferroelectrics* **104**, 25 (1990); G. Burns, *Phase Transitions* **5**, 261 (1985).

³ S. C. Abrahams, P. B. Jamieson, and J. L. Bernstein, *J. Chem. Phys.* **54**, 2355 (1971), and the references quoted there to their earlier papers.

⁴ M. E. Lines and A. M. Glass, *Principles and Applications of Ferroelectrics and Related Materials* (Clarendon, Oxford, 1977).

⁵ B. A. Scott, E. A. Gress, B. L. Olson, G. Burns, A. W. Smith, and D. F. O'Kane, *Mater. Res. Bull.* **5**, 47 (1970).

⁶ G. Burns, *Solid State Physics* (Academic, New York, 1985).

⁷ R. L. Byer and C. B. Roundy, *Ferroelectrics*, **3**, 333 (1972).

⁸ G. Burns and F. H. Dacol, *Phys. Rev. B* **28**, 2527 (1983); *Jpn. J. Appl. Phys.* **24**, Suppl. 24-2, 85 (1986).

⁹ A. M. Glass, *J. Appl. Phys.* **40**, 4699 (1969).

¹⁰ T. Shrout, Ph.D. thesis, Penn. State Univ., 1981.

¹¹ P. Asadipour, M. S. thesis, Penn State Univ., 1986.

¹² G. Burns and F. H. Dacol, *Solid State Commun.* **58**, 567 (1986).

¹³ G. Burns and F. H. Dacol, *Phys. Rev. B* **30**, 4012 (1984); G. Burns, *ibid.* **13**, 215 (1976).

¹⁴ G. H. Smolenskii, *Proceedings 2nd IMF, Kyoto, 1969*, *Phys. Soc. Jpn.* **26** (1970).

¹⁵ G. Burns and B. A. Scott, *Solid State Commun.* **13**, 423 (1973).

¹⁶ N. Setter and L. E. Cross, *J. Appl. Phys.* **51**, 4356 (1980).

¹⁷ L. E. Cross, *Ferroelectrics* **76**, 241 (1987).

¹⁸ M. E. Lines, *Phys. Rev. B* **5**, 3690 (1972).

¹⁹ L. Neel, *Compt. Rend. Acad. Sci.* **228**, 664 (1949).

²⁰ C. Sundius, M. S. thesis, Penn State Univ., 1984.

APPENDIX 10

THE ELECTRICAL PROPERTIES OF ANTIFERROELECTRIC LEAD ZIRCONATE-FERROELECTRIC LEAD ZINC NIOBATE CERAMICS WITH LANTHANUM.

J.S.Yoon, V.S.Srikanth and A.S.Bhalla
Materials Research Laboratory,
Pennsylvania State University, University Park, PA 16802

Abstract

The electrical properties of antiferroelectric lead zirconate(PZ) with relaxor ferroelectric lead zinc niobate(PZN) are studied from an application viewpoint of the field-induced phase transition near the morphotropic phase boundary. According to the addition of lanthanum, the curie point decreased with increasing lanthanum up to 3m/o, whereas for AF-FE boundary it increased with increasing lanthanum. Over 4m/o lanthanum, it can be find paraelectric and antiferroelectric region. The effect of composition of lanthanum and temperature on the dielectric, pyroelectric and P-E hysteresis are reported.

I. Introduction

Most of the antiferroelectric or ferroelectric oxide ceramics with relaxor are important for piezoelectric, pyroelectric device application as actuators¹⁻³. Among the vast range of perovskite structure compounds, solid solution compositions of antiferroelectric lead zirconate(PZ) with ferroelectric perovskite give interesting piezoelectric and pyroelectric properties near their antiferroelectric(AF) - ferroelectric(FE) phase transition and morphotropic phase boundary.

Lanthanum-modified lead zirconate titanate(PLZT) ceramics have interesting electrooptic properties. Their electrical and structural properties were initially reported by Heartling and Land⁴.

In this study, electrical properties of the antiferroelectric lead zirconate with a relaxor ferroelectric lead zinc niobate with composition of MPB, $0.929\text{PbZrO}_3\text{-}0.071\text{Pb}(\text{Zr}_{1/3}\text{Nb}_{2/3})\text{O}_3$, were investigated to the dependence of the change of lanthanum, PZZN-Lx (1 x 5).

II. Experimental Procedure.

1. Ceramic preparation.

Ceramics were prepared by conventional sintering technique used by reagent grade oxide powders of PbO, La_2O_3 , ZrO_2 , ZnO, and Nb_2O_5 as a raw materials. To compensate for the PbO loss during firing, 2w/o excess PbO was added.

After mixing in ball milling with alcohol for 12-14hr, the powders were calcined at 800°C for 1hr. Calcined powders were ground, and mixed with 3w/o of PVA binder, and were pressed into disk 12mm in diameter for cutting for the desired shape, and about 1 mm in thickness. The binder was evaporated during a double steps heat treatment at 300°C for 2hr and 500°C for 2hr⁵. Pressed disks were sintered at 1250°C for 1hr in PbO atmosphere with PbO-ZrO₂ source powder.

After sintering, ceramics were alternatively cut and polished, and were coated with sputtered gold electrode for electrical measurements.

2. Electrical measurements.

The dielectric constants were measured at frequencies of 100Hz, 1KHz, 10KHz, and 100KHz over a temperature range of -80°C - 240°C by using an automated dielectric measurement system with a multi frequency LCR meter and a desktop computer.

A modified Sawyer-Towe circuit was used to recorded the P-E hysteresis behavior of the samples at a various temperatures⁶. The electric field was measured by the X-axis of the oscilloscope, and polarization of the sample was measured by the Y-axis.

The pyroelectric properties were investigated with the Byer-Roundy method⁷. To measure the pyroelectric properties, one side of the circular sample of thickness over 0.2mm was electrode by gold sputtering. On otherside, a 5mm circular spot electrode was sputtered through a mask.

Specimens for the pyroelectric property were poled by dynamic method in air oven with an electric field 30KV/cm at 185°C.

The pyroelectric and P-E hysteresis measurements were carried out to determine the saturate polarization, remanent polarization, coercive field, the depolarization temperature, and phase transition.

III. Results and Discussion.

Figure 1 is the plot of the phase relations of the PZZN ceramics. It was based on the dielectric measurement, pyroelectric measurement, and P-E hysteresis measurement. According to the these measurements, it can be divided four regions. Those are paraelectric, ferroelectric-HT, ferroelectric-LT, and antiferroelectric region. The phase boundary of high temperature ferroelectric phase-low temperature ferroelectric phase at -60°C was determined by dielectric measurement. The boundary of

ferroelectric - antiferroelectric for the PZZN 930 - 935 was located at 70°C - 80°C and for the PZZN 925 - 928 was -5°C - -15°C. For the room temperature, it was divided by PZZN 928 - 930 with the large change of the slope. This feature means that it can be switch the phase from an antiferroelectric state to ferroelectric state at the small change of temperature near the PZZN 928 - 930 at the room temperature.

Figure 2 was SEM photographs of PZZN-L0 and PZZN-L3. They show a dense and uniform grain size in the sintered samples. The samples were thermally etched at 1200°C for 30min and the average grain size of PZZN-L0 and PZZN-L3 were 4µm and 2µm, respectively.

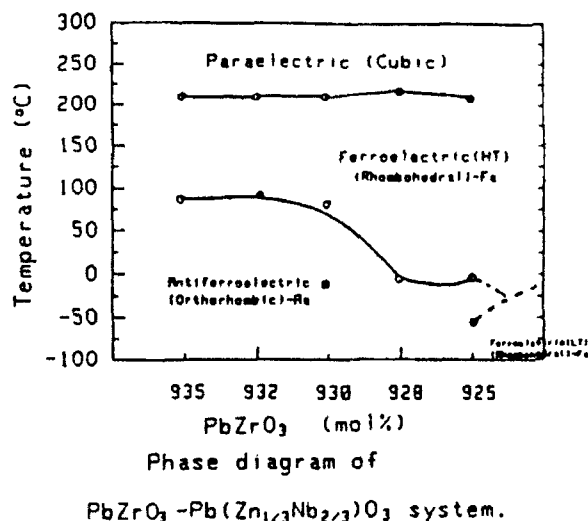


Fig. 1. Phase relations of the PZZN solid solution system at the AF-FE phase boundary.

Figure 3 shows the temperature dependence of the dielectric constants for PZZN-L0 and PZZN-L2 during the cooling. The dielectric constant of PZZN-L0 increased to peak value of 9000 at the transition temperature, $T_c=219^\circ\text{C}$. The dielectric constant of the PZZN-L2 show anomalies behavior at 70°C and T_c was 204°C. This anomalies between the phase boundary between the antiferroelectric phase(AF) and the ferroelectric phase(FE). Over the transition temperature, the ferroelectric phases were changed to paraelectric phase.

Figure 4 shows the temperatures dependence of the dielectric constants for PZZN-L series. The transition temperature of PZZN-L3 was 184°C, but T_c was increased with the increasing of the amount of lanthanum⁶. In case of PZZN-L9, T_c was 235°C.

Figure 5 shows the temperature dependence of the pyroelectric coefficient and the remanent polarization of PZZN-L0 and PZZN-L2. The measurements to find the phase boundary

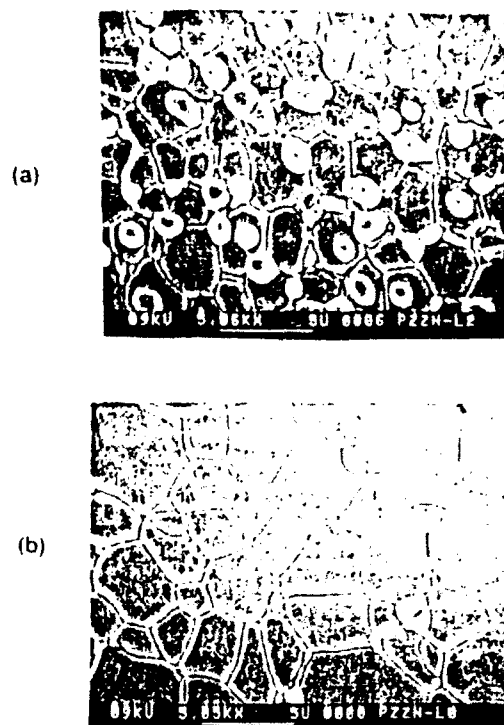


Fig. 2. SEM photograph of the surfaces of the PZZN-L0(a), and PZZN-L2(b) ceramics. The surfaces were thermally etched at 1200°C for 30min. (bar=1µm)

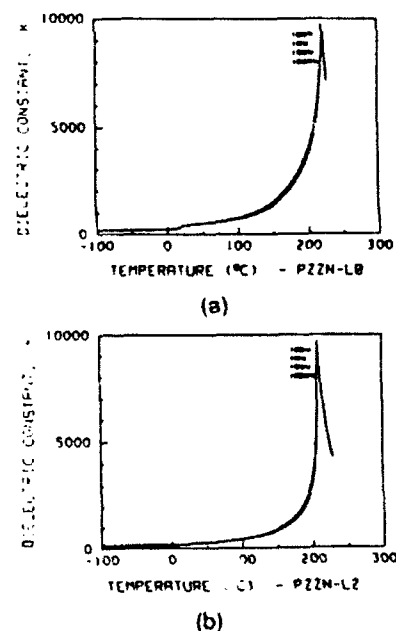


Fig. 3. Temperature dependence of the dielectric constants for PZZN-L0(a) and PZZN-L2(b) showing T_c .

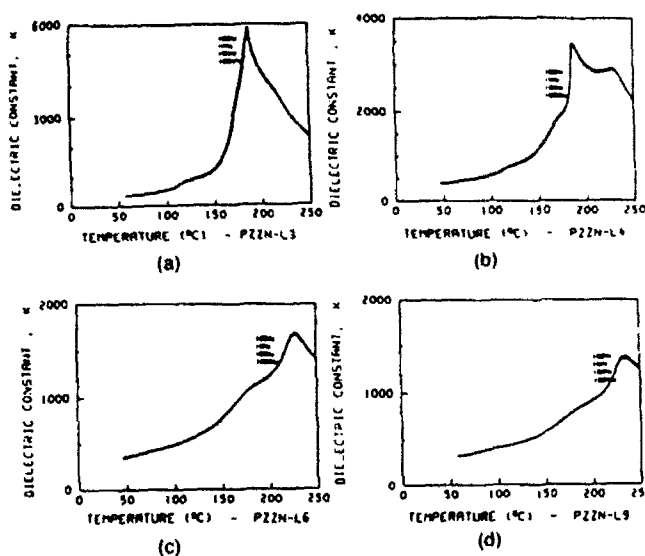


Fig. 4. Temperature dependence of the dielectric constants for PZZN-L3(a), PZZN-L4(b), PZZN-L6(c), and PZZN-L9(d) showing T_c .

composition were made during the heating cycle with a typical heating rate of 4°C/min. In the pyroelectric coefficient of the PZZN-L0 and PZZN-L2, two pyroelectric peaks corresponding to orthorhombic-to-rhombohedral and cubic-to-rhombohedral are clearly observed at 80°C and 204°C, respectively.

The hysteresis nature was investigated using a modified Sawyer-Tower circuit applying an ac field of about 30KV/cm. Figure 6 shows the P-E hysteresis loops observed for PZZN-L ceramics at various temperatures. The samples of the PZZN-L0 shows the ferroelectric behavior and increase the coercive field, E_c , and the remanent polarization, P_r , according to the increasing amount of the lanthanum. The ferroelectric of the PZZN-L system was highly sensitive to composition and temperature. P_r reaches a maximum value of 30 $\mu\text{C}/\text{cm}^2$ at PZZN-L2. In the PZZN-L3, it could find hysteresis loop at 145°C. It meant that an antiferroelectric phase can be forced into a field-induced ferroelectric phase with the remanent polarization and the field-induced ferroelectric state is expected to remain stable even after the electric field is removed. According to the hysteresis, it shows AF-FE boundary is located between PZZN-L0 and PZZN-L2 at 80°C, but between PZZN-L2 and PZZN-L3, boundary is 145°C.

Figure 7 is the plot of the phase relations of the PZZN-L solid solution system. It was based on the dielectric measurement, pyroelectric measurement, and P-E hysteresis measurement. According to these measurements, it can be divided three regions. Those are paraelectric, ferroelectric, and antiferroelectric region. The phase boundary for PZZN-L0 - PZZN-L2 was located at 80°C and for the PZZN-L3 was 145°C. Over the PZZN-L4, there are antiferroelectric and paraelectric phases.

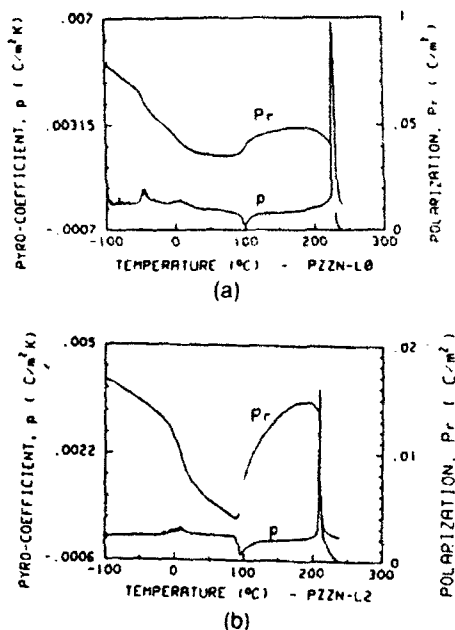


Fig. 5. Temperature dependence of pyroelectric coefficient(p) and polarization(P_r) of PZZN-L ceramics; (a) PZZN-L0 (b) PZZN-L2

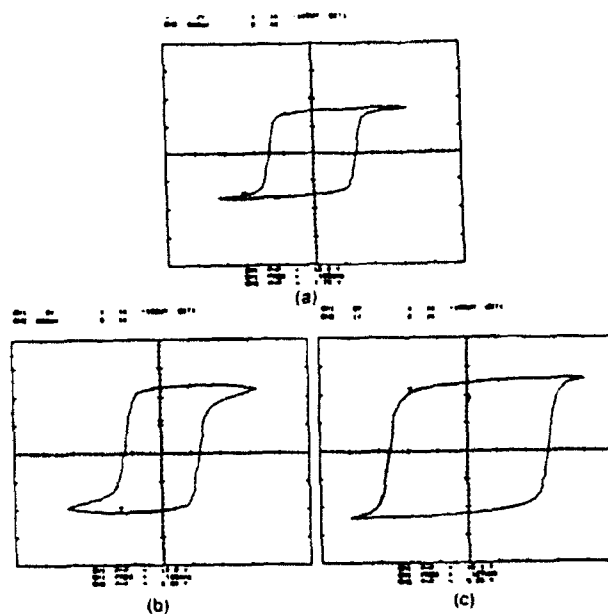


Fig. 6. D-E hysteresis loops of PZZN-L ceramics at various temperature showing ferroelectric. (a) PZZN-L0, $E_c = 15.9 \text{ KV/cm}$, $P_r = 21.2 \mu\text{C}/\text{cm}^2$ (b) PZZN-L1, $E_c = 7.3 \text{ KV/cm}$, $P_r = 24.5 \mu\text{C}/\text{cm}^2$ (c) PZZN-L2, $E_c = 5.98 \text{ KV/cm}$, $P_r = 30.6 \mu\text{C}/\text{cm}^2$

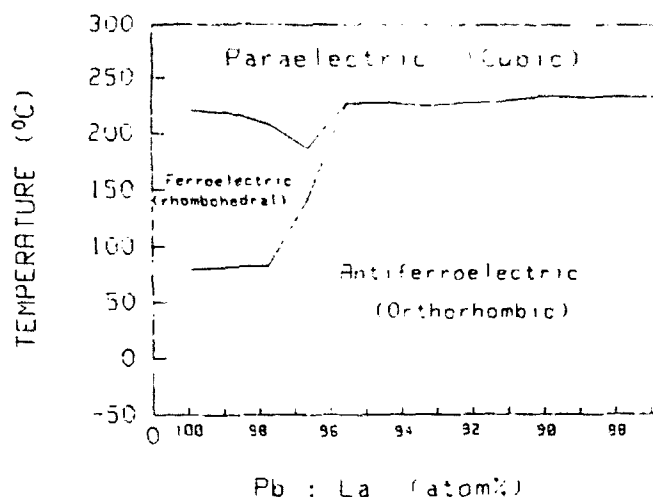


Fig. 7. Phase relations of the PZLN-L solid solution system.

IV. Conclusion

- 1) It could be divided three regions: paraelectric, ferroelectric, and antiferroelectric region.
- 2) The curie temperature decreased with increasing lanthanum up to 3m/o, whereas for AF-FE boundary it increased with increasing lanthanum.
- 3) Over 4m/o lanthanum, it can be find paraelectric and antiferroelectric region.

Reference

1. B.Jaffe, W.R.Cook, Jr., and H.Jaffe, *Piezoelectric Ceramics*, Academic Press, New York, 1971.
2. H.Jaffe, "Piezoelectric Ceramics", *J. Am. Ceram. Soc.*, **41** [11] 494-498 (1957).
3. E.Sawauguchi, "Ferroelectricity versus Antiferroelectricity in the Solid Solutions of PbZrO_3 and PbTiO_3 ", *J. Phys. Soc. Jpn.*, **8** 615-629 (1953).
4. G.H.Hearling and C.E.Land, "Hot-Pressed (Pb,La)(Zr,Ti) O_3 Ferroelectric Ceramics for Electrooptic Applications", *J.Am.Ceram.Soc.*, **54** [1] 1-11 (1971).
5. G.S.Snow, "Improvements in Atmosphere Sintering of Transparent PLZT Ceramics", *J.Am.Ceram.Soc.*, **56** [9] 479-480 (1973).
6. H.Diamurt, K.Drenk, and R.Pepinsky, "Bridge for Actuate Measurement of Ferroelectric Hysteresis", *Rev. Sci. Instrum.*, **28** [1] 30-34 (1957).

7. R.L.Byer and C.B.Roundy, "Pyroelectric Coefficient Direct Measurement Technique and Application to a NSEC Response Time Detector", *Ferroelectrics*, **3** 333-338 (1972).
8. W.A.Schulze, T.G.Miller, and J.V.Biggers, "Solubility Limit of La in the Lead Zirconate-Titanate System", *J.Am.Ceram.Soc.*, **58** [1-2] 21-23 (1975).

APPENDIX 11

The DC Field Dependence of the Piezoelectric, Elastic and Dielectric Constants For a Lead Zirconate-Based Ceramic.

E.F. Alberta, D.J. Taylor and A.S. Bhalla

Materials Research Laboratory, The Pennsylvania State University, University Park, PA 16802, U.S.A.

T. Takenaka

Faculty of Science and Technology, Science University of Tokyo, Noda, Chiba-Ken, 278 JAPAN.

ABSTRACT

Large pyroelectric figures of merit, F_V and F_D have been found in the solid solution $x\text{-PbZrO}_3$ [PZ] - $y\text{-Pb(Zn}_{1/3}\text{Nb}_{2/3})\text{O}_3$ [PZN] - $z\text{-PbTiO}_3$ [PT] (PZNT). Previous work within this system has also shown a DC field induced ferroelectric-antiferroelectric transition. This paper will further explore the electrical field dependence of the elastic constant (s_{11}^E), piezoelectric coefficient (d_{31}) and dielectric constant (K_{33}) near this phase transition.

INTRODUCTION

As sensor and transducer technology advances there is an increasing need for smart materials. When evaluating materials for smart applications, the weak field dependence of the dielectric and piezoelectric constants can be effective guides. Earlier studies in solid solution system of the relaxor ferroelectric PMN and the ferroelectric PT have shown strong weak field induced piezoelectric effect. Antiferroelectric materials have also been shown to exhibit this desired non-linear response. It was for this reason that the solid solution of the ferroelectric PT, and antiferroelectric PZ and relaxor PZN has been chosen to be explored for possible use as a smart sensor material under weak DC fields.

Solid solutions containing PZ have been widely studied in the past due to the antiferroelectric [AF] to ferroelectric [FE] phase transition and the existence of morphotropic phase boundaries. The system PZZN combines PZ with PZN. This system has been shown to possess a room temperature orthorhombic AF to rhombohedral FE phase boundary at $x \sim 93\%$ PZ. This system looks promising for piezoelectric and pyroelectric applications with $F_V = 0.31 \times 10^{-10} \text{ C}\cdot\text{cm/J}$ and $F_D = 0.35 \times 10^{-8} \text{ C}\cdot\text{cm/J}$, low coercive fields of 8 to 10 kV/cm, large piezoelectric coupling coefficients such as $k_{15} \sim 50\%$ and remanent polarizations on the order of 25 to 30 $\mu\text{C}/\text{cm}^2$.

This paper will explore the dielectric and room temperature piezoelectric properties of PZNT and PZZN compositions near the MPB. For the rest of this paper the PZNT(x/z) compositions with $z = 0$ mol% PT will be referred to as PZZN(x).

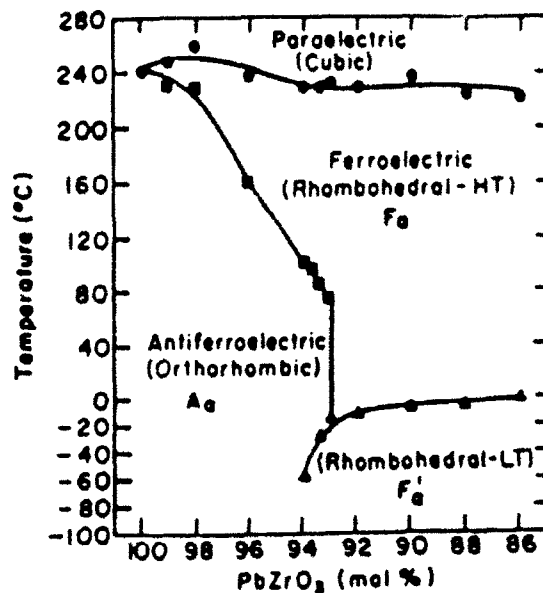


Figure 1: PZZN phase diagram.

EXPERIMENTAL PROCEDURES

Ceramic samples were prepared by the normal ceramic mixed oxide techniques. Samples were then thinned and polished to a 1- μm Diamond finish and gold sputtered electrodes applied. Room temperature polarization versus electric field hysteresis loops were then studied at 10 Hz using a modified Sawyer-Tower circuit. A silicone oil bath was used to prevent electrical breakdown during these experiments.

The temperature dependence of the dielectric constant was measured at various frequencies in a temperature range from -100°C to 250°C using a computer controlled measurement system consisting of a multifrequency LCR meter (HP4274A, Hewlett Packard Co.), desktop computer (HP 9816) and nitrogen fed furnace. Various DC bias voltages were then applied to the sample by an external power supply.

For resonance measurements the samples were prepared as long, thin bars with typical dimensions of $20 \times 2 \times 0.2 \text{ mm}$. Specimens were polished thin so as to allow the application of fields between 15 and 20 kV/cm with 600 Volts or less. These bars were then poled at 15 kV/cm for ten minutes at 100°C in a stirred silicone oil bath. All resonance measurements were made using an HP 4192A Impedance Analyzer.

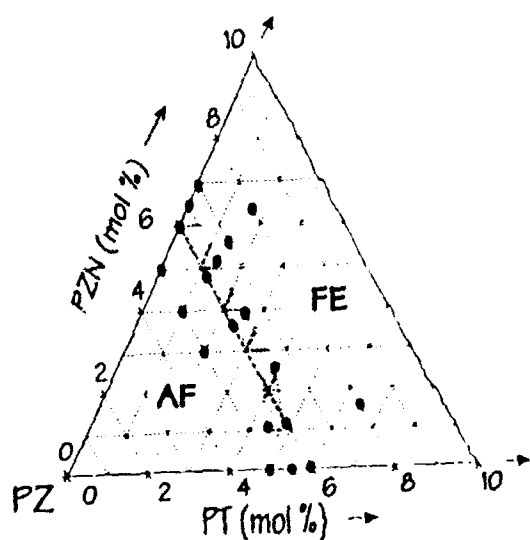


Figure 2: Room Temperature PZNT phase diagram.

The calculation of the real and complex compliance, s_{11} , piezoelectric coefficient, d_{31} , dielectric constant, ϵ_{33} , and coupling coefficient, k_{31} , was made using the equation for the admittance of a bar resonator (1).

$$Y = \frac{j\omega l w}{t} \left(\epsilon_{33}^* - \frac{d_{31}^2}{s_{11}^*} \right) + \frac{j 2\omega d_{31}^2}{(\rho s_{11}^*) s_{11}^*} \tan \frac{1}{2} \omega l (\rho s_{11}^*)^{\frac{1}{2}} \quad (1)$$

where:

w = width, ρ = density, t = thickness,
 ω = frequency and l = length

Since this equation is for an ideal resonator the piezoelectric coefficients are assumed to be complex quantities i.e.:

$$s_{11} = s'_{11} + j s''_{11} \quad (2)$$

$$d_{31} = d'_{31} + j d''_{31} \quad (3)$$

$$\epsilon_{33} = \epsilon'_{33} + j \epsilon''_{33} \quad (4)$$

The complex admittance equation is then solved by the method described by Smits and latter by Damjanovic. This method involves an iterative calculation using an initial guess of the elastic constant and three values of the admittance near resonance.

RESULTS

(1) Hysteresis:

A summary of hysteresis data can be found in figure 3. this shows the room temperature AF - FE transition occurs between compositions (93.2/0) and (92/0). It also shows that the remanent polarization increases with increasing mol% PT for example the net remanent polarization increases from 0 to 30 to 38 $\mu\text{C}/\text{cm}^2$ as the composition of PT is increased in the series (93.5/0), (93.5/2.6) to (93.5/3.9). Low coercive fields on the order of 10 kV/cm have also been found in all the compositions measured. It is also interesting to note that increasing the concentration of PZN enhances the "squareness" of the Hysteresis loop (not shown here) which may have several device applications.

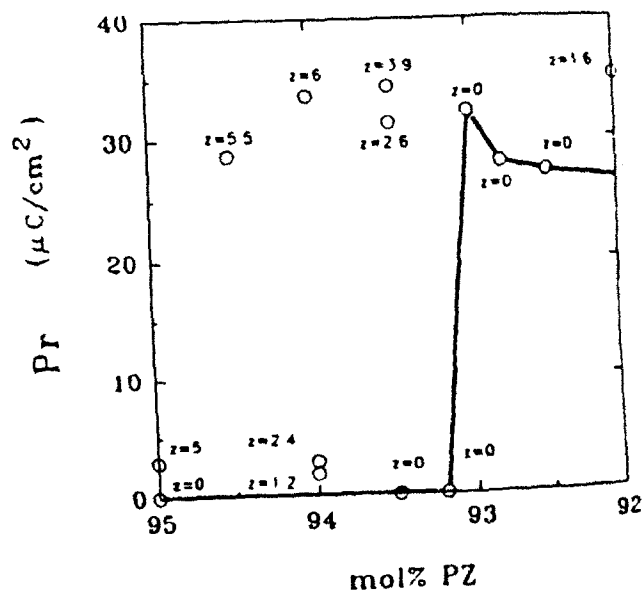


Figure 3: Room temperature remnant polarization data plotted versus mol% PZ. The line indicates the room temperature antiferroelectric to ferroelectric phase boundary. (z=mol% PT)

(2) Dielectric Study:

Figure 5 shows the average maximum dielectric constant at the Curie temperature (T_c) from heating and cooling cycles as a function of mol% PZ. Maximum dielectric constant decreases as the concentration of PZN is increased. Also, as expected, increasing the concentration of PT increases the maximum dielectric constant at T_c . The variation in T_c with mol% PZ can be seen in figure 4. This, for example, shows an increase of 10°C between PZNT(93.5/2.6) and PZNT(93.5/3.9) which is an increase in PT of 1.3 mol%.

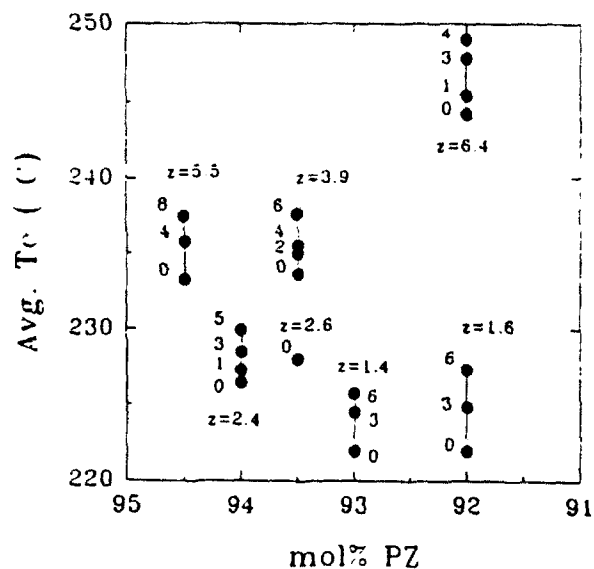


Figure 4: Average T_c at kHz. Superscripts indicate the applied bias in kV/cm. ($z = \text{mol\%PT}$)

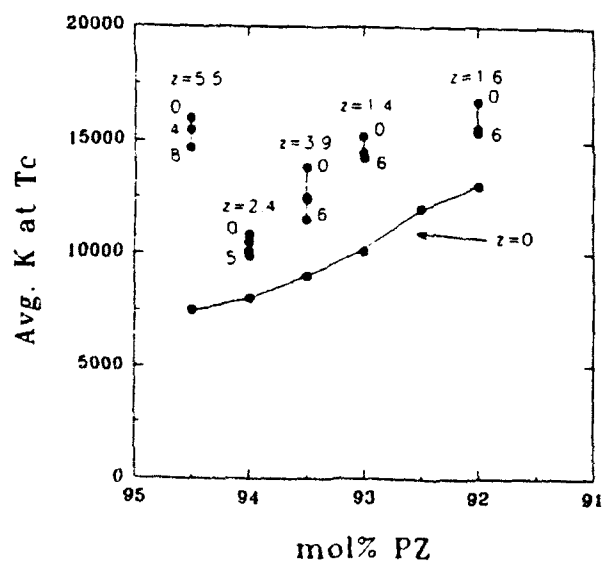


Figure 5: Average maximum dielectric constant at T_c measured at 1 kHz. Superscripts indicate applied bias in kV/cm. ($z = \text{mol\%PT}$)

The influence of DC bias is also demonstrated in figures 4 and 5. The average dielectric constant at T_c for PZNT(93.5/2.6) can be seen to increase from 234 at 0 kV/cm to 238 at 6 kV/cm. The bias field also causes a shift in T_c which can be seen in figure 4. This shows the increase in T_c for various compositions in the PZNT as the bias field on each sample is increased.

The dielectric constant has been found to have only a minute dependence on frequency. However, it has a thermal hysteresis when comparing heating and cooling cycles, especially at the lower temperature FE-FE transition (figure 6).

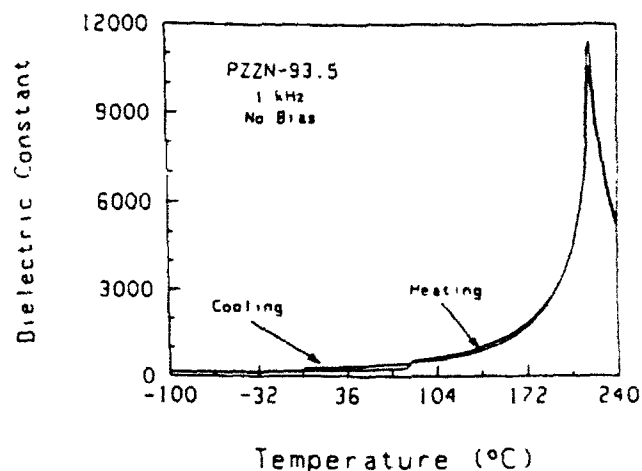


Figure 6: Dielectric constant for PZNT-93.5 measured at 1 kHz with an no applied bias. Note the large thermal hysteresis in the lower temperature AF-FE phase transition.

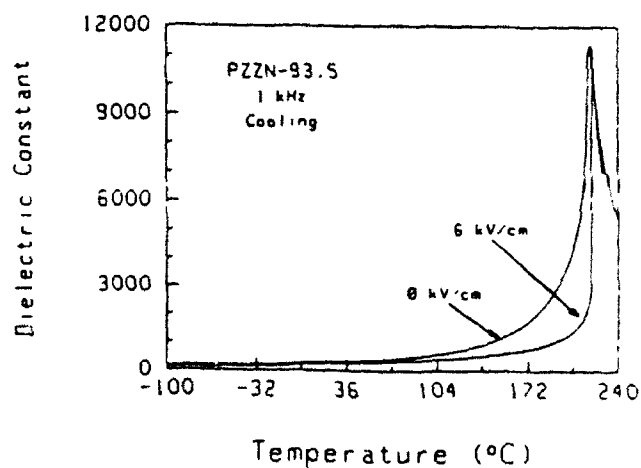


Figure 7: Dielectric constant for PZNT-93.5 measured at 1 kHz with an applied bias of 0 kV/cm and 6 kV/cm.

(3) Piezoelectric Study:

Figures 8 and 9 show the dependence of the room temperature real piezoelectric coefficient, d_{31} , and elastic coefficient, s'_{11} , on the applied electric field. The zero field d_{31} coefficient was measured using a Berlincourt d_{31} meter and was found to be approximately 50 to 60 pC/N for all samples just after poling. d'_{31} and d''_{31} both show approximately linear behavior even in the room temperature AF compositions. This could be due to a field forced AF-FE transition during the poling process, which was conducted at $\sim 100^\circ\text{C}$ with 15 kV/cm applied for 10 minutes then cooled, with the field still applied, to 25°C . It is interesting to compare figure 4 and figure 8. PZZN(93.5) when poled at room temperature is not FE, as indicated in figure 4. However, when poled at 100°C (figure 8) the sample is FE. This seems to be clear evidence that the FE phase is metastable at room temperature in the antiferroelectric compositions.

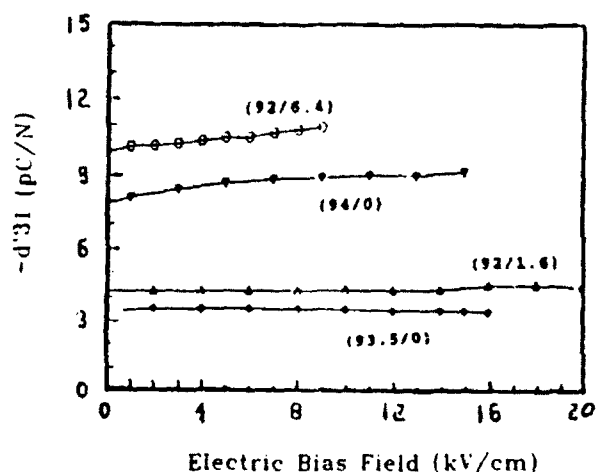


Figure 8: Real piezoelectric coefficient, d'_{31} , as a function of electrical bias field for various PZNT compositions. (All samples poled at 100°C .)

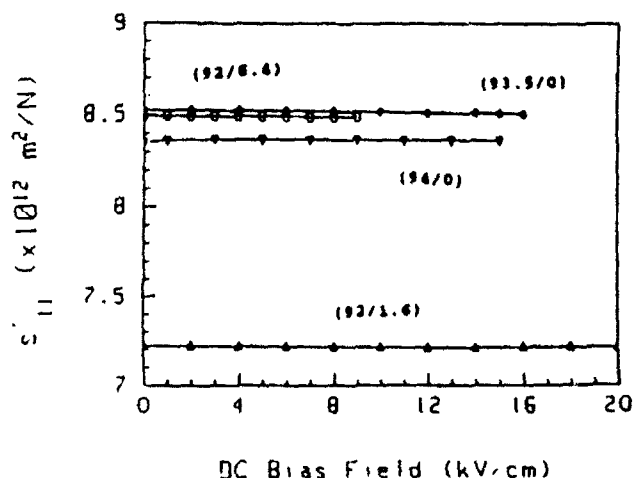


Figure 9: Real elastic coefficient, s'_{11} , as a function of electrical bias field for various PZNT compositions.

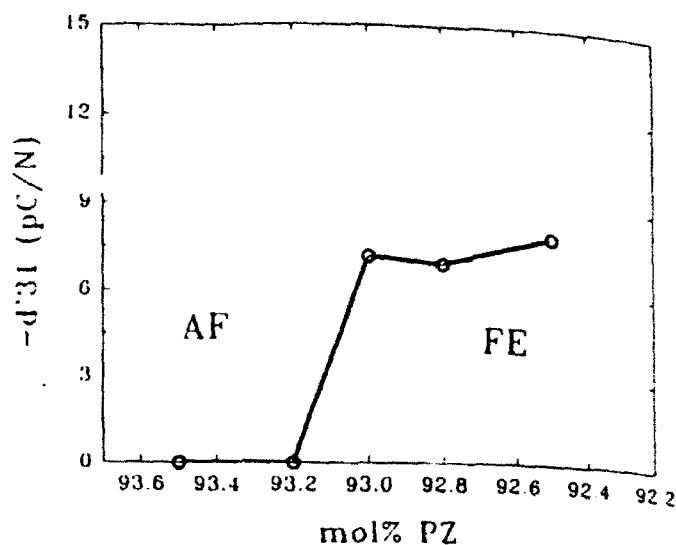


Figure 10: Real piezoelectric coefficient, d'_{31} , as a function of mol% PZ. This indicates the room temperature AF-FE phase boundary is between $x=93.0\%$ and $x=93.2\%$ PZ.

To determine the position of the AF-FE boundary above room temperature the samples were thermally depoled and then poled various temperatures. After the samples were poled their resonant behavior was observed, if none was found the process was repeated at a slightly higher temperature. By this method the AF-FE boundary was located.

The coupling coefficient k_{31} shows a slight increase for the compositions studied. The response is still, however, quite linear with values between 2% and 8%. Dielectric and piezoelectric loss were found to be between 2% and 10%. Mechanical loss was independent of field with a value of 0.3% to 0.5%.

Measurements were completed on PZZN compositions of $x = 92.5, 92.8, 93.0, 93.2$, and 93.5 mol% PZ. From a combination of these data the phase diagram of the PZZN system has been refined. This diagram (figure 11) pinpoints the AF-FE phase transition at room temperature to be between PZZN(93.2) and PZZN(93.0). The paraelectric and ferroelectric low to high temperature phase transition temperature data was obtained from dielectric anomalies and averaged between heating and cooling cycles of $5^\circ\text{C}/\text{min}$. Resonance and hysteresis data was then used to determine the AF-FE boundary.

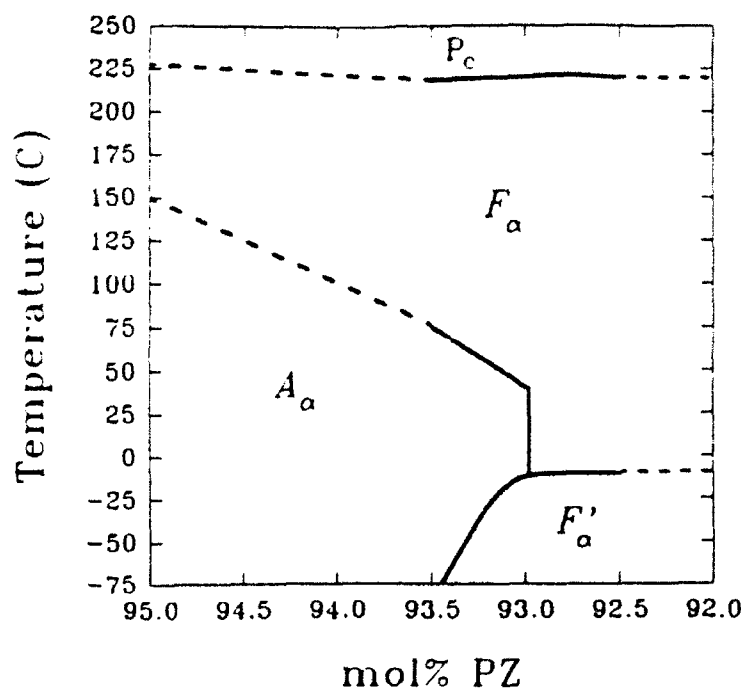


Figure 11: Experimentally determined PZZN phase diagram.

CONCLUSIONS

Various compositions in the PZNT system have been studied to find their weak field piezoelectric and dielectric response at room temperature. Some of the conclusions that have been made are:

(a) Hysteresis results indicate that the location of the AF-FE boundary is between $x = 92.8\%$ and $x = 93.2\%$ PZ. Large values of P_r ($\sim 30 \mu\text{C}/\text{cm}^2$) and low values of E_c ($\sim 10 \text{ kV}/\text{cm}$) for $x < 92.8\%$ PZ have been obtained. Also, with decreasing PZ concentrations hysteresis loops become increasingly square in nature.

(b) Room temperature dielectric constants near 250 have been measured and can be altered with suitable compositional adjustments. Large hysteresis in heating and cooling cycles has been displayed, especially in the low to high temperature rhombohedral phase transition. Curie temperatures near 225°C have been found to decrease with both increasing bias field and increasing concentrations of PT.

(c) Piezoelectric coefficient d_{31} at 25°C was found to be approximately $-10 \text{ pC}/\text{N}$ and linear with electrical bias fields of up to $15 \text{ kV}/\text{cm}$. The real elastic coefficient s'_{11} was found to be $\sim 8.5 \times 10^{-10} \text{ m}^2/\text{N}$ and constant for electric bias fields of up to $20 \text{ kV}/\text{cm}$. The piezoelectric coupling coefficient k_{31} was found to be between 2% and 8%.

(d) The PZZN phase diagram has been refined to show the AF-FE boundary at room temperature to be between PZZN(93.2) and PZZN(93.0). Also, after poling at elevated temperature, the ferroelectric phase has been shown to be stable when cooled to room temperature.

REFERENCES

- [1] R.E. Newnham, Q.C. Xu, S. Kumar and L.E. Cross, Smart Ceramics from Smart Materials, Structures, and Mathematical Issues, Ed. by C.A. Rogers, Lancaster: Technomic Publishing Co. Inc., 1989.
- [2] D.J. Taylor, Ph.D. Thesis, The Pennsylvania State University, 1992.
- [3] Takenaka, A.S. Bhalla and L.E. Cross, "Dielectric, Piezoelectric and Pyroelectric Properties of Lead Zirconate-Lead Zinc Niobate Ceramics," J. Am. Ceram. Soc., 72 [6] 1016-23, 1989.
- [4] D. Damjanovic, Ph.D. Thesis, The Pennsylvania State University 1987.
- [5] E.F. Alberta, D.J. Taylor and A.S. Bhalla, "The DC Field Dependence of the Piezoelectric, Elastic and Dielectric Coefficients of a Lead Zirconate-Based Ceramic," presented at the Amer. Ceram. Soc. 92nd Annual Meeting, Minneapolis, Minn., April 12-16, 1992.

APPENDIX 12

The Ratio of Rhombohedral and Tetragonal Phases on the Morphotropic Phase Boundary in Lead Zirconate Titanate

Wenwu CAO and L. Eric CROSS

Materials Research Laboratory, The Pennsylvania State University,
University Park, PA 16802, U.S.A.

(Received November 13, 1991; accepted for publication March 7, 1992)

A method is introduced to determine the statistical distribution of energetically degenerate but geometrically inequivalent states in a temperature induced phase transition in solids. The method has been employed to calculate the ratio of the rhombohedral and tetragonal phases in the $\text{Pb}(\text{Zr}, \text{Ti}_{1-x})\text{O}_3$ solid solution of the morphotropic phase boundary (MPB) composition. Our results indicate that the MPB determined by Jaffe, Cook and Jaffe [*Piezoelectric Ceramics* (Academic Press, London, 1971) p. 136] from structural measurements should be shifted to the rhombohedral side, which is more consistent with the MPB determined from dielectric measurements.

KEYWORDS: ferroelectric ceramic, PZT, lead zirconate titanate, morphotropic phase boundary

A phase diagram representing the subsolidus phase relations in the system $\text{PbZrO}_3\text{--PbTiO}_3$ taken from the book by Jaffe, Cook and Jaffe¹⁾ is given in Fig. 1. The system contains the well known solid solution series $\text{Pb}(\text{Zr}_x\text{Ti}_{1-x})\text{O}_3$ (PZT) which exhibits a variety of phase changes. In this system the most interesting compositions are for those on or near the so-called morphotropic phase boundary (MPB) (see the nearly vertical line on Fig. 1). PZTs in this compositional region have superior piezoelectric properties and are the primary materials currently used in most piezoelectric transducers and actuators. As shown in Fig. 1 the ferroelectric phase is rhombohedral on the left-hand side and tetragonal on the right-hand side of the MPB line, respectively (note: there should be a co-existence region of the two phases which is not shown in this phase diagram). The MPB in Fig. 1 as quoted from the book (Jaffe, Cook and Jaffe, p. 136) "is considered as that composition where the two phases are present in equal quantity".

The MPB drawn on a phase diagram is a composi-

tional boundary which is defined as the composition for which the free energies of two adjacent phases are equal. From thermodynamics, the free energy of a solid solution system depends on the following variables: temperature, pressure and composition. The compositional variable in the PZT case has a special property, it can only be directly accessed in certain temperature range. Out of that temperature range, the compositional variable can not be changed while keeping other variables fixed, as we know that a PZT solid solution can not be formed at room temperature. In order to change the composition at room temperature, one has to first heat up the system so that a single phase solid solution can be formed, then cool the system back down to room temperature after the new composition is formed. This special property of the compositional variable prevents direct thermodynamic analysis with this variable, and hence invalidates the transition hysteresis argument²⁾ in the explanation of the coexistence of two phases. Although the phase transition from the rhombohedral structure to the tetragonal structure must be of first order, it can not be realized while keeping the temperature unchanged, because the composition is not a directly accessible thermodynamic variable below a certain temperature limit. This is to say that we should address the temperature induced transition process in order to understand the effects of changing composition below a certain temperature limit.

There are two types of phase mixing: one is the mixing of phases of different chemical compositions and the other is the mixing of phases with different structures but identical chemical composition. At a first glance, it appears that the two problems seem to be similar, but they actually have quite different nature. The former reflects the law of mass conservation (obeying the lever rule), but the latter is actually a statistical distribution problem. It is the intention of this paper to provide a simple method dealing with the latter case.

From thermodynamic analyses, it is shown that the paraelectric-ferroelectric transition for compositions near the MPB is of second order within the experimental

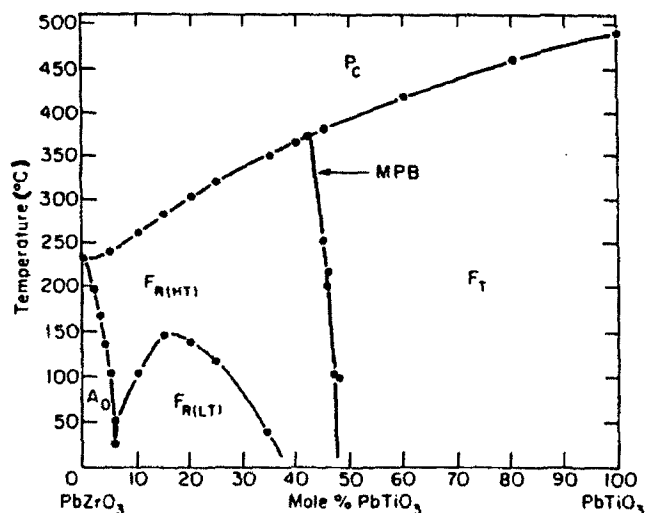


Fig. 1. Phase diagram of $\text{Pb}(\text{Zr}, \text{Ti}_{1-x})\text{O}_3$ [after Jaffe, Cook and Jaffe, ref. 1].

error," we therefore expect strong thermal fluctuations to occur near the transition temperature T_c . This thermal fluctuation is the sole driving force for the phase transition. For convenience we will work in the order parameter space. When the system is cooled down near T_c from the paraelectric phase, the magnitude of the thermal induced instant polarization $|P_{\text{inst}}|$ increases as the potential well around $P=0$ becomes flatter and flatter. Below T_c , the fluctuation is gradually frozen and the system acquires a new configurational state with a finite polarization. In a second order phase transition the transition process happens in a continuous fashion; but in a first order phase transition, a finite spontaneous polarization is obtained at the phase transition. The two cases are illustrated in Fig. 2 for a one-dimensional system, where the shaded area represents the level of thermal energy. In a one-dimensional system the number of allowed (two) orientations of the instant polarization is the same as that of the spontaneous polarization. But in two- and three-dimensional systems, there are no orientational constraints for thermal fluctuation (determined by the dimensionality of the problem only) although the magnitude of P_{inst} is regulated by the potential well around the origin. However, the allowed orientations for the spontaneous polarization P_0 are limited. The thick line and the solid dots in Fig. 3 illustrated this situation for a two-dimensional problem representing a square to rectangular ferroelectric phase transition. There are no orientational

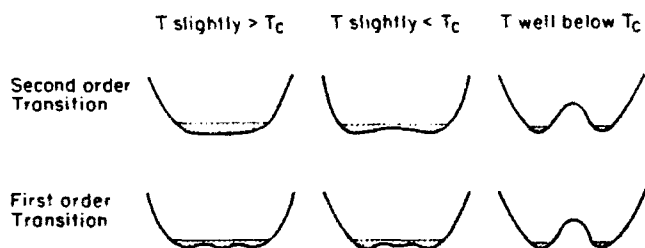


Fig. 2. Illustration of the potential wells and thermal fluctuations near the critical temperature T_c for both second and first order phase transitions in one dimension. The shaded areas represent thermal energy.

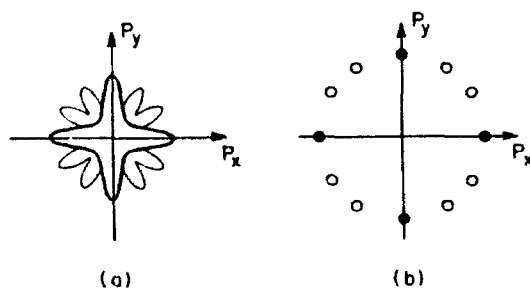


Fig. 3. Representation of fluctuating state and the ferroelectric states in order parameter space for a two-dimensional problem. (a) The thick and the thin lines are the profiles for the polarization fluctuations of the square-rectangular and square-oblique phase transitions, respectively, near T_c . (b) The solid dots are the degenerated rectangular ferroelectric states and the open circles are the degenerated oblique ferroelectric states, respectively, well below T_c .

constraints for P_{inst} in the fluctuating state [profile is represented by the thick line in Fig. 3(a)] but only four orientations for P_0 [solid dots in Fig. 3(b)] are allowed well below T_c .

The question we try to address in this paper is: what is the probability p_i for the system in Fig. 3(a) to become the i th low symmetry ferroelectric states in Fig. 3(b)? For the two-dimensional problem mentioned above, the answer $p_i = 1/4$ may be obtained intuitively since the four low-temperature rectangle states are completely equivalent, i.e., these states are energetically degenerate and structurally identical. But in more general situations, intuition fails to provide an answer, for instance, the case shown in Fig. 3 where the energetically degenerated rectangle (solid dots) and the oblique (open circle) states are structurally different. In this case we need to follow a well-defined mathematical method to calculate these probabilities. Such a calculation is particularly useful for the study of PZT system, because at the MPB we have precisely such a situation, i.e., the tetragonal and rhombohedral phases are energetically degenerate.

It is obvious that the probability calculation is only meaningful in the fluctuating state. After the system being frozen into one of the low temperature states, thermal energy is no more effective to carry the system from one configuration to another. Our calculation is based on the following assumption:

The instant polarization P_{inst} is orientationally ergodic in the fluctuating state near T_c .

In other words, we assume that the thermal motion has no orientational preference, although as shown in Fig. 3, the magnitude $|P_{\text{inst}}|$ is regulated by the potential configuration and is a function of direction and temperature. An immediate inference from the assumption is that the average total polarization of the system is zero in the fluctuating state, or more concisely, $\langle P_{\text{inst}} \rangle = 0$ but $\langle P_{\text{inst}}^2 \rangle \neq 0$.

Now we try to correlate this thermal fluctuation with the transition probabilities to different structural phases. The assumption tells us that the trigger from the surrounding thermal bath is isotropic, but the actual structural change resulting from the trigger depends on the potential energy configuration. Because only a few isolated orientations for P_0 are allowed below T_c in the order parameter space, we expect that all P_{inst} oriented in the vicinity of an allowed polarization direction can potentially develop into that final polarization state. Hence we can assign each allowed polarization state an effective solid angle Ω_i in a three-dimensional order parameter space, the probability p_i of that state being formed under the trigger of thermal fluctuation is represented by $\Omega_i/(4\pi)$, where 4π is the normalization constant.

The next task is to define the boundaries of these solid angles. Imagine we apply a small dc field E to lift the degeneracy of the system. Under this field the system will be forced to develop into one of the allowed low temperature states whose polarization vector has the smallest possible angle with the applied electric field. If this field is applied to the system from another angle, it can either in-

duce the same polarization state or a different state depending on whether or not the field is still oriented inside the effective solid angle of that state. Considering at a temperature slightly below T_c , there are two adjacent energetically degenerate states represented by P_a and P_b respectively, in the order parameter space (P_a and P_b form an angle Φ), the boundary of the two effective solid angles for these polarization states may be defined by

$$E \cdot P_a = E \cdot P_b \quad (1)$$

Taking the coordinate systems as shown in Fig. 4 we can write eq. (1) in the following form,

$$P_a \cos \phi = P_b \cos (\Phi - \phi). \quad (2)$$

Interestingly, the magnitude of the electric field has dropped out in eq. (2), hence if we take the limit $E \rightarrow 0$, the result in eq. (2) will still hold.

In reality, the problems of interest are those cases for which $P_a = P_b$, therefore, eq. (2) can be further simplified to

$$\phi = \Phi / 2. \quad (3)$$

Equation (3) states that the boundary of two effective solid angles is a plane in the order parameter space passing through the bisector of the angle Φ and perpendicular to the plane containing P_a and P_b . If there exist more than two degenerate states, a boundary may be defined for each pair of adjacent effective solid angles using eqs. (2) or (3).

After the boundaries are defined, the remaining task becomes straightforward. We draw a polyhedron in the order parameter space surrounding the origin, whose edges are on the solid angle boundaries defined by eq. (3). For a PZT of MPB composition, the degenerated ferroelectric states include both rhombohedral and tetragonal phases. Assuming for the simplest case that $P_T = P_R = a$, then the corresponding polyhedron is shown in Fig. 5. The solid angle calculation can be written in terms of a surface integral on each of the corresponding surface which subtends that solid angle, for example

$$\Omega_{\text{OHIJK}} = \iint_{\text{OHIJK}} \frac{a \, ds}{(r^2 + a^2)^{3/2}} = 4 \int_0^b \int_0^b \frac{a \, dx \, dy}{(x^2 + y^2 + a^2)^{3/2}}, \quad (5)$$

$$b = \frac{\sqrt{3}-1}{\sqrt{2}} a;$$

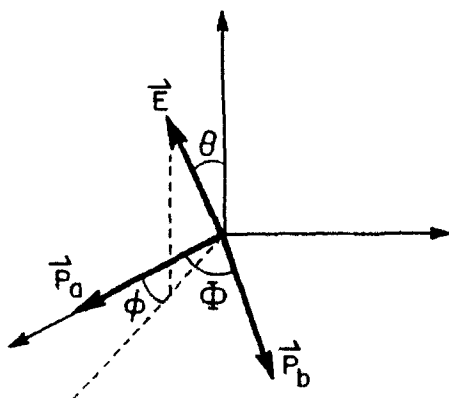


Fig. 4. Coordinate system used in the calculations of eqs. (2) and (3).

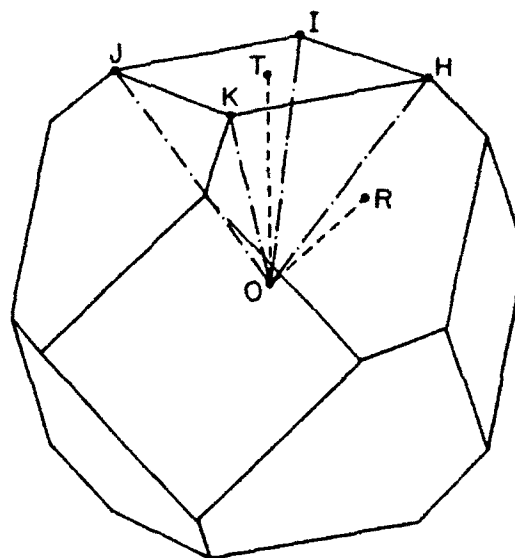


Fig. 5. The probability distribution polyhedron for PZT of the MPB composition, $OT = OR$. The solid angle subtended by the surface IJKH with respect to the origin O divided by 4π represents the probability of the system being transformed into $(00P_a)$ state.

where ds is the area element on the surface $\square\text{HIJK}$ and r is the distance between ds and the center point T on that surface (Fig. 5). The integration of eq. (5) can be carried out to give an analytic solution

$$\Omega_{\text{OHIJK}} = 4 \arcsin \left(\frac{3 - \sqrt{3}}{6} \right). \quad (6)$$

From this result and the arguments given above we conclude that for PZT of the MPB composition, the probability ratio for a system to be frozen into rhombohedral and tetragonal phases from the fluctuating state is given by

$$\frac{\text{Rhombohedral}}{\text{Tetragonal}} = \frac{1 - 6\Omega_{\text{OHIJK}}/4\pi}{6\Omega_{\text{OHIJK}}/4\pi} = \frac{\pi - 6 \arcsin \left(\frac{3 - \sqrt{3}}{6} \right)}{6 \arcsin \left(\frac{3 - \sqrt{3}}{6} \right)} \approx 1.459 \approx 3:2 \quad (7)$$

A ceramic system may be treated as an ensemble of domains, and each domain can be considered to be the system we have discussed above. Then, eq. (7) represents the molar ratio of the rhombohedral and tetragonal phases for a PZT ceramic of the MPB composition. This molar ratio can be calculated directly from X-ray diffraction intensities, therefore eq. (7) provides a criterion for the determination of the MPB.

Thermodynamics tells us that maximum values of many physical quantities should appear at the MPB composition due to the existence of maximum number of energetically degenerated states. However, several experimental results reveal that these maxima do not match with the MPB on Fig. 1 but often slightly deviate to the rhombohedral side.^{4,5)} Our analysis above gives a reasonable explanation to this controversy. Naturally, if we use the ratio of 3:2 instead of 1:1 as the criterion for

the MPB, the MPB line on Fig. 1 would shift to the rhombohedral side.

The novel idea presented in this paper is to take into account the geometrical constraints in the calculation of the statistical distributions of those energetically degenerated states in solids. Through this paper we also intend to bring people's attention on treating solid systems, those thermodynamic theories developed for gas and liquid systems may not be valid and should be augmented to incorporate the characteristics of solids.

Finally, we like to point out that a special property pertaining to this problem has been used implicitly, i.e., the homotopy mapping between the real space and the order parameter space. Strictly speaking, thermal motion occurs in real space not in order parameter space. But because the order parameter is a vector in our problem, there is a one point to one point mapping between the

real space and the order parameter space, therefore we did not emphasize the difference between the two spaces in the text. However, if the order parameter is not a vector, one can not use the theory developed in this paper.

One of the authors (W.C.) wishes to thank Drs. M. Grutzeck and A. Saxena for helpful comments. This research was supported by Air Force Office of Scientific Research under Grant No. AFOSR-91-0433.

References

- 1) B. Jaffe, W. R. Cook and H. Jaffe: *Piezoelectric Ceramics* (Academic Press, London, 1971) p. 136.
- 2) V. A. Isupov: *Fiz. Tver. Tela* **12** (1970) 1380. Translation: *Sov. Phys.-Solid State* **12** (1970) 1084.
- 3) M. J. Haun, F. Furman, H. A. McKinstry and L. E. Cross: *Ferroelectrics* **99** (1989) 27.
- 4) W. Wersing: *Ferroelectrics* **7** (1974) 163.
- 5) K. Carl and K. H. Hardtl: *Phys. Status Solidi a* **8** (1971) 87.

APPENDIX 13



A TRANSMISSION ELECTRON MICROSCOPY INVESTIGATION OF THE R3m - R3c PHASE TRANSITION IN $\text{Pb}(\text{Zr,Ti})\text{O}_3$ CERAMICS

C.A. Randall, M.G. Matsko, W. Cao, and A.S. Bhalla
Materials Research Laboratory
The Pennsylvania State University
University Park, PA 16802, USA

(Received 28 September 1992 by A. Pinczuk)

A transmission electron microscopy (TEM) study was performed on $\text{Pb}(\text{Zr,Ti})\text{O}_3$ compositions within the R3m - R3c phase region. The low temperature phase is owing to a displacive phase transition involving oxygen octahedral tilts. The associated superlattice reflections as a result of the tilt are detectable by electron diffraction. Dark Field diffraction contrast imaging of the superlattice reflections reveals antiphase boundaries (APB) associated with the octahedral tilt domains. Interaction between the octahedral tilt antiphase boundaries and the ferroelectric domain structures of the R3c phase is studied and discussed.

1 - Introduction

The perovskite solid-solution between end-member PbTiO_3 and PbZrO_3 is the basis of important technological ceramics used in the piezoelectric, pyroelectric and electro-optic devices.¹⁻³ The phase diagram of PbTiO_3 - PbZrO_3 is illustrated in Figure 1. The phase diagram contains a variety of regions of displacive phase transitions and there are antiferroelectric and several ferroelectric phases in the low temperature regime. Compositions between Zr/Ti ratios 90/10 and 65/35 reveals a ferroelectric - ferroelectric transition between rhombohedral space groups R3m -> R3c. This transition involves the oxygen octahedra tilt about the $\langle 111 \rangle$ directions.⁴ The aim of this investigation is to study the inter-relationship between octahedral tilt domain structures and the high temperature ferroelectric domain structures. There have been virtually no studies regarding the domain structures of octahedral tilt systems in perovskites.⁵ The transmission electron microscope offers an attractive means to study this subtle phenomena owing to electron scattering factors for oxygen being much larger than the corresponding x-ray scattering factors. The diffraction contrast imaging also allows a direct means to study the domain states and their interactions with the ceramic microstructure.⁶

2 - Experimental

Ceramic samples of $\text{Pb}(\text{Zr,Ti})\text{O}_3$ were prepared using the conventional solid-state sintering techniques. The starting raw material powders, PbO , ZrO_2 , and TiO_2 , were of analytical grade quality. Two compositions were made for this study $\text{Pb}(\text{Zr}_{0.9}\text{Ti}_{0.1})\text{O}_3$ and $\text{Pb}(\text{Zr}_{0.65}\text{Ti}_{0.35})\text{O}_3$. These compositions were batched according to the stoi-

chiometric ratios and taking into account the loss of ignitions. The raw powders were ball milled with ethanol solvent for 48 hours for complete mixing. Perovskite phases were fully formed after calcining for four hours at 900°C, as determined by X-ray diffraction studies. The calcined powder was ball milled for 24 hours. Binder and 1 wt% excess PbO was added to 80 mesh sieved powders. Green pellets with 60% theoretical density were formed using uniaxial pressure followed by binder burnout at 550°C for 1 hour. Sintering was undertaken at 1250°C for 2 hours to form pellets with 91-94% theoretical density and with less than 1% weight loss.

TEM samples were made by grinding and polishing ceramics to a thickness = 50 μm . These

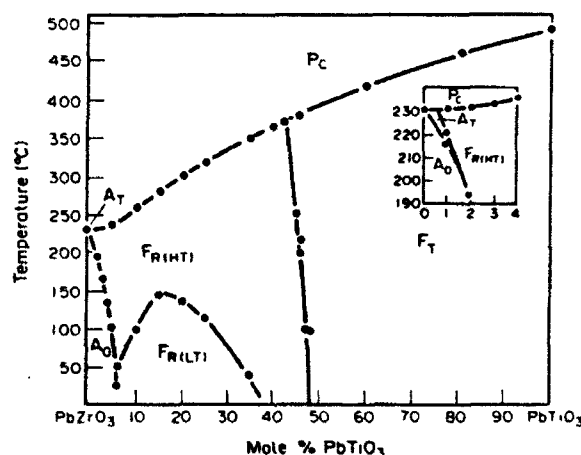


Fig. 1. The PbZrO_3 and PbTiO_3 phase diagram [Jaffe, Cook, Jaffe (1971)].

sections were mounted on 3 mm copper grids using Devcon 5-minute epoxy. Ion beam thinning was performed at 10° with argon ion beams accelerated to 4 KV and a beam current ≈ 1 mA. TEM observations were made using a Philips 420 STEM at 100 KV. A Gatan liquid nitrogen two-tilt stage was used to make in situ TEM observations between 80°C to -180°C .

3 - Results

Figures 2(a) and (b) show the $[110]$ zone axis diffraction patterns revealing $(h+1/2, k+1/2, l+1/2)$ pseudo cubic superlattice reflections in $\text{Pb}(\text{Zr}_{0.9}\text{Ti}_{0.1})\text{O}_3$ and $\text{Pb}(\text{Zr}_{0.65}\text{Ti}_{0.35})\text{O}_3$ respectively. It is found that by heating the $\text{Pb}(\text{Zr}_{0.65}\text{Ti}_{0.35})\text{O}_3$ sample to 80°C the superlattice reflections disappear, figure 2(c), and conversely cooling to lower temperatures with the Gatan liquid nitrogen stage the intensity of the diffrac-

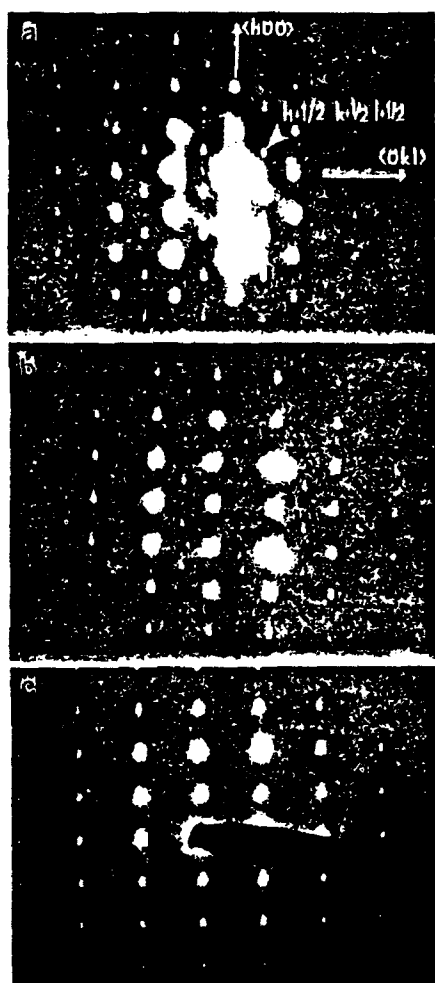


Fig. 2. $[110]$ Zone axis diffraction patterns (a) $\text{Pb}(\text{Zr}_{0.9}\text{Ti}_{0.1})\text{O}_3$, (b) $\text{Pb}(\text{Zr}_{0.65}\text{Ti}_{0.35})\text{O}_3$, both at room temperature, and (c) $\text{Pb}(\text{Zr}_{0.65}\text{Ti}_{0.35})\text{O}_3$ at 80°C .

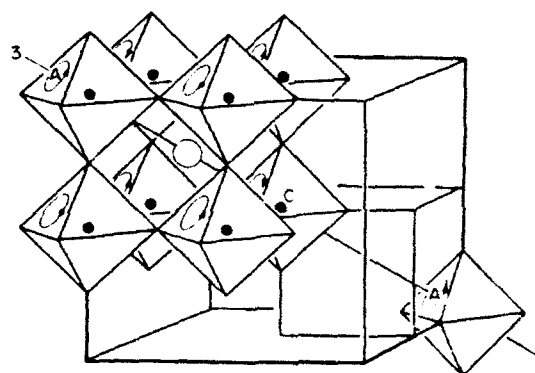


Fig. 3. Schematic representation of the oxygen octahedral-tilting in $R3c$ phase.

tion spots increases. This suggests that these reflections are, therefore, associated with a displacive phase transition in the material. The $(h+1/2, k+1/2, l+1/2)$ diffractions are consistent with the neutron diffraction study performed by

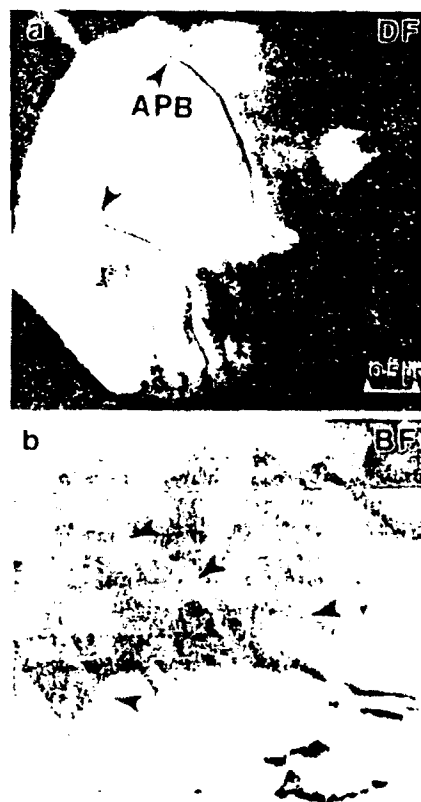


Fig. 4. (a) Dark field image of octahedral-tilt superlattice reflection revealing antiphase boundaries (APB); (b) multiple bright field image of same area revealing typical 180° domain wall contrast.

Glazer.⁴ Glazer predicted the origin of this superlattice to be oxygen octahedral tilts within the simple perovskite structure. The oxygen octahedral shifts with equal components about the pseudo-cubic perovskite axis as to give an effective clockwise and anticlockwise rotation of oxygen octahedra about the $\langle 111 \rangle$ directions parallel to the ferroelectric dipole displacements of the R3m phase, Figure 4.

Figure 4(a) shows the dark field diffraction contrast image associated with the superlattice reflection in a $\text{Pb}(\text{Zr}_{0.9}\text{Ti}_{0.1})\text{O}_3$ subgrain. A dark ribbon-like boundary is observed under these imaging conditions, and this is believed to be a wall separating out-of-phase octahedral tilt variants. Figure 4(b) shows the same subgrain imaged under a multiple beam bright field spatial perturbation between the 180° ferroelectric domain walls and the octahedral antiphase boundaries.

Figure 5(a) shows a bright field image which reveals ferroelectric twin structures and inversion 180° ferroelectric domains in a rhombohedral ferroelectrics.⁷ Figure 5(b) shows the same crystallite imaged in dark field with a superlattice reflection. The antiphase boundary contrast is again observed and shows a strong interaction with the twin boundaries, generally was found antiphase boundaries are terminated on the twin boundaries, grain boundaries, or alternatively contained within the closed loops. The antiphase boundaries in the $\text{Pb}(\text{Zr,Ti})\text{O}_3$ ceramics predominantly terminates on either twin boundaries or grain boundaries. Region X in Figure 5(b) shows an example of the antiphase boundary terminating at a $\{110\}$ twin domain region and Y shows an antiphase boundary coincident with a $\{001\}$ domain wall.

4 - Discussion

From the above results we can infer that the R3m ferroelectric phase has only twin and inversion domains. Twin domains being 109° or 71° type and twin on habit planes $\{110\}$ and $\{100\}$, respectively. These observations are consistent with earlier observations on modified rhombohedral $\text{Pb}(\text{Zr,Ti})\text{O}_3$ ceramics.⁸ The octahedral tilt transition is driven by a zone boundary soft mode resulting in the doubling of the unit cell. This transition gives rise to two additional variants which are separate from each other with antiphase boundaries. The antiphase boundaries are slightly perturbed by 180° domain walls and are strongly perturbed by the twin boundaries. In some incidents we noted that the antiphase boundaries were joined with the walls in which case it may imply that a coupling between the gradients of the tilt and the polarization may be present.

Acknowledgements

This research was supported by Air Force Office of Scientific Research under Grant No. AFOSR-91-0433 and by Office of Naval Research under Grant No. N00014-92-J-1510. We also wish to thank Dr. Ian Reany for many discussions during his work and also JoAnn Mautz for typing this manuscript.

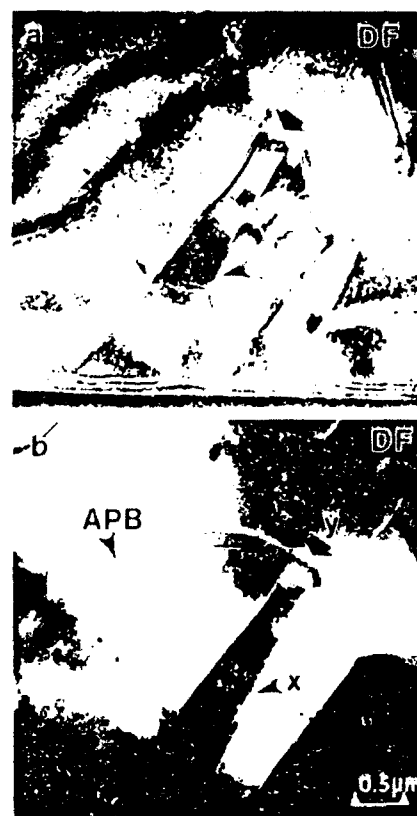


Fig. 5. (a) Dark field image of ferroelectric domain walls; (b) Dark field image of superlattice reflection revealing interaction of APBs with twin domain walls.

References

1. B. Jaffe, W.R. Cook, and H. Jaffe, *Piezoelectric Ceramics*, Academic Press, London, New York (1971).
2. M.E. Lines and A.M. Glass, *Principles and Applications of ferroelectrics and Related Methods*, Clarendon Press, Oxford (1977).
3. A. Moulson and S. Herbert, *Electroceramics: Materials-Properties-Applications*, Chapman and Hall, London, New York, Tokyo, Melbourne, Madras.
4. A.M. Glazer, *Acta Cryst.* **A31**, 756-762 (1975).
5. E.L. Colla, I.M. Reaney, and N. Setter, European Conference on the Applications of Polar Dielectrics, Conf. Proc. In press, (1992).
6. P.B. Hirsch, A. Howie, R.B. Nicholson, D.W. Pashley, and M.J. Whelan, *Electron Microscopy of Thin Crystals*, Butterworth, London (1977).
7. I.M. Reaney, Private Communication.
8. C.A. Randall, D.J. Barber, and R.W. Whatmore, *J. Mat. Sci.* **22** 935 (1987).

APPENDIX 14

90° - Domain Reversal in $\text{Pb}(\text{Zr}_x\text{Ti}_{1-x})\text{O}_3$ Ceramics

Shaoping Li*, Chi-Yuen Huang**, A.S. Bhalla*, L.E. Cross*

* Materials Research Laboratory, The Pennsylvania State University, University Park, PA 16802

** Department of Mineral Engineering, National Cheng Kung University, Tainan, Taiwan, 70101

Abstract

In this study, a simple and direct method has been proposed, which allows to be used for quantitatively distinguishing the mechanisms of domain reorientation processes in polycrystalline materials. By using this method, the 90°-domain reorientation in the $\text{Pb}(\text{Zr}_x\text{Ti}_{1-x})$ ceramic under the electric field was examined through the X-ray diffraction analysis. It was found that the polarization switching in the PZT ceramic with the composition near the morphotropic phase boundary is predominantly controlled by the two successive 90° domain processes rather than 180° domain wall reversal. Experimental results also indicate that the coercive field of the ceramics is related to the cooperative deformation associated with each grain, which arises from 90°-domain reversal process.

1. Introduction

The interrelationship between the dynamic behaviors and the microstructures (intrinsic domain structures) of ferroelectric ceramics is of great significance. The investigation of polarization reversal in ferroelectric ceramics is of both theoretical and practical interest. Recently, a lot of efforts have been put into developing polycrystalline ferroelectric thin films as non-volatile memory devices using the capability of switching the direction of remnant polarization under the influence of an electric impulse. In fact, the polarization reorientation processes are intimately associated with the basic dynamic memory capability and the switching threshold of polycrystalline thin film memory devices, as well as the basic fatigue and degradation behavior of thin film devices. With regard to this, the mechanisms of the domain reversals in PZT polycrystalline systems have a special and important aspect.

Early investigations for the dynamical behavior of 90° type domain walls (90° in tetragonal, 71° and 109° in the rhombohedral phase) and 180° domain walls in PZT ceramics have been carried out in the past three decades [1-6]. Based on the bias dependence measurements of dielectric constants, polarization, and spontaneous strain in certain PLZT ceramic systems, it has been suggested that the processes of polarization reversal may be characterized by two successive 90° type domain processes rather than by the direct 180° domain switching processes. Apparently, all previous research results seemed to be adequate, however, they are by no means quantitatively conclusive because no any direct experimental methods could distinguish the mechanisms of the polarization reversal processes in the polycrystalline materials.

In general, the mechanism of polarization reversal processes in single crystals is explained by the nucleation and growth of new antiparallel domains. Ferroelectric ceramics consists of many randomly orientated grains. Therefore, the polarization reversal mechanism and switching behavior in ferroelectric polycrystalline materials is rather complicated and depends upon many conditions [7]. Usually, the polarization reversal processes in ferroelectric polycrystalline materials is substantially different from those in single crystals. In this work, a simple and direct method has been proposed, which can be used for quantitatively

distinguishing the mechanisms of domain reorientation processes in polycrystalline materials. It has been directly confirmed that the polarization switching processes in PZT ceramic with the composition within the morphotropic phase boundary is predominantly dependent upon two successive 90° domain reversal processes.

II. Experimental Procedure

The specimens used here are of chemical composition $\text{Pb}(\text{Zr}_{0.52}\text{Ti}_{0.48})\text{O}_3 + 0.5 \text{ wt. \% Nb}_2\text{O}_5$, which is within the morphotropic phase boundary. The ceramics were prepared by the conventional mixed-oxide process. The final sintering temperature is 1180 °C -- 1250 °C for 2-3 hrs. The scanning electron micrographs (Fig. 1) show the average grain size of the ceramic to be 3 μm - 3.5 μm . The domain structures can be clearly observed through the environmental scanning electron microscope without coating the samples [7].



Figure 1. The SEM micrographs of the PZT ceramic with the composition within the morphotropic phase boundary.

The samples were cut in the dimensions of (8mm \times 8mm \times {0.5 - 0.8 mm}) and electroded with gold for the dielectric and strain measurements. For the X-ray analysis measurements, the thin vacuum deposited silver electrodes were used on the faces exposed to the X-rays in order to reduce the extra-diffraction of the electrodes. Before making silver electrodes, the surfaces of the samples were polished and etched. X-ray diffraction measurements were performed on an automatic X-ray diffractometer using $\text{CuK}\alpha$

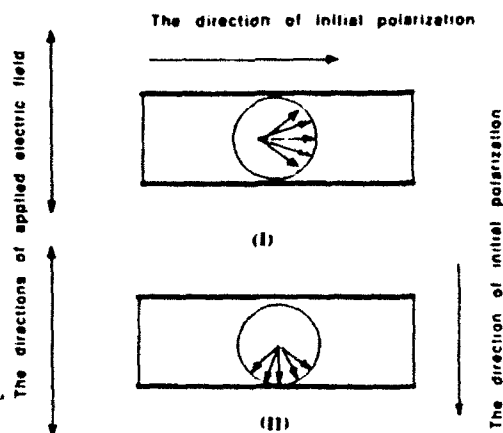


Figure 2. Shape and initial polarization orientation of specimens for two different cases.

(a) The initial direction of remnant polarization parallel to the surface of the plate sample.

(b) The initial direction of remnant polarization perpendicular to the surface of the plate sample.

radiation ($\lambda = 1.5418 \text{ \AA}$). The experimental data were processed with the software developed by the Materials Research Lab at Penn State. The X-ray patterns were recorded at a scan rate of $2\theta = 0.3^\circ \text{ min}^{-1}$. The low scanning rate was chosen in order to enhance the intensity of the diffraction. The ceramic specimens were initially poled in two different ways in accordance with the sample shape, as shown in Fig. 2. The depth of X-ray penetration in this PZT system is estimated to be $1 \mu\text{m}$.

III. Results and Discussions

3.1. Principle of X-ray analysis

It is well known that PZT ceramics contain many 90° and 180° domains. The electric field will force them move toward the direction favorable to the total system energy. According to Friedel's law, the reversal of 180° domains during the polarization process could not be detected by the X-ray diffraction method. Therefore, it is believed that the change of ratio $I(002)/I(200)$ is caused by the switching of 90° domain alone [8,9]. In general, the intensity of any (hkl) reflection, relative to that from a random specimen, is proportional to the volume fraction of domains having their (hkl) planes parallel to the plate surface. Regarding this study, the intensity of $I(002)$ reflection is proportional to the volume fraction of domain having the polarization direction parallel to the normal of surface of plate specimens.

Based on the general principle of X-ray diffraction, the diffractive intensity $I(hkl)$ for (hkl) plane can be usually expressed by [9]

$$I_{(hkl)} = C A I_0 L |F_{(hkl)}|^2 N_{(hkl)} p_{(hkl)} \quad (1)$$

where, I_0 stands for incident X-ray diffraction, L , Lorentz angle factor; $F(hkl)$, structure factor for (hkl) plane; $N(hkl)$, iterating factor; A , absorption factor and C is known as measuring system constant. Once the measuring conditions and specimens are defined, C can be calculated. $p(hkl)$ is the crystal plane orientation density which is defined as the volume fraction of the crystal grains with (hkl) plane parallel to specimen surface. Obviously, for a

specimen with the preferred orientation of the (hkl) plane, its $p(hkl)$ should be constant and can be taken as 1, therefore, one has

$$I_{p(hkl)} = C A I_0 L |F_{(hkl)}|^2 N_{(hkl)} \quad (1')$$

From the definition of diffraction intensity, it easily follows that the diffraction intensity for the (hkl) planes should be proportional to the volume fraction of domains (both 90° and 180° domains) in which the (hkl) planes are parallel to the surface of the plate specimens. Since there may be two possible kinds of domain reversal processes during the polarization switching, the measured $I(002)$ and $I(200)$ should contain the contributions of the planes (002) and (200) within both 90° reversal domains and 180° reversal domains, respectively, that is:

$$I(002) = n_1 [90^\circ] I_p(002) + n_2 [180^\circ] I_p(002) \quad (2)$$

$$I(200) = g_1 [90^\circ] I_p(200) + g_2 [180^\circ] I_p(200) \quad (3)$$

and,

$$n_1 + n_2 + g_1 + g_2 = 1$$

where, n_1 and n_2 are the 90° and 180° domain volume fractions, respectively, which have the (002) plane parallel to the surface of the plate specimens. g_1 and g_2 are the 90° and 180° domain volume fractions, respectively, which have the (200) plane parallel to the surface of the plate specimens. It should be noted that n_1 and g_1 are the function of applied electric field, whereas the n_2 and g_2 are always constants during the domain reversal processes. The domain volume ratio between the domains with the polarization direction perpendicular to the surface and those having the direction

of their polarizations parallel to the surface of the plate specimen could be expressed as follows:

$$R = K \frac{I(002)}{I(200)} \quad (4)$$

here, K is special coefficient. Since the change in diffraction intensities are only caused by 90° domains, the X-ray intensities of $I(002)/I(200)$ under the influence of the electric field could represent the characteristics of 90° domain reversal. The changing rate of $I(002)/I(200)$ may reveal some information about the mechanism of the domain reorientations.

In the following, we shall discuss two different cases of polarization reorientation to distinguish the polarization reorientation processes between 90° domain reversal and 180° domain reversal processes. It should be noted that in reality the domains can never be perfectly aligned. The distribution of polarization directions always obey the certain axial distribution, as shown in Fig. 3. The $I(002)$ and $I(200)$ are measured by their average values.

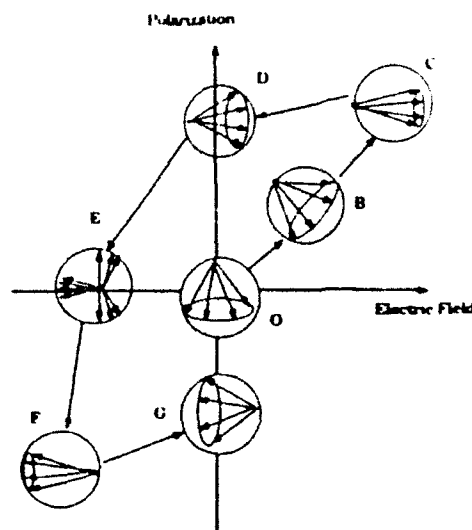


Figure 3 Two dimensional representation of the vector model showing the spatial distribution of domains at different stages of the polarization reversal.

The Case I

For the case I of Fig. 2, the initial directions of polarization in most domains are parallel to the surface of the plate specimen. If an electric field is applied to the direction normal to the surface of the plate specimen, the polarization reversal process will be expected to be following the model in Fig. 3. As the applied electric field increases, the direction of polarization will gradually be changed. With a sufficiently strong electric field, the polarization directions in the ceramic will change their distribution direction. Eventually, all polarization directions will be lined up nearly parallel to the plus direction shown at point C via the 90° domain wall reversal process. The intriguing feature is that in this process only 90° domain reorientation is involved and no 180° domain wall reversal process occur since the initial direction of polarization is perpendicular to the applied electric field. From eq (3) and eq (4), one obtains

$$R \Big|_{0 \rightarrow C} = \frac{I(002)}{I(200)} = \frac{n_1 [90^\circ] I_p(002)}{n_2 [90^\circ] I_p(200)} \quad (5)$$

and $n_1 + n_2 = 1$. Eq.(5) means that R is equal to the diffractive intensity ratio of $\{n_1[90^\circ] I_p(002) + n_2[90^\circ] I_p(200)\}$ within the unit volume of per 90° domain. It should be noted that, in general, the unit volume of per 90° domain is not necessarily equal to the unit volume of per domain if considering the coexistence of both 90° and 180° domains. From eq.(5), the changing rate of R as a function of electric field can be expressed as

$$\left. \frac{dR}{dE} \right|_{O \rightarrow C} = \frac{d\{n_1[90^\circ] I_p(002) + n_2[90^\circ] I_p(200)\}}{dE} \quad (6)$$

where R is the measured value of ratio $I(002)/I(200)$. The changing rate of $I(002)/I(200)$ from point O to the point C reflects only the feature of 90° domain wall reorientation.

The Case 2

When the intensity of electric field is decreased from the point C to point D, the domain polarization turns back to the nearest easy direction in the favour of lowering the internal energy. If the applied electric field is increased further in the minus direction from the point D to point F, the domain polarizations pointing in the plus direction are reversed. This may involve both the 90° and 180° domain switching processes. Thus, from eqs.(2) and (3), we have

$$R|_{D \rightarrow F} = \frac{I(002)}{I(200)} = \frac{n_1[90^\circ] I_p(002) + n_2[180^\circ] I_p(002)}{g_1[90^\circ] I_p(200)} \quad (7)$$

where, $n_1 + n_2 + g_1 = 1$. It should be noted that no 180° domain reversal occurs in the direction perpendicular to the applied field. Thus, eq.(7) can be expressed as

$$R|_{D \rightarrow F} = \frac{I(002)}{I(200)} = \frac{n_1[90^\circ] I_p(002) + n_2[180^\circ] I_p(002)}{g_1[90^\circ] I(200)} \quad (8)$$

$$= (n_1 + g_1) \alpha; \text{ where: } \alpha = \frac{[n_1[90^\circ] I_p(002) + n_2[180^\circ] I_p(002)]}{g_1[90^\circ] I_p(200)(n_1 + g_1)}$$

where: $(n_1 + g_1) = (1 - n_2)$, which is the volume fraction of total 90° domains in the material. α is the ratio of diffractive intensity with the unit volume of per 90° domain. α is also a function of electric field and dependent upon the entire domain polarization reversal process. Precisely speaking, since only the $(n_1 + g_1)$ portion of 90° domains contributes to the diffraction intensity of R (or $I(002)/I(200)$) in eq.(8), thus, the contribution of 90° domains to R in the process from point D- point F should not be exactly the same as that to the intensity R in the process from point O- point C. In order to compare the features of these two domain reversal processes, we can define that the changing rate of diffraction intensity is the same within the unit volume of per 90° domain with respect to these two domain switching processes. Therefore, from eq.(8), one should have

$$\left. \frac{dR}{dE} \right|_{D \rightarrow F} = (n_1 + g_1) [90^\circ] \alpha \quad (9)$$

$$= (n_1 + g_1) [90^\circ] \left. \frac{dR}{dE} \right|_{O \rightarrow C}$$

Naturally, unlike eq.(6), which describing a pure 90° domain wall reorientation process, it can be found that from eq.(9), the changing rate of R as a function of the electric field will also be affected by $(n_1 + g_1)$. Obviously, if $(n_1 + g_1)$ is equal to 1, the polarization reversal process will be a pure type of 90° domain one and eq.(9) will become exactly the same as eq.(6). In contrast, if $(n_1 + g_1)$ is equal to zero, this means that no 90° domain reversal will

occur, and no X-ray information can be obtained. Eq.(9) is an approximate expression which is precisely valid only if large amounts of 90° domains are involving in the polarization switching processes. The detail discussions can be found in Ref.[7]. Compared to eq.(9) and eq.(6), it could be asserted that if 90° domain wall reorientation is the main process in the polarization switching process from point D to point F, the changing rate of the measured ratio dR/dE would be slightly less than those from the point O to the point C according to eq.(9). In other words, the feature of domain reversal process from point D to point F is most likely a pure type of 90° domain reorientation between point D and point F. Conversely, if 180° domains are predominantly involving the polarization reversal process from the point D to the point F, the changing rate of the measured dR/dE would be much smaller than that from point O to point C because of the small $(n_1 + g_1)$. Here we assume the internal energy states at points O and D are the same. This assumption is, in practice, almost fulfilled. In short, eq.(9) could be used as the criterion for qualitatively evaluating the characteristics of the dynamic behavior of domain reorientation processes in ceramics in terms of X-ray analysis techniques.

3.2. Experimental Results and Conclusions

In practice, in order to sort out the mechanisms of domain reorientation in the ceramic specimens, we have to examine both the features of the dependence of $I(hkl)$ as a function of applied electric fields and the changing rate of $I(002)/I(200)$ as a function of the applied electric field (or $d\{I(002)/I(200)\}/dE$) in some details. Fig.4. show the XRD profiles of (002) and (200) peaks for plate PZT samples in the case of different polarization orientations. It can be seen from Fig.(4a) that when the normal direction of the plate is perpendicular to the polarization direction, the (200) peak is much higher than the (002) peak of the sample. Conversely, for samples with the normal direction of the plate parallel to the poling direction,

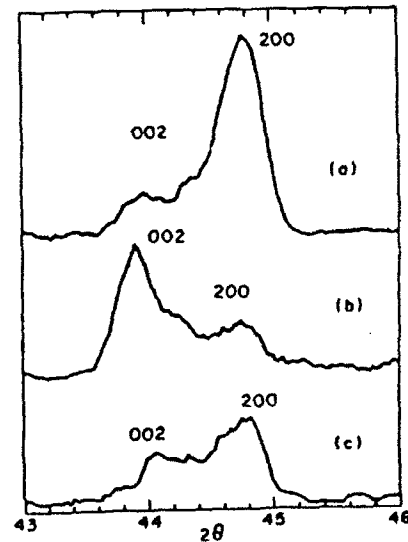


Figure 4. The XRD profiles of (002) and (200) peaks for plate PZT samples of different orientation of polarization. (a) X-ray intensity profile of a poled ceramic plate sample with its normal direction perpendicular to the poling direction. (b) X-ray intensity profile of a poled ceramic plate sample with its normal direction parallel to the poling direction. (c) X-ray intensity profile of an unpoled ceramic sample.

as shown in Fig. (4b), the (002) peak is much higher than (200) peak. Fig. (4c) is the case of an unpoled sample. Since no preferred orientation exists, the intensity of (200) peak is about twice as that of (002) peak.

Fig. 5. presents the ratio $I(002)/I(200)$ as a function of the applied electric field in the case (II) of Fig. 2. In Fig. 5, the magnitude of the applied electric field at points D and D' are almost exactly equal to the coercive fields of the P-E (polarization-electric field) hysteresis loop and S-E (strain-electric field) hysteresis loop measured at ultra-low frequency.

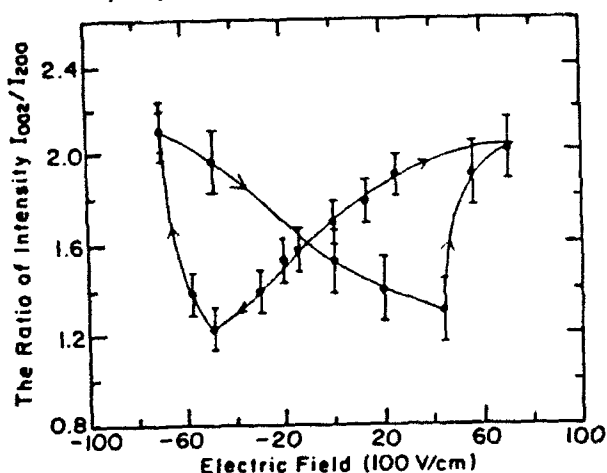


Figure 5. The ratio of $I(002)/I(200)$ as a function of the applied electric field for the case II of Fig. 2.

Since the ratio $I(002)/I(200)$ represents the characteristics of 90° domain reversal, it indicates that the coercive field of polarization switching is closely related to the 90° domain reversal in this ceramic sample.

Fig. 6 presents the ratio of $I(002)/I(200)$ as a function of the applied electric field from point O to point D' for the case I of Fig. 2.

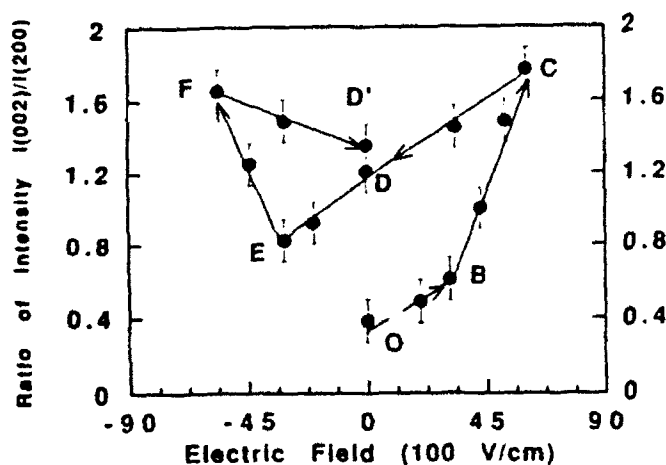


Figure 6. The ratio of $I(002)/I(200)$ as a function of the applied electric field for the case I of the Fig. 2.

As discussed above, from the point O to point C, the domain reorientation is a pure 90° domain type. If polarization reorientations involving both the 180° and 90° domain reversal processes from point D to point F, then the slopes of $I(002)/I(200)$ as a function of electric fields from the point D to the point F should be substantially smaller than those from point O to point C. The slopes of the dR/dE in the Fig. 6, are listed in the Table I.

Table I. Changing rate of $I(002)/I(200)$ v.s. the applied electric field for the cases of Fig. 6

Lines	Slopes
O---B	$(0.95 \pm 0.2) \times 10^{-2}$
B---C	$(4.2 \pm 0.3) \times 10^{-2}$
D---E	$(1.1 \pm 0.2) \times 10^{-2}$
E---F	$(3.2 \pm 0.3) \times 10^{-2}$

From Table I, it can be clearly found that there is no substantial difference in the absolute values of the slopes between the O-B line and the D-E line or between the B-C line and the E-F line. This argument strongly suggests that the entire polarization reorientation process from point O to point F is predominantly controlled by the 90° domain reversal process. In other words, eq. (9) could be approximately satisfied by the experimental data. The estimated value of $(n_1 + g_1)$ is around 0.7 - 0.8.

Therefore, it can be concluded that the 90° domain reorientation plays a major role in terms of the polarization switching in the PZT bulk ceramic with the composition within the morphotropic phase boundary.

Acknowledgements

This research has been supported in full by the Office of Naval Research.

Reference

1. N.B. Chaim, M. Brunstein, J. Grunberg and A. Seidman, "Variations of the Dielectric Constant of PZT Ferroelectric Ceramics with Electric Field", *Ferroelectrics*, Vol. 6 pp299-305 (1974) and "Electric field dependence of the dielectric constant of PZT ferroelectric ceramics", *J. Appl. Phys.* Vol. 45(6) pp2398-2405 (1974)
2. N.A. Schmidt, "Coercive Force and 90° Domain Wall Motion in Ferroelectric PLZT Ceramics with Square Hysteresis Loops", *Ferroelectrics*, Vol. 312 pp105-112 (1981)
3. P. Gerhlsen and G. Kruger, "Coercive Field in Fine-Grained PLZT Ceramics", *Ferroelectrics* Vol. 11 pp489-492 (1976)
4. G. Kruger, "Domain Wall Motion Concept to Describe Ferroelectric Rhombohedral PLZT Ceramics", *Ferroelectrics* Vol. 11 pp417-422 (1976)
5. N. Uchida and T. Ikeda, "Temperature and Bias Characteristics of $\text{Pb}(\text{Zr}, \text{Ti})\text{O}_3$ Families Ceramics", *Jan. J. Appl. Phys.* 4 (11) pp867-874 (1965)
6. Y. Masuda and A. Baba, "D.C. Bias and Frequency Dependence of the Dielectric Constant PZT Family Ferroelectric Ceramics", *Jan. J. Appl. Phys.* Vol. 24 pp113-116 (1985)
7. Shaoping Li, "Extrinsic Contributions to the Response in Ferroelectric Ceramics", Ph.D. Thesis, Penn State University, 1992
8. J. Mendida and L. Pardo, "A XRD Study of 90° Domains in Tetragonal PLZT Under Poling", *Ferroelectrics*, Vol. 54 pp199-203 (1984)
9. Y.W. Zeng, W.R. Xue and G.F. Fu, "Investigation on Switching Behavior of 90° Ferroelectric Domains in $(\text{Pb}_{0.85}\text{Sm}_{0.10}\text{Ti}_{0.05}\text{Mn}_{0.02})\text{O}_3$ Piezoelectric Ceramics of Ultra-High Electromechanical Anisotropy by the X-ray diffraction Technique", *J. of Mat. Sci.* 22 pp4294-4299 (1991)

APPENDIX 15

Quasi Lumped Parameter Method for Microwave Measurements of Dielectric Dispersion in Ferroelectric Ceramics

Shaoping Li, Sheen Jyh, Q. M. Zhang, Sei-Joo Jang, A. S. Bhalla and L. E. Cross

Materials Research Lab., Penn State University, University park, PA 16802

Abstract

In this work, a modified lumped parameter method has been discussed which, we believe, is especially suitable for microwave measurements of dielectric dispersion in high dielectric materials in a particular frequency region. The method combines some of the features of both the lumped parameter method and the distributed parameter method. Dielectric dispersions for $\text{PbZr}_{1-x}\text{Ti}_x\text{O}_3$, BaTiO_3 and $\text{Ba}_x\text{Sr}_{1-x}\text{TiO}_3$ ceramics in the frequency domain from 1 MHz to 1 GHz are presented. This paper also discusses the principle of the measurement and the accuracy of the experimental data which is retrieved.

1. Introduction

Dielectric properties of ferroelectric materials and their frequency dependence are of great importance in many applications. Dielectric dispersion in ferroelectric materials has been measured and discussed by many authors [1-6]. The measurement of relative dielectric constant (ϵ') and loss tangent ($\tan\delta$) in ferroelectric materials at microwave frequencies is made difficult by the large dielectric constant and loss tangents exhibited by these materials. In general, high frequency dielectric measurement techniques are mainly divided into two sections, (1) the transmission techniques, and (2) the resonant techniques, among which only the transmission techniques have the swept frequency capability. The transmission techniques for microwave measurements on dielectric samples can be classified into two categories. One is the lumped capacitance method and the other is the distributed parameter method. In practice, however, the microwave measurements for high dielectric materials in the frequency range 100 MHz -- 2 GHz can not be made accurately by either of these two methods, even though the microwave equipments have been improved significantly in the past few decades. The objective of this study is to measure the dielectric dispersions of high dielectric constants materials at the frequency range 1 MHz- 2 GHz.

II. Limitations of Conventional Methods

In the lumped capacitance method, a dielectric sample was placed on the end of a shorted coaxial line and the complex reflection coefficient was measured by the time domain reflectometer (TDR) through the vector-voltage ratio of the reflected wave to the incident wave from the sample [7]

$$\Gamma = \frac{V_{\text{ref}}}{V_{\text{inc}}} = \Gamma_x + j\Gamma_y = |\Gamma|e^{-j\theta} \quad (1)$$

where V_{ref} is the voltage of the reflected wave and V_{inc} represents the voltage of the incident wave. The complex reflection coefficient was a function of the complex permittivity, and thus, the real and imaginary parts of the relative permittivity may be expressed as follows [7,8]

$$\epsilon' = \frac{2|\Gamma|\sin\theta}{\omega C_0 Z_0 (|\Gamma|^2 + 2|\Gamma|\cos\theta + 1)} \quad (2)$$

$$\epsilon'' = \frac{1 - |\Gamma|^2}{\omega C_0 Z_0 (|\Gamma|^2 + 2|\Gamma|\cos\theta + 1)} \quad (3)$$

The basic assumption for the lumped capacitance method is that the electric field is uniform throughout the sample. In other words, this means that the measured reflection coefficient is equal to the intrinsic reflection coefficient of samples, which is caused by the complex permittivity of the sample. If this basic requirement could not be satisfied, the accurate results would not be obtained by using the lumped capacitance method. At higher frequencies, the lumped capacitance method breaks down in several respects. (1) The measured capacitance of the sample cannot be simply related to the real dielectric constant of the sample because of the non-uniform variation of the electric field throughout the sample. In other words, for high dielectric constant materials, due to the wave compression, the basic assumption for the lumped impedance technique loses validity at the high frequency. It is, therefore, required that the thickness of the sample should be around the order of a few percent of a wavelength at the highest frequency of interest in order to obtain rather accurate experimental data. If the material has the dielectric constant around 1000 at the frequency of 1 GHz, the corresponding thickness of the sample should be the order of 100 μm . The other dimensions of specimens should also be much less than the wavelength of light. (2) The fringe field effects [9] and the inability of the measurement equipment also affect the accuracy of measured experimental data severely. At the high frequencies, the fringing fields are usually no longer negligible. The smaller cross section of samples decreases the fringe field, however, machining the sample becomes difficult. In addition, due to the limitations of measurement instruments, the maximum readable capacitance value within 5% accuracy is always limited at the higher frequencies. Detailed discussions can be found in Ref. [13]. On the other hand, it is known that the distributed transmission method does not require the uniform field assumption. In this method, however, the wave guide is the primary medium of microwave propagation. If the cutoff frequency is around 300 MHz, the wave guide dimensions should be around the order of 0.5 m. Nevertheless, it is not reasonable in practical cases.

III. The Principle of the Proposed Measurement Method

As discussed above, due to the influence of fringing fields and the difficulty of sample machining, it is difficult to satisfy the requirement of the critical thickness which is imposed by the assumption of the lumped impedance technique. The question, therefore, arises as to whether or not the lumped impedance method can be modified in order to extend the scope of its applications. Usually, in the high frequency region, the dimension of the sample does not fulfill with the critical requirement of the sample dimension in terms of the basic assumption of the lumped parameter method. Therefore, the measured reflection coefficient is not exactly equal to the intrinsic reflection coefficient of the sample. Hence, the measured reflection coefficient is not solely related to the complex permittivity, which is affected also by the losses and the phase shift of the measuring signal during the electromagnetic wave passing through the sample. In order to overcome these difficulties, accurately describe the measurement situation and make the measurement practical, the measured sample can be considered as a "quasi-transmission" line. Precisely speaking, in this situation we may visualize the measured sample comprising of two parts, as shown in Fig. 1. Part I is a very thin layer, which is thin enough to be equivalent to an ideal lumped capacitance system. The reflection coefficient of this part represents the intrinsic properties of the measured materials. Part II is the rest of the sample (the shadowed area), which is a "lossy transmission line" or a distributed component, and could be described by a simple two-port network, as shown in Fig. 1(c).

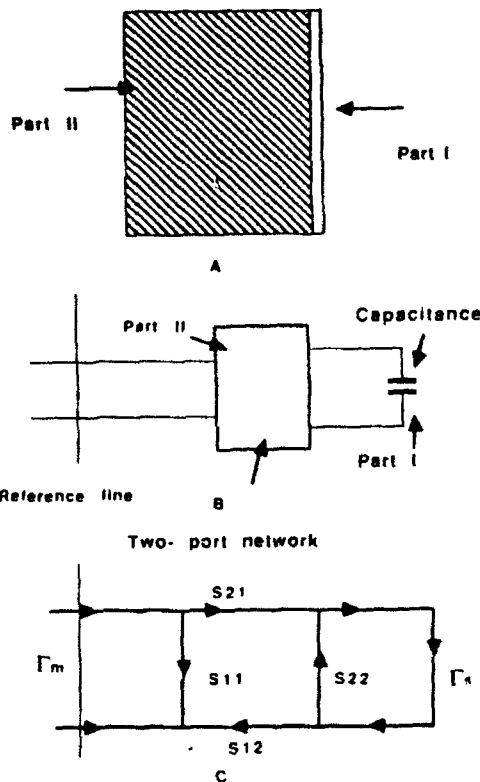


Figure 1. (a) Schematic drawing of the sample imaged as the two parts of a "lossy quasi-lumped transmission line". (b) Equivalent circuit of the real sample. (c) Terminated two-port network with the S_{ij} parameters to describe the nature of the sample.

The equivalent circuits of the specimen are also shown in Figs. 1(b) and 1(c). According to this equivalent circuit, the relationship between the measured reflection coefficient and intrinsic reflection coefficient can be expressed as [10]

$$\Gamma_s = \frac{1}{S_{12}S_{12} + S_{22}} \quad (4)$$

In reality, as long as the thickness of the measured samples does not fulfil the critical requirement of lumped parameter method, it can be considered that part II exists in the measured sample, which will cause attenuation of the signal amplitude and the phase shift of the measured signal when the measured signal goes through the samples. Therefore, by using eq.(4), intrinsic reflection coefficients of the sample can be retrieved and obtained from the measured reflection coefficient provided the S_{ij} parameters are known.

In a simplified case (here we assume $S_{11}=S_{22}$, $S_{12}=S_{21}$), according to the theory of the distributed parameter method [5,11], S_{11} and S_{12} can be expressed in terms of the sum of reflected and transmitted waves and can be numerically evaluated by [11]

$$S_{11} = \rho \frac{1 - \exp(-2\gamma l)}{1 - \rho \exp(-2\gamma l)} \quad (5)$$

$$S_{12} = \frac{[1 - \rho] \exp(-2\gamma l)}{1 - \rho \exp(-2\gamma l)} \quad (6)$$

where

$$\rho = \frac{1 - (\epsilon^*)^{1/2}}{1 + (\epsilon^*)^{1/2}}; \quad \gamma = \alpha + j\beta = j\omega(\mu^* \epsilon^*)^{1/2}$$

and ϵ^* is the relative complex permittivity. From eqs (5) and (6), it is very obvious that when the measurement frequency is very low, S_{11} approaches to zero and S_{12} is equal to 1. Thus, from eq.(4), it can be found that Γ_m is equal to Γ_s . This is the case in an ideal lumped capacitance situation. Fig. 2. presents the theoretical calculations of S_{11} and S_{12} as a function of the frequencies.

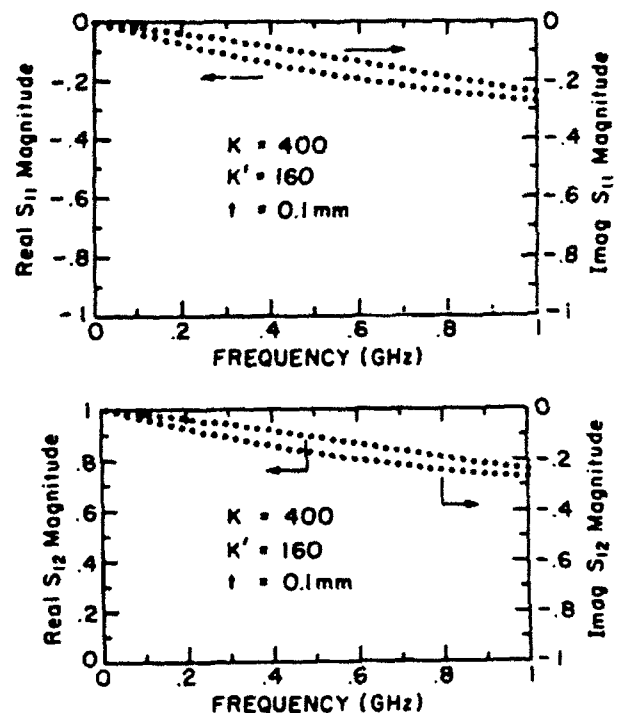


Figure 2. Theoretical calculations of the real and imaginary parts of the S_{ij} parameters v.s. frequency. (a) Theoretical calculated real and imaginary magnitudes of S_{12} (b) The S_{11} versus frequency in the range 1Hz-1GHz.

As discussed above, in the real measurements, if the measured frequencies go up very high, Γ_s will be strongly affected by the electromagnetic wave absorption and phase shift inside part II of the sample. In principle, as long as the influence of part II in the sample is not very large, which may be considered as a small perturbation term in terms of Γ_s , (this condition is always fulfilled in practice), we can obtain the intrinsic reflection coefficient of the sample (Γ_s) by retrieving the measured reflection coefficients (Γ_m) from eq.(4) through the numerical evaluated S_{ij} parameters. Finally, the complex dielectric dispersion ($\epsilon(\omega) = \epsilon' - j\epsilon''$) can be obtained from the intrinsic reflection coefficient of the sample Γ_s by

$$\epsilon^* = \frac{(1 - \Gamma_s)}{[(1 + \Gamma_s) 2 \pi f C_0 Z_0]} \quad (7)$$

where Z_0 is the characteristic impedance of the impedance analyzer $C_0 = \epsilon_0 a/d$

IV. Experimental Results and Discussions

The $\text{Pb}(\text{Zr}(\text{Ti}-x)\text{O}_3)$, BaTiO_3 and $\text{Ba}_{0.5}\text{Sr}_{0.5}\text{TiO}_3$ ceramics were prepared by the conventional mixed-oxide process. The samples were cut to approximately the plate shape. Their dimensions were much smaller than the wavelength of light. Before making the electrodes, the surfaces of specimens were polished, etched and annealed in order to keep the contributions of surface layer low. The complex reflection coefficient of the sample was recorded with HP 4191A impedance analyzer, with a test frequency range from 1 MHz to 1 GHz. The frequency dependence of dielectric constants and their losses for PZT ceramics are shown in Fig 3.

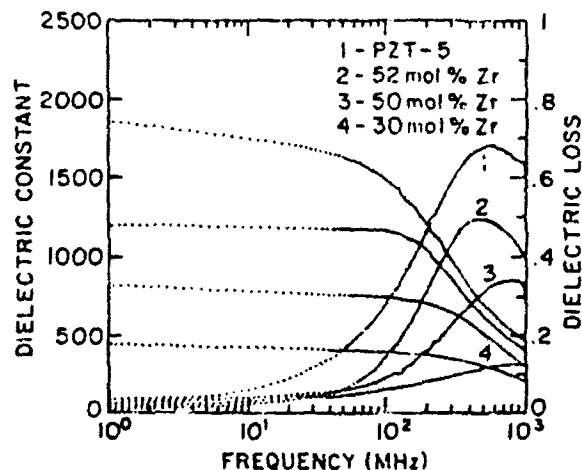


Figure 3. Dielectric constants and losses vs. frequencies in the PZT system.

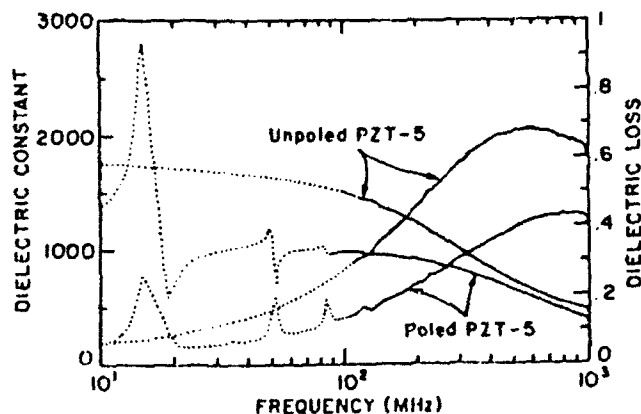


Figure 4. The dielectric dispersion in poled and unpoled PZT ceramics.

These results are similar to those of previous investigations [1]. From our results, however, it can be found that the minimum relaxation frequency (or the resonance frequency of domain wall motions) occurs in the ceramic with the composition near the morphotropic phase boundary. These experimental data are useful for estimating the effective mass of domain wall motions [13]. Fig 4 shows the dielectric dispersions of both poled and unpoled PZT ceramic samples. The piezoelectric resonances can be clearly observed at very high frequency (around 100 MHz) due to the sample dimensions, implying that the measured data are reliable.

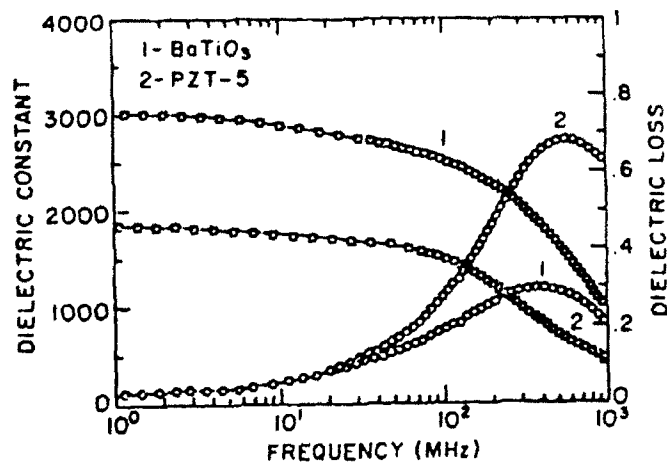


Figure 5. The dielectric dispersion in PZT-5 and BaTiO_3 ceramics

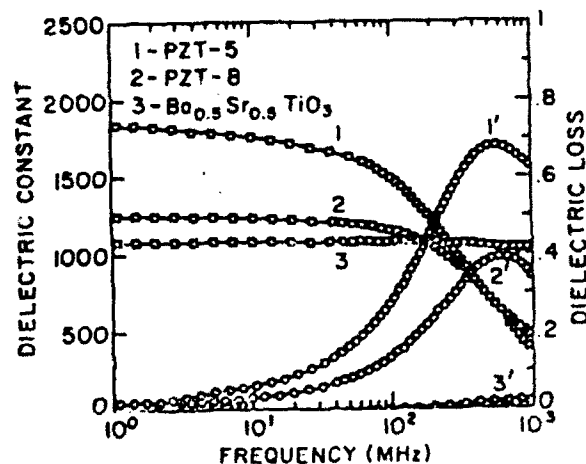


Figure 6. The dielectric dispersion in soft PZT, hard PZT and $\text{Ba}_{0.5}\text{Sr}_{0.5}\text{TiO}_3$ ceramics

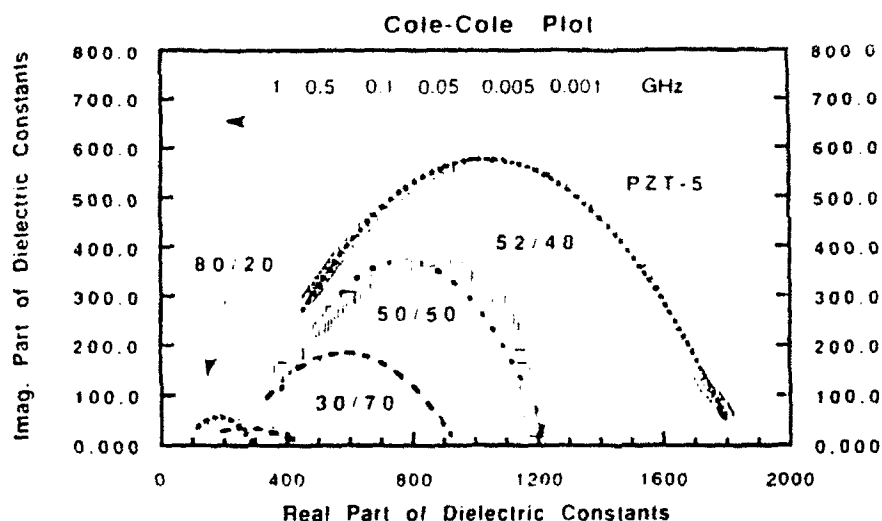


Figure 7 Cole - Cole plot of the complex dielectric constants of PZT ceramics with different Ti concentration

The dielectric dispersion in PZT, BaTiO₃ and Ba_{0.5}Sr_{0.5}TiO₃ have been presented in Figs 5 and 6. It can be found that the real value of dielectric constant of Ba_{0.5}Sr_{0.5}TiO₃ is almost independent of measured frequencies, which is basic consistent with previous studies [5, 12]. It should be noted that since the S_0 parameter was estimated by the initially assumed dielectric constants, and the measurement instruments have some limitations, the measurement error is still rather significant regarding materials with ultra low loss tangents. In fact, at the frequency of 1 GHz, the measured dielectric losses (0.017-0.02) are almost one order of magnitude larger than the true values [5, 12]. FIG 7 presents a Cole - Cole plot of the complex dielectric constants of the PZT system. In summary, a quasi-lumped parameter method is discussed, which is suitable for the impedance measurements of ferroelectric ceramics in a particular frequency range (1 MHz- 2 GHz).

Acknowledgement

Authors thank Dr. U. Selvaraj for supplying the sol - gel powders of Ba_{0.5}Sr_{0.5}TiO₃ for ceramic sample preparation. This research was supported by the Office of Naval Research.

References

1. O. Kersten and G. Schmidt, "Dielectric Dispersion in PZT Ceramics", *Ferroelectrics* Vol 67, pp191-197 (1986)
2. A.V. Turik, K.R. Chernshov and V.D. Komarov, "Dielectric Dispersion in Ferroelectrics with Perovskite Structure over the Meter-Wave Range", *Ferroelectrics* Vol 6 pp45-47 (1973)
3. M.M. Maglione, R. Bohmer, A. Loidl and U.T. Hochli, "Polar Relaxation Mode in Pure and Iron-Doped Barium Titanate", *Physical Review B*, Vol. 40(16) pp11441- 11444 (1989)
4. Y.M. Poplavsk, V.G. Tsykalov, and V.I. Molchanov, "Microwave Dielectric Dispersion of the Ferroelectric and Paraelectric Phases of Barium Titanate", *Sov. Phys. Solid State* Vol 10, pp2708-2712 (1969)
5. M.T. Lanagan, "Microwave Dielectric Properties of Antiferroelectric Lead Zirconate", Ph.D. Thesis, The Pennsylvania State University (1987)
6. Von Hippel A.R. "Ferroelectricity, Domain Structure, and Phase Transitions of Barium Titanate", *Revs. Modern Phys.* 22(3) pp221-237 (1950)
7. S.S. Stuchly et al., "Permittivity Measurements at Microwave Frequencies Using Lumped Elements", *IEEE Trans. Instrum. Meas.* Vol IM-23 pp56-62 (1974), "A Combined Total Reflection-Transmission Method in Application to Dielectric Spectroscopy", *IEEE Trans. Instrum. Meas.* Vol IM-27 pp 285-288 (1978); "A Lumped Capacitance Method for the Measurement of the Permittivity and Conductivity in the Frequency and Time Domain-- A Further Analysis", *IEEE Trans. Instrum. Meas.* Vol IM-24(1) pp27-35 (1975), and "A Time-Domain Technique for Measurement of the Dielectric Properties of Biological Substances", *IEEE Trans. Instrum. Meas.* Vol IM-21 pp425-430 (1972)
8. T. Ichino, H. Ohkawara, and N. Sugihara, "Vector Impedance Analysis to 1000 MHz", *J. Hewlett-Packard*, pp22-31 (1980)
9. M.F. Iskander and S.S. Stuchly, "Fringing Field Effect in the Lumped- Capacitance Method for Permittivity Measurement", *IEEE Trans. Instrum. Meas.* Vol IM-27 pp107-109 (1978)
10. S.F. Adams, "Microwave Theory and Applications (Prentice-Hall Engle- Wood Cliffs, NJ, 1969
11. Van. Gemert M.J.C., "High- Frequency Time - Domain Methods in Dielectric Spectroscopy", *Phillips Res. Repts.* 28 pp530-572 (1973)
12. J.B. Horton and G.A. Burdick, "Measurement of Dielectric Constant and Loss Tangent in Materials Having Large Dielectric Constants", *IEEE Trans. Microwave Theory Tech* Vol 23, pp873-875 (1968) and U. Syamaprasad, R.K. Galgali and B.C. Mohanty, "Dielectric Properties of the Ba_{1-x}Sr_xTiO₃ System" *Materials Letters* 7 (1988) pp197-201
13. Shaoping Li, "Extrinsic Contributions to the Response in Ferroelectric Ceramics", Ph.D. Thesis, Penn State University, 1992